Submerged supersonic air intakes

An experimental investigation and inviscid study into their performance

K.J.W. Kwakman

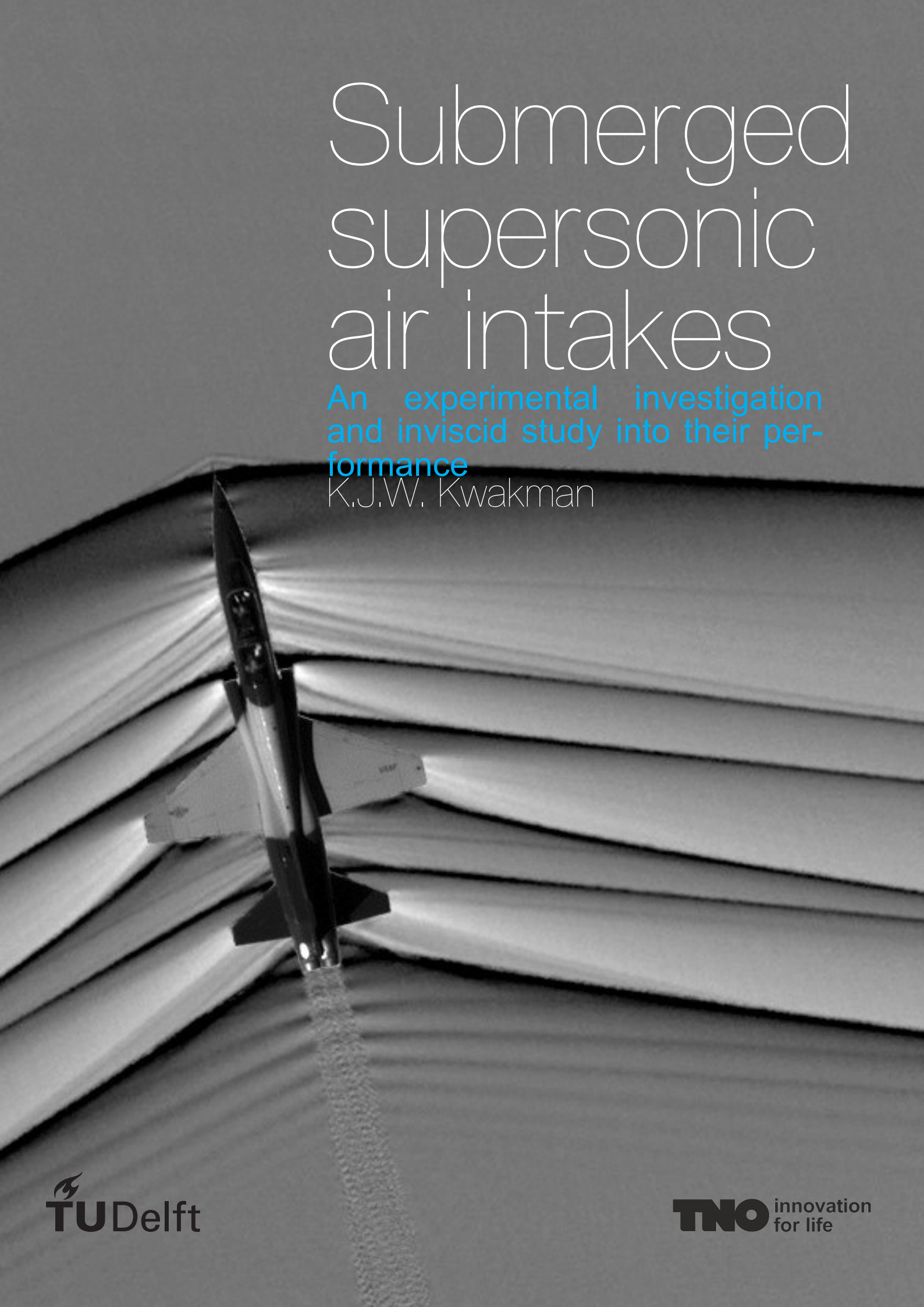

TU Delft

TNO innovation for life

Cover photo by NASA: https://technology.nasa.gov/patent/TOP2-271

Submerged supersonic air intakes

An experimental investigation and inviscid study into their performance

by

Koen Johannes Wilhelmus Kwakman

to obtain the degree of Master of Science
at the Delft University of Technology,
to be defended publicly on 26 June 2019.

Student number:	4091817	
Project duration:	29 January 2018 – 26 June 2019	
Thesis committee:	Dr. ir. B. W. van Oudheusden	TU Delft, committee chair
	Dr. ir. F. F. J. Schrijer,	TU Delft, supervisor
	Ing. R. G. Veraar,	TNO, external supervisor
	Dr. ir. E. Mooij,	TU Delft

This thesis is confidential and cannot be made public until 26 June 2019.

TU Delft

TNO innovation for life

Abstract

Since ramjet propulsion eliminates the need for oxidizers, it provides an alternative to classic rocket engines for missiles and projectiles. However, to capture free-stream air, ramjet engines require large supersonic air intakes, which can be an operational nuisance. A possible alternative is to make the supersonic intakes flush with the vehicle body by "submerging" them into the side of the fuselage: a Submerged Supersonic Intake (SSI). Due to supersonic expansion, submerging will incur some aerodynamic losses, which will lead to reduced ramjet engine performance. To assess the feasibility of SSI's, finding the magnitude of SSI performance losses compared to regular supersonic intakes is necessary.

The performance losses involved with submerging a supersonic intake can be found by finding the upper limit of the SSI operational domain, which this report aims to do in two ways. The first is to investigate performance losses by an inviscid study into SSI performance characteristics and the thrust coefficients of ramjets equipped with SSI's, to find the theoretical maximum to SSI performance. The second way is to carry out an experimental campaign to validate an existing viscous analytical model: the Submerged Ramjet Intake Model (SRIM), which may later be used in optimizing SSI's, to include viscosity into the analysis.

The experimental campaign focused on measuring the total- and static pressure, mass flow and Mach number, as well as visualizing the flow in the SSI models. Two different SSI geometries were produced to conduct experiments in the ST-15 wind tunnel at Delft University of Technology. Measurements of static pressure and schlieren visualization were successfully performed. Partical Image Velocimetry (PIV) was planned, but turned out to be impossible due to hardware limitations. To compensate for the lack of velocity measurements from the canceled PIV measurements, a method was devised to derive the Mach number in the SSI model internal channel from the schlieren images, from which mass flow and total pressure could be computed.

The experimental results were used to validate the SRIM. Overall, the SRIM showed good agreement with the experimental results, with differences of 5% at the highest for the most important intake characteristics of mass flow and total pressure recovery. Although some discrepancies and uncertainties remained, which were studied and used suggest future experiments and improvements to the SRIM.

An inviscid study was also performed. Using a routine to compute optimal inviscid intake performance, the maximum attainable total pressure ratios of regular and submerged intakes were computed. It was found that with increasing Mach number and expansion angle, SSI performance quickly deteriorates. More important, however, is the effect of submergence on the ramjet engine thrust capabilities. An inviscid thrust coefficient analysis was conducted which showed that the reduced total pressure ratio of submerged supersonic intakes has limited effects on thrust coefficient. However, it became apparent that reduced capture area due to the supersonic expansion has a much larger influence on the thrust coefficient when comparing submerged and regular intakes of similar size.

This report provides two methods of computing the consequences of submerging a supersonic intake in terms of performance. An inviscid method was presented to use in early stages of missile design, and an existing quick analytical model with viscous capabilities was validated so that it may be used in optimization schemes for more detailed analysis. Using these tools missile designers can assess whether the operational gains of submerging a supersonic intake outweigh its losses.

Preface

This document marks the end of my thesis work and it would not have been what it is today without the help of some amazing people. The first being my group of supervisors, Ronald Veraar, Ferry Schrijer and Bas van Oudheusden, all of whom I had the chance to get to know on a personal level, which made this project all the more bearable. I would like to thank Ronald for helping me by granting me access to his extensive knowledge of ramjet engines and their supersonic air intakes, which he always managed to explain in a very comprehensive manner, something that I found to be no mean feat. I also very much appreciated his frequent words of encouragement. Ferry was a great help in setting up complicated measurement systems and post-processing heaps of data - which I barely knew anything about - and gave me invaluable feedback in the process of writing this document. The slightly more outside perspective of Bas never failed to give me very useful insights, both content-wise as well as in managing the vast amounts of work to be done.

The second group of people who played a huge part in the realization of this work are the technicians in the High Speed Lab, part of the faculty of Aerospace Engineering at Delft University of Technology. Especially Peter Duyndam, Dennis Bruikman and Frits Donker-Duyvis. Frits was the key factor in planning experiments and making the drawings required to produce the wind tunnel models used in the experimental campaign. Without his expertise no experiment would have ever happened. Then there are Peter and Dennis, who helped with wind tunnel operations, such as changing nozzle blocks and running the wind tunnel. Their technical insight and expertise were essential to the success of the experiments, just like their endless patience with my amateurism at the start of the experimental campaign.

The third group I would like to thank are my fellow interns and colleagues at TNO for their support and help in small things, but especially for the opportunity to take a first-hand look into the inner workings of a professional engineering environment. Their enthusiasm for their work was very contagious and I am certain that the lessons I learned from them will help me in my future career.

Then there are the basement residents, who I have gotten to know very well in the last few months. During the long weeks of data-processing and writing it was a great consolation to have friends in the same situation since, as they say: trouble shared is trouble halved. I thank you for sharing my burden.

Since this document also marks the end of my time as a student, I also want to thank some people who made my student life unforgettable, which I would like to do in my native language.

De realiteit liep achter bij de ambitie.

S.J.B.M. Bastiaansen

Bovenstaande woorden bezigde mijn goede vriend Sjoerd in een gesprek waar ik voor de zoveelste keer aan het klagen was over het feit dat het maar niet opschoot met (een deel van) mijn thesisproject. Ik vond in deze quote veel gelijkenissen met verscheidene elementen van mijn thesis: tekeningen die niet goed waren, onderdelen die te laat kwamen en schrijven dat significant langer duurde dan gepland. Stuk voor stuk bronnen van vertraging, die overigens lang niet altijd aan overmacht te wijten waren. Toen ik langer nadacht over deze woorden vond ik dat ze ook erg goed aansluitten bij mijn studententijd in het algemeen. Alleen, na verdere analyse van de vertragingsbronnen in mijn studententijd kon ik slechts concluderen dat deze bijna alleen maar een positieve invloed hebben gehad. Te weten: De jongens van HJC Überhaupt, aan wie ik vrienden voor het leven heb. De jongens en meisjes van D.S.B. 't Vatt, die een zeer grote (en grotendeels goede) invloed hebben gehad op mijn vorming als persoon. Bestuur 50 van de VSSD, van wie ik lessen heb geleerd die ik in geen collegebank had kunnen opdoen. KAKO 2017, met wie ik door intense samenwerking een band heb gesmeed waar ik nog steeds van geniet. Al deze mensen en anderen hebben een enorme bijdrage geleverd aan mijn ervaringen als student, en zonder hen zou mijn studententijd zeer waarschijnlijk korter, maar zeer zeker minder

memorabel geweest zijn.

Afsluitend is daar nog mijn lieve vriendin Megan, die voor heel wat prettige afleiding heeft gezorgd tijdens dit enorme project. Bedankt voor het bankhangen, de uitjes en je eeuwige geklets. Het was allemaal erg welkom als ik even mijn gedachten moest verzetten. Mijn broertje Jos, die ook in Delft studeert en er zeer waarschijnlijk (en gelukkig voor mijn ouders) niet zo lang over gaat doen als ik. En als laatste, maar wel het belangrijkste, mijn ouders: Wim en Rina Kwakman. Zonder hun onvoorwaardelijke steun op alle denkbare vlakken had ik het nooit zover kunnen schoppen. Er zijn door het bovenstaande ongetwijfeld momenten geweest waarin ze me hadden kunnen schieten, maar ondanks alles hebben ze altijd voor me klaar gestaan, waarvoor ik ze nooit genoeg zal kunnen bedanken.

K.J.W. Kwakman
Delft, June 2019

Contents

List of Figures

List of Tables

Nomenclature

Abbreviations

AAM	Air-to-Air Missile
CAD	Constant-Area Duct
MBDA	Matra BAE Dynamics Alenia
MDM	Modified Diffusion Model
PIV	Particle Image Velocimetry
PS	Pseudo-shock
SRIM	Submerged Ramjet Intake Model
SSI	Submerged Supersonic Intake
TNO	Netherlands Organisation for Applied Scientific Research (Dutch: Toegepast Natuurwetenschappelijk Onderzoek)

Greek symbols

β	shock angle
χ	limiting contraction ratio
δ_0^*	upstream boundary layer displacement thickness
η_K	intake kinetic efficiency
η_n	exhaust nozzle kinetic efficiency
η_R	intake total pressure ratio
η_{cc}	combustion chamber kinetic efficiency
η_{KE}	overall engine kinetic efficiency
γ	ratio of specific heats
μ	Mach angle
ν	Prandtl-Meyer angle
θ	expansion angle
φ	flow displacement angle

Roman symbols

$\dot{m}$	mass flow
A	cross-sectional area
D	hydraulic diameter
f	friction coefficient
F	force

F_n net thrust

L interaction length

L^* non-dimensional interaction length

l_B separation bubble length

M Mach number

m mass

M_{ω_∞} Mach number downstream of spilt normal shock

n total number of shocks

p pressure

q_e upstream dynamic pressure

R specific gas constant for dry air

Re Reynolds number

S_e^* separation state criterion

T temperature

t time

V velocity

Super- or subscripts

$'$ supersonic core region of pseudo-shock

$''$ subsonic outer region of pseudo-shock

0 quantity of free-stream air flowing into the engine

∞ Free stream conditions

* sonic conditions

c capture area conditions

cad constant area duct

e quantity at engine exit

r regular supersonic intake

s submerged supersonic intake

sc supercritical intake operating conditions

t total conditions

$throat$ throat conditions

v valve conditions

1

Introduction

Recent years have seen the adaption of ramjet engines into air-to-air missiles (AAM). Whilst ramjet engine technology is rather dated, it proves to be a viable alternative to regular rocket motors. Examples are the MBDA Meteor [28], shown in Figure 1.1, and the Nammo Solid Fuel RamJet projectile, shown in Figure 1.2, the latter being fired from a 155mm artillery gun. Since ramjet engines use atmospheric air as oxidizer, total propellant weight can be reduced significantly compared to traditional rocket motors. The reduced propellant weight can result in increased payload, speed or range. Ramjet engines are well suited to missiles and projectiles because of their simplicity, which reduces the cost of a single round of ammunition, opposed to more complex forms of propulsion. Implementing a ramjet engine means that a supersonic air intake has to be placed somewhere on the vehicle. Conventionally, a supersonic intake is located at the nose of the projectile, where it is placed in the undisturbed free-stream flow. The Nammo Solid Fuel RamJet projectile shown in Figure 1.2 is an example of a nose-mounted supersonic intake. Nose-mounted supersonic intakes pose a challenge for the implementation of guidance and control hardware, which is typically also located in the nose, and is often essential to the accuracy of projectiles designed for long range. Alternatively, the air intakes can be located in scoops on the side of a missile, like the MBDA Meteor missile in Figure 1.1. Here, some fuselage interference occurs, which can be limited by offsetting the intakes at sufficient distance from the fuselage. However, such side-scoops, or regular intakes take space that may be limited, e.g. in the internal weapons bay of a Joint Strike Fighter, or in the case of gun-fired ammunition, would require sabot[1] rounds, seen in Figure 1.3, which do not utilize the full caliber potential of the gun. Concluding, implementing ramjet engines in projectiles poses two design problems:

- The ideal place for a supersonic intake, the nose, is occupied by essential guidance and control hardware, and
- side-scoop intakes are impractical for space-saving reasons or because the projectile needs to be fired from the barrel of a gun without a sabot.

A possible solution to these design problems is submerging the supersonic air intakes in the side of the fuselage so that they are flush with the vehicle body, such an intake is called a Submerged Supersonic Intake (SSI). Due to aerodynamic effects, mainly supersonic expansion, submerging an intake will incur some losses. The size of these aerodynamic losses is entirely dependent on the efficiency of the submerged supersonic intake, and will also determine the chances of this proposed technology being implemented. Therefore, it is important to find the upper limits of SSI's operational capabilities, which can be done in two ways.

The first way is performing inviscid studies into the aerodynamic losses involved with submerging a supersonic intake. Finding the origins of the losses and quantifying the losses as a function of their origins will provide designers with the tools to determine the maximum attainable efficiencies of SSI's.

[1] A sabot is a device that keeps sub-caliber ammunition in the center of the barrel of a gun. Next to that, it can also serve as a seal to prevent leaking of propellant gases when firing. After exiting the barrel the sabot separates from the projectile.

Figure 1.1: MBDA Meteor missile suspended under a jet fighter wing, taken from [1]

The inviscid intake optimization approach of Oswatitsch [34], for example, provides a very good basis for inviscid studies and for the development of tools that can be used to investigate inviscid intake performance in early design stages.

However, inviscid studies only provide so much information. To enable more complicated design requirements a second way to find the limits of SSI operational capability is needed. Modern day optimization techniques provide a solution. By coupling quick analytical models with optimization schemes, optimal intake geometries can be found for customized design requirements. At TNO, such a quick analytical model was developed to calculate the viscous performance of SSI's, the Submerged Ramjet Intake Model (SRIM). This model is based on a combination of interacting analytical models that have been validated individually. However, due to a lack of readily available experimental data on SSI's the model has not yet been validated in its entirety. A reliable SRIM enables TNO engineers to find SSI geometries optimized to their design requirements. This will facilitate the design process and might ultimately produce the first implementation of a submerged supersonic intake.

Since little literature is readily available on submerged supersonic intakes, it was decided to design and execute an experimental campaign to obtain the necessary data for SRIM validation. This thesis report describes the experimental research and subsequent investigation into the validity of the SRIM. Next to that, this report provides inviscid theories to compute both the SSI's efficiencies and their influence on the entire ramjet engine cycle. Subsequently, both the engine and intake efficiencies are investigated for submerged and regular supersonic intakes to find what the relative losses are and where they originate.

Keeping in mind the above, the research objectives of this thesis work are as follows:

1. Create a better understanding of the performance of a submerged supersonic intake by qualitatively and quantitatively describing the flow using wind tunnel experiments.

2. Determine how the Submerged Ramjet Intake Model relates to reality by comparing its results to the experimental data gathered in the wind tunnel tests.

3. Perform a feasibility study on submerged supersonic intakes by comparing computational and experimental data to the theoretical maximum for both regular and submerged intakes.

These research objectives translate to the following research questions and subquestions.

1. **What is the flow behavior in a submerged supersonic intake?**

   To accurately describe the flow in a submerged supersonic intake the flow must be measured qualitatively and quantitatively. From this information performance characteristics can be determined and - at a later stage - compared to regular intake performance and results from the SRIM.

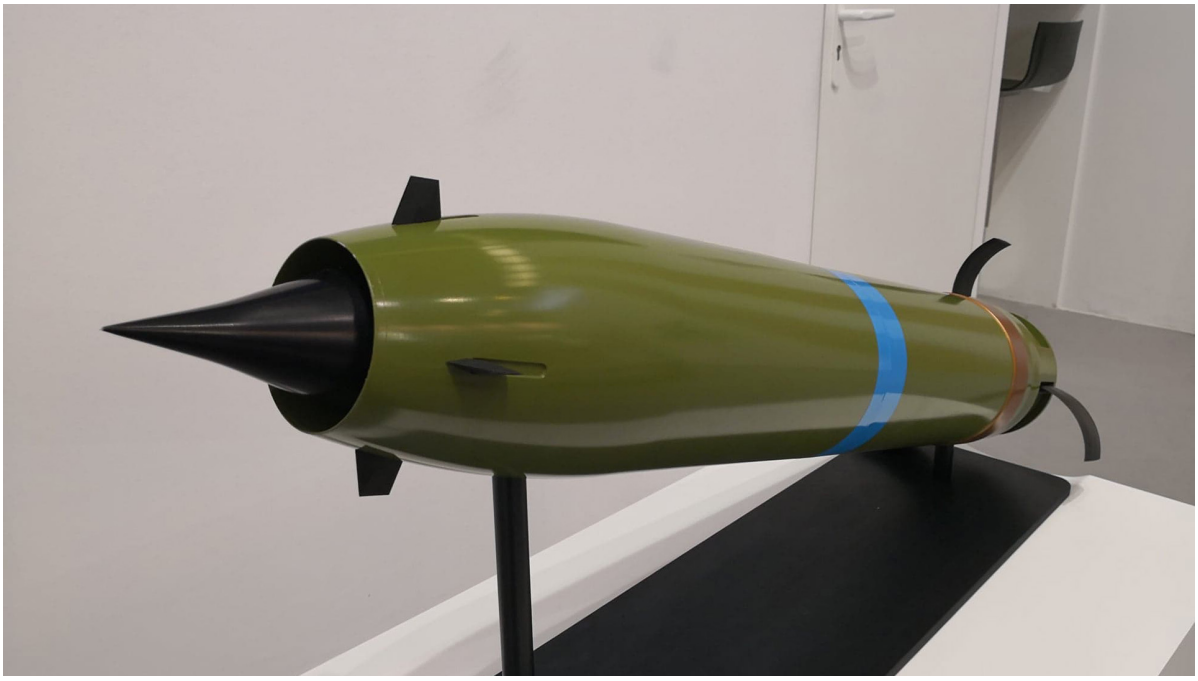

Figure 1.2: Mock-up of a Nammo Solid Fuel Ramjet 155mm projectile, taken from [2]

(a) Sub-caliber projectile with sabot, taken from [3]

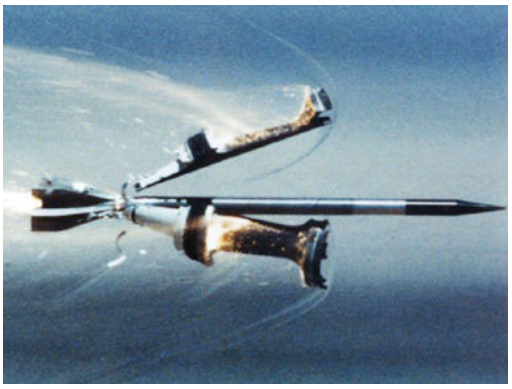

(b) Sabot separation after projectile leaves the barrel, taken from [4]

Figure 1.3: Sabot ammunition

(a) *What are the flow characteristics in the submerged supersonic intake?*
Visualize the flow in the intake to identify relevant flow phenomena that occur, such as the expansion, oblique shock system and pseudo-shock.

(b) *What are the performance characteristics of the submerged supersonic intake?*
To determine the overall performance of the submerged supersonic intake, quantitative data is needed. Find the values for:

i. Total and static pressure recovery
ii. Mass flow at the end of the internal channel
iii. Mach number at the end of the internal channel

(c) *What is the flow behavior around the different individual components of the intake?*
The complete intake needs to be measured as well as all its components individually to see the interaction between the components.

2. **What are the differences between the experimental data and the results from the Submerged Ramjet Intake Model?**

To determine the accuracy of the SRIM, possible differences between experimental and computational data need to be studied to find the reason behind their occurrence. When the causes of the differences are clear they may be used to improve the SRIM.

(a) *What are differences in flow behavior?*
Flow patterns modelled in the SRIM, such as the boundary layer behavior, shock wave boundary layer interaction and pseudo-shocks should be comparable to the experimental data. If they are not, what causes this?

(b) *What are differences in intake performance?*
How does the submerged intake compare to its analytical counterpart w.r.t. performance characteristics such as (total) pressure recovery, flow deceleration, mass flow, etc.?

(c) *Can the differences in flow behavior and intake performance be used to improve the SRIM?*
With the insights gained in the experimental investigation, can the SRIM be improved to calculate the performance of a submerged supersonic intake more accurately?

3. **What are the differences between a submerged- and regular supersonic intake?**

To assess the feasibility of the submerged supersonic intake as an alternative for a regular supersonic intake, the differences in flow behavior and performance need to be investigated.

(a) *What are the losses that follow from submerging a supersonic intake and are they acceptable?*
To assess the feasibility of the submerged supersonic intake as an alternative for a regular supersonic intake, the differences in optimal performance need to be investigated.

(b) *Can Oswatitsch's method be used to design a submerged intake?*
Oswatitsch [34] presents a simple method to design an optimal inviscid intake. This might be used to design a submerged supersonic intake. What limitations does a submerged intake impose on the Oswatitsch method?

(c) *What are the maximum attainable (inviscid) efficiencies of submerged and regular intakes?*
To get an idea of the losses involved with submerging an intake, inviscid models can be used to predict the upper limit of submerged and regular intake performance.

(d) *How does the performance of a submerged supersonic intake compare to the inviscid performance of a regular intake?*
To find if submerging an intake is feasible the relative losses need to be known.

This thesis report seeks to answer the above research questions in the following way. First, Chapter 2 will cover some basic supersonic intake knowledge and establish a baseline for supersonic intake performance, based on several sources for computational and experimental data. The Submerged

Ramjet Intake Model and the workings of its submodels will also be introduced. Chapter 3 will present the methodology and experimental facilities and methods used to obtain the necessary experimental data. Chapter 4 describes the experiments that were done and some challenges which presented themselves, along with the solutions found to deal with them. Chapter 5 presents the data analysis to obtain the necessary results to answer the research questions. In Chapter 6 the comparison is made between the results from the SRIM and the experimental results, both qualitatively and for the quantities mentioned in the research questions. Chapter 7 uses the validated SRIM to make an estimation on the consequences of submerging a supersonic intake on performance of the intake itself and the ramjet engine as a whole. Chapter 8 presents the answers to the research questions that have been found in the experiments and validation of the SRIM. Chapter 9 will provide some recommendations for future work.

2

Supersonic air intake theory

To understand the remainder of this thesis report, a base of knowledge about supersonic air intakes needs to be established. This chapter on supersonic air intake theory aims to do this by introducing several essential topics. First, regular supersonic air-breathing propulsion theory will be discussed, such as thrust equations, aspects of the supersonic intake configuration, operational conditions and loss incurring viscous effects. Second, performance limits will be presented: the theoretical boundaries of the performance domain. Experimental and computational supersonic intake results will also be given. Third, the predicted effect of submerging a supersonic intake will be presented. Using inviscid theory the theoretical losses can be computed. Fourth and final, computational aspects, assumptions and shortcomings of the Submerged Ramjet Intake Model (SRIM) and their consequences for the experimental campaign will be presented and discussed.

2.1. Supersonic intake basics and operations

Establishing the baseline knowledge will start off with general terms and phenomena that are found in supersonic air intakes. This section will present basic knowledge on supersonic intake configurations and operations which will act as a foundation for the rest of supersonic intake theory discussed in this chapter.

2.1.1. Basic thrust equations

The basic thrust equations provide a good place to start discussing supersonic air intake basics. Deriving the basic thrust equation can give a good idea of the influence the intake has on overall engine operations.

The derivation of the basic thrust equation starts with Newtons second and third laws of motion. Using Newton's third law, which states that every force has an equal and opposite force, it can be derived that to propel an airborne vehicle, a force has to be applied to the air surrounding it. In the case of a ramjet, this is done by taking in a mass of air and accelerating it. Therefore, the derivation starts with Newtons second law of motion:

$$F = m\frac{dV}{dt} \tag{2.1}$$

In the case of a moving fluid, as happens in the ramjet engine, both the mass and velocity are dependent of time. Therefore,

$$F = \frac{d}{dt}(mV) \tag{2.2}$$

The change in mass can be written as the *mass flow rate* or $\dot{m}$. Applying the definitions of different stations in the intake shown in Figure 2.1 to this equation, the thrust force produced by the engine can then be written as:

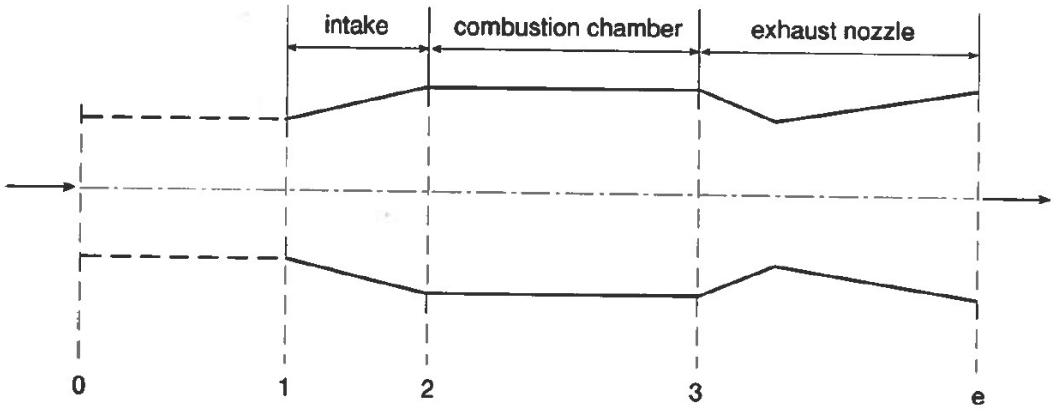

Figure 2.1: Schematic of a ramjet engine with definitions of stations between engine parts, taken from [45]

$$F = \dot{m}_e V_e - \dot{m}_0 V_0 \tag{2.3}$$

Two things are missing from equation 2.3. One, the mass flow at the engine exit equals the mass flow flowing into the engine plus fuel flow into the engine, assuming no mass flow is lost. Two, the pressure difference at the exit which also adds to the engine thrust. Then, equation 2.3 becomes

$$F_n = \left(\dot{m}_0 + \dot{m}_{fuel}\right) V_e + \left(p_e - p_0\right) A_e - \dot{m}_0 V_0 \tag{2.4}$$

Equation 2.4 represents the net thrust of an air-breathing engine. The first two terms on the right hand side are the gross thrust and the last term on the right hand side is known as the ram drag, which is the drag caused by the deceleration of the airflow into the engine.

In most engines, the pressure difference between exit and ambient pressure is low to prevent over- or under-expansion of the jet flow leaving the engine. This results in a relatively low contribution to the thrust from the pressure-area term. The remaining terms indicate the necessity for high mass flow and pressure recovery in intakes. The thrust can be increased by a larger velocity difference between the entrance and exit of the engine, requiring a high pressure ahead of the exit nozzle. An intake with high pressure recovery contributes to a large velocity increase. Assuming the mass of the fuel is relatively small compared to the air, which is usually the case, a high mass flow entering the engine ”magnifies” the velocity difference

2.1.2. Thrust coefficient

The engine thrust as described above is the ultimate measure of the performance of a ramjet engine with submerged intake. However, for comparison amongst intakes, especially regular intakes, the thrust should be non-dimensionalized. Equations to do so were derived by Wittenberg in his comprehensive study on ramjet performance [45]. This section will provide a method to derive the thrust coefficient from data available in this study, drawing heavily from Wittenberg’s material. Using this method will allow for the comparison of performance of submerged and regular intakes in a ramjet engine.

To come up with an equation for the thrust coefficient, Wittenberg non-dimensionalizes the thrust equation given in 2.4. However, the equation is simplified and an ideal ramjet engine is assumed first. This implies two things:

- The mass flow of the fuel is very small compared to the mass flow of air in the engine ($\dot{m}_{fuel} \ll \dot{m}_0$). This means that the term $\dot{m}_{fuel}$ can be dropped from the equation.
- The exhaust nozzle is assumed to have optimal expansion. This means that the static pressure in the exhaust nozzle equals the ambient pressure ($p_e = p_0$), eliminating the pressure-area term from the thrust equation.

These simplifications leave the thrust equation to be:

$$F_n = \dot{m}_0 \left(V_e - V_0\right) \tag{2.5}$$

Non-dimensionalizing with the dynamic pressure q_0 and area of the streamtube entering the engine A_0, one gets.

$$C_F = \frac{F_n}{q_0 A_0} = \frac{\dot{m}_0 \left(V_e - V_0\right)}{\frac{1}{2}\rho_0 V_0^2 A_0} \tag{2.6}$$

Noticing that the mass flow ($\dot{m}_0 = \rho_0 A_0 V_0$) can be divided out, the thrust coefficient becomes:

$$C_F = 2\left(\frac{V_e}{V_0} - 1\right) \tag{2.7}$$

Wittenberg goes on to derive the thrust coefficient as a function of engine overall kinetic efficiency and heat input. The full derivation is omitted here, but can be looked up in [45].

$$C_F = 2\left(\sqrt{\frac{T_{t_3}}{T_{t_0}}\eta_{KE}} - 1\right) \tag{2.8}$$

The heat input ($\frac{T_{t_3}}{T_{t_0}}$) is given in terms of the total temperature ratio of the free-stream conditions and the post-combustion chamber conditions, whilst the kinetic efficiency (η_{KE}) can be defined as the product of the individual efficiencies of the intake (η_K), combustion chamber (η_{cc}) and exhaust nozzle (η_n):

$$\eta_{KE} = \eta_K \eta_{cc} \eta_n \tag{2.9}$$

where:

$$\eta_K = 1 - \frac{1}{\frac{\gamma-1}{2}M_0^2}\left(\frac{1}{\eta_R^{\frac{\gamma-1}{\gamma}}} - 1\right) \tag{2.10}$$

$$\eta_{cc} = 1 - \frac{\left(\frac{p_{t_3}}{p_{t_2}}\right)^{-\frac{\gamma-1}{\gamma}} - 1}{\eta_R^{\frac{\gamma-1}{\gamma}}\left(1 + \frac{\gamma-1}{2}M_0^2\right) - 1} \tag{2.11}$$

$$\eta_R = \frac{p_{t_2}}{p_{t_0}} \tag{2.12}$$

As can be seen from equation 2.11, Wittenberg derives that the combustion chamber efficiency is dependent of the intake efficiency, next to the inflow Mach number and total pressure ratio in the combustion chamber. Since the scope of this report does not include combustion chamber thermodynamics, a typical ratio will be given for the total pressure loss in the combustion chamber, at $\frac{p_{t_3}}{p_{t_2}} = 0.98$. Similarly, the efficiency of the exhaust nozzle is also beyond the scope of this report, but its performance is of influence on the final result for thrust coefficient. Therefore also a typical value of $\eta_n = 0.98$ will be assumed. To keep the comparison between the submerged and regular intakes fair, the assumed values for combustion chamber total pressure loss and exhaust nozzle efficiency will be used for both the submerged and regular intake analysis.

2.8 with its subsequent definitions and assumptions for engine efficiency provides a set of equations with which the thrust coefficient of an engine with a given intake can be derived. A method to design an intake for such a study will be given in Section 2.3.1. With the intake characteristics known, one unknown remains in equation 2.8, which is the heat input in the engine. Assuming a typical value for this is not trivial, therefore Wittenberg came up with the generalized thrust coefficient, given by:

$$\frac{\frac{C_F}{2}+1}{\sqrt{T_{t_3}/T_{t_0}}} = \sqrt{\eta_{KE}} \tag{2.13}$$

Using the generalized thrust coefficient in equation 2.13 eliminates the heat input from the comparison, allowing for a comparison between just the engine characteristics.

2.1.3. Supersonic intake configuration

The high mass flow into the engine needs to be captured by the intake. Supersonic flow entering an intake is compressed in three consecutive stages: the supersonic diffuser which decelerates the incoming flow to a Mach number much lower than the free-stream Mach number. Then the flow enters a constant area duct which houses the terminal shock that decelerates the flow to subsonic velocities. Finally the subsonic diffuser further decelerates the flow. Across the streamtube entering the intake a distinction can be made between the compression surface and cowling, as can be seen in Figure 2.2. The former having shock-generating wedges and typically starting ahead of the latter. However, in some cases no clear distinction can be made between the two. Additionally, a bleed system may be employed to mitigate viscous losses in the intake. This section briefly describes each of these flow devices.

Supersonic diffuser

The supersonic diffuser is the first flow compression device the incoming air encounters. It can be sorted into three types: an external, internal or mixed compression supersonic diffuser. The three types are shown in Figure 2.2

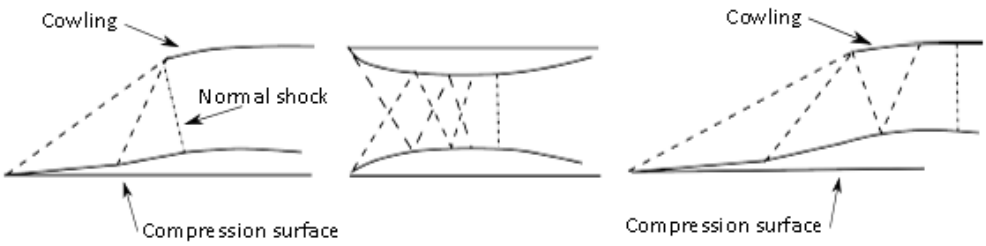

Figure 2.2: Three types of supersonic diffusers, from left to right: external, internal and mixed compression intakes [41]

External compression diffusers typically compress the flow using one or more ramps that cause a shock system, in this report the combination of ramps is called the compression surface. The term external originates from the fact that this compressive shock system exists outside an enclosed area. Usually, the ramps are designed such that in design conditions, the shock waves meet at the start of the cowling - which usually is the upper part of the intake - as to minimize mass flow loss (see Section 2.1.4). The flow passing through a shock wave is compressed at the loss of total pressure. The shock system can be optimized to minimize the total pressure losses by a method proposed by Oswatitsch [34], for more information see Section 2.3.1. Note that to compress the flow to a low supersonic Mach number, the flow needs to be deflected. For the flow to move further down the intake channel, its deflection has to be counteracted, which is typically done in the constant area duct.

Internal supersonic diffusers are defined by a compression surface and cowling that start at the same streamwise location, meaning the incoming flow is enclosed from the leading edge of the intake. Thus, the compressive shock system exists inside a channel. In some cases, an internal compression diffuser is symmetrical and no distinction can be made between compression surface and cowling. An advantage of internal diffusers is the ability to use reflected shock waves to compress the flow. This can help reduce the size of the intake relative to its throat area because the reflected shock waves cancel the flow deflection. A disadvantage of internal diffusers is the limiting contraction ratio, or Kantrowitz limit [22], which limits the design of internal diffusers since the flow has to accelerate to supersonic

conditions when starting the intake. More on this subject in Section 2.1.4. Another disadvantage is the size of the boundary layers in internal diffusers, which is relatively large compared to external diffusers, increasing the effect of viscosity.

Mixed compression diffusers consist of a combination of external and internal compression. If designed well, it can provide the best aspects from internal and external compression diffusers. Viscous effects can be mitigated and flow deflection can be canceled by making use of reflecting shock waves. The limiting contraction ratio still applies to the internal compression part of the diffuser.

Constant-area duct

In design conditions, the constant-area duct starts where the terminal shock begins. In an ideal and inviscid case, this would be a single strong normal shock wave that reduces the flow Mach number from larger to smaller than unity, which would require only a short throat section. In practice, the terminal normal shock interacts with the local boundary layer and stretches out, with several shock waves of decreasing strength along its length. More on this in Section 2.2.2. The shock wave-boundary layer interaction is called a pseudo-shock, and within it a core of supersonic flow exists. Due to the behavior of supersonic flow in diverging channels (supersonic flow accelerates in diverging channels) such as the subsonic diffuser, it is vital to supersonic intake performance that the flow is completely subsonic when entering the subsonic diffuser.

Subsonic diffuser

The subsonic diffuser consists of a diverging channel aft of the constant area duct where the subsonic flow is further decelerated and compressed. The shape of the subsonic diffuser is characterized in most texts by its angle of divergence or conical half-angle, which is typically around 3 to 5 degrees [26]. Subsonic diffuser design has some influence on intake pressure recovery [13, 46], but these effects are not in the scope of this study.

Boundary layer bleed

Viscous effects in the intake can severely affect the performance of a supersonic intake. Since a boundary layer contains less mass flow and less energized air, ingesting a thick boundary layer results in lower mass flow into the engine and lower pressure ratios due to ingestion of less kinetic energy, respectively. To mitigate these viscous losses, a (part of) the boundary layer can be removed by bleed slots, hereby forgoing some mass flow for increase total pressure recovery. Next to the obvious pressure losses, other viscous effects can appear that are detrimental to intake operation. To illustrate the importance of boundary layer bleed, some of these adverse flow phenomena resulting from large boundary layers will be described briefly.

As mentioned earlier, the terminal normal shock in the constant area duct in practice consists of a series of normal shocks, called a pseudo-shock. A special type of shock wave-boundary layer interaction within internal ducts lies at the origin of pseudo-shocks, which can adversely influence the pressure recovery in an intake, compared to a single normal shock. Ikui et al. [21] found that the boundary layer thickness at the start of a pseudo-shock adversely influences the pressure recovery across it. Therefore it is important to reduce boundary layer thickness ahead of the pseudo-shock. A more elaborate description of pseudo-shocks is given in Section 2.2.2.

A thick boundary layer in an adverse pressure gradient, as is commonly found in the internal duct of a supersonic intake, is susceptible to separation. Boundary layer separation can cause a large blocking effect in the intake, which can cause the flow to ”spill out” of the intake, in literature known as an intake unstart (see Section 2.1.4). Intake unstart is undesirable in itself, but it can also trigger a shock oscillation or ”buzz”, which is also detrimental to intake performance. More on this in Section 2.1.4.

To prevent the boundary layers in the intake from becoming too thick, several types of boundary layer bleed have been applied. The most popular are the ram- and flush-type bleed slot. A ram-type bleed slot creates a parallel channel that divides the boundary layer from the rest of the flow. The height of the ram bleed can be based on the expected boundary layer thickness. The flush type bleed slot branches off the boundary layer flow. In order for this to work, a pressure differential is needed in the

bleed channel. To achieve the pressure difference a flush bleed is typically placed just downstream of a shock wave, where pressure is high.

The boundary layer bleed slot can be put in different stations in the intake. A fuselage bleed slot is placed ahead of the compression surface of an intake that is mounted on the side of a vehicle, thereby removing the thick boundary that builds up on the fuselage [16]. Sometimes flush bleeds slots are placed on the compression surface to preserve its thin boundary layer as to not to disturb the delicate shock system on the compression surface [34]. Most commonly, boundary layer bleed is placed around the start of an intake's internal channel, ensuring the smallest possible boundary layer in the internal intake flow [8].

2.1.4. Supersonic intake operation

A supersonic intake can operate in multiple modes, depending on the conditions in the engine downstream of the intake, which are introduced in this section. In addition, several aerodynamic phenomena that may occur during intake operation can adversely influence performance. This section will describe those phenomena and how they may influence design considerations.

Design conditions

Usually, a supersonic intake is designed for specific operating conditions, specifically Mach number and intake back pressure. The need for designing for a specific Mach number is self-evident, whilst the design back pressure is given by the pressure needed in the combustion chamber of the ramjet engine. The back pressure in the intake determines the position of the terminal normal shock. Shown in Figure 2.3 are the shock systems of an external compression intake with combinations of on- and off-design Mach numbers and terminal normal shock positions.

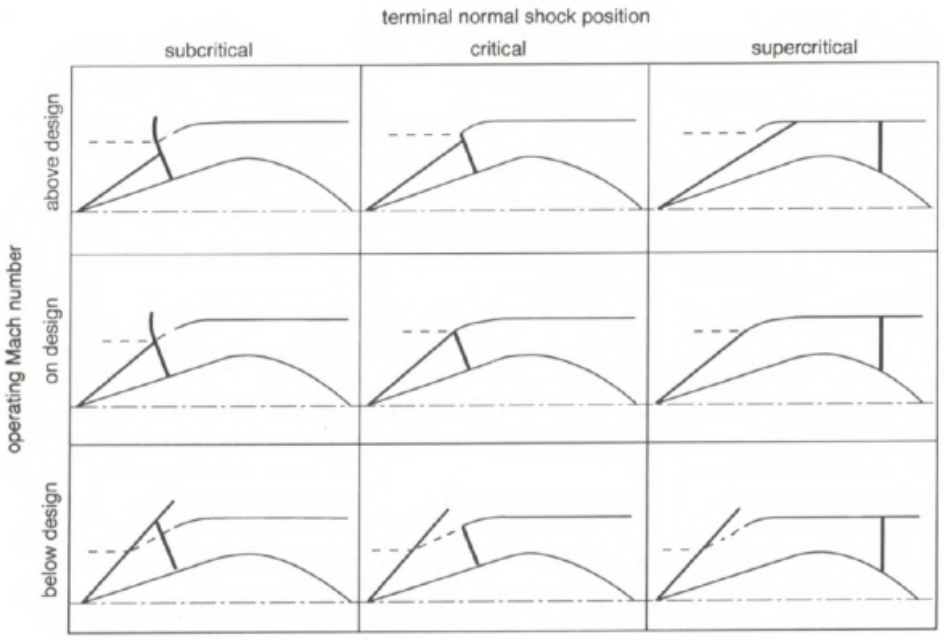

Figure 2.3: Different operating modes of a supersonic intake [26], in text [42]

An external compression supersonic intake is almost always designed such that the shock system made by the compression surface impinges on the leading edge of the cowling. In that way, the maximum mass flow is achieved whilst all airflow goes through the shock system to be compressed in the most efficient way. When the operating Mach number is below design, the streamline that bounds the capture area is deflected by the oblique shock system ahead of the internal duct, causing the mass flow into the intake to be reduced, as can be seen from the dashed line in the middle lower tile in Figure 2.3. In addition to the lost mass flow, below design operating Mach number results in supersonic spillage

drag, since some of the flow intended to enter the intake goes around in at supersonic speeds, causing added drag to the intake.

When the operating Mach number is above design, some of the flow entering the internal channel has not gone through the oblique shock system. This incurs losses because the oblique shock system is the most efficient way of compressing the flow. In addition, the flow in the internal channel has now gone through two different shock systems, causing a shear layer in the internal flow. When this shear layer comes close to the boundary layer, separation can occur which may result in intake unstart or even shock oscillations, discussed later in this section.

As mentioned, the terminal normal shock position is determined by the intake back pressure. In a ramjet engine, the back pressure will be determined by the conditions in the combustion chamber and, more specifically, the fuel flow into the engine.

In design conditions, the terminal normal shock will be located at the entrance of the internal channel, as is shown in the middle column of Figure 2.3. This is called the critical condition. In supercritical condition, the back pressure is lower and the terminal normal shock moves downstream into the internal channel. For subcritical conditions, the back pressure is higher than its design value and the normal shock can be expelled from the internal channel, forming a bow shock in front of the intake. This is when subsonic spillage drag occurs, since subsonic flow is spilled around the intake incurring additional drag. The location of the terminal normal shock can influence the total pressure ratio of the supersonic intake. The scope of total pressure ratios that can be reached by moving the terminal normal shock in the intake will later be referred to as the dynamic range of the intake.

The relation between the different operating modes and their total pressure recovery can be illustrated using Figure 2.4. It shows the total pressure recovery versus the capture area ratio, which is the ratio between the area of the captured streamtube at free-stream conditions and the area of the intake at the start of the internal channel. Note that Figure 2.4 is given for the design Mach number.

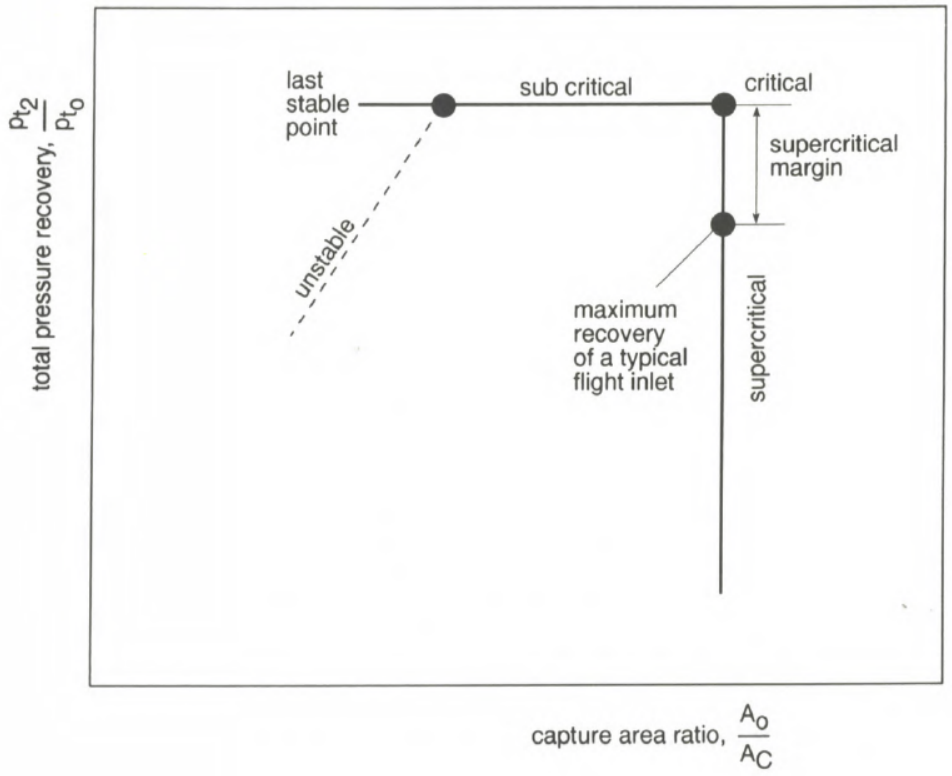

Figure 2.4: Qualitative description of the operating conditions of an air intake [26], in text [42]

When the engine starts, the flow in the intake must accelerate from subsonic to supersonic conditions, which requires a normal shock to move through the intake. When the supersonic flow is established, the supercritical condition has been reached. When the back pressure is increased, the

terminal normal shock is forced upstream, until it reaches the entrance of the constant area duct. The intake is now in the critical condition. In Figure 2.4, movement from supercritical to critical condition is represented by the vertical line at the maximum capture area ratio. The critical condition is the design operating condition because it gives the highest total pressure ratio for the highest capture area ratio, which means the mass flow is at its maximum. When the back pressure is increased from the critical condition, the terminal normal shock will be expelled from the internal channel, and interacts with the oblique shock system, causing the aforementioned shear layer. Also, the capture area ratio decreases since the terminal normal shock deflects the streamtube ahead of the internal channel entrance. In Figure2.4 the decrease in capture area ratio is represented by the horizontal line with the caption subcritical. Increasing the back pressure even more causes the oblique-normal shock interaction to move upstream even further, which can result in the shear layer being ingested and triggering shock oscillations.

Limiting contraction ratio

To operate optimally, a supersonic intake must ”start”, meaning the flow must settle at its design conditions. For this to happen, the flow in the intake must accelerate from subsonic to supersonic velocities reaching the supercritical condition. Then, the back pressure is increased to achieve critical condition. The crux in this process is achieving supersonic conditions in the internal duct, especially for intakes that utilize internal compression, which - by definition - means converging ducts. This stems from the behavior of sub- and supersonic flow in converging ducts: supersonic flow decelerates, whilst subsonic flow accelerates in converging ducts.

As explained above, to start a supersonic intake, a terminal normal shock must settle at or aft of the internal channel throat. When the intake is fully choked, a bow shock exists in front of the converging channel. If the choking is relieved, the bow shock should be ”swallowed” and the flow accelerated to supersonic conditions. However, due to the fact that subsonic flow accelerates in a converging duct, the possibility exists that sonic conditions are reached before the channel throat. The flow is then choked and the terminal normal shock is unable to move downstream and reach design conditions.

The rate with which sonic conditions are reached is determined by the contraction ratio, and thus one can speak of a limiting contraction ratio for which sonic conditions are reached exactly at the throat of the channel. Kantrowitz and Donaldson [22] were the first to derive an expression for this limit and therefore it is sometimes referred to as the Kantrowitz limit. Seddon and Goldsmith [38] provide a different derivation with the same results. The limiting contraction ratio is a function of free-stream Mach number and ratio of specific heats, given by:

$$\chi = \left(\frac{A_{throat}}{A_c}\right)_{lim} = \left(\frac{\gamma-1}{\gamma+1} + \frac{2}{(\gamma+1)\,M_\infty^2}\right)^{\frac{1}{2}} \times \left(\frac{2\gamma}{\gamma+1} - \frac{\gamma-1}{(\gamma+1)\,M_\infty^2}\right)^{\frac{1}{\gamma-1}} \tag{2.14}$$

Shock oscillations

As mentioned before, shock oscillations or buzz may occur under specific conditions. The cycle of shock oscillations is a follows. The back pressure in the intake is increased so that the terminal normal shock is expelled out of the internal channel and forms a detached bow shock ahead of the intake: the forward limit of the oscillation. Due to the reduced velocity of flow entering the intake, the bow shock causes the mass flow at the intake entrance to be smaller than the mass flow at the intake exit, which in turn enables the terminal normal shock to be swallowed again: the rearward limit of the oscillation. At this point the mass flow at the entrance is larger than at the exit, filling up the intake, expelling the terminal normal shock and the cycle starts over again. When shock oscillations occur, they may be relieved by lowering the back pressure in the intake which for a ramjet engine can be achieved by throttling down the engine and in an experimental set-up the exit valve may be opened.

Uncontrolled events can trigger shock oscillations, as was mentioned earlier in this chapter. The increase in back pressure needed to expel the terminal normal shock and start buzz can accidentally be caused by a blockage of the internal flow, usually as the result of boundary layer separation. This separation can simply occur when a very thick boundary layer encounters the strongly adverse pressure gradient in the internal channel. Or, when a shear layer comes close to the boundary layer in the internal flow, which was found experimentally by Ferri and Nucci [14] and therefore is called the Ferri

criterion. The shear layer introduces two regions of different conditions in the internal flow and the lower-velocity region is prone to separation. However, as the distance between shear layer and channel wall increases, the likeliness of separation and thus shock oscillation reduces.

2.2. Viscous effects

The two prevailing viscous effects that are of importance in a supersonic intake are shock wave-boundary layer interaction and the pseudo-shock. The basics of both will be described in this section. In addition, Fanno flow is briefly discussed, since it may occur within the intake internal channels in certain conditions.

2.2.1. Shock wave-boundary layer interaction

The complex flow phenomenon of a shock wave interacting with a boundary layer is rather easy to understand quantitatively, according to Green [18]. Figure 2.5 shows two forms of shock wave-boundary layer interaction as they appear in a supersonic intake. An incoming shock wave impinging on a flat surface and a shock wave caused by a ramp.

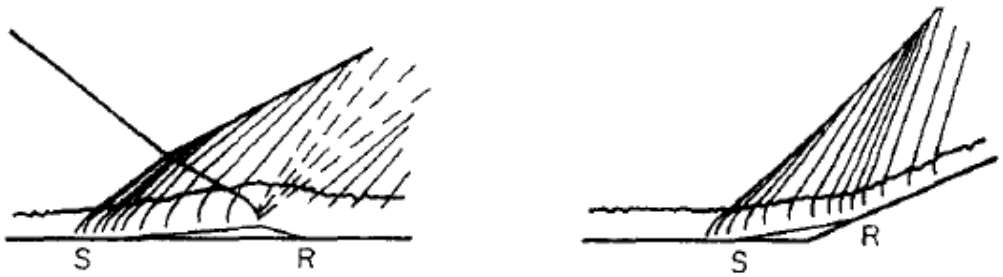

(a) Reflected shock (b) Ramp shock

Figure 2.5: Schematic drawings of shock wave boundary layer interaction with separation [18]

Starting with the reflected shock wave of Figure 2.5a. An incoming oblique shock reflecting on a wall cannot penetrate the subsonic layer in the boundary layer, due to the fact that subsonic flow is unable to experience a discontinuous change in pressure. Instead, the pressure differential between the flow up- and downstream of the shock is spread out, increasing the thickness of the subsonic layer. When the incoming shock is strong enough, this may even locally separate and reattach the flow in the subsonic layer, indicated in Figure 2.5a by an S and R, respectively. The thickening of the subsonic layer causes the incoming flow to be deflected upstream of the impinging shock wave. The deflection causes Mach waves which eventually combine into a reflected shock wave that originates slightly ahead of where the incoming shock reaches the surface.

Boundary layer interaction of shock waves caused by a ramp, as shown in Figure 2.5b, have workings very similar to that of reflected shock waves. The shock wave caused by the ramp imposes a pressure differential on the subsonic layer whose thickness rapidly increases, causing flow deflection and consequently Mach waves that combine into a shock originating ahead of the ramp. For shock waves of sufficient strength, the flow may also separate and reattach, as shown in Figure 2.5b by and S and R.

Note that whilst the modelling of ramp and reflected shocks is similar, a significant difference exists for laminar and turbulent boundary layers. In a supersonic air intake, a turbulent boundary layer is more desirable because of its relative insensitivity to the adverse pressure gradients typically found in intakes. Laminar boundary layers are undesirable for shock wave-boundary layer interaction, because of their sensitivity to adverse pressure gradients. A laminar boundary layer can separate for slight pressure rises [15, 23] and cause a bigger separation bubble [35], increasing the chance of significant blockage. Usually, the boundary layer transitions to a turbulent state rather quick due to the adverse pressure gradient. Reducing the probability of disadvantageous consequences of separation.

The difficulty in modelling this type of flow lies in the fact that areas of sub- and supersonic flow mix and interact. The outer supersonic region being more or less inviscid, whilst the subsonic layer near the wall experiences large shear gradients. The different properties of all these interacting flow areas makes shock wave-boundary layer interaction a very difficult flow to model. However, some good efforts have been made. The methods used in the SRIM, both laminar and turbulent, will be discussed in Section 2.5.

2.2.2. Pseudo-shock

A pseudo-shock is special form of shock wave-boundary layer interaction in an internal channel. An extensive review of pseudo-shocks was done by Matsuo [27]. He describes the development of the pseudo-shock with increasing upstream Mach number using the illustrations in Figure 2.6. For duct flow with supersonic Mach numbers close to unity ($1.0 < M_1 < 1.2$), a normal shock wave exists in the duct. Towards the duct walls, a weak shock wave-boundary layer interaction exists. When the upstream Mach number is increased ($1.2 < M_1 < 1.5$), the pressure differential across the shock wave becomes high enough to separate the subsonic layer in the boundary layer, causing oblique shocks to be formed ahead of the normal shock wave. The interaction between the oblique and normal shock causes a bifurcated shock wave. For even higher Mach numbers ($M > 1.5$) the subsonic layer becomes very thick at the bifurcated shock wave, and then reduces slightly, which creates a diverging supersonic region, accelerating the flow again. The accelerated flow causes another bifurcated shock wave and the process repeats itself a few times. The region of consecutive shock waves is called a shock train, and is part of the pseudo-shock.

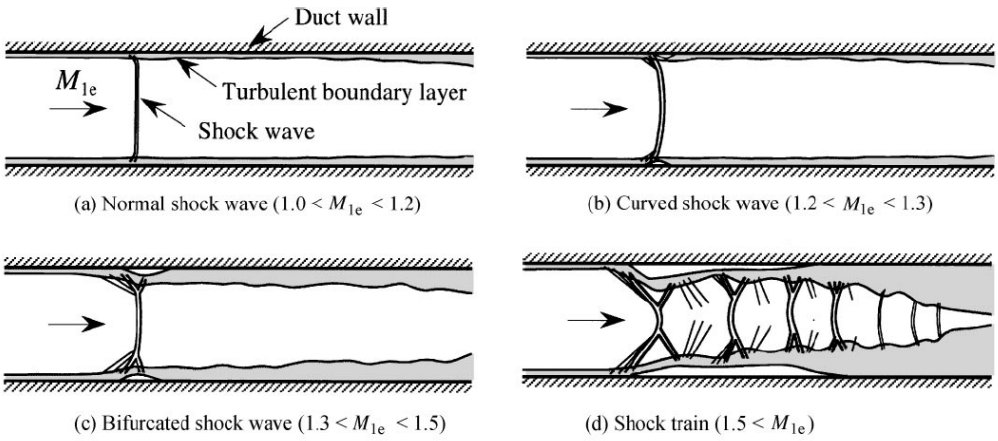

Figure 2.6: Pseudo-shock development with increasing Mach number. The supersonic flow region is indicated in white, and subsonic in grey. [27]

Figure 2.7 shows the full pseudo-shock along with the static pressure distribution along its length. The shock train region, described above, is the first part of the pseudo-shock. From the pressure distribution the influence of the recurring shock can be seen clearly. After the shock train a mixing region exists, where slightly supersonic flow dissipates into subsonic. Because this mixing region consists of a subsonic flow with a supersonic core, it is important that it is fully contained by a constant-area duct, since the two regions behave oppositely in converging or diverging ducts.

The importance of containing the pseudo-shock in a constant area duct (or throat) was shown by McLafferty et al. [29], who investigated the efficiencies of supersonic intakes with varying ratios of pseudo-shock to throat length. He found that the maximum total pressure recovery is found when the throat length is equal or slightly larger than pseudo-shock length, see Figure 2.8. The graph shows data from McLafferty et. al., summarized by Mahoney [26].

When the throat length starts to exceed the pseudo-shock length, the pressure recovery starts to degrade again. This can be seen in the data from McLafferty (Figure 2.8) but also in the static pressure distribution in Figure 2.7, where after point 2 the static pressure starts to decrease again. What happens here is that the flow has been turned completely subsonic, and then the well-known Fanno flow phenomenon starts, which will be discussed in the next section.

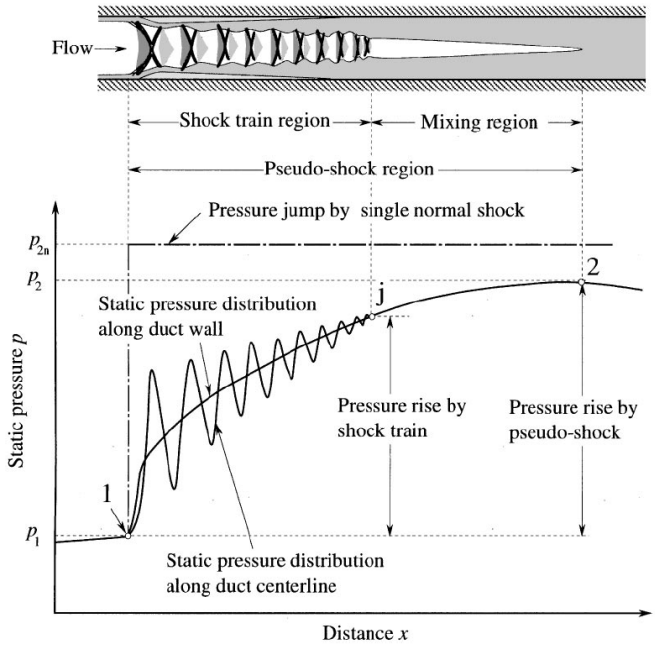

Figure 2.7: Schematic representation of pseudo-shock and static pressure rise over its length. The supersonic flow region is indicated in white, and subsonic in grey. [27]

2.2.3. Steady channel flow with friction

Under the assumption that a fluid is a perfect gas with constant specific heat and that the flow at the wall is adiabatic, channel flow can be modeled. For one-dimensional steady flow and differential equation can be derived to compute the streamwise Mach number distribution for flows in closed channels with arbitrary shape, as done by [6]:

$$\frac{dM}{dx} = \frac{2M\left(1+\frac{\gamma-1}{2}M^2\right)\left(D'-\gamma f M^2\right)}{D\left(M^2-1\right)} \tag{2.15}$$

Where $D' = \frac{dD}{dx}$ and f is the friction coefficient. Given the Mach number distribution and upstream flow properties, isentropic relations can be used to find additional flow properties (e.g. pressure, temperature and density) throughout the internal channel flow.

A special case of this steady one-dimensional viscous flow described in equation 2.15 is Fanno flow, where the channel has constant cross-sectional area. In Fanno flow, it is found that steady sub- or supersonic flow tends to accelerate or decelerate, respectively, to sonic conditions. Since the channel is of constant area and therefore $D' = 1$, the equation for Mach number distribution in Fanno flow is easily found from 2.15:

$$\frac{dM}{dx} = \frac{2M^3\left(1+\frac{\gamma-1}{2}M^2\right)\gamma f}{D\left(M^2-1\right)} \tag{2.16}$$

Referring to the previous section, in the case where the pseudo-shock ends some distance before the end of the constant area duct, Fanno flow can start, accelerating the flow towards sonic conditions which would cause some static pressure loss, as can be seen in Figure 2.7. In addition to static pressure loss, total pressure is lost to friction effects.

2.3. Supersonic intake performance

Comparing submerged supersonic intakes with their regular counterparts will require a benchmark of regular supersonic intake performance. This section seeks to establish such a base for comparison, so that an estimation of the losses involved with submerging a supersonic intake can be made later. First,

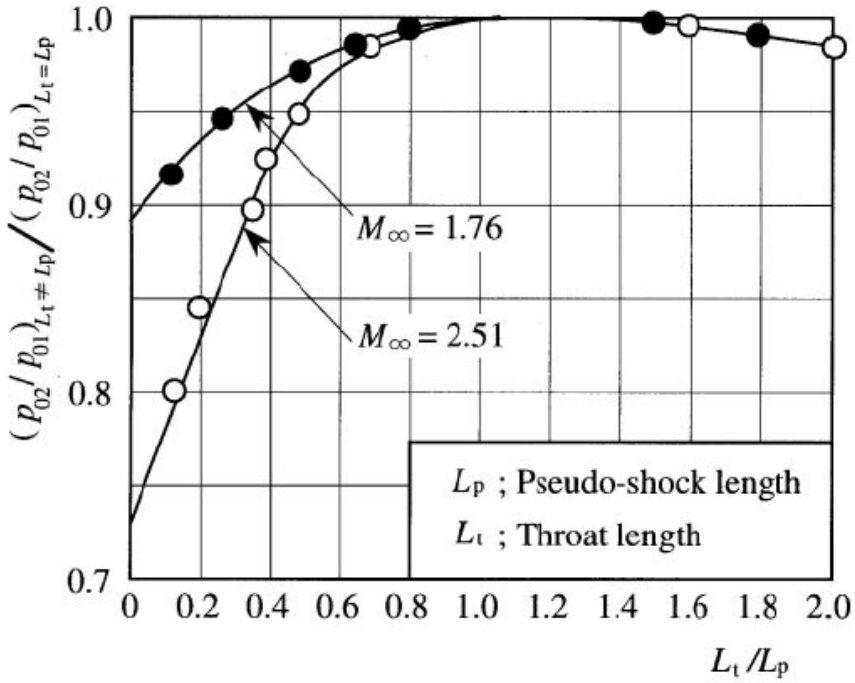

Figure 2.8: Ratio of total pressure recovery at any throat length to total pressure recovery if throat length equals pseudo-shock length vs. ratio of throat to pseudo-shock length. Image credits: Matsuo [27], in text Mahoney [26]

an inviscid method to compute the theoretical maximum performance of an intake will be described. Then, intake performance of experimental and computational studies will be presented.

2.3.1. Optimization of theoretical performance using the Oswatitsch approach

As mentioned in Section 2.1.3, a method to minimize pressure losses in the oblique shock system of an external compression ramp was proposed by Oswatitsch [34]. Using this inviscid method, a maximum theoretical efficiency can be obtained for any intake. The method works as follows: take an inviscid supersonic intake with a shock system consisting of n shocks, including the terminal normal shock. Oswatitsch proved that the $n-1$ oblique shocks compress the flow most efficiently when they are of equal strength. The full proof is beyond the scope of this report, but the method to compute the upstream Mach number (M_i) and shock angle (β_i) will be given below.

Starting with M_{n-1}, the free-stream Mach number M_0 can be determined by:

$$\frac{1+\frac{\gamma-1}{2}M_0^2}{1+\frac{\gamma-1}{2}M_{n-1}^2} = \left(\frac{\frac{4\gamma}{(\gamma+1)^2}y_0 - 1}{y_0 - 1}y_0\right)^{n-1} \tag{2.17}$$

Where

$$y_0 = \frac{1}{2}\left(1 + h + \left|\sqrt{1 - \frac{\gamma^2+1}{\gamma}h + h^2}\right|\right) \tag{2.18}$$

and

$$h = \frac{(\gamma-1)\,M_{n-1}^4 + \frac{5-\gamma}{2}M_{n-1}^2 - 1}{\frac{3\gamma+1}{2\gamma}M_{n-1}^2 - 1} \tag{2.19}$$

It may seem counter-intuitive to compute the free-stream Mach number as a function of M_{n-1}, the Mach number upstream of the terminal normal shock. However, the terminal shock in the throat, which

is the same as the n^{th} shock in Oswatitsch's model, is of great importance for the intake efficiency. Furthermore, with modern computational power it is easy and inexpensive to reverse the relation given in equations 2.17 through 2.19 by applying an interpolation method.

For the next step in Oswatisch's method, some variables need to be defined

$$x_i = \frac{\gamma - 1}{2} M_i^2 + 1;\ y_i = \frac{\gamma - 1}{2} M_i^2 \sin^2(\beta_i) + 1 \tag{2.20}$$

and

$$f_i = \frac{\gamma + 1}{\gamma - 1} \frac{y_i - 1}{y_i};\ g_i = \frac{\gamma - 1}{\gamma + 1} \frac{1}{\frac{4\gamma}{(\gamma+1)^2} y_i - 1} \tag{2.21}$$

Using these definitions, Oswatitsch has proven that, for maximum total pressure recovery

$$y_0 = y_1 = y_2 = \ldots = y_{n-2} \tag{2.22}$$

and

$$x_{i+1} = x_i f_i g_i;\ \text{for } i = 0, 1 \ldots n - 2 \tag{2.23}$$

From the above equations it can be derived that y_i is a measure of shock strength, since it must remain constant across all oblique shocks. x_i is a measure of upstream velocity and the product $f_i g_i$ represents the factor with which the Mach number is reduced across an oblique shock.

With equations 2.22, 2.23 and a known y_0 from equation 2.18, x_i and y_i at all stations 1 through $n-2$ can be computed. From the definitions for x_i and y_i (equation 2.20), the Mach numbers and shock angles of each shock can be computed. Since the shock angle of the normal shock is $90°$ by definition, and its upstream Mach number was given or reverse engineered, all Mach numbers and shock angles are now known. Subsequently, with the knowledge of all shock angles and some other dimensional intake data, such as intake channel height, the full geometry of the intake can be computed using simple trigonometry.

Using oblique shock relations the total pressure ratio of an intake with n shocks can be computed as a function of free-stream Mach number. Figure 2.9 shows those results.

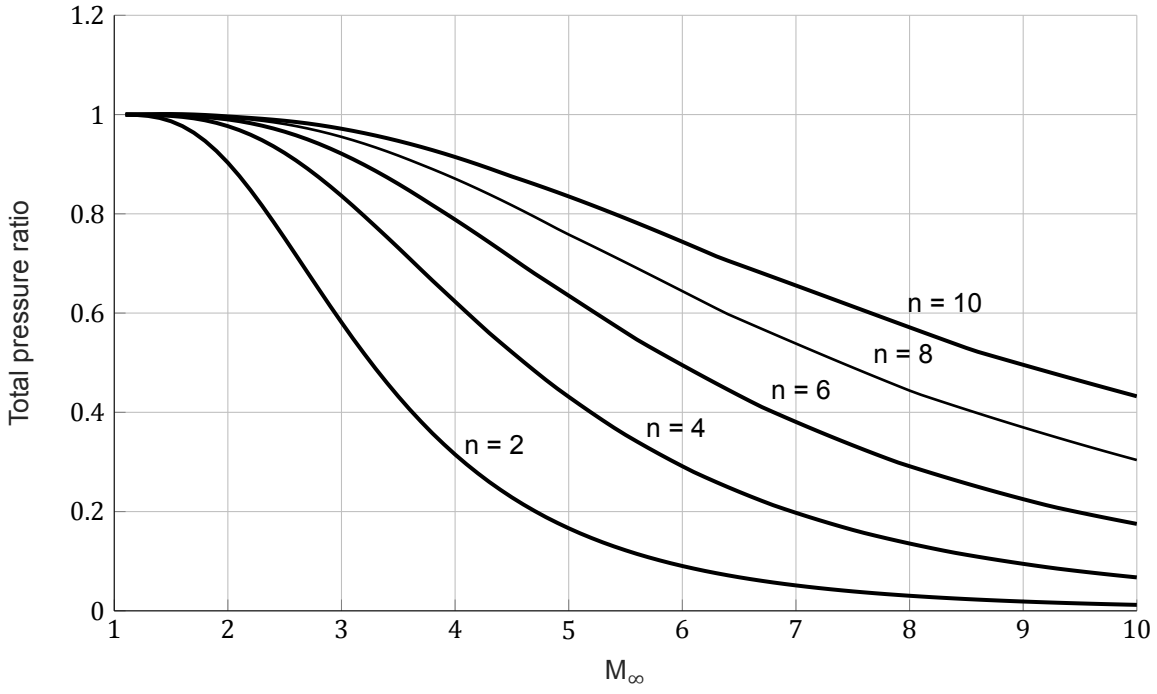

Figure 2.9: Total pressure ratios of Oswatitsch intakes with n-1 oblique shocks and one normal shock for varying free-stream Mach numbers

In Figure 2.9, a clear tendency is visible that for increasing Mach number the total pressure ratio of a supersonic intake deteriorates rather fast. This can be expected since stronger shock associated with higher Mach numbers cause higher entropy losses. A way to mitigate losses is to increase the number of shocks, reducing the strength of each individual shock. However, this leads to a more complex intake design, which is not always desirable.

When the number of shocks in the Oswatitsch method goes to infinity, an isentropic intake surface is obtained. Connors and Meyer [11] introduced another method to compute such an intake, based on an inverted Prandtl-Meyer expansion fan, also known as a compression fan. Upon investigation, the Oswatitsch method for very high numbers of shocks ($n > 100$) yielded nearly equal results to the method of Connors and Meyer. The difference was likely only caused by a computational limit on the number of shocks in the Oswatitsch routine.

Whilst an isentropic intake may seem very efficient, it has its limitations. The flow cannot be compressed fully isentropically for two reasons. First, the leading edge of the intake always causes a shock wave. For the leading edge to not cause a shock wave, its deflection of the flow needs to be infinitesimally small, which is structurally impossible. Next, an isentropic compression surface cannot bring the flow to subsonic velocities. Therefore a terminal normal shock is always needed in the intake, reducing the intakes efficiency.

2.3.2. Supersonic intake studies

In addition to theoretical maxima provided by inviscid studies, this section will present experimental and computational data on the performance of supersonic air intakes. Figure 2.10 shows experimental and computational results for the several numbers of shocks and one isentropic intake compared to their theoretical maxima as determined by the method provided by Oswatitsch. The graphs in Figure 2.10 provide a good basis of comparison for the submerged supersonic intakes. It shows several experimental and computational studies into supersonic intake performance. The total pressure ratios of intakes with a bleed slot is shown in Figure 2.10, along with the total pressure ratio of the same intake without a bleed slot, illustrating the benefit a bleed slot can have on supersonic intake performance. The results shown in Figure 2.10 will be used later in this report in a comparison with the performance results of the submerged supersonic intakes.

2.4. Submerging a supersonic air intake

To submerge an supersonic intake, it is a geometric necessity to turn the flow into the fuselage at some angle, called the expansion angle. This requires subjecting the flow to a supersonic expansion, which accelerates the flow. The concept of supersonic expansion was first described by Prandtl and Meyer, and has since become staple in any standard textbook on supersonic aerodynamics, such as Anderson [5].

Prandtl and Meyer argued that flow expanding can be modelled by an infinite number of Mach waves that increase the flow velocity isentropically. All the Mach waves together are called the Prandtl-Meyer expansion fan. To calculate the Mach number of flow around a convex angle, they introduced the Prandtl-Meyer function:

$$\nu(M) = \sqrt{\frac{\gamma+1}{\gamma-1}} \cdot \arctan \sqrt{\frac{\gamma-1}{\gamma+1}\left(M^2-1\right)} - \arctan\sqrt{M^2-1} \tag{2.24}$$

Using this exact analytical function the Prandtl-Meyer angle of the flow can be calculated. This Prandtl-Meyer angle is representative of the flow deflection angle and hence

$$\theta = \nu(M_2) - \nu(M_1) \tag{2.25}$$

where θ is the expansion angle and subscripts 1 and 2 indicate flow conditions upstream and downstream of the expansion fan, respectively.

Using equations 2.24 and 2.25, the flow acceleration around a convex angle can be computed for given deflection angle and upstream Mach number. When the downstream Prandtl-Meyer angle $\nu(M_2)$ is known, numerical interpolation can be used to find the Mach number downstream of the expansion.

The Prandtl-Meyer method for computing the Mach number behind a supersonic expansion can be combined with Oswatitsch method for computing the maximum intake efficiency as a function of free-stream Mach number to investigate the maximum theoretical efficiency of a submerged intake. Figure 2.11 shows an inviscid analysis for total pressure ratio of submerged supersonic intakes with respect to free-stream Mach number. The performance of a regular intake at equal free-stream Mach number is also shown as a comparison. The significance of Figure 2.11 is that it shows the inviscid losses of submerging an intake. Thus, for a Mach number of 3, an intake with $n = 4$ shocks loses approximately 0.2 on its total pressure ratio when it is submerged using a 14° expansion angle. This does not include any other viscous losses that may also occur. When the expansion angle increases, the Mach number behind the expansion increases also further reducing intake efficiency.

2.5. Submerged Ramjet Intake Model

The Submerged Ramjet Intake Model (SRIM) was developed by a graduate intern at TNO to provide fast calculations for submerged supersonic intake efficiency [41]. To ensure low computational cost, the SRIM consists of several interacting analytical sub-models, rather than expensive CFD computations. The SRIM computes the flow around expansion section and compression surface and the flow into the constant area duct in a submerged supersonic intake. The analysis ends at the end of the constant area duct, so the SRIM does not enable computation of flow into the subsonic diffuser.

First, this section describes the Submerged Ramjet Intake Model and its sub-models, along with some shortcomings that may exist in these sub-models. After that, the inputs and outputs are described. Whilst the inputs are rather trivial: characteristics of the free-stream flow and a geometric description, the outputs are derivative of the sub-models and important to note since they require comparison with experimental results. At last, it presents some additional assumptions made by the developer. For a more detailed description of the SRIM the reader is referred to Van Wijk [41].

2.5.1. Analytical models

The analytical models used in the SRIM are typically well-established methods to compute part of the flow in the submerged supersonic intake. Whilst all models are validated individually, their interaction with each other has not yet been validated. When the sub-models have any shortcomings they will be discussed as well.

Method of characteristics

A well-known and proven method to model supersonic inviscid flow is the method of characteristics, where the flow is calculated along lines (characteristics) of constant properties (invariants). Its power lies in the fact that it is an exact method, and therefore very accurately predicts the inviscid supersonic flow. Note that by using the method of characteristics, an assumption is made that the flow is inviscid. This assumption does not hold for the flow close to the intake walls, where a boundary layer estimation is done.

The method of characteristics used in the SRIM includes calculations for varying entropy, since the shock waves located in and around the intake will likely be of non-uniform strength. This causes the flow to be rotational, according to Crocco's theorem. Thus, the model used is a rotational method of characteristics by Krasnov [24]. The output of this model is the Prandtl-Meyer angle and entropy throughout the flow field. From the Prandtl-Meyer angle, an inverse method is needed to calculate the Mach number to, with the now known entropy, calculate other flow properties.

In the method of characteristics, the Prandtl-Meyer angle is used to describe Mach number. To compute the Mach number as a function of Prandtl-Meyer angle, Hall [19] came up with an approximate function consisting of a quotient of two polynomials. The constant of these polynomials are dependent of the ratio of specific heats, γ. Therefore, the assumption has to be made that γ is constant throughout the flow. Van Wijk [41] calculated that, granted the validity of this assumption, the error of Hall's inverse function is below 0.02% for Mach numbers below 5.

Another shortcoming of the method of characteristics is that it breaks down when two characteristics of the same family cross, or when the flow encounters a shock wave. In the SRIM this is remedied by creating flow areas contained by reflecting shocks and the internal channel walls, wherein the method

of characteristics is computed. When a shock is encountered, flow changes across the shock are determined according to the oblique shock relations and a new flow area starts. This is done until the end of the intake or the start of the pseudo-shock is reached.

The propagation of the reflected shock waves through the internal channel depends on the shock wave boundary layer interaction, discussed later, but also on the rapidly changing flow conditions within the intake. A method by Hartley [20] is used to calculate the shock angle based on the local flow properties for both strong and weak shocks. This method contains a set of exact equations, meaning the solution is very accurate.

Boundary layer estimation

The viscous boundary layers along the intake walls are complex flow phenomena that require significant computational effort to fully model. Because a lot of boundary layer parameters are not very relevant within the scope of intake modelling in the SRIM, integral boundary layers are used. These provide the model with appropriate predictions for the development of the boundary layer in the intake.

Two integral boundary layer methods are implemented: one for turbulent and one for laminar boundary layers. Both will be discussed below. The integral boundary layer methods take the external velocity u_e from the method of characteristics and flow parameters such as pressure and temperature, depending on whether the boundary layer is turbulent or not, to compute a boundary layer displacement thickness δ^*. This value is used to alter the edges of the inviscid domain, and then the method of characteristics is run again in an iterative process. However, for the SRIM it turned out that more than one iteration did not significantly improve the solution, so only one iteration is used for computation [41].

A turbulent method by Sasman and Cresci [12] is used to model the turbulent boundary layer. The method predicts the development of the incompressible shape factor in a transformed coordinate system based on wall friction C_f, external Mach number M_e, local temperature and a transition point in the intake. This incompressible shape factor is then calculated back to the displacement thickness in the physical plane using an approximate method described by Reshotko and Tucker [36].

The performance of this combined method was validated by Van Wijk on several datasets featuring favourable pressure gradients caused by a supersonic expansion, and was proven to be of sufficient accuracy [41].

The laminar boundary layer displacement thickness is computed by an approximate method by Cohen and Reshotko [9]. Quite similar to the turbulent method, its implementation into the SRIM is a prescribed dataset from which relevant query points are interpolated. The accuracy of this is stated to be ”within 10% for the first $300mm$ running distance” [41], which is supposed to be ”one of the most accurate programmable general methods available for the laminar case” [30].

Shock wave-boundary layer interaction

The phenomenon of shock wave-boundary layer interaction as described in Section 2.2.1 is modelled in the SRIM by methods described by Souverein et al. [40] for the turbulent case and by Katzer [23] for the laminar case. Both methods try to find a measure of upstream propagation of the (reflected) shock wave.

The turbulent shock-wave method by Souverein et al. [40] starts with defining a so-called separation criterion, that is dependent of upstream properties:

$$S_e^* = k\frac{\Delta p}{q_e} \tag{2.26}$$

Where S_e^* is the separation state criterion which indicates separated flow for $S_e^* \geqslant 1$, ΔP is the pressure rise imposed by the shock system, q_e is the upstream dynamic pressure and k is a constant for which

$$k = 3.0 \text{ if } Re_\theta \leqslant 1 \times 10^4 \tag{2.27}$$

$$k = 2.5 \text{ if } Re_\theta > 1 \times 10^4 \tag{2.28}$$

Next to that, Souverein et al. found that the non-dimensional interaction length L^* is given by:

$$L^* = \frac{L}{\delta_0^*} \cdot \frac{\sin\beta \sin\varphi}{\sin(\beta - \varphi)} \tag{2.29}$$

According to Souverein et al., the results of equation 2.29 and 2.26, along with experimental data could be fitted with an exponential fit line, namely $L^* = 1.3S^{*3}$. Van Wijk [41] came up with a better fit for the data available, which is $L^* = 2.1S^{*1.9}$. This fit is in the same order of accuracy as the measurement uncertainty of the validation data for both separated and attached flow. Using this fit, the non-dimensional interaction length can be found from upstream properties. The result of Van Wijk's adaptation should be compared to experimental data of the entire intake to see whether the change is justified.

Katzer [23] investigated oblique shock waves impinging on laminar boundary layers. He found a relation for the length of the separation bubble l_B

$$\frac{l_B}{\delta_0^*} \frac{M_1^3}{\left(Re_{x_0}/C\right)^{\frac{1}{2}}} = 4.4 \frac{p_3 - p_{inc}}{p_1} \tag{2.30}$$

where C is the Chapman-Rubesin constant $C = \frac{\mu_w T_\infty}{\mu_\infty T_w}$. The subscripts 1 and 3 indicate the values up- and downstream of the interaction. p_{inc} is a constant equal to $1.85\sqrt{2}$. This value is disputed by others, such as Greber et al. [17] and Rizzetta et al. [37], who think p_{inc} should be $2\sqrt{2}$ and $1.57\sqrt{2}$, respectively.

Both cases of shock wave boundary layer interaction mentioned above, the ramp flow and reflected shock wave flow, are modelled by the SRIM using the same methods. Despite the different nature of both flows, the modelling methods are remarkably accurate for both types of flow. However, Van Wijk [41] states that minor differences between ramp flow and reflected shocks remain. Therefore it may be worthwhile to look into the accuracy of the shock wave boundary layer interaction methods using experimental submerged intake data.

Pseudo-shock

The pseudo-shock phenomenon was already discussed in Section 2.2.2. The SRIM uses a semi-empirical computation method to model the pseudo-shock in the form of the Modified Diffusion Model by Ikui et. al. [21]. This model uses the local Mach number, boundary layer thickness, static pressure and density to compute the length, Mach number distribution and pressure distribution in the pseudo-shock. For a fully detailed description of the Modified Diffusion Model refer to Ikui et al. [21], but a brief overview of the inputs, computations and outputs will be given below.

The Modified Diffusion Model assumes that the pseudo-shock consists of a core of supersonic flow that diffuses into subsonic flow over the length of the pseudo-shock. The mass flows of the supersonic core and the subsonic diffusion region at the pseudo-shock start are calculated with the assumption that, pre-pseudo-shock, the subsonic diffusion region consists only of the subsonic layer in the turbulent boundary layer in the channel. The mass flow of each region is determined based on the local properties, namely boundary layer thickness, channel geometry, flow density and flow velocity. From these mass flows, a mass flow fraction at the start of the pseudo-shock μ_1 is determined:

$$\mu_1 = \frac{\dot{m}''_1}{\dot{m}''_1 + \dot{m}'_1} \tag{2.31}$$

Where the supersonic region is indicated by a single accent ($'$) and the subsonic region by a double accent ($''$). The mass flow fraction is then inserted into an empirical relation to obtain the non-dimensional pseudo-shock length:

$$\frac{L}{D} = 3700\left(M'_1 - 1\right)^{3.8} \mu_1 \tag{2.32}$$

Using the result of empirical equation in 2.32, along with pre-pseudo-shock data, analytical equations are used to obtain the static pressure and Mach number behind the pseudo-shock. Then, total pressure can be determined from isentropic relations. At last, using a differential equation the development of Mach number in both the super- and subsonic region is derived, as well as the pressure distribution across the entire pseudo-shock.

In their paper presenting the Modified Diffusion Model (MDM), Ikui et al. [21] dispute its accuracy. The model prediction for static pressure distribution within the pseudo-shock has increasing discrepancies with experimental values with increasing Mach number and upstream boundary layer thickness. Ikui et al. attribute this to the separation phenomena, which become increasingly prominent for high Mach numbers and thick boundary layers, and are not taken into account in the MDM. Ikui et al. show that for a Mach number of $M = 1.76$ and a non-dimensionalized displacement thickness of $\frac{\delta^*}{D} = 0.0451$ at the start of the pseudo-shock, the MDM prediction is accurate. Although for $M = 2.16$ and $\frac{\delta^*}{D} = 0.0651$, the solution starts to deteriorate. Pseudo-shock start Mach numbers exceeding 2.16 are achieved in the SRIM, but the typical boundary layer displacement thickness is much lower than given by Ikui et al., in the order of $\frac{\delta^*}{D} = 0.01$. This makes the accuracy of the MDM hard to pinpoint exactly. However, the Modified Diffusion Model is more comprehensive and accurate than earlier methods in terms of static and total pressure ratios across the pseudo-shock, especially at its low computational cost. The accuracy of the MDM should therefore be thoroughly evaluated in the SRIM validation.

Two important adaptations were made to the Modified Diffusion Model when it was implemented in the SRIM. Due to the geometry of the submerged intake, the boundary layers on the upper and lower walls of the internal channel are of different thickness at the start of the pseudo-shock. The Modified Diffusion Model in the SRIM was adapted to take this into account by adding two different boundary layers into the mass flow fractions of the sub- and supersonic regions. Next to the asymmetric boundary layers, the Modified Diffusion Model is a two-dimensional method, whilst the SRIM takes into account the internal channel width. The side wall boundary layers are also included into the mass flow fractions in the pseudo-shock calculations.

The adaptations to the Modified Diffusion Model were validated with experimental data by Wang et al. [43] and the results are shown in Figure 2.12. Whilst the three-dimensional adaptation has better agreement with the experimental data than the two-dimensional method, it was still not fully accurate. Note that the pseudo-shock length in Figure 2.12 plays no role, since in the experimental set up, no pressure measurements were done beyond $\frac{x}{D} = 10$. However, due to the discrepancy in pressure distribution, the pseudo-shock behavior should be carefully reviewed in the experiments.

2.5.2. Interaction of sub-models

Like a supersonic intake, the SRIM has several flow conditions it can analyze: the supercritical and critical flow, and for every computation, both conditions are computed, first the supercritical and then the critical condition. To understand how the SRIM moves through the computational domain of the SSI, Figure 2.13 shows a visualization of the SRIM output for the supercritical condition. It is important to note that for the supercritical condition the computational domain is divided into triangular flow blocks that are always bound by two shock waves and a wall element, as indicated in Figure 2.13 by A1, A2 (for external flow) and 1, 2, 3, 4 and so forth (for internal flow). In each flow block the computational routine listed below is completed before moving on to the next block, directly downstream.

1. The SRIM performs the Method of Characteristics inside the flow block.
2. With the solution of the Method of Characteristics at the wall, the integral boundary layer analysis is done.
3. Using the boundary layer displacement thicknesses along the wall, new virtual flow surfaces are made, on which the Method of Characteristics is redone.

When moving between blocks or sub-models, flow information is transferred through interpolation. The routine of steps, applied to all flow block from upstream to downstream computes the supercritical condition flow. When the supercritical flow condition has been computed, the critical condition can be performed. By interpolation, the internal channel flow characteristics at a specified pseudo-shock start

location are translated to suitable inputs for the Modified Diffusion Model. Thereby, the critical condition flow is always dependent on the supercritical condition solution in the SRIM.

2.5.3. Inputs and outputs

As was mentioned, the inputs of the model are rather trivial. Typical for any aerodynamic model, they consist of a description of the free-stream flow and a flow device geometry. In addition, specific for the SRIM is a definition of the boundary layer in terms of momentum thickness. The outputs are important to describe since they need to be compared to experimental results, which is a factor in determining what quantities to measure in the experiments.

In the SRIM, the flow is described in terms of the stagnation values of pressure and temperature. A Mach number is also given to relate these to static terms by isentropic flow relations, and the momentum thickness of the incoming boundary layer is defined. The geometry is defined by a sets of points that describe the flow surfaces. A script exists that produces these sets of points based on geometric quantities such as expansion angle and radius, size and angle of the constant area duct and the angle and length of an optional extra flow deflection surface. The SRIM also enables a custom geometry as input.

The outputs of the SRIM are given by several of the sub-models. The method of characteristics computes a grid of nodes on which all relevant flow parameters are known, and the integral boundary layer methods return the boundary layer characteristics on points along each flow surface. Lastly, the pseudo-shock sub-model returns the pseudo-shock length and the Mach number and (total) pressure behind it as the most important parameters. From these outputs, all relevant flow information around a submerged supersonic intake can be computed. Therefore, the output of the SRIM is not a restrictive factor in its validation.

2.5.4. Model assumptions

To simplify calculations, Van Wijk made some assumptions to the flow that is calculated in the SRIM. Some are trivial, such as steady state flight, adiabatic wall and perfect gas assumptions, but others may need some verification by experimental data. These are listed below.

- **Boundary layer bleeds have no upstream influence.** The bleed slot is designed in such a way that it will not choke and affect the flow upstream of the intake. This is easily verified, since a choked bleed slot will be visible on schlieren imagery.
- **Transition occurs instantly on a specified location.** This will most definitely not be the case, but it is something to take into account. To validate the SRIM, the transition points in the computer simulated intake and the experimental model should be the same.
- **Shock wave boundary layer interactions force transition.** All boundary layers downstream of a shock wave will be turbulent. This may be verifiable using schlieren photography.

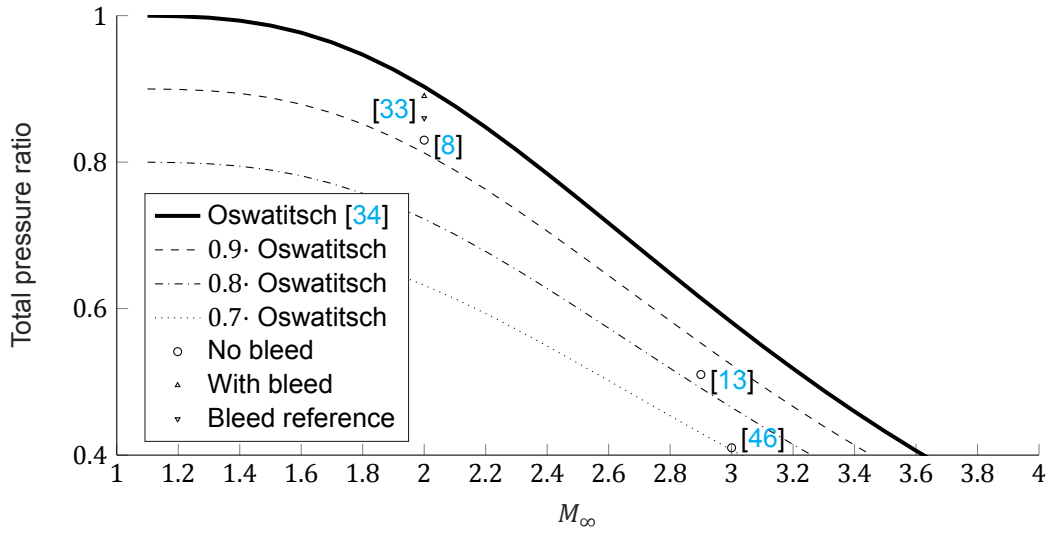
Total pressure ratio
M_∞
Oswatitsch [34]
0.9· Oswatitsch
0.8· Oswatitsch
0.7· Oswatitsch
No bleed
With bleed
Bleed reference
[33]
[8]
[13]
[46]

(a) n = 2

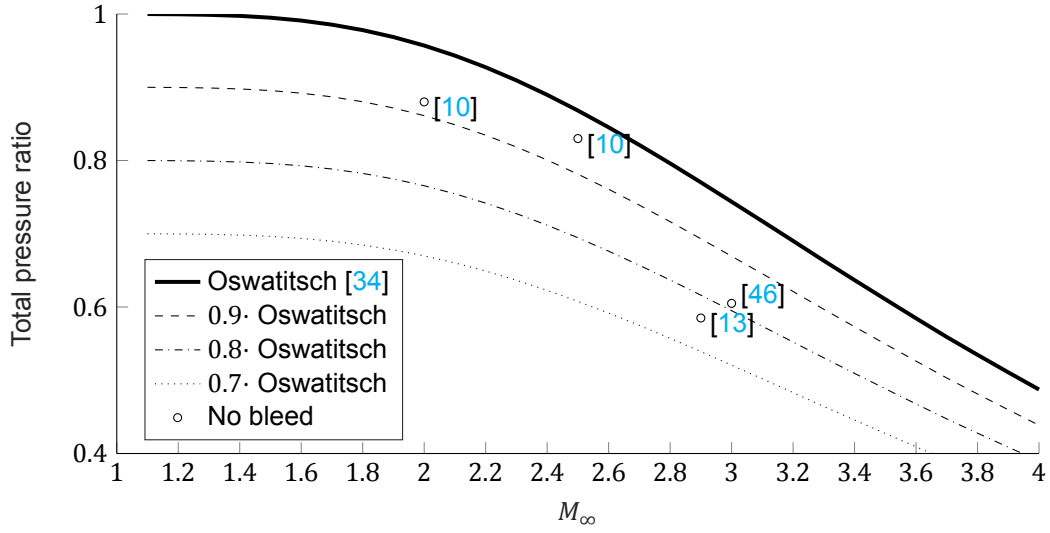
Total pressure ratio
M_∞
Oswatitsch [34]
0.9· Oswatitsch
0.8· Oswatitsch
0.7· Oswatitsch
No bleed
[10]
[10]
[46]
[13]

(b) n = 3

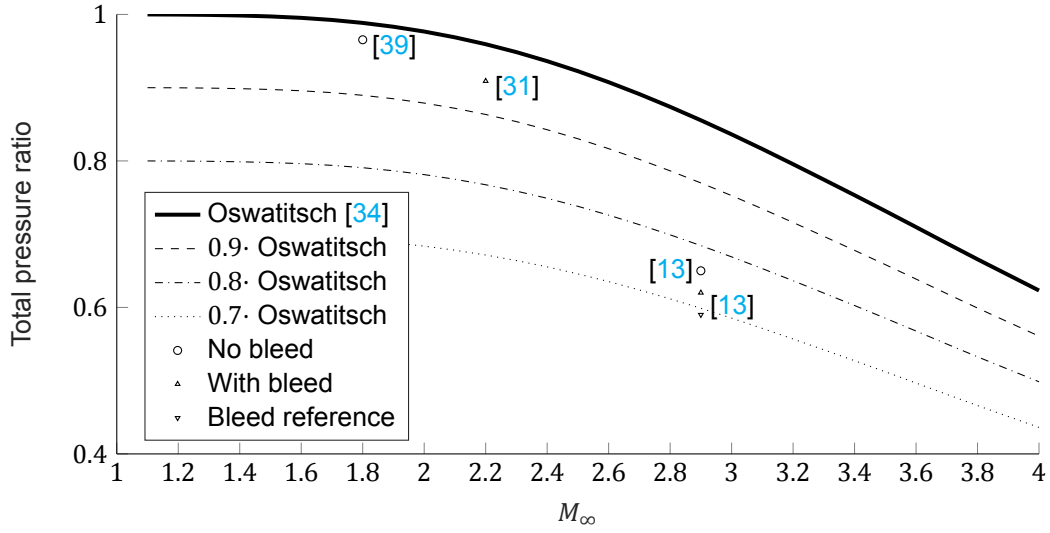
Total pressure ratio
M_∞
Oswatitsch [34]
0.9· Oswatitsch
0.8· Oswatitsch
0.7· Oswatitsch
No bleed
With bleed
Bleed reference
[39]
[31]
[13]
[13]

(c) n = 4

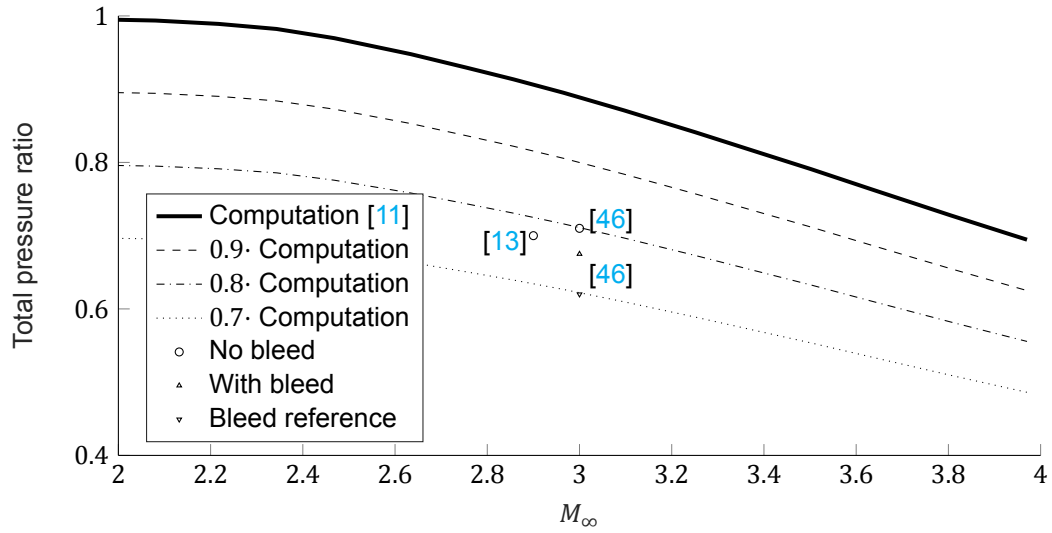

(d) Isentropic intake

Figure 2.10: Total pressure ratios vs. Mach number of several experimental studies and inviscid values for two-dimensional intakes of the same number of n-1 oblique shocks and one normal shock, as well as an isentropic intake.

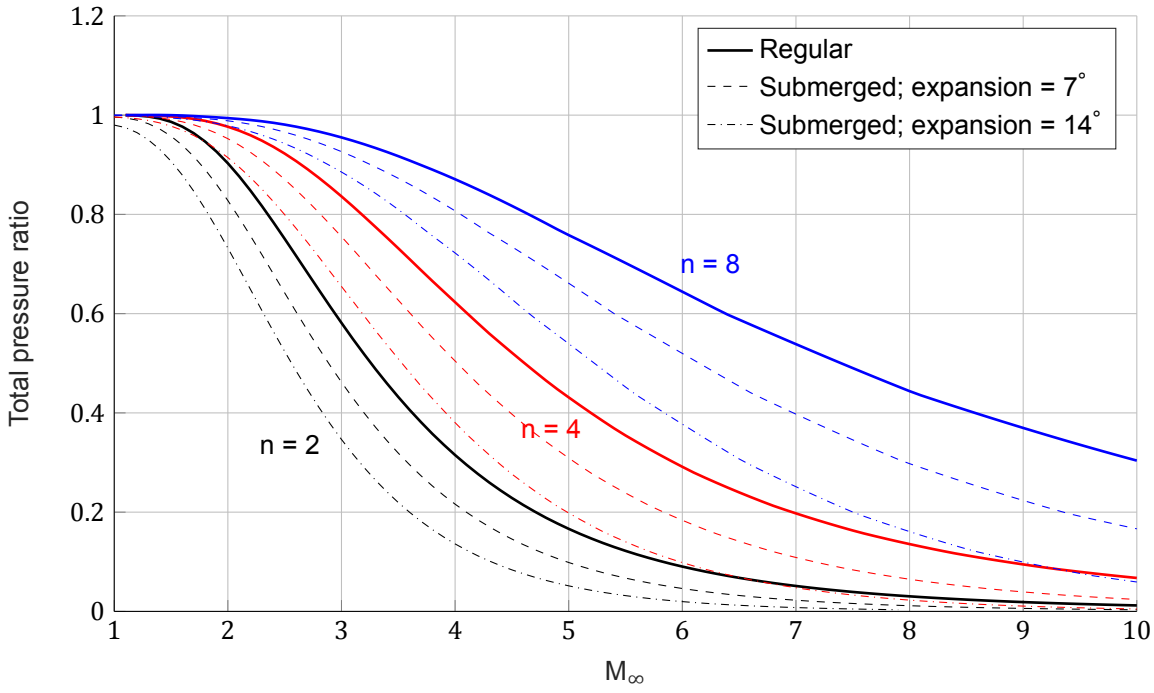

Figure 2.11: Total pressure ratios of three submerged Oswatitsch intakes at 14° and 7° expansion angles with n-1 oblique shocks and one normal shock for varying free-stream Mach numbers and their regular counterparts

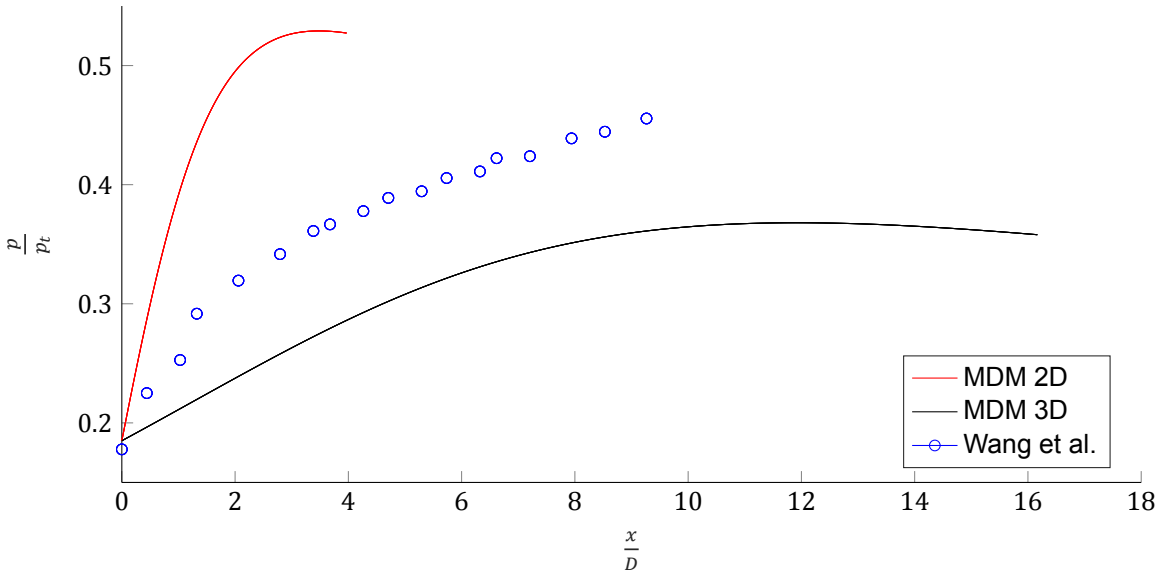

Figure 2.12: Results of the two-dimensional MDM, the three-dimensional asymmetric adaptation and experimental data for an asymmetric pseudo-shock from Wang et al. [43], with $M = 1.79$ and $D = 0.274$

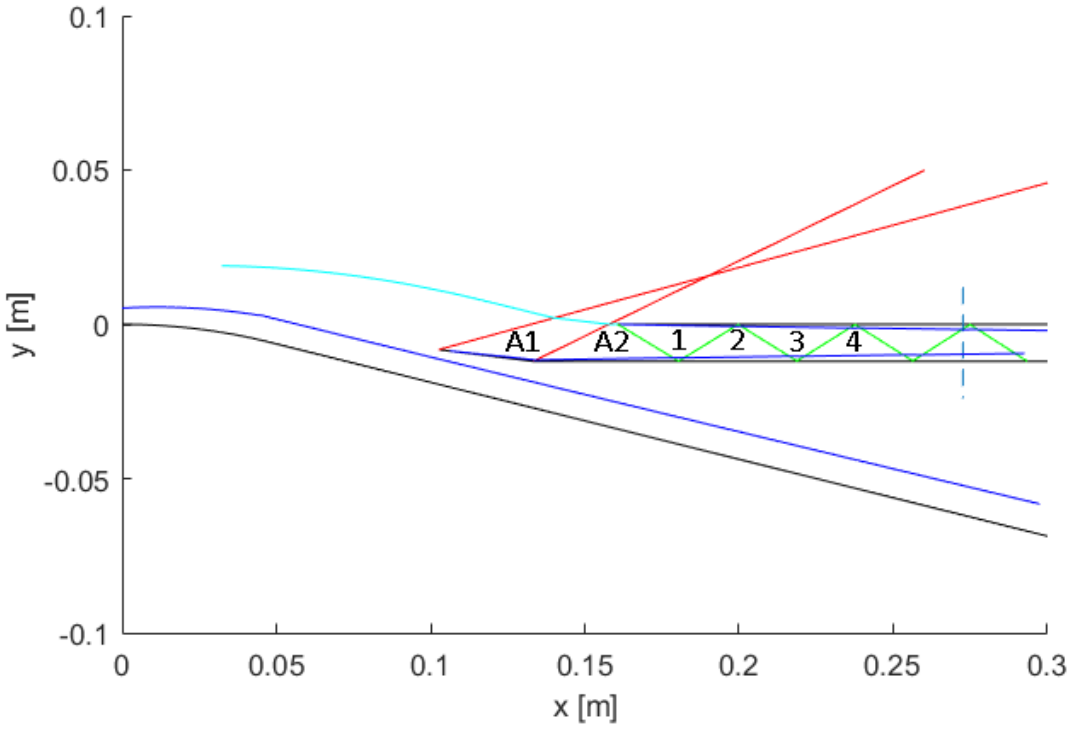

Figure 2.13: Visualization of SRIM output. Flow surfaces are shown in black, external shocks in red, internal shock in green. The dark blue line indicates the boundary layer edges and the cyan line is the top of the streamtube flowing into the intake.

3

Experimental methodology and facilities

The rationale behind the experiments and the facilities necessary to obtain the data needed for reconstruction of the flow field in a submerged supersonic intake is discussed in this chapter. To ensure reproducibility of the experiments performed in this research, the wind tunnel, intake models and measurement systems that were used during the experiments need to be described in detail. First, the characteristics of the wind tunnel used in experiments are described. Second, the design choices and configuration of the submerged supersonic intake model as well as the regular supersonic intake used as a test bed for the experimental facilities. Last, the measurement systems used to obtain the required data are listed.

3.1. Methodology

Since the goal of this work is to validate the Submerged Ramjet Intake Model (SRIM), the focus of the experiments is to obtain data that can be compared to the SRIM output, specifically in terms of important supersonic intake characteristics, i.e. total and static pressure, mass flow and visual flow characteristics. This section will explain the rationale behind the experiments.

Since the submerged supersonic intake has two distinct parts, the expansion section and the actual submerged intake, it was decided to divide the experiments into two separate slots. Testing the expansion section without the submerged intake first would give information about the flow around it, and whether it actually behaved as predicted by the SRIM. Also, it allowed acquisition of some much needed experience in experimental work. During the second slot the complete submerged supersonic intake model was tested. However, before this was done, a regular supersonic intake with known performance was tested to set up and verify the measuring systems.

Whilst the SRIM was designed to be able to process a large variation of intake geometries, it was decided to keep the wind tunnel model geometries relatively simple. Although this reduced the efficiency of the intake models tested, the simple geometries would facilitate SRIM validation since interference between flow phenomena was limited. The selected geometries were an intake with a single oblique shock and one terminal normal shock, which brought the number of shocks to $n = 2$, and a double oblique shock intake with one terminal normal shock, making $n = 3$. Henceforth these geometries will be referred to as the single and double shock intakes, or by their total number of shocks $n = 2$ and $n = 3$.

The SRIM is very versatile in terms of its output data. However, validation should be based on the most important factors of a supersonic intake: (total) pressure and mass flow. To obtain these characteristics from the flow in the SSI model, knowledge about the flow velocity, static and total pressure and total temperature is needed. This will be measured by pressure and temperature gages in the settling chamber, pressure gages in the SSI model, schlieren imagery and Particle Image Velocimetry (PIV).

Gages in the settling chamber will measure the stagnation conditions in the flow, with which the pressure ratio of the intake will be determined. Pressure gages in the SSI model will measure the local static pressure that will determine the intake performance. The schlieren images serve as an easy way to visualize the flow for qualitative comparison with the SRIM output. The PIV measurements will provide the flow direction and velocity in the entire flow field, which, in combination with the static

Figure 3.1: The ST-15 wind tunnel hall at the High-speed laboratory.

pressure, enables the computation of total pressure in the entire intake.

During experiments it was found that PIV measurements were not possible for Mach numbers greater than 2 due to hardware limitations. Therefore, further PIV measurements were canceled. The PIV setup, experiment description and results are briefly discussed in Appendix B. Note that due to the cancellation of the PIV experiments, data for flow velocity lacked in the final data set, which needed to be solved. The solution is discussed in Chapter 5.

3.2. Wind tunnel

The experiments were be performed in the ST-15 supersonic wind tunnel at the High-speed Laboratory of the faculty of Aerospace Engineering at Delft University of Technology, see Figure 3.1 and 3.2. The ST-15 is a blow-down wind tunnel with a relatively long running time of 18 minutes before recharging of the pressure vessel is necessary. The upstream nozzle of the ST-1 consists of interchangeable sets of liners also called Mach blocks, which can realize Mach numbers of 1.5, 2, 2.5 and 3 in the 150 by 150 mm test section. The Mach blocks can also be replaced by specialized nozzle blocks for particular needs, as in this experiment, see Section 3.3.

The ST-15 features side-mounted doors which fully open to replace Mach blocks and gain access to the test section, as shown in Figure 3.3. The lower nozzle block shown here is adapted to simulate the fuselage of a missile containing a submerged supersonic intake. The doors of the ST-15 contain relatively large windows of 250 mm diameter to allow optical access to the test-section for non-intrusive measurement techniques such as Schlieren and PIV.

Other than the side doors, access to the ST-15's test section is possible via a retractable rear diffuser, which is mounted on wheels and can be pushed back with an hydraulic system. This provides access to the rear of the test section.

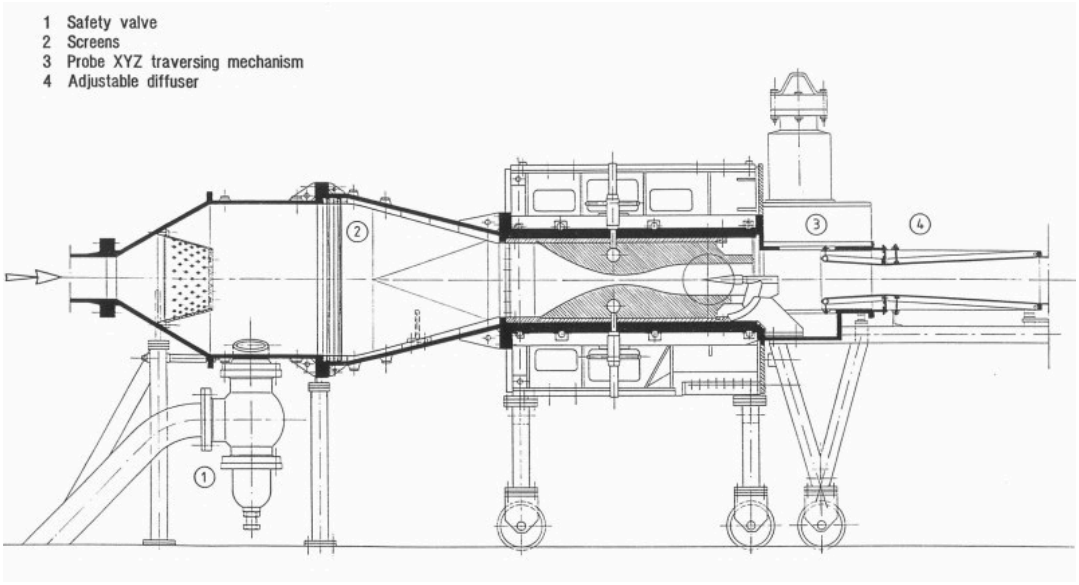

Figure 3.2: Schematic drawing of the longitudinal cross-section of the ST-15 wind tunnel.

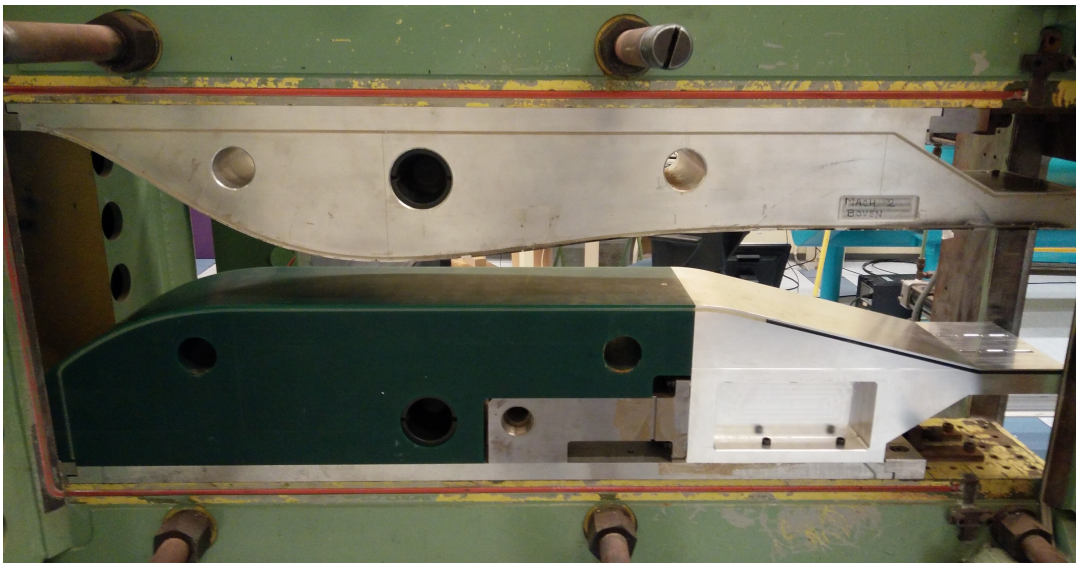

Figure 3.3: The ST-15 wind tunnel with open doors and visible Mach blocks. The green lower nozzle block, the plug nozzle block [44], represents the missile fuselage featuring a submerged supersonic intake. Here it is shown with the expansion section and support of the submerged supersonic intake model attached.

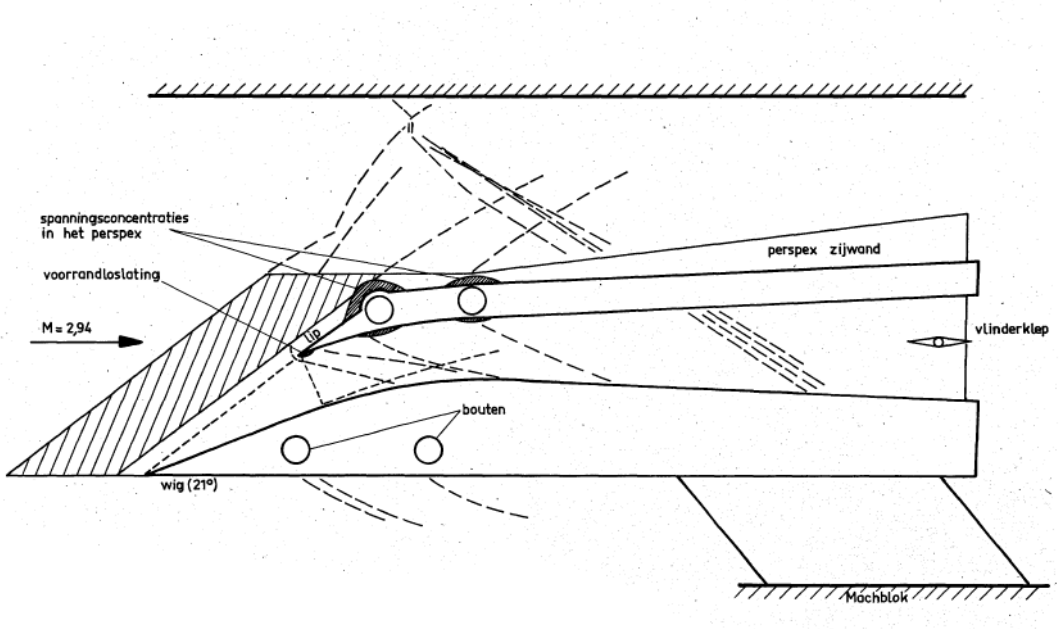

Figure 3.4: Schematic drawing of the Nebbeling and Bannink intake model.

3.3. Model description

As mentioned earlier, two different wind tunnel models were used. An existing regular supersonic intake that was used as a test bed for the measuring systems and the actual submerged supersonic intake model. The features of the regular intake model are presented. Next, the design procedure of the SSI wind tunnel model is discussed and the resulting intake model is introduced.

3.3.1. Nebbeling and Bannink intake

As a way to set up the measuring systems while some parts of the submerged supersonic intake were still in production, an intake previously investigated by Nebbeling and Bannink [32] was tested. The intake is described extensively in their memorandum [32], but for completeness, a summary will be given here.

The intake is equipped with an external supersonic diffuser with a single wedge of 21° deflection angle, designed for a Mach number of 2.94. This wedge produces a shock wave that impinges on a curved cowl lip, which is the start of the internal channel. The sidewalls of the intake are made of transparent perspex material that allows for optical access. In the sidewalls, elongated slots are made that allow the movement of the wedge relative to the cowl lip, to adjust for changes in the operating conditions. At the leading edges, the outside of the sidewalls is tapered to form a sharp edge as to minimize the influence of the sidewalls on the intake. Because the oblique edges of the transparent perspex can distort light, they are painted matte black to minimize their interference with schlieren photography.

The subsonic diffuser of the intake consists of a channel with an adjustable total divergence angle from 5° to 7°. At the end of the subsonic diffuser, a butterfly valve is placed over the full intake width to control the mass flow through the channel. The butterfly valve can be controlled via a rod on the outside of the intake (see Section 3.3.3 for more details). The intake is attached to the bottom Mach block of the ST-15 with fixed supports. See Figure 3.4 for a schematic drawing of the intake.

In the experiments discussed in their memorandum [32], Nebbeling and Bannink only performed shadowgraph photography on the intake. For the present experimental campaign both schlieren visualization and pressure measurements were performed on the intake. For the latter, pressure holes were drilled in the intake. These holes consist of a 0.6 mm diameter hole in the surface, tapering out at a depth of 3 mm to accommodate a 2 mm metal tube that communicates the local pressure to a pressure measuring device. The locations of the pressure holes in the Nebbeling and Bannink intake are

Table 3.1: Table of pressure hole locations in the Nebbeling and Bannink intake. s being the distance along the surface, starting at each surface leading edge.

	Lower surface	Upper surface
s [mm]	25	35
	55	110
	155	

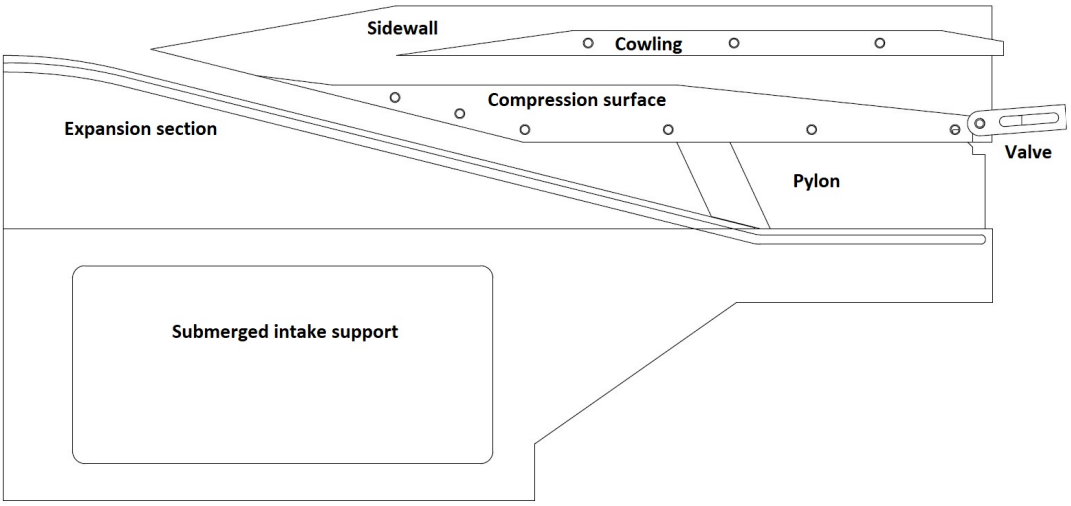

Figure 3.5: Schematic drawing of the dual shock submerged supersonic air intake intake model

given in Table 3.1. The locations were chosen such that a pressure orifice was located on the wedge, upstream of the cowl, and in the internal channel, in the constant area duct and close to the butterfly valve, on both the upper and lower walls.

3.3.2. Submerged supersonic intake

Obtaining data to validate the SRIM was done through experiments, for which a wind tunnel model had to be designed. Considerations made during the design process are discussed in this section. Then, the developed SSI wind tunnel model and its individual parts are presented.

Figure 3.5 shows an schematic overview of the submerged intake. A double shock compression surface is shown here. The single shock compression surface has similar design. As described in Section 2.1, a supersonic intake has several stages of compression, these can be found here as well. Note that the compression surface is located some distance downstream of the expansion section. This allows for the disposal of the boundary layer built up on the nozzle block and expansion section, essentially forming the submerged variant of fuselage bleed (see Section 2.1.3 for more information). After the single or double shock compression caused by the compression surface leading edge, the intake forms an internal channel consisting of a constant area duct with a height of $12mm$ and a subsonic diffuser afterwards. The length of the constant area duct was designed based on the length of possible pseudo-shocks (see Section 2.1) in the channel, so that the internal flow will be fully subsonic before it enters the subsonic diffuser. The subsonic diffuser is realized by a $6°$ outward deflection in the compression surface. Together with the straight internal cowling wall, this makes a subsonic diffuser with divergence angle of $3°$. Since the SRIM does not have the capability to analyze a subsonic diffuser, in terms of validating the SRIM, its only function is to stabilize the flow in the rest of the SSI model.

The design process of the submerged supersonic intake model described above started with the recommendations made by Van Wijk [41]. He suggested an intake model spanning the width of the ST-15's test section to mimic the two-dimensional nature of the SRIM. However, after some consideration, it was decided to design a submerged supersonic intake wind tunnel model of finite width, bounded by transparent sidewalls, similar to the intake of Nebbeling and Bannink described above.

This was done for two reasons, the most important being the likeliness of the wind tunnel not starting due to model blockage. An intake model spanning the test section width requires the lower compres-

sion surface and upper cowling to be attached via supports to the lower and upper test section walls, respectively, as the internal channel needs to be clear of any obstruction. These supports would take up large spaces in the test section, causing too much model blockage for the wind tunnel to achieve supersonic flow in the test section, as per the limiting contraction ratio (see Section 2.1.4).

The second reason for the choice in favor of a finite width wind tunnel model is the wind tunnel wall boundary layer. An intake model of test section width would have ingested turbulent boundary layers of large thickness due to their long path along the wind tunnel side walls. These thick boundary layers would have very likely interfered with several measurements. E.g., the readability of schlieren imagery would have been compromised by the turbulent flow in the boundary layers. Also, the pressure distribution in the internal channel would have been affected. Correcting for these effects would have been difficult because measurements on these boundary layers are nontrivial.

The width of the intake model was decided based on the width of the attachment slots in the submerged intake support, described below. This part was already produced when the decision to narrow the submerged supersonic intake model was made. The attachment slots provided the lower limit of the intake model width, the were located $50mm$ apart. By taking into account the slot dimensions and allowing for some space around the holes in the compression surface part where the SSI model is attached to the supports, the internal width of the intake was decided to be $67mm$.

The different parts of the submerged supersonic intake model will be discussed below. Technical drawings of all parts can be found in Appendix D.

Submerged intake support

The submerged supersonic intake model is attached to the so-called plug nozzle block, designed by Wisse for his PhD research [44], which is the green lower nozzle block in Figure 3.3. The plug nozzle block mimics the fuselage to which the submerged supersonic intake would be attached. The SSI support was designed specifically to fit to the plug nozzle block and to support the expansion section (see next section). Slots with a length of $2cm$ are milled out in the support to which the pylons (Figure D.7) and the intake model (Figures D.3 and D.4) can be attached, which in turn support the rest of the intake via the transparent sidewalls. The slots in the support are elongated on purpose, allowing the intake to be moved up or downstream, giving the intake model some flexibility to adjust the bleed slot to dispose of the entire boundary layer.

Expansion section

The submerging of the supersonic intake means that the flow must be turned into the vehicle body. This happens at the expansion section, named after the supersonic expansion that occurs when flow encounters a convex corner.

The expansion section and its support for the rest of the intake model, described above, are attached to the plug nozzle block, shown as the green lower nozzle block in Figure 3.3. Note that since the expansion section is attached to the plug nozzle block, its width equals the test section width, as designed by Van Wijk.

The angle with which the expansion section deflects the flow was chosen to be $14°$. This was deemed by Van Wijk [41] to be a good compromise between pressure losses due to flow expansion and optical access, since high expansion angles would incur more pressure losses in the intake, as mentioned in Chapter 2, and low expansion angles would move the actual intake downstream beyond the region where optical access is available. The expansion angle of $14°$ is the minimum angle for which the constant area duct is fully within the area of optical access, enabling schlieren and PIV measurements of the pseudo-shock. Since this is an important part of the flow field in the intake, the expansion angle was chosen a such. The expansion radius was set at $200mm$, an arbitrary choice since the expansion radius size has little effect on the flow over the expansion section [41].

The expansion section was milled out of aluminium using CNC tooling, leaving a roughness on the flow surface. It was decided to leave it since the effect of the roughness on the flow would be undetectable by the measuring systems used. The boundary layer thickness on the expansion section as predicted by the SRIM is approximately $10mm$, whilst the size of the surface roughness would be in the order of magnitude of $0.1mm$. It was therefore assumed that the surface roughness was non-influential to the boundary layer development and left on the expansion section.

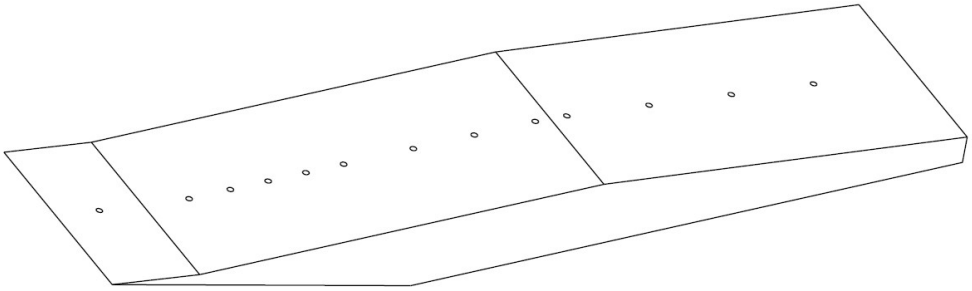

Figure 3.6: Isometric view of the compression surface with the location of the pressure holes

Compression surface

The compression surface is equivalent to the initial wedge in an regular supersonic intake with external compression, producing the oblique shock the flow encounters first. Two compression surface parts were produced, both will deflect the flow after expansion back to the free-stream direction. This was decided based on practical grounds, since the available vertical space in the test section was limited. One of the compression surfaces does deflects the flow with a single oblique shock with a flow deflection angle of $14°$ and the other with two oblique shocks, each shock having a flow deflection angle of $7°$. Note that due to manufacturing limitations, the leading edge of the compression surface has a slight bluntness to it, specifically, its diameter of curvature is around $0.1mm$. This may cause the shock causes by the leading edge to detach somewhat. Next to that, the edge supposed to cause the second shock in the dual shock intake shows not an instantaneous but a curved deflection, again, due to production limitations. This may also affect the intakes performance, for it may cause an isentropic compression fan rather than a shock wave.

The compression surface has pressure holes similar to the ones in Nebbeling and Banninks intake. They have an $0.6mm$ diameter at the flow surface, and a $3mm$ diameter on the other side where a tube is attached to connect the pressure hole to the pressure sensor. A shallow channel was made to stow the tubes, which run through a hole in the wind tunnel side to the measuring equipment. The locations of these pressure holes are shown in Table 3.2. The locations of the holes were chosen with the length of a pseudo-shock in mind. To accurately measure the pressure rise in the pseudo-shock it was assumed that a minimum of four pressure holes need to be present. Thus, in the minimum pseudo-shock length predicted by the SRIM, which occurs at a free-stream Mach number of 2, four pressure holes were equally spaced. After that, more pressure holes were spaced for the longer pseudo-shock at the higher Mach numbers of 2.5 and 3. Four pressure holes were also located in the subsonic diffuser, since, despite the SRIM not returning data for the flow in this part of a SSI, it may return valuable results. For the dual shock compression surface, one pressure hole was located on the lip, and one after the second shock deflection. The single shock compression surface also has a pressure hole slightly aft of its leading edge, to measure the pressure ahead of the internal channel. Figure 3.6 shows the locations of the pressure holes on the compression surface. The pressure holes dedicated to measuring the pseudo-shock can be clearly seen tightly spaced at the upstream part of the straight constant area duct section.

Table 3.2: Pressure hole locations in the compression surface of the submerged supersonic intake for the single and double shock variant. x being the distance along the x-axis w.r.t. the part's leading edge.

	x [mm]												
Single shock	30	44	57	70	83	108	128	150	161	189	218	248	
Double shock	10	40	60	73	86	99	123	144	165	176	205	234	262

Cowling

The cowling makes the upper part of the intake's internal channel. The experimental campaign featured tests at different Mach numbers, which result in shock waves of different angles at the compression surface. As explained in Section 2.1.4, when an intake encounters above design Mach numbers, the oblique external shock system may enter the internal channel, which is undesirable. Thus, since the SSI model will be tested at multiple Mach numbers, it is important that the cowling can be moved forward and aft in streamwise direction. This is achieved by having slots in the sidewalls where the cowling is attached.

The locations of the pressure holes in the cowl are presented in Table 3.3. Like the compression surfaces, the cowling has a channel to accommodate the pressure tubes. The locations of the pressure holes were determined in a similar fashion as for the compression surface.

Table 3.3: Pressure hole locations in the cowling of the submerged supersonic intake for the single and double shock variant. x being the distance along the x-axis w.r.t. the part's leading edge.

	x [mm]										
Cowling	9	24	39	54	69	84	99	120	150	180	210

Like the compression surface parts, the cowling leading edge has a slight bluntness, with a diameter of approximately $0.1mm$, which may cause detachment of the shock protruding from it, possibly affecting the experimental result.

Mass flow control valve

The end of the internal channel is marked by the mass flow control valve. It was designed as an asymmetrical valve with its axis next to the compression surface, as shown in Figure 3.5, as well as having a slit in the middle, which can be seen in the technical drawing in Figure D.10. This was due to the intention of performing PIV measurements in the submerged supersonic intake model. Trough the slit, a PIV-laser sheet would be able to illuminate PIV particles inside the internal channel.

During testing of the submerged supersonic intake model, it appeared that the force required to close the asymmetrical valve was too large for the control system (see Section 3.3.3) to deliver, due to the asymmetrical loading on the valve. Since the PIV measurements were canceled, the requirement for laser sheet access became redundant and the asymmetrical valve was replaced by a symmetrical butterfly-type valve in the middle of the subsonic diffuser, which required less torque to operate under loading. Pictures of the butterfly valve are shown in Figure 3.7. Due to the short-term nature of replacing the valve, little effort was put into design of the butterfly valve, and its rectangular cross section may have interfered with the turbulent flow in the subsonic diffuser.

Sidewalls and supports

The sidewalls are attached to the compression surface and cowling to make the internal channel. They are made from transparent perspex to allow for optical access in the channel. To minimize their influence on the flow, the leading edges are tapered and subsequently painted matte black to minimize light distortion that may influence schlieren measurements, similar to the Nebbeling-Bannink intake.

The sidewalls feature metal strips that reinforce the locations where they are attached to the other parts. The metal strips and bolts are made flush with the surface to minimize interference in the flow.

The intake is supported by two stainless steel pylons that connect the expansion section support and the compression surfaces. The pylons have a tapered leading edge to minimize flow interference and a notch in the trailing edge where pressure tubes can run sheltered from the supersonic flow in the test section.

3.3.3. Valve control

As explained in Chapter 2, flow in the intake must start by settling the shock system in the design positions. This requires a normal shock to run through the intake. As by the limiting contraction ratio, the internal channel should be as unobstructed as possible. To do so, the mass flow valve must be completely opened. Then, to run the intake efficiently, critical operating conditions must be reached by gradually closing the valve. Because no physical access is possible while the wind tunnel is running, active control of the valve in the test section is necessary.

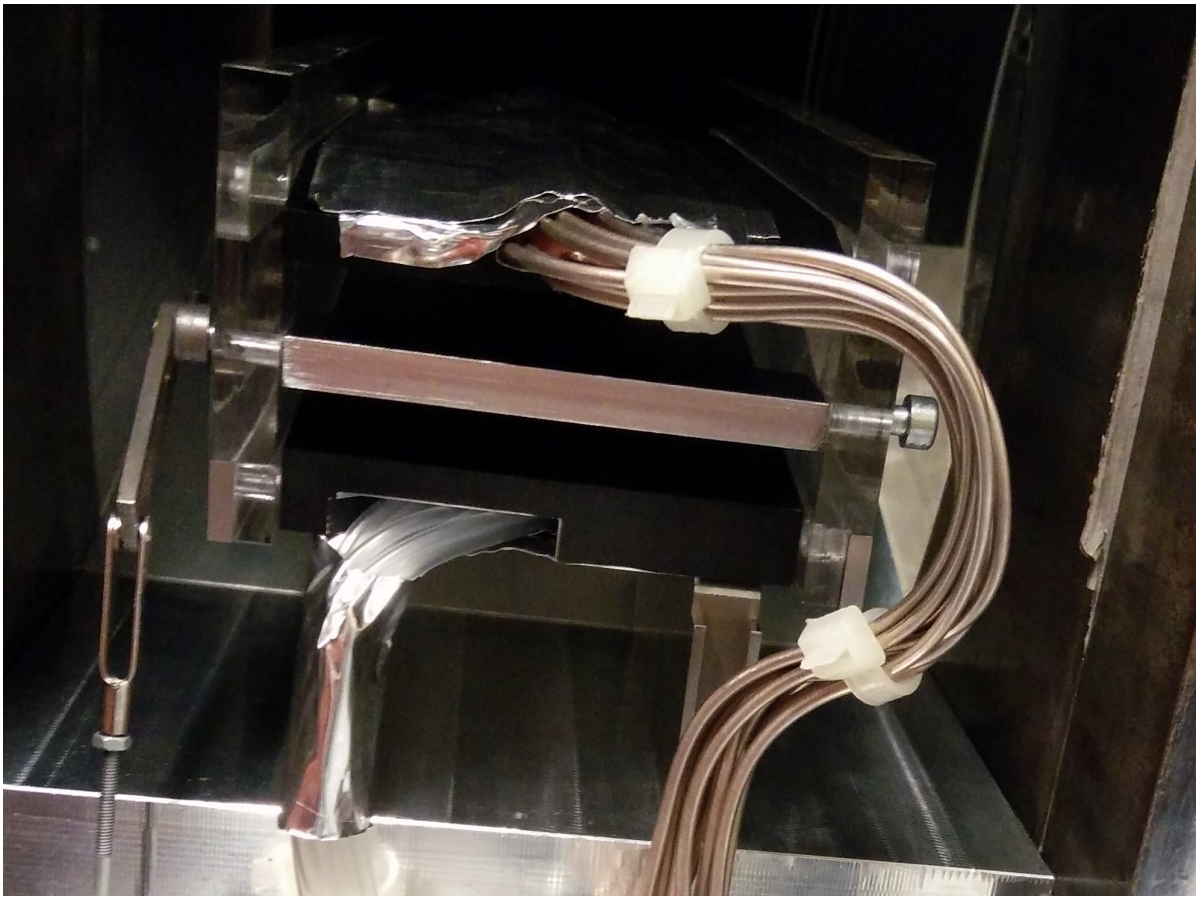

(a) Photographed from the rear

(b) Photographed from the side

Figure 3.7: Butterfly valve in at the end of the subsonic diffuser in the submerged supersonic intake model

Figure 3.8: Picture of the actuation system that drives the mass flow control valve at the back of the intake

The flow control valve is actuated by an electric servo. The servo used for this purpose is a Robbe Futaba S3003, with a torque of $4.10 kgcm$. As can be seen in Figure 3.8, the servo is attached to the expansion section support with metal clamps. From there it actuates a rod that moves the arm, creating a rotation to open or close the valve.

The servo was controlled using an Arduino controller that could set the servo anywhere in its $180°$ range accurate to $1°$. The translation to the valve angle setting was determined by measuring the the valve angles at all servo settings. This gave an accurate calibration table to relate the servo angle to the valve angle. Using the valve angle, the channel area at the valve could be determined. A linear relation between the Arduino controlled servo setting and valve angle does not exists due to the geometry of the actuation system, but the accuracy of the valve angle could be determined using the calibration tables. At valve settings near intake critical conditions, where the flow is most sensitive to valve deflection, a $1°$ increase in servo angle translated to approximately $0.5°$ valve angle increase.

3.4. Measuring systems

The experiment called for measuring systems that can visualize and quantify the flow in the submerged supersonid intake model. Steady static pressure measurements were performed using a rotating Scanivalve system, the wind tunnel conditions were measured continuously using pressure sensors and a thermocouple, and a schlieren system was used to visualize the flow. Also, some PIV measurements were done, so the PIV equipment used will be listed.

3.4.1. Scanivalve

The pressure holes in the cowling and compression surface of the intake were all attached to a Scanivalve 48D3-305 pressure sensor, shown in Figure 3.9. The Scanivalve system features a single pressure sensor in a circular arrangement of input valves. The Scanivalve connects each input valve to

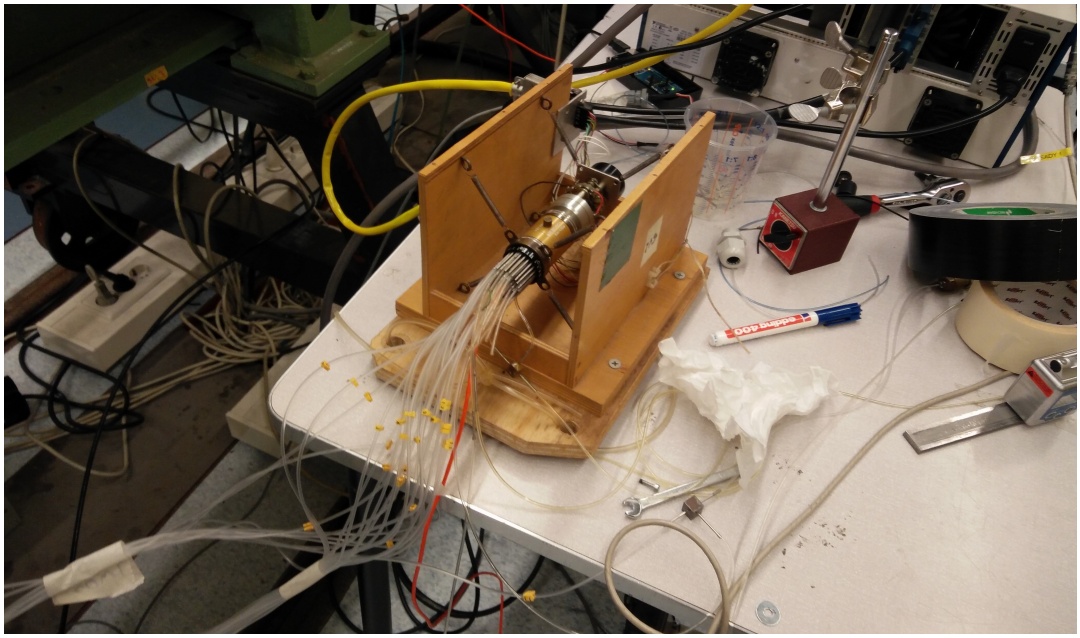

Figure 3.9: Picture of the Scanivalve pressure measurement system connected to pressure tubes leading to the submerged supersonic intake wind tunnel model.

the sensor successively and measures its output. This method takes some time to complete all measurements, which means the Scanivalve can only be used for steady flow. The limit to the Scanivalve measurement system was found to be $2.5bar$. The settling chamber pressure was to be set so that the wind tunnel started and the pressure at the Scanivalve holes did not exceed $2.5bar$.

3.4.2. Wind tunnel conditions

The conditions in the wind tunnel are measured at a rate of $5Hz$ by a continuous measuring system. The pressure and temperature in the settling chamber, pressure just upstream of the expansion section at both wind tunnel walls are measured over the entire run of the wind tunnel. The most downstream pressure hole of the compression surface was also measured by the continuous system. At this location, the Mach number is small, so this pressure hole gives a good indication for the total pressure in the intake.

The pressure transducers were of the Druck PDCR 820 type, connected to a National Instruments 9237 bridge input model. The temperature was measured using a National Instruments 9207 voltage and current input module through a Newport 202A-J thermocouple meter (J-type thermocouple). Both temperature and pressure measurements were fed into a computer outfitted with LabView using a National Instruments cDAQ-9174 USD chassis.

3.4.3. Schlieren photography

For the visualization of the flow in the submerged supersonic intake, the well-established method of schlieren photography was used. The setup of the schlieren system was already present in the ST-15 wind tunnel hall, parts of which can be seen in Figure 3.1. A Z-type schlieren setup is used, with a light source with pinhole of $2mm$ and a horizontal schlieren knife orientation. A schematic of the setup is shown in Figure 3.10.

The camera to capture the images was an Imperx Bobcat CCD camera of 1624 by 1236 pixels, equipped with a lens of $80mm$ focal length. This resulted in a capture size of $0.105mm$ per pixel. This translates to a spatial resolution of approximately $0.17m$ in the x- and $0.13m$ in the y-direction, which covers the x-axis from $0.1m$ to $0.27m$ and the y-axis from $-0.06m$ to $0.07m$ in the coordinate system of Figure 2.13.

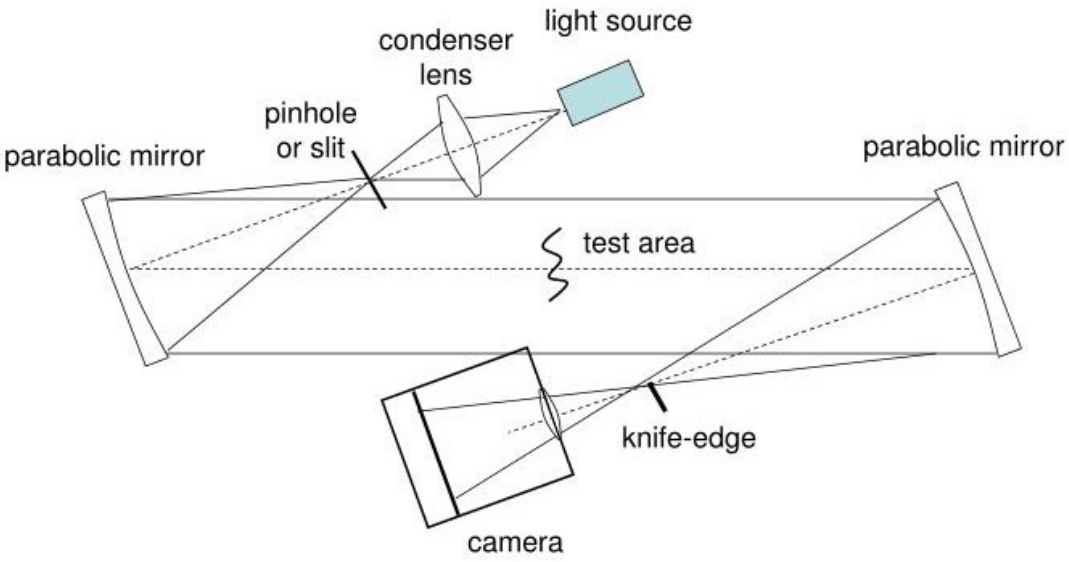

Figure 3.10: Schematic of the Z-type schlieren setup, taken from [7]

4

Experiments

For logistical reasons to be discussed later in the chapter, the experiments were divided into two slots. During the first slot, the flow around the sole expansion section was measured. The second slot was used to test the full submerged supersonic intake model. In this chapter, the methodology of the experiments will be presented, along with a description on some events and particularities that emerged during testing. This will provide explanation for measurement choices and list lessons learned for future research.

4.1. Expansion section experiments

In the first experimental only the expansion section of the submerged supersonic intake was tested. The goal of this test slot was twofold: obtain data on the flow behavior around the expansion section, and gain experience with testing in the ST-15 and operating the measurement systems.

4.1.1. Test matrix

The planning of this test slot was designed with the downtime of changing the Mach blocks in mind. The amount of Mach nozzle block changes was minimized whilst still conducting measurements at the three Mach numbers of 2, 2.5 and 3. This meant running all tests; schlieren and PIV for one Mach number before changing the nozzle block. It was advised to perform schlieren measurements before PIV measurements, this resulted in the test matrix shown in Table 4.1. Note that no geometric changes could be made to the expansion section and the pressure measuring system was not available. Thus, outside capturing the flow images for schlieren and PIV for each Mach number, no further variation in testing was possible.

4.1.2. Model set-up

Experimental set-up for test slot one started with installing the plug nozzle block with the submerged supersonic intake support attached into the ST-15. This proved difficult since the total length of the plug nozzle block and support exceeds the ST-15 side door width, as can be seen in Figure 4.1. Therefore, installing required the green plug nozzle block to be detached from its steel base plate and put into the test section. Then the parts could be joined together again.

Table 4.1: Test matrix for expansion section experiments

M_∞	$p_{sc}[bar]$	Measuring technique
2	3.1	Schlieren PIV
2.5	6.0	Schlieren PIV

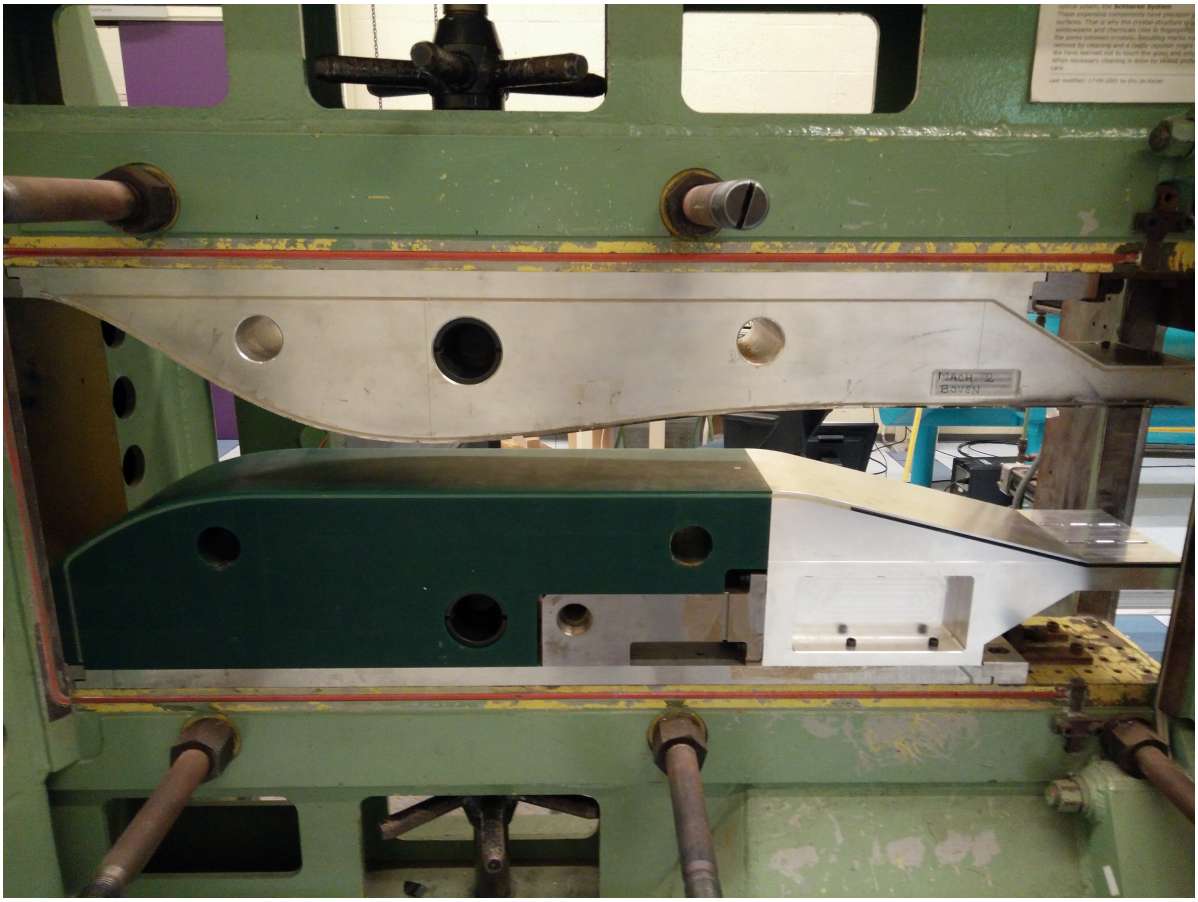

Figure 4.1: Plug nozzle block, submerged supersonic intake support and expansion section installed in the ST-15

Table 4.2: Results of inviscid pressure calculation for different Mach numbers

M_∞	$M_{expansion}$	$p_t[bar]$	$p_{expansion}[bar]$	$p_b[bar]$
2	2.55	4.1	0.22	1.64
2.5	3.18	6.9	0.14	1.67
3	3.85	12	0.09	1.65

4.1.3. Settling chamber pressure

During testing it turned out that due to the extra expansion in the test section, the minimum settling chamber pressure for the wind tunnel to start was significantly higher than normal. For a Mach number of 2, this resulted in a settling chamber pressure of $4.1bar$ and for a Mach number of 2.5, the minimum settling chamber pressure was $7.0bar$. Before installing the nozzle block for Mach 3, a quick inviscid calculation was performed, based on the ST-15 back pressure for Mach 2 and 2.5, to estimate the required settling chamber pressure for started Mach 3 flow.

The theoretical Mach number behind expansion was computed using the Prandtl-Meyer expansion theory. Then, using isentropic flow relations, the pressure in the test section behind the expansion was computed. After the test section, the flow must reach subsonic conditions again by a strong normal shock. The pressure behind this shock was deemed to be the back pressure of the wind tunnel and was computed to be around $p_b = 1.65bar$ for both Mach 2 and 2.5 flow. Then the computation was reversed to see what the settling chamber pressure needed to be to reach the same back pressure conditions with Mach 3 flow before the expansion. The results of this inviscid calculation are shown in Table 4.2. The required settling chamber pressure turned out to be around $12bar$, which was beyond the operating conditions of the pressure transducers in the ST-15, meaning testing at a Mach number of 3 was impossible.

4.1.4. Schlieren measurements

Most of the schlieren system is specific to the ST-15. The schlieren images were captured as planned for Mach 2 and 2.5 flow. A good exposure time per frame was found to be $15\mu s$ and series of 100 images were shot per test case at a capture rate of $5Hz$. The exposure time originates from a trade-off between contrast in the picture due to the amount of lighting and flow displacement. A longer exposure time results in more contrast but also larger flow displacement in the image. For high-speed unsteady flows, the latter can deteriorate the accuracy of the schlieren image when the exposure time is too long. For the current case of the expansion section, however, the flow is very steady and thus a longer exposure time can be justified to achieve better contrast in the picture. And the exposure time of $15\mu s$ was found to give sufficient contrast.

To determine the flow Mach number behind the expansion, a piece of copper tape was stuck to the expansion section. This introduces a small step of approximately $0.15mm$ on the surface from which a Mach wave would emanate. The angle of this Mach wave can be used to determine the Mach number behind the expansion experimentally. This method depends on the assumption that the wave produced by the copper tape is weak.

4.2. Full submerged supersonic intake model experiments

During the second test slot the complete submerged supersonic intake model was tested. The intake of Nebbeling and Bannink, described in Section 3.3.1, was installed and tested first to calibrate and verify the working of the measurement systems. This section will describe the planning of experiments performed on the submerged supersonic intake models, problems that arose and their solutions. With the lessons learned from test slot one, a test matrix was designed. The submerged supersonic intake model was set up in the wind tunnel. Figure 4.2 shows the SSI model in the ST-15.

4.2.1. Test matrix

As was learned in the first test slot, testing could only be done at Mach 2 and 2.5 because of the higher settling chamber pressure required to start the wind tunnel due to the extra expansion involved with the SSI model. Furthermore, the submerged supersonic intake model provided two different configurations. These were all tested at three operating conditions: supercritical, critical, and a hybrid mode, with the pseudo-shock staring approximately halfway into the constant area duct, which was called the

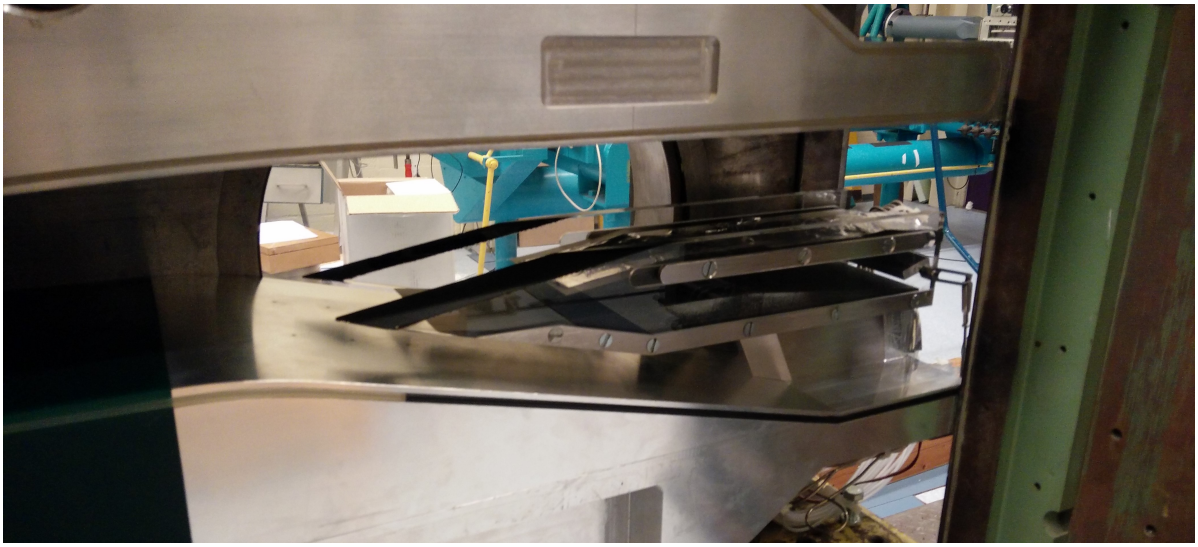

Figure 4.2: The submerged supersonic intake model in the double shock configuration in the test section of the ST-15.

Table 4.3: Test matrix of the test slot for the submerged supersonic intakes

Intake	M_∞	$p_{sc}[bar]$	$T_{sc}[K]$	Re_∞ [-]	Measurement
Single shock	2.5	5.0	277.8	6.74e5	Find critical valve deflection Supercritical condition Slightly supercritical condition Critical condition
	2	3.1	279.0	5.32e5	Find critical valve deflection Supercritical condition Slightly supercritical condition Critical condition
Double shock	2	3.1	279.8	2.25e5	Find critical valve deflection Supercritical condition Slightly supercritical condition Critical condition
	2.5	5.0	278.4	6.47e5	Find critical valve deflection Supercritical condition Slightly supercritical condition Critical condition

slightly supercritical condition. As mentioned earlier, the intake must start in the supercritical condition, whereafter the critical condition is reached by closing the valve at the end of the internal channel. This was done first for each combination of Mach number and intake configuration to find the valve deflection at which the intake model reached critical condition.

Unlike the first test slot, where only one configuration was available, in the case of the submerged supersonic intake model, two configurations required testing at two Mach numbers. Since changing a nozzle block was less time-consuming than changing the configuration of the intake model, the intake configuration was only changed once, and the nozzle blocks twice. The total test matrix is shown in Table 4.3. With the exception of the measurement to find the critical condition, each measurement was done threefold. For each measurement, the wind tunnel was started, the right operating condition found, measurements done and the wind tunnel was turned off. This method was elected above running the wind tunnel for a longer period of time and conducting three measurements in a single run, because then phenomena in the model may have influenced one another. The Reynolds numbers in Table 4.3 were computed using free-stream values of velocity, density and dynamic viscosity. The length scale was chosen to be the internal channel height, since it is a also relateble to the two-dimensional flow in the SRIM.

4.2.2. Schlieren measurements

To find suitable schlieren settings some trail and error was used. Figure 4.3 shows the unprocessed schlieren images that resulted from the attempted settings. Figure 4.3a shows the schlieren image with an exposure time of $15\mu s$, equal to the exposure time used in the expansion section test slot. A good contrast was obtained, but the turbulent flow in the constant area duct is not captured adequately due to the high flow displacement during the exposure time. An exposure time of $8\mu s$ was found to improve the quality of the visualization of the turbulent flow, at an acceptable loss in contrast, as shown in Figure 4.3b. The orientation of the schlieren knife had been horizontal in the previous two images, and was changed to vertical, which resulted in the image in Figure 4.3c. This was not seen as in improvement, as the pseudo-shock visualization became less pronounced and the boundary layers were indistinguishable because their density gradient was not captured. Per measurement between 100 and 200 images were taken, at a capture rate of $5Hz$.

(a) $15\mu s$ exposure time per frame with horizontal schlieren knife orientation

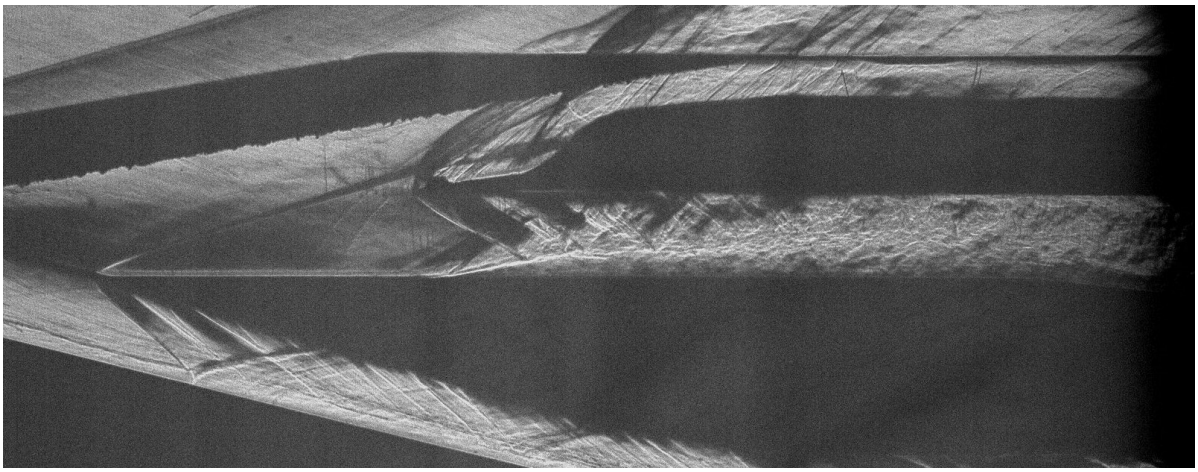

(b) $8\mu s$ exposure time per frame with horizontal schlieren knife orientation

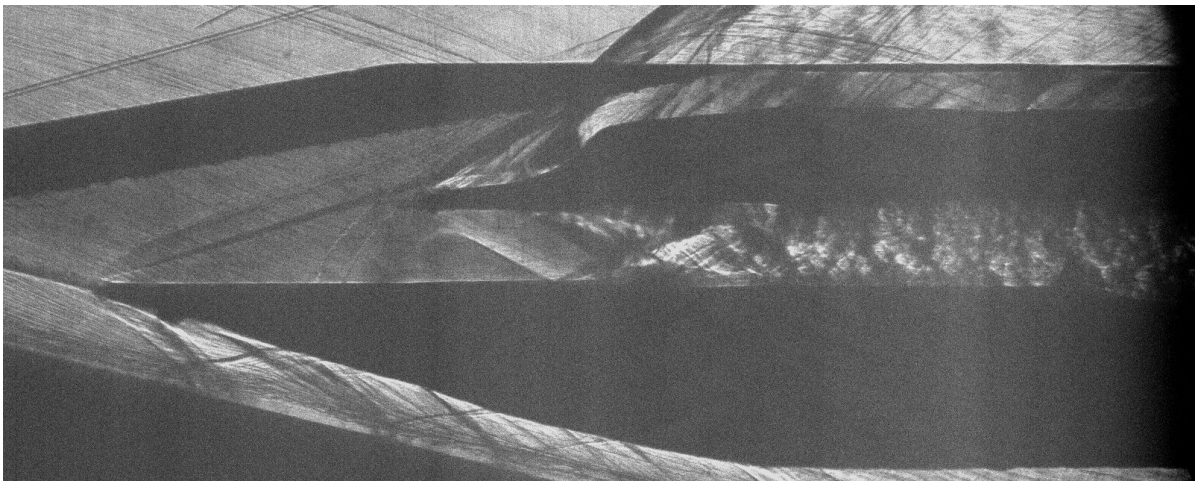

(c) $8\mu s$ exposure time per frame with horizontal schlieren knife orientation

Figure 4.3: Three unprocessed schlieren images at different exposure times with varying schlieren knife orientations

5

Data processing

To compare the experimental performance of the SSI models, the raw data that was obtained from the measurement systems needs to be processed such that it will be readily comparable to SRIM outputs. In addition to the usual organizing and processing of raw data, the absence of data on flow velocity in the SSI wind tunnel model needs to be circumvented. This is done by extracting the Mach number from schlieren images. This chapter describes the processing operations performed on the raw data to obtain the necessary results.

The wind tunnel conditions need to be translated to SRIM input to enable SRIM calculations with equivalent boundary conditions as the experiments. The SRIM inputs are pressure and temperature in the settling chamber, free-stream Mach number and pseudo-shock start location. The pressure and temperature in the settling chamber represent total conditions. Since the settling chamber characteristics are measured continuously throughout the wind tunnel run, a large array of data is available. The SRIM inputs for total pressure and temperature are computed by averaging the values when they are steady. Free-stream Mach number is computed using the total pressure and the static pressure upstream of the test section. Lastly the SRIM needs the start location of the pseudo-shock, which is determined from the schlieren images.

To facilitate data processing, the raw data was saved in `.mat`-files which provide easy MatLab access. This was especially time-saving for the cumbersome schlieren processing method (see Section 5.1). The flow chart of the script that loaded raw data and saved it to the `.mat`-files is shown in Figure 5.1.

5.1. Schlieren imagery

The schlieren visualization is the key to the qualitative flow analysis. In addition, as will be seen later, they need to be used to acquire quantitative data about the flow velocity, since the PIV measurements were canceled. This section will explain the processing of the schlieren images to obtain the required data for further computations. The most important information to be derived from these images are the shock angles caused by the compression surface, Mach angles in the internal channel for the supercritical condition and pseudo-shock locations for the critical condition. Also, the shock system calculated by the SRIM can be overlayed on the schlieren images. This gives a good qualitative comparison of the computational and experimental flow. To do so, a mapping of the image pixels to the Cartesian coordinates used by the SRIM needs to be known.

Per run, anywhere between 100 and 200 schlieren images were made. Since the method of acquiring relevant data from each image is rather cumbersome, an average schlieren image per run is taken. From this average image a no-flow image - taken when the wind tunnel is turned off - is subtracted to increase the visibility of relevant flow phenomena by subtracting static features such as scratches in the model and streaks due to residual PIV oil, giving a clear image for all operating conditions. Shown in Figure 5.2, a schlieren image for the supercritical condition is shown. Because the supercritical condition has a stable shock system in the intake, the average image does not deviate much from the individual images.

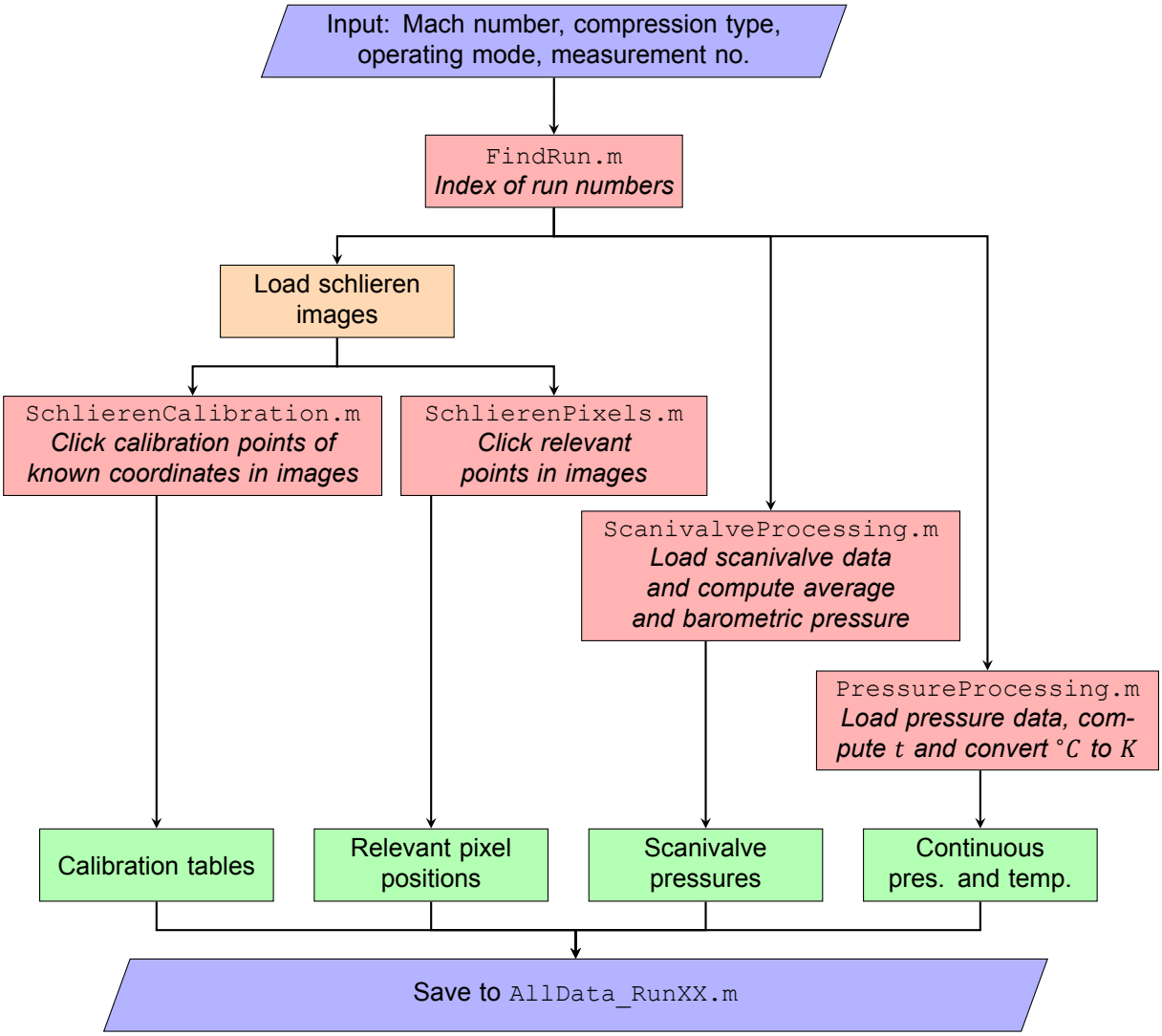

Figure 5.1: Flowchart of MatLab script `SaveRawData.m`

To understand the images that will be shown in this report, a general discussion on the schlieren images will be presented. An effort will be made to name the SSI model parts, shocks and other phenomena in the schlieren images. Figure 5.2 shows a schlieren image of the double shock intake in the supercritical condition. The entire image is shown, so that all relevant phenomena can be discussed. Starting in a the top of the image, a dark band can be spotted. This is the edge of the upper Mach block which marks the top of the test section. In the upper right corner, the Mach block meets a curved edge, which is the edge of the wind tunnel window. On the opposing side of the image, at $y \approx 0.04m$, two dark streaks can be seen. These are two shocks emanating from the transition from the plug nozzle block to the expansion section, which was verified extrapolating from the schlieren images of the expansion section experiments, see Figure 5.3 A small step always occurs between two parts, which in the case of supersonic flow always causes a (weak) shock. The shocks can be seen to reflect from the upper wall of the test section, but the reflections do not influence the flow into the intake. The black trapezoid emanating towards the upper right corner from the left side of the picture at $y \approx 0$ is the tapered leading edge of the sidewall. It was painted black to remove any interference in the schlieren measurements the tapered transparent surface might have, as explained in Section 3.3.2. Emanating from the sidewall leading edge is a shock, which starts at the left edge of the picture at $y \approx 0.01$ and moves towards the upper right corner. The expansion section is the large dark triangular surface in the lower left corner, and above it is the bleed slot between the compression surface part and the expansion section. Some

shock waves and oil streaks can be seen in the bleed slot, but it is definitely not choked, which was an assumption made in the SRIM by Van Wijk [41]. The lipped compression surface is shown in this image, above the bleed slot. The shock emanating from its leading edge is clearly visible, but the shock caused by the second deflection is less pronounced. Directly above the compression surface is the internal channel. Here, in the supercritical condition, the reflecting internal shock wave is seen to bounce through the channel. Other than the compression surface, the internal channel is bounded by the cowling. Its leading edge is around $x \approx 0.17$, where it causes a shock wave that emanates towards the upper right corner of the image. The shock wave is quite irregular due to the pressure tubes on top of the cowling, whose contour marks the top of the cowling in the image of Figure 5.2.

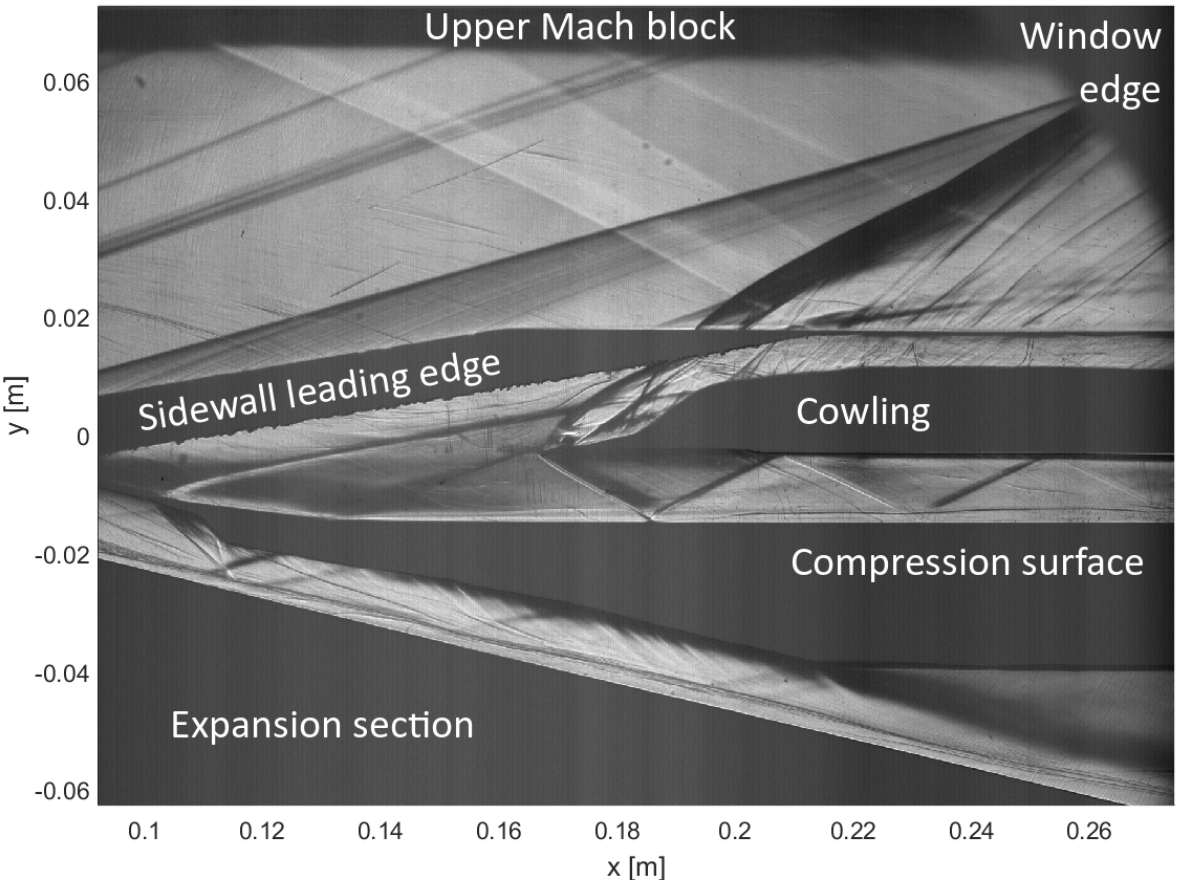

Figure 5.2: Processing image of the supercritical condition of double shock intake at a Mach number of 2.5

5.1.1. Schlieren calibration procedure

To create a mapping of the Cartesian coordinates on the schlieren images, a calibration needs to be performed. Having an accurate mapping of the Cartesian coordinates to the pixels in the schlieren images enables overlaying SRIM results to schlieren images, which will help in validating the SRIM later on. To construct a mapping, at least three points are needed which are easily and accurately discernible in the schlieren image and have known Carthesian coordinates; the calibration points. In the single shock case the compression surface leading edge, start of the subsonic diffuser and the cowl leading edge are the calibration points. In the double shock intake, the second shock deflection point, the compression parts lower corner and the cowl leading edge are the calibration points. These are indicated in Figure 5.4.

5.1.2. Shock angle determination

As mentioned at the start of this section, the most important data in the schlieren are the shock angles and pseudo-shock start position. The shock angles are determined by taking two points on a shock.

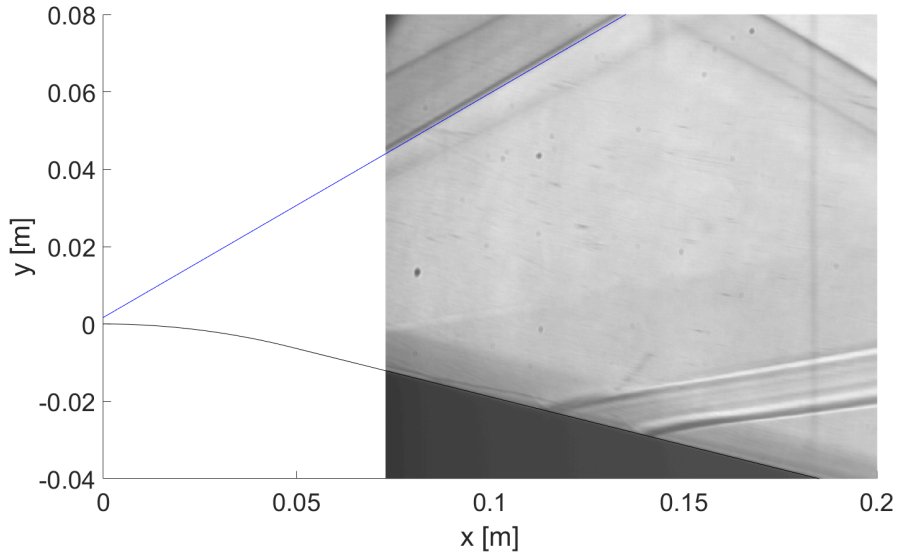

Figure 5.3: Verification of the origin of the shock waves in the upper left corner of the schlieren images.

Using simple geometry, the angle of the wave in the image can then be determined from the pixel coordinates. To obtain a shock angle that can be related to Mach number, the flow angle is also needed. This is determined using the same method as the wave angle, by taking two points on the surface upstream of the wave. By computing the difference between these two angles in the image, the shock angle is found. Using this method all relevant shocks in the schlieren image are determined, which are the external compression shocks for all flow conditions, and the shock waves in the internal channel for the supercritical condition.

5.1.3. Pseudo-shock start point

For the pseudo-shock encountered in the critical condition, the start point needs to be determined so that the SRIM can take this into account. The pseudo-shock start point is of great influence on the total pressure ratio of the intake, because the boundary layer thickness and Mach number change over the length of the constant area duct.

Unlike the supercritical condition, the critical condition of the intake - where the shock in the internal channel is on the verge of being expelled - can be unstable, with the pseudo-shock start point oscillating in the internal channel. The phenomenon of shock oscillations was described in Section 2.1.4. An example of the pseudo-shock oscillating in the internal channel is given in Figure 5.5. In the series of schlieren images, the pseudo-shock can be seen to move slightly forward, then be completely expelled in the third picture of the series. After this, the pseudo-shock retreats to aft of its original position since the back pressure is lower due to the reduced mass flow in the instances before. At last, the pseudo-shock returns to its original position. In the case shown in Figure 5.5, no obstructions were inserted in the flow to trigger the oscillation. The instability was most likely triggered by the shape of the butterfly valve in the subsonic diffuser. Since the butterfly valve was a short-term solution to the original one malfunctioning, very little design effort was put into the replacement. The rectangular cross-section of the butterfly valve, shown in Figure 3.7, is likely to interfere with the turbulent flow in the subsonic diffuser, and may sometimes trigger a short blockage in the flow resulting in the shock oscillation shown in Figure 5.5.

To filter out the incidental pseudo-shock oscillation an average schlieren image was found to be a good method of determining the pseudo-shock start point. The average image shows the location where the pseudo-shock starts most of the time for unstable flow. In cases where the pseudo-shock was stable, it gives a very clear location of the start of the shock.

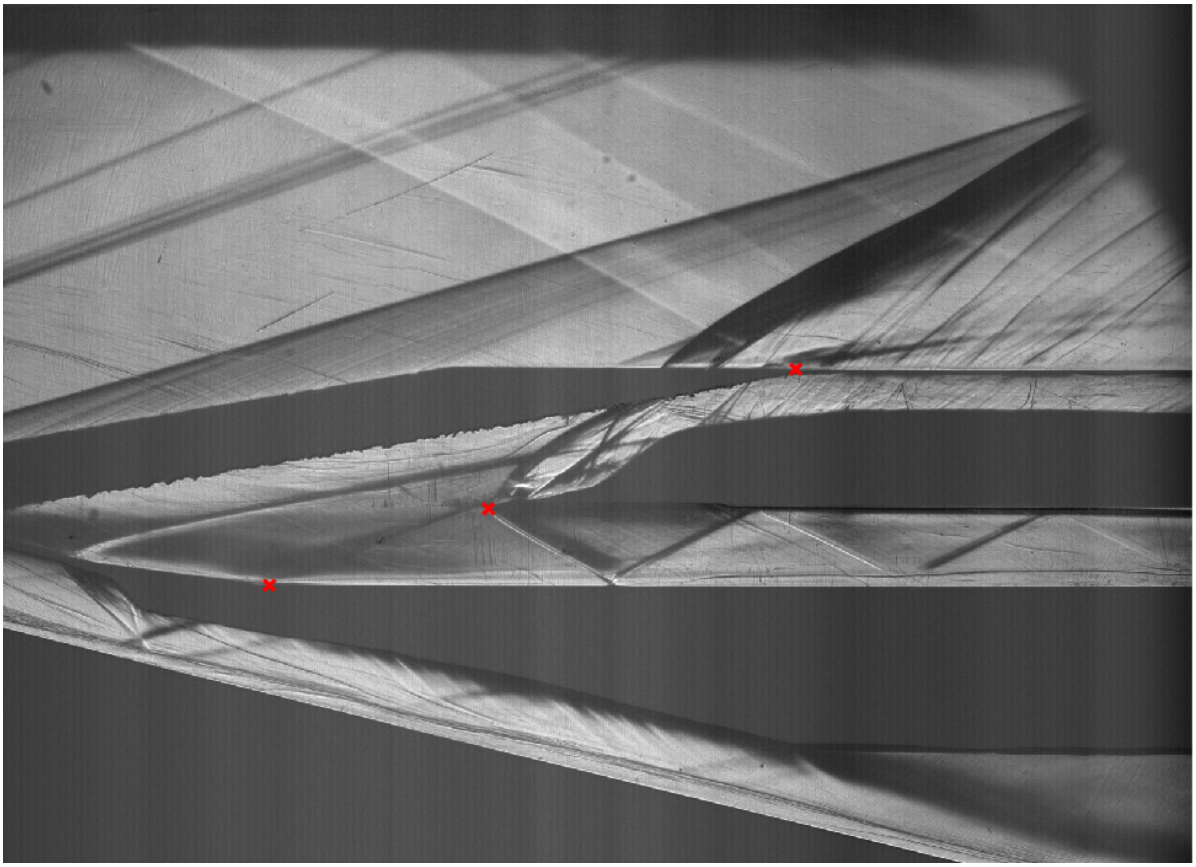

Figure 5.4: Schlieren processing calibration points of the double shock intake

5.2. Static pressure measurements

The static pressure readings of the Scanivalve are taken from the intake internal channel. This data is used in further calculations of the total pressure ratio (Section 5.3), but can be used on its own to compare the SRIM internal channel pressure as well.

The static pressure measurements as made by the Scanivalve are stored in text files and read by the script `SaveRawData.m`. The pressure values are separated into the upper and lower values and the locations are loaded as well. Then, in the following script `SVvalidation.m` (see Figure 5.7), the wind tunnel operating conditions are taken from the continuous data as input for the SRIM. The SRIM computation is performed using the same conditions as in the measurement and returns the predicted internal static pressure to be compared to the Scanivalve data. The average Scanivalve data is plotted as well as the individual measurements. For reference, the boundaries of the constant-area duct are shown as well. Figure 5.8 shows the output of the Scanivalve processing for the example case of the double shock intake a a Mach number of 2.

5.3. Total pressure computation method

As mentioned earlier, the total pressure recovery is one of the most important measures of supersonic intake efficiency. However, the SSI wind tunnel model lacks the capabilities of directly measuring the total pressure in its internal channel. This section describes an approach to compute the total pressure using the available pressure data and schlieren images.

The time-varying pressure measurement at the end of the subsonic diffuser gives a good indication of the total pressure in the internal channel, since the Mach number at its location will be relatively low. However, it will have a nonzero value, and to accurately determine the total pressure in the intake, it needs to be determined. Therefore a method was devised to compute the Mach number at the end of the internal channel from the internal channel mass flow.

The assumption made for this method is that for the critical and supercritical conditions, the flow

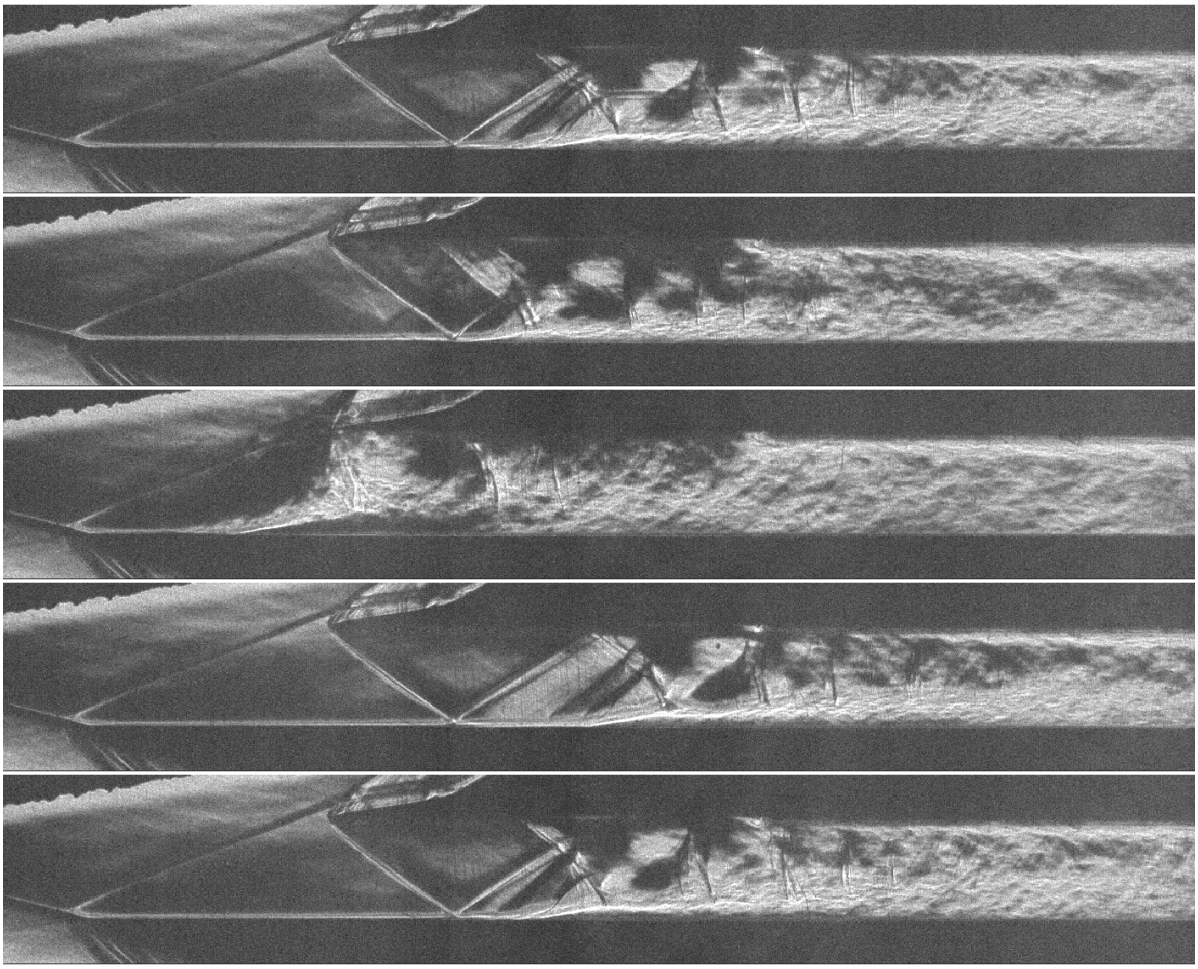

Figure 5.5: Series of schlieren images of oscillating pseudo-shock in single shock SSI at $M = 2$ in chronological order, the time between frames is $0.2s$

ahead of the internal channel is equivalent. As such, the flow into the channel - and therefore the mass flow - for supercritical and critical conditions is equal. This assumption breaks down when the intake condition becomes subcritical and the terminal shock is expelled, since the flow ahead of the internal channel is no longer equivalent to critical conditions.

This assumption is useful because the leading edge of the cowling, at the start of the internal channel, causes a weak shock wave that reflects through the internal channel. These reflecting shock waves are captured on the schlieren images and can be clearly seen in Figure 5.2, for example. Assuming the shock wave in the internal channel is very weak, the shock angles are approximately equal to the Mach angles and subsequently the Mach number in the constant area duct can be determined. For a known Mach number, an equation can be derived to compute the mass flow. The derivation starts with the definition for mass flow, which is:

$$\dot{m} = \rho A V \tag{5.1}$$

Using the equation of state and the well-known definition for speed of sound, this equation can be rewritten to be dependent of measured or calculable variables, such as temperature, static pressure and Mach number. The equation is as follows:

$$\dot{m} = \frac{p}{RT} A M \sqrt{\gamma R T} \tag{5.2}$$

This can be rewritten to:

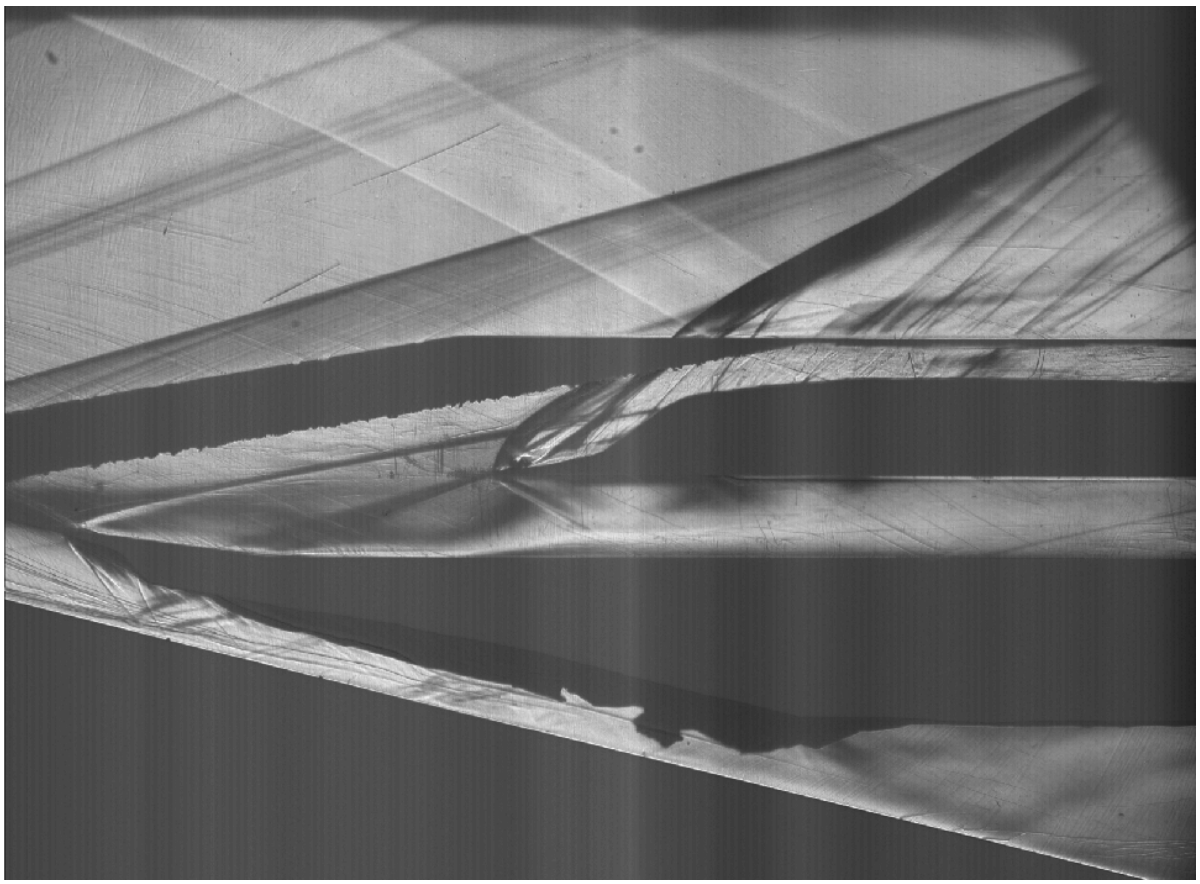

Figure 5.6: Processing image of the critical condition of double shock intake at a Mach number of 2.5

$$\dot{m} = \frac{pAM\sqrt{\gamma}}{\sqrt{RT}} \tag{5.3}$$

Where p is the local static pressure, A is the local cross-sectional area of the channel, M is the local Mach number, T is the local flow temperature, γ is the ratio of specific heats and R is the specific gas constant for air.

Since a shock wave is adiabatic and thus temperature remains constant, the local static temperature T can be computed from the total temperature T_t in the flow - which is measured in the wind tunnel settling chamber - and the Mach number. Note that by using this equation, the assumption is made that the walls of the wind tunnel model are adiabatic, which in reality they are not.

$$\frac{T_t}{T} = 1 + \frac{\gamma - 1}{2} M^2 \tag{5.4}$$

Combining equations 5.3 and 5.4, one obtains an equation for the mass flow in terms of Mach number, local static pressure, total temperature and channel cross-sectional area. All necessary variables can be obtained from the data for the supercritical intake condition: the Mach number was determined by measuring shock angles of the reflecting internal shock wave in supercritical operating condition, the local static pressure is taken from the Scanivalve data, the total temperature is the settling chamber temperature, and the channel cross-sectional area is known from the intake geometry. The resulting equation then becomes:

$$\dot{m}_{sc} = p_{sc} A_{cad} M_{sc} \sqrt{\gamma \left(\frac{1 + \frac{\gamma-1}{2} M_{sc}^2}{RT_t} \right)} \tag{5.5}$$

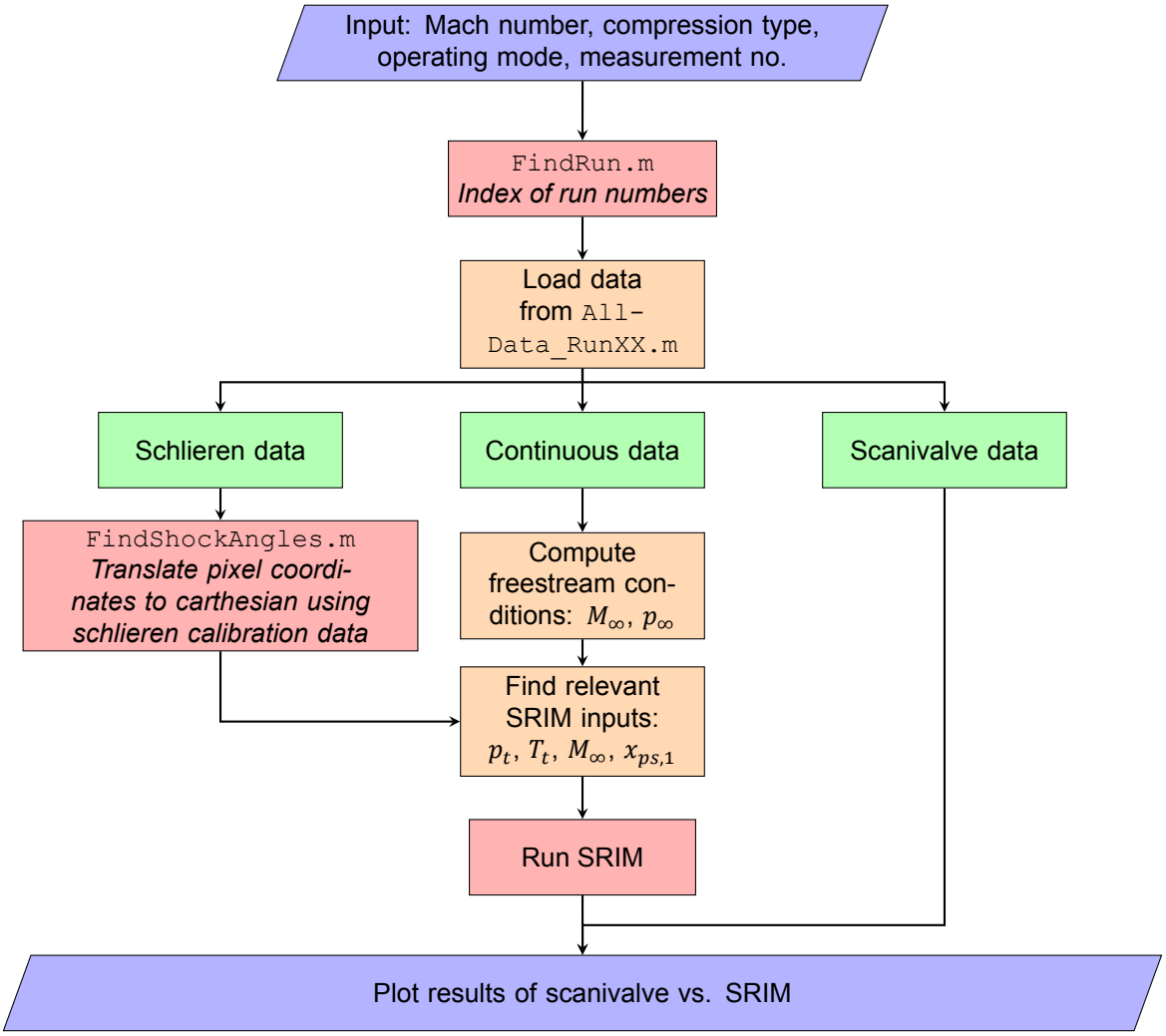

Figure 5.7: Flowchart of MatLab script `SVvalidation.m`

Remember the assumption that the reflecting shock in the internal channel is very weak, so that the shock angle can be assumed to be equal to Mach angle. Hence, the Mach number in the supercritical condition is based on the shock angle of the reflected shock wave inside the internal channel:

$$M_{sc} = \frac{1}{sin(\mu)} \tag{5.6}$$

Equation 5.5 gives the mass flow through the internal channel in the supercritical condition and, by assumption, also the mass flow for the critical intake condition. This provides useful information about the flow in critical condition. Starting with equation 5.5 and rewriting it to have only Mach number in the left-hand side:

$$M_v = \frac{\dot{m}_{sc}\sqrt{RT_v}}{p_v A_v \sqrt{\gamma}} \tag{5.7}$$

Equation 5.4 for total temperature is a function of Mach number, therefore it should be included into equation 5.7 and rewritten.

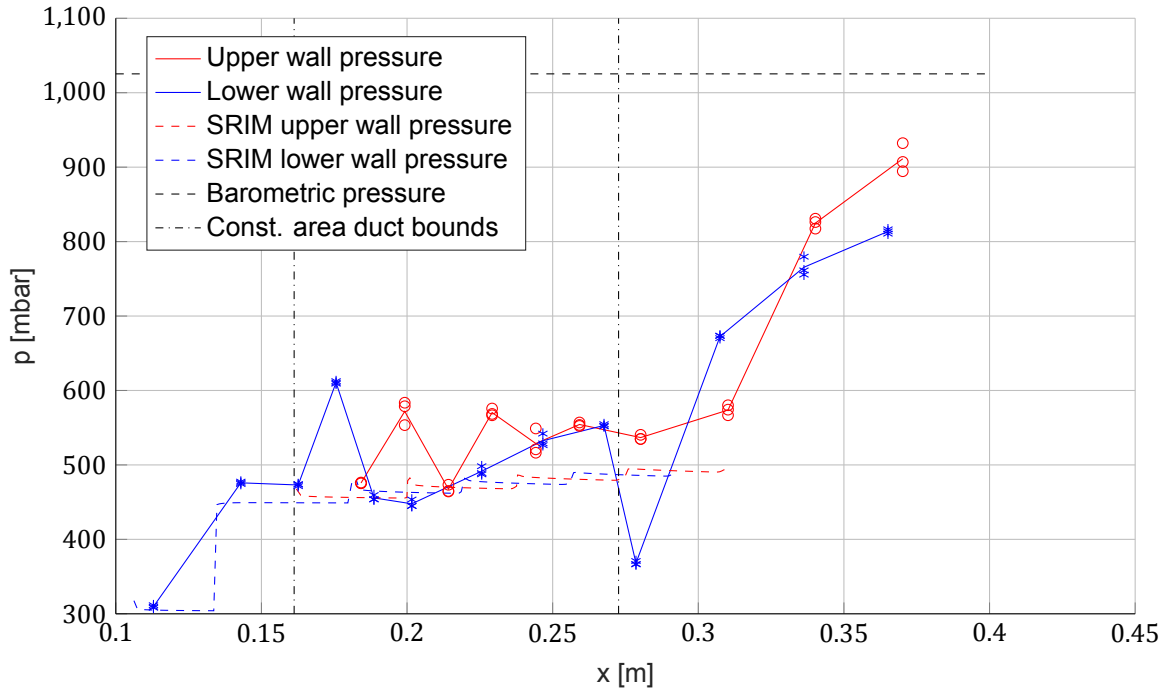

Figure 5.8: Example of results from `SVvalidation.m` for the double shock intake at Mach 2

$$M_v = \frac{\dot{m}_{sc}\sqrt{RT_t}}{p_v A_v \sqrt{\gamma\left(1+\frac{\gamma-1}{2}M_v^2\right)}} \tag{5.8}$$

By rewriting equation 5.8 and squaring both its sides, a quadratic equation with the square of the Mach number as variable can be obtained:

$$p_v A_v M_v \sqrt{\gamma\left(1+\frac{\gamma-1}{2}M_v^2\right)} = \dot{m}_{sc}\sqrt{RT_t}$$

$$p_v^2 A_v^2 \gamma\left(M_v^2+\frac{\gamma-1}{2}M_v^4\right) = \dot{m}_{sc}^2 RT_t$$

$$p_v^2 A_v^2 \frac{\gamma(\gamma-1)}{2}M_v^4 + p_v^2 A_v^2 \gamma M_v^2 - \dot{m}_{sc}^2 RT_t = 0 \tag{5.9}$$

Using the quadratic formula, equation 5.9 can be solved for the square of the Mach number. Taking the square root of this term will yield Mach number at the valve:

$$M_v = \sqrt{\frac{-p_v^2 A_v^2 \gamma \pm \sqrt{\left(p_v^2 A_v^2 \gamma\right)^2 - 4\left(p_v^2 A_v^2 \frac{\gamma(\gamma-1)}{2}\right)\left(-\dot{m}_{sc}^2 RT_t\right)}}{2\left(p_v^2 A_v^2 \frac{\gamma(\gamma-1)}{2}\right)}} \tag{5.10}$$

Using equation 5.10 it is possible to calculate the Mach number at any given point in the internal channel where static pressure and the cross-sectional area is known.

Remember that the static pressure at the valve was measured using the wind tunnel condition measurement system. This measurement is used to determine the Mach number at the valve. Using this Mach number, the static pressure reading and the intake geometry, the total pressure in the channel can be computed using the isentropic relation:

$$\frac{p_{t,v}}{p_v} = \left(1+\frac{\gamma-1}{2}M_v^2\right)^{\frac{\gamma}{\gamma-1}} \tag{5.11}$$

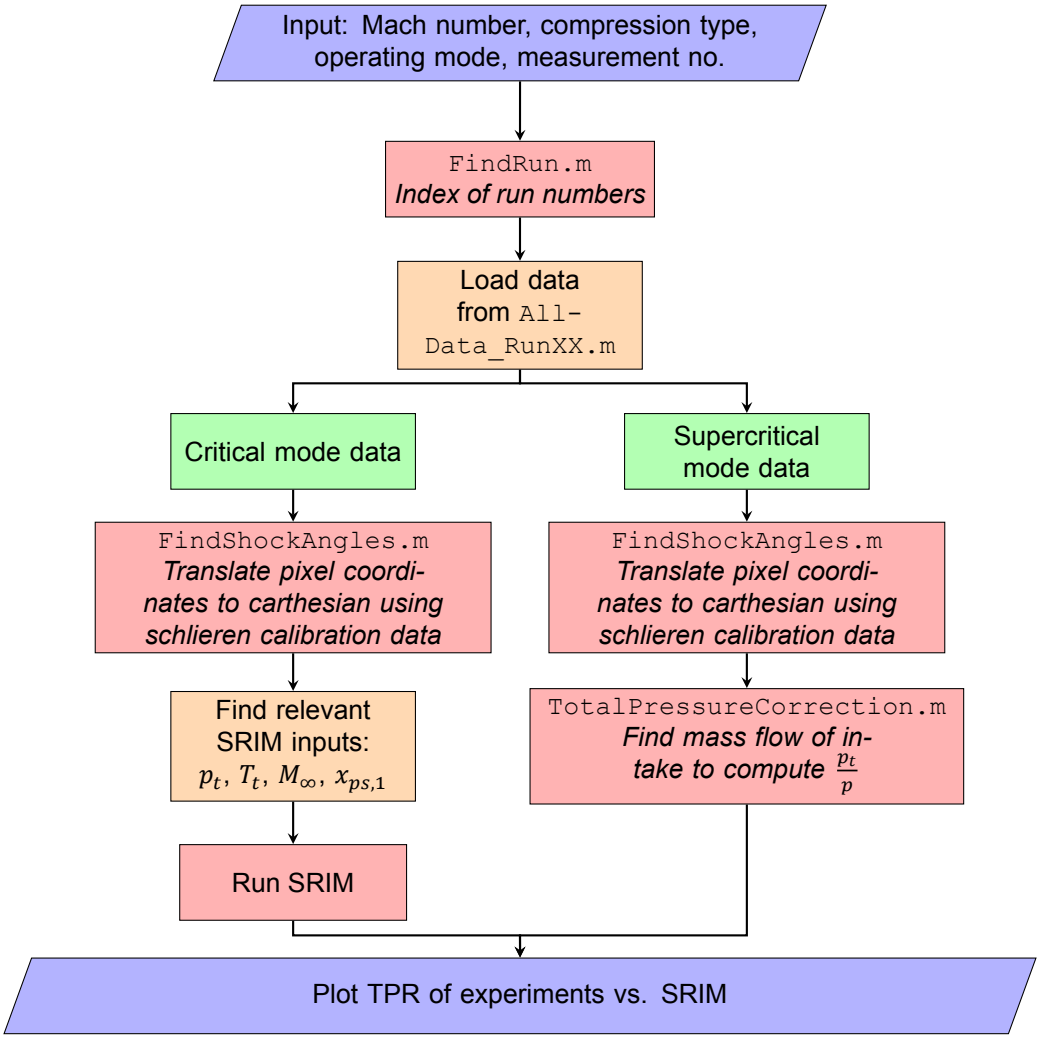

Figure 5.9: Flowchart of MatLab script `TPRvalidation.m`

Now that the total pressure in the intake is known, it can be related to the total pressure in the flow, which is the settling chamber pressure. This gives the total pressure ratio over the intake.

5.4. Example case for total pressure computation method

To illustrate this method further, a single case will be taken to show the procedures and computational steps taken in post-processing the data. For this purpose the case of a double shock intake at a free-stream Mach number of 2 is used. One of the three measurements is taken for further analysis. In computing the final total pressure ratio for this case, the results of all three measurements are averaged.

As outlined in Section 5.3, to find the total pressure in the channel in the critical condition, the mass flow of the supercritical condition must be found, since this is equal to the critical mass flow by assumption. Equation 5.5 can be consulted to find the data necessary to compute the supercritical mass flow $\dot{m}_{sc}$. These are, for the supercritical condition:

- **Static pressure in the internal channel**

  The static pressure in the internal channel was measured by the Scanivalve system (see Section 3.4.1) and processed and saved along with the valve locations known from the wind tunnel model design (see Section 5.2). Per measurement, the saved data of the pressure valves located in the internal channel is extracted and outliers are removed, see Section 5.5.2 for further information. The pre-processed data is averaged for further computation, giving $\overline{p}_{sc} = 501.73Pa$.

- **Mach number in the internal channel**

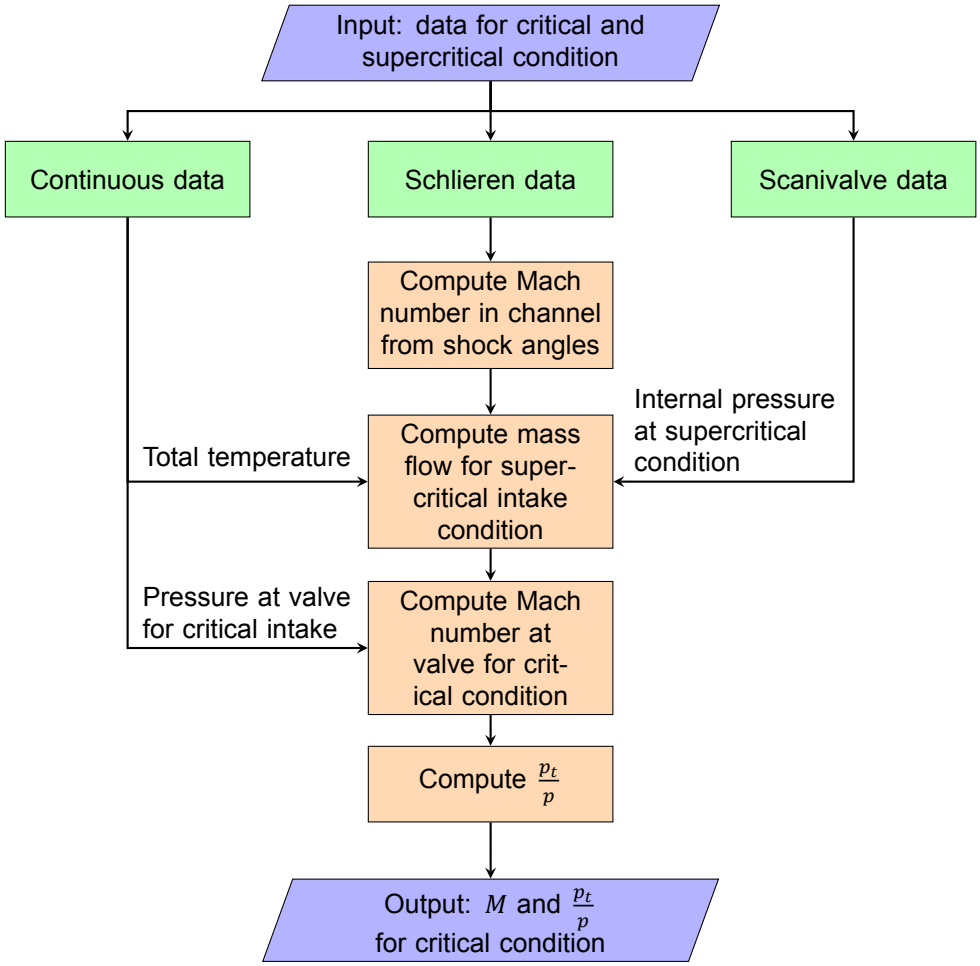

Figure 5.10: Flowchart of MatLab script `TotalPressureCorrection.m`

The Mach number in the internal channel is taken from the schlieren images, as explained in Section 5.1. The schlieren processing scheme gives shock angles of the internal reflecting waves from which the Mach number can be determined using the following relation:

$$M_{sc} = \frac{1}{sin\,(\mu_{sc})} \tag{5.12}$$

Since several internal shock waves, and therefore several internal Mach numbers exist, the average is taken, being $\overline{\mu}_{sc} = 35.3°$. Thus, like the internal pressure, the Mach number for the supercritical internal channel is $\overline{M}_{sc} = 1.73$.

- **Total temperature in the system**

  The total temperature in the system can be taken from the settling chamber temperature in the continuous data. Note that this data contains the part where the wind tunnel is still starting, thus datapoints of settled flow need to be extracted before also averaging the total pressure, yielding $\overline{T}_t = 279.53K$.

- **Internal channel cross-sectional area**

  The cross-sectional area of the internal channel can simply be taken from the wind tunnel model design. With the width and height being $67mm$ and $12mm$ respectively, this results in $A = 8.04cm^2$.

Inserting these values into equation 5.5 yields:

$$\dot{m}_{sc} = \overline{p}_{sc} A \overline{M}_{sc} \sqrt{\gamma \left(\frac{1 + \frac{\gamma-1}{2} \overline{M}_{sc}^2}{R \overline{T}_t} \right)} = 0.3685 kgs^{-1} \tag{5.13}$$

Now that the mass flow through the internal channel is known, equation 5.10 can be used to compute the Mach number at the valve. For this, the conditions at the valve must be collected. These are:

- **Static pressure at the valve.**

  The static pressure at the valve was, along with the Scanivalve, also measured by the continuous measuring system. The value of the static pressure stabilized when the wind tunnel has started at a value of $p_v = 1992 mbar$.

- **Total pressure in the system for the critical condition**

  The temperature in the settling chamber was measured by the continuous system. Due to the expansion involved with a blow-down wind tunnel like the ST-15, the total temperature changes somewhat after supersonic flow has settled. It is averaged at a value of $T_t = 276.3$.

- **Channel cross-sectional area at the valve**

  Obtained from the wind tunnel model geometry, this turns out to be $A_v = 15 cm^2$. The valve does not interfere since at the minimum deflection it is located approximately $13 mm$ downstream of the pressure orifice.

Along with the mass flow computed in equation 5.13 and the data listed above, equation 5.10 becomes:

$$M_v = \sqrt{\frac{-p_v^2 A_v^2 \gamma \pm \sqrt{\left(p_v^2 A_v^2 \gamma\right)^2 - 4\left(p_v^2 A_v^2 \frac{\gamma(\gamma-1)}{2}\right)\left(-\dot{m}_{sc}^2 R T_t\right)}}{2\left(p_v^2 A_v^2 \frac{\gamma(\gamma-1)}{2}\right)}} = 0.29 \tag{5.14}$$

With the Mach number at the valve known, equation 5.11 can be used to compute the total pressure at the valve, which is $p_{t,v} = 2111 mbar$. The total pressure ratio is then easily calculated using the settling chamber pressure, and for this case is 0.68. The results of the entire run of this particular case of the double shock intake at a Mach number of 2 can be found in Figure 5.11. To see how the experimental results compare with the results from the SRIM, its total pressure performance is also included in the graphs for total pressure and total pressure ratio. Note that the total pressure ratio computation method is most likely not accurate when the flow has not fully started yet, thus the data of Figure 5.11 starts when the tunnel flow in the wind tunnel has fully settled.

5.5. Shortcomings of post-processing

Other than the assumptions it is based on, the method to compute the total pressure in the submerged supersonic intake model has some more shortcomings that require discussion. The Scanivalve data shows outliers in some measurements, which will be explained. The results of a study into the propagation of error through the total pressure computation method will be presented also. First, however, a small validation exercise will be performed to investigate whether the total pressure method is valid throughout the entire internal channel.

5.5.1. Validation of total pressure correction method using static pressure data

In the derivation of the total pressure correction method, it was stated that it can be used to compute the Mach number at any given point in the internal channel where static pressure and cross-sectional area are known. A statement that can be put to the test by applying the total pressure correction method to the static pressure values of the SSI in critical condition. With the mass flow being known, the Mach number and total pressure for each pressure hole can be derived from the local cross-sectional area and static pressure measurements. Plotting the distribution of the total pressure as computed by

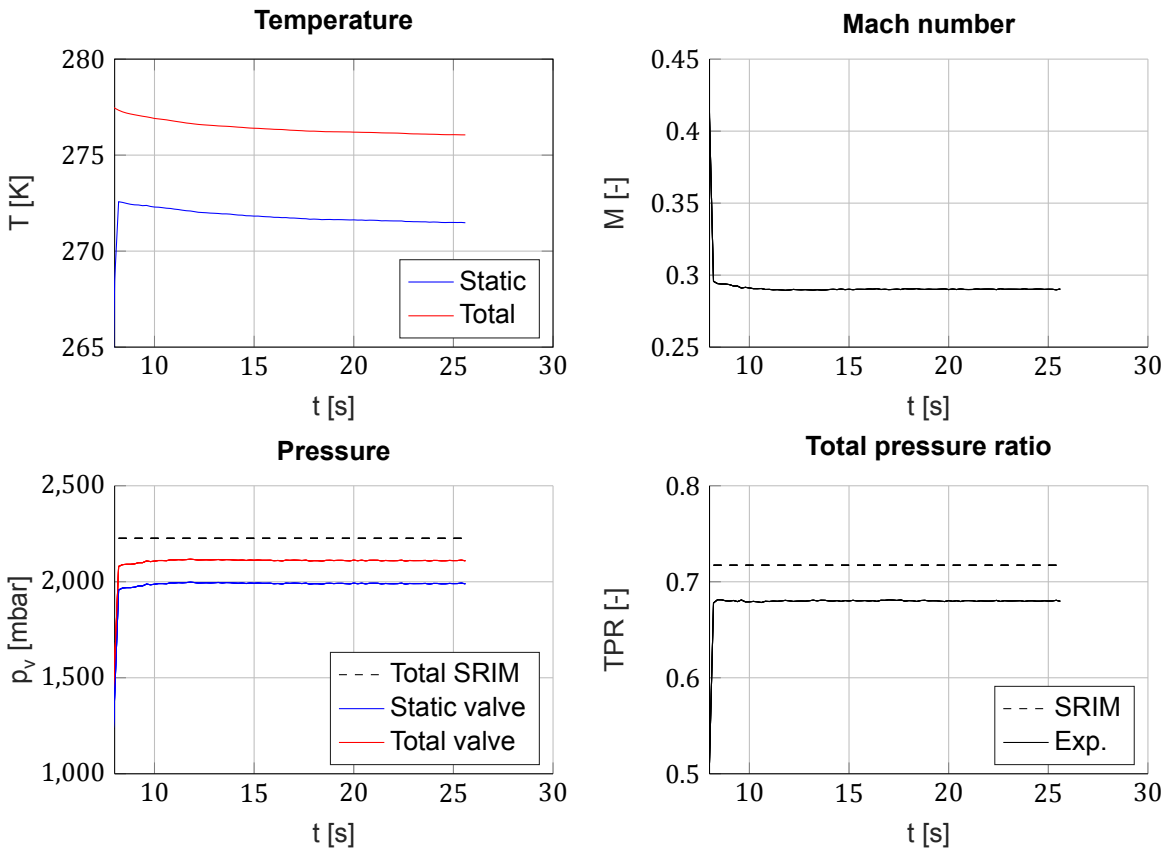

Figure 5.11: Results of the total pressure ratio computation method for the double shock intake at Mach 2.

the total pressure correction method throughout the internal channel will provide information about its validity.

Figure 5.12 shows the result of the total pressure correction method being applied to the static pressure data of the double shock SSI model at $M = 2$. Two interesting phenomena occur: the first being the total pressure remaining relatively constant throughout the subsonic diffuser. However, friction losses in the subsonic diffuser dictate that the total pressure should reduce. The second being the total pressure in the constant area duct decreasing and increasing again, which goes against the second law of thermodynamics and is most likely caused by the unsteady pseudo-shock flow in the constant area duct.

It can be concluded that the total pressure correction method for is not indisputable when calculating the flow in the internal channel. Most likely, this is caused by the unsteady flow in the constant area duct and subsonic diffuser, resulting from the pseudo-shock flow. However, at this point, it is the only method of obtaining information about the Mach number and subsequently the total pressure in the internal channel.

5.5.2. Outliers in static pressure data

As mentioned at the start of this chapter, some of the static pressure results have outliers in the data. Figure 5.13 shows the measurement with the most pronounced outliers: the double shock intake in supercritical condition at a Mach number of 2.5. Figure 5.13 shows the values of three measurements, so the outliers are relatively consistent, indicating that the problem is not a random error.

A possible solution can be found itself when the pressure valve locations are plotted on the schlieren images of the measurement, shown in Figure 5.14. For the second upper surface pressure valve reading, it can be seen that the reflecting internal shock wave impinges very close to the pressure orifice, thereby increasing the pressure reading. The same applies for the fifth pressure orifice. This can be an indication that the reflecting internal shock causes the extreme values in the static pressure measurements.

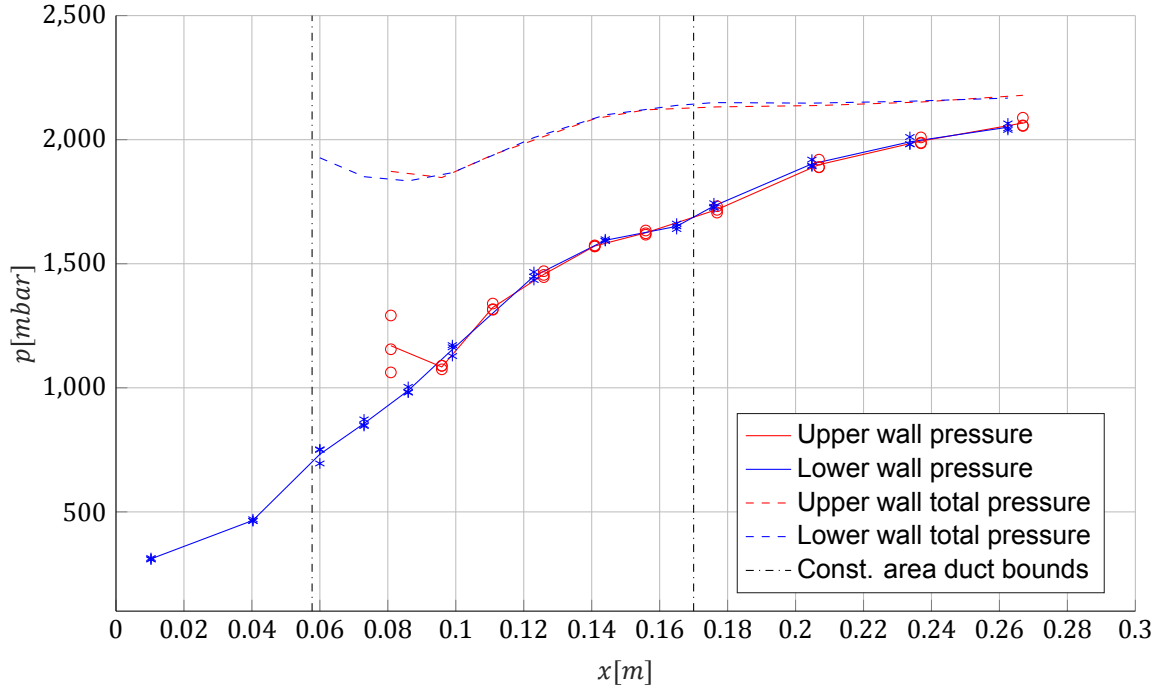

Figure 5.12: Total pressure in the internal channel for the double shock SSI at $M = 2$, computed by applying the total pressure correction method to the static pressure data

An explanation for this is provided by Liepmann et al. [25], who investigated the surface pressure of a boundary layer with different shock variations reflecting on it. For a ”weak impulse-type wave” - a quick succession of a shock and expansion wave caused by a flat surface - the surface pressure of the boundary layer is shown in Figure 5.15, along with a schematic of the impulse-type wave. This type of wave is very similar to the reflecting wave caused by the cowl leading edge in the submerged supersonic intake model. Looking at Figure 5.15, it is clear that for the turbulent boundary layer a large peak in surface pressure exists at the location where the impluse-type wave impinges on the surface. From this information it can be deduced that the shock wave impinging on the pressure valve as shown in Figure 5.14 causes the pressure peak in the static pressure data. This is sufficient cause to exclude these measurements from further analysis.

5.5.3. Error propagation study

To analyze the accuracy of the calculated total pressure ratio, an error propagation study is performed. Several sources of error exist in the total pressure ratio computation method, of which the measurement of the internal shock angles is the most error sensitive, as will be seen in this section. Furthermore, the computation of the magnitude of error will be described.

The main sources of error in the total pressure ratio calculations can be deduced from equation 5.5 seeing as that is where the computation starts. Note hereby that the Mach number in the supercritical condition M_{sc} is dependent of Mach angle μ in the internal channel. Also, the channel cross-sectional area is assumed to be without error. The error in pressure is assumed to be $3mbar$ because of sensor and calibration errors. The remaining variable, total temperature is taken from the measurement data. The error is determined by computing the standard deviation of data obtained during a dry run, i.e. no flow in the wind tunnel. As explained in Section 5.1, the Mach angles in the internal flow are obtained using a manual method, which is prone to error. Table 5.1 shows the absolute and relative magnitude of the error. It is clear that the error of the shock angle has the largest relative magnitude.

Assuming that error remains small and the sources are uncorrelated, the propagation of error can be calculated using linearisation. Let quantity y be dependent of k variables, such that $y = f(x_1, x_2, ..., x_k)$. To compute the error in y one should determine the dependency of y of each variable x_i by taking the derivative $\frac{\partial y}{\partial x_i}$. This dependency needs to be evaluated locally and multiplied by the error. Then, the

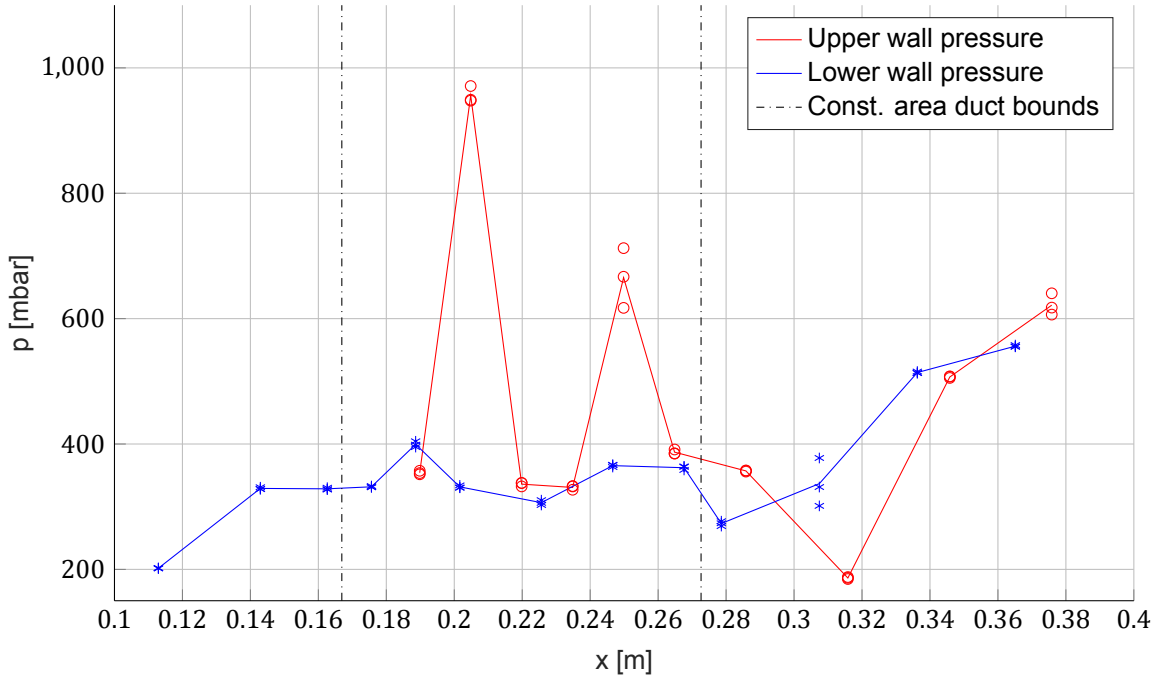

Figure 5.13: Scanivalve data of the double shock intake at a Mach number of 2.5. Extreme outliers are easily discernible for the upper wall pressure measurements.

Table 5.1: Absolute and relative (compared to typical parameter size) magnitude of error for each input variable in the total pressure calculation method.

ε	Value	Relative size [%]
μ	1°	3.33
p_{sc}	$3mbar$	0.6
p_v	$3mbar$	0.15
T_t	$0.1K$	3.57e−4

total error of y, ε_y, can be computed by taking the norm of the products of local dependencies and errors in each variable, such that

$$\varepsilon_y = \sqrt{\left(\frac{\partial y}{\partial x_1}\cdot\varepsilon_{x_1}\right)^2 + \left(\frac{\partial y}{\partial x_2}\cdot\varepsilon_{x_2}\right)^2 + \ldots + \left(\frac{\partial y}{\partial x_k}\cdot\varepsilon_{x_k}\right)^2} \tag{5.15}$$

Equation 5.15 needs to be applied to equations 5.6, 5.5, 5.10 and 5.11. Meaning that every equation the derivative in every variable needs to be found. This process is shown with an example in Appendix A. As can be seen from the equations in Appendix A, the error propagates through the computation. The values of error are for the example of the dual shock intake at Mach 2 are shown in Table 5.2.

Of the relative errors in Table 5.2 the relative error size of the total pressure stands out, since it decreases almost sevenfold compared to the error in Mach number. This can be explained by the fact that the error in Mach number goes through equation 5.11, where its $\frac{2\gamma}{\gamma-1}$-exponent is taken. Since the

Table 5.2: Absolute and relative (compared to typical parameter size) magnitude of error for each output variable in the total pressure calculation method.

ε	Value	Relative size [%]
M_{sc}	4.25e−2	2.45
$\dot{m}_{sc}$	$1.26\text{e}{-2}kgs^{-1}$	3.43
M_v	0.99e−2	3.29
p_t	$9.18mbar$	0.43

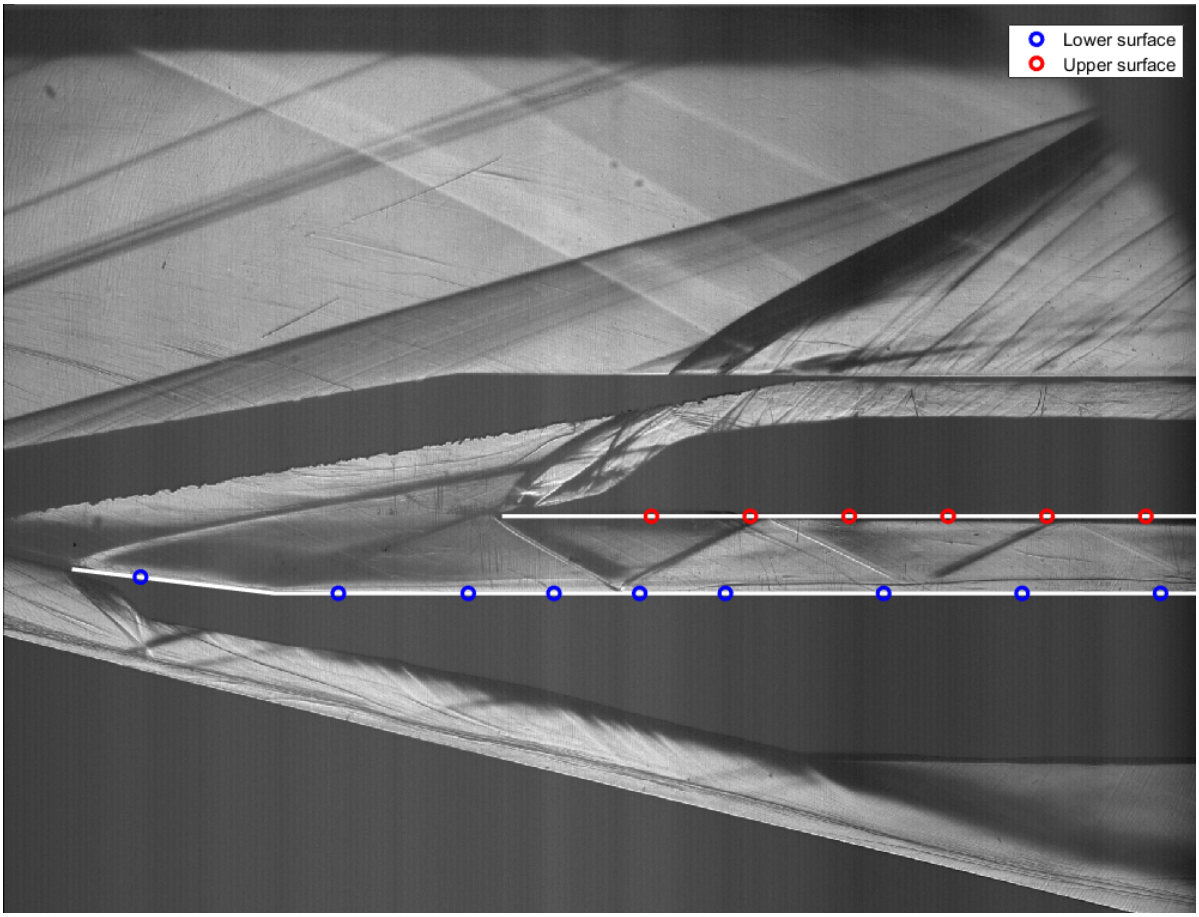

Figure 5.14: Schlieren image of double shock intake in supercritical condition with the location of the pressure holes indicated. Shock waves can be seen impinging on two of the pressure holes, corresponding to the outliers in the pressure measurements.

value of the error is smaller than one, taking its power will reduce it even further.

In the end, the error in total pressure is approximately 0.4% for 1° of error in Mach angle. A linear relation exists between the error in shock angle and the error in total pressure. This makes sense, since the method that was used in based on linearization of the equations and small error.

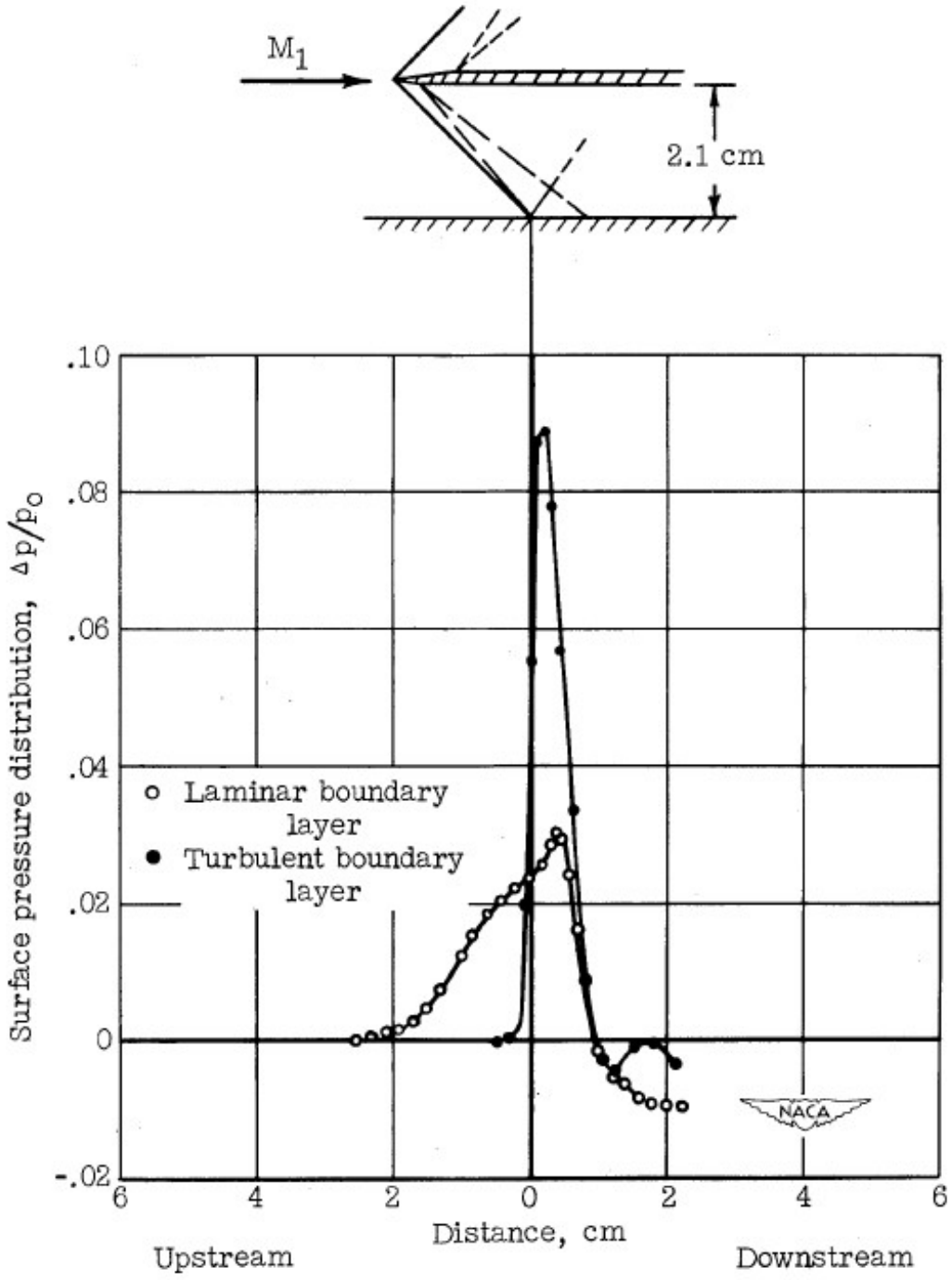

Figure 5.15: Influence of ”impulse-type wave” on the surface pressure, taken from Liepmann et al. [25]

6 Validation

The validation of the Submerged Ramjet Intake Model will start with the qualitative analysis of the flow field in the oblique shock system and the internal channel, in both the supercritical and critical condition. The schlieren images will be used to point out and analyze differences between the SRIM predicted flow field and the flow field in the submerged supersonic intake model. The qualitative analysis is particularly focused on the shocks in the intake: namely, the oblique compression shock system, the reflecting shock in the internal channel in supercritical condition and the pseudo-shock for the critical condition. Then, some quantitative analysis will be done by looking at the static and total pressures in the intake, and comparing them with the SRIM predictions. Also, some initial SRIM assumptions are reviewed using the available experimental data.

6.1. Oblique shock system

As was shown in Chapter 2, the oblique shock system is essential for the intake efficiency. It is important, therefore, that the SRIM predicts it correctly. This section will compare the SRIM prediction with the experimental results to determine the accuracy and to see whether improvements are necessary.

Table 6.1 shows the shock angles in the oblique shock system of the SSI. Note that the experimental shock angles are taken for the part where the shock is straight, since in some flow cases, a slight curve is visible close to the origin, which will be discussed later. Notable is the excellent agreement between the SRIM and the experimental values for the first shock angle. These are all within the assumed 1° error of the experimentally determined shock angle. The second shock is less accurate, since it is not always easily discernible in the schlieren images. This will also be discussed later in this section. The agreement of the SRIM with an inviscid analysis of the flow is to be expected since outside of the boundary layer predictions and the pseudo-shock, the SRIM assumes inviscid flow. The validity of this assumption will have to be tested using other flow parameters.

6.1.1. Curved leading edge shock

Figure 6.1 shows the averaged schlieren image of the first two shocks created by the double shock intake at a Mach number of 2, overlaid with SRIM results for the same case. Looking at the first shock, caused by the leading edge of the compression surface, the shock is slightly curved close to the

Table 6.1: Shock angles in the oblique shock system of the SSI model for an inviscid case along with experimental and SRIM results.

		First shock angle			Second shock angle		
M	Configuration	Inviscid [°]	SRIM [°]	Exp. [°]	Inviscid [°]	SRIM [°]	Exp. [°]
2	Single shock	36.1	36.1	36.4	N/A	N/A	N/A
	Double shock	29.2	29.4	29.1	32.9	33.1	37.6
2.5	Single shock	30.5	30.4	30.7	N/A	N/A	N/A
	Double shock	23.7	23.6	24.6	26.4	25.9	29.6

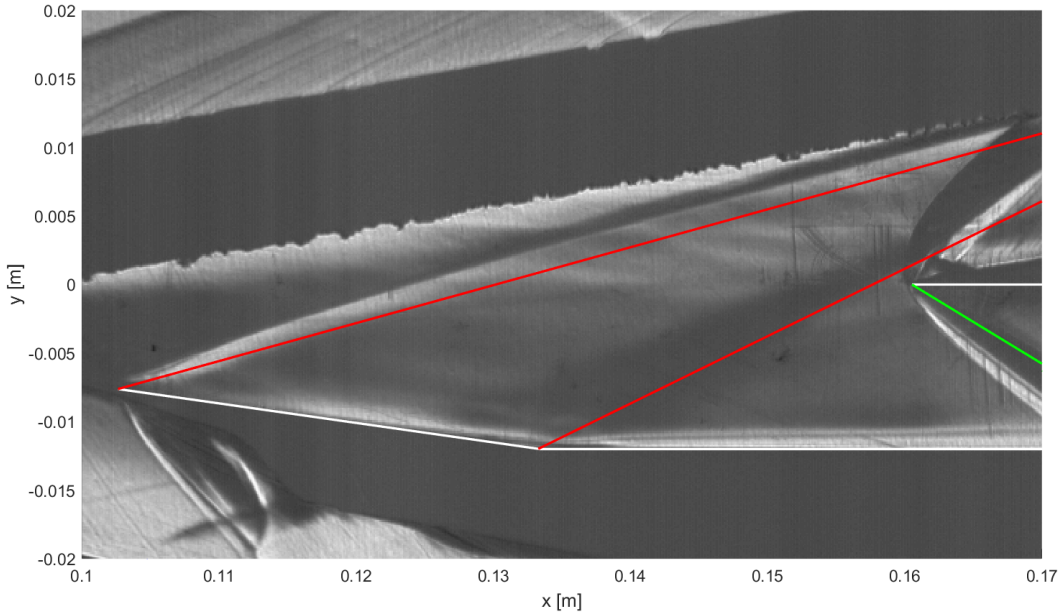

Figure 6.1: Detail of the averaged schlieren image of external compression shocks on the double shock intake at Mach number 2

leading edge. The curvature is caused by a Mach gradient in the flow, possibly caused by the boundary layer on the expansion section, which can be verified by looking at the schlieren photographs of the expansion section. Figure 6.2 shows schlieren measurements of the expansion section. In both images a Mach wave caused by a piece of tape attached to the surface is visible. From the curvature in these Mach waves close to the surface, it can be seen that a velocity gradient exists. This is most likely the boundary layer that has built up in the wind tunnel nozzle and increased in size through the expansion. To see whether this boundary layer influences the flow into the SSI wind tunnel model, its thickness is determined to be approximately $0.01m$ in the y-direction. The vertical direction is chosen because it is the easiest method of comparison.

Figure 6.3 shows the bleed slot of the SSI intake model with the most curvature in its leading edge shock, since the intake leading edge is right on the edge of the schlieren picture spatial resolution, the bleed slot height was chosen as a measure of comparison. It can be seen that the height of the bleed slot is slightly larger than the $0.01m$ of the boundary layer thickness determined from the expansion section test shown in Figure 6.2. Therefore it can be concluded that the SSI wind tunnel model leading edge is right on the edge of the expansion section boundary layer, and some influence may still exist. However, when looking at the flow in the bleed slot in Figure 6.3, it can be seen that the shocks in that channel are rather straight, and close to the surface they seem to dissipate into a boundary layer much thinner than derived from Figure 6.2. For all the other flow cases, a similar effect occurred, which was the reason for deciding not to increase the bleed slot height (by moving the SSI model downstream, as described in Chapter 3) for further testing. In addition, the SRIM prediction for the boundary layer thickness was also plotted in Figure 6.3, and is shown to be fully contained by the bleed slot. To confirm that the leading edge shock curvature is caused by the thick expansion section boundary layer, the bleed slot width should be increased in future experiments.

Another cause of the curved leading edge shock is the somewhat blunt leading edges on the SSI wind tunnel model parts. Due to limitation in the production process, the cowl and compression surface parts both do not have a very sharp leading edge, the diameter being approximately $0.1mm$. This may cause the oblique shock to detach and curve around the leading edge. A similar thing can be noticed on the cowl shock, which also has a slight curvature to it.

Finally, the curvature may also be caused by three-dimensional flow effects in to the intake. Since the SSI wind tunnel model has sidewalls that also develop boundary layers, some flow may spill into the intake and influence the flow. Since the experiments performed focused on two-dimensional flow, no possibilities exist to verify the presence of three-dimensional flow effects.

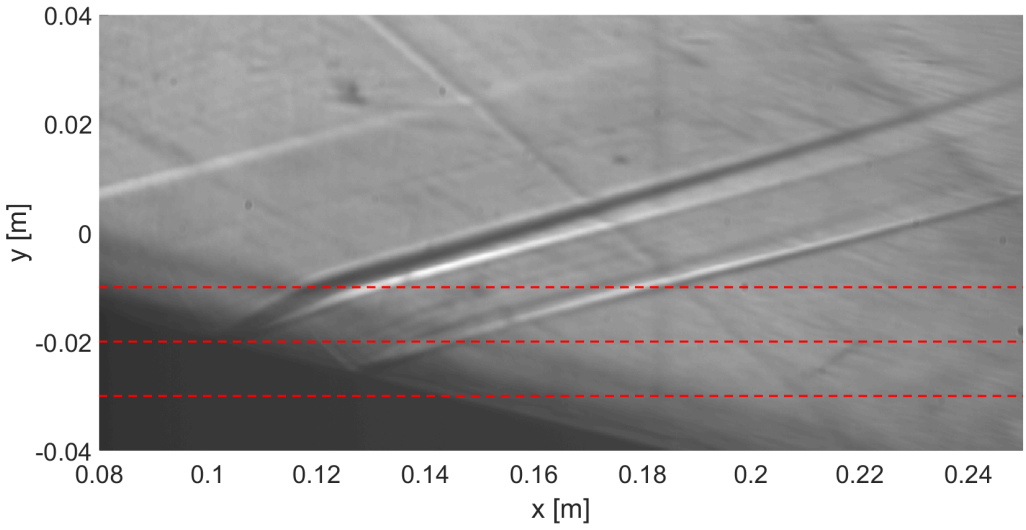

(a) $M = 2$

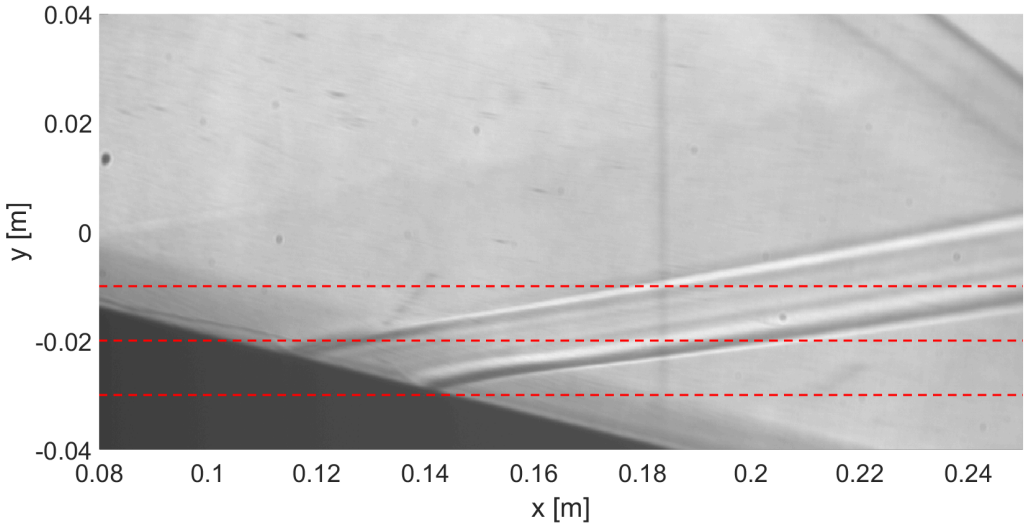

(b) $M = 2.5$

Figure 6.2: Schlieren images of the flow around the expansion section. The shock waves are caused by a piece of tape stuck to the surface. The red dashed lines are to aid in determining the vertical boundary layer thickness.

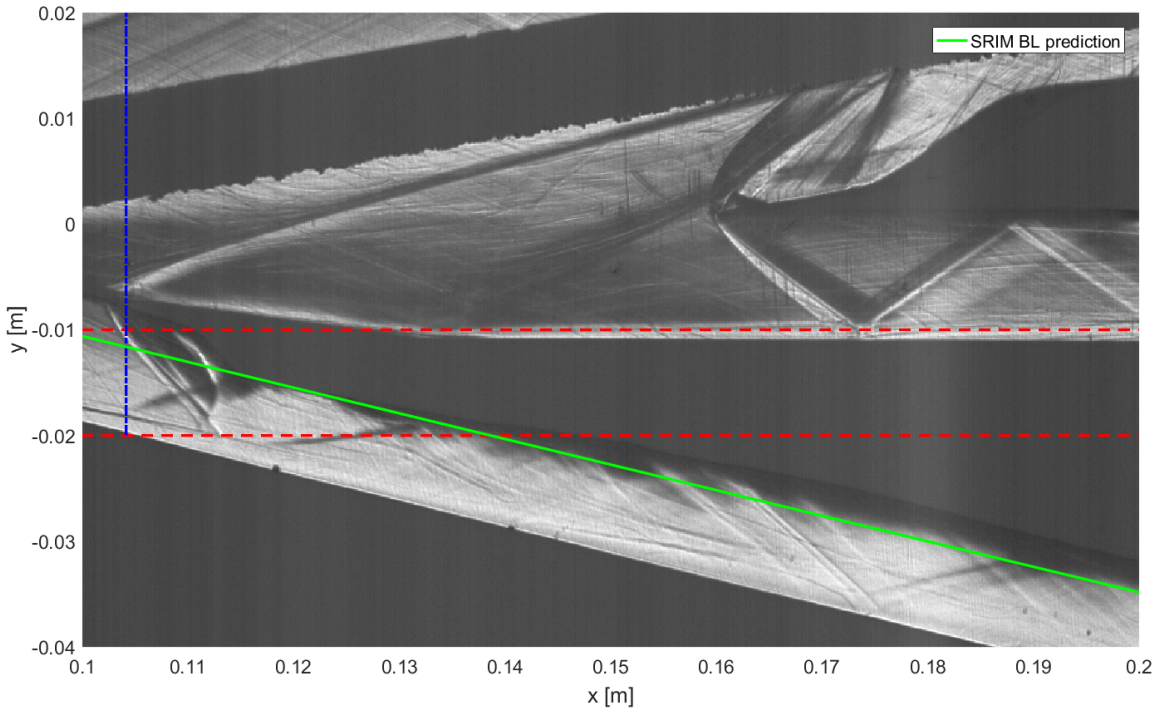

Figure 6.3: Detail of of a schlieren image of the double shock intake at $M = 2$, focusing on the bleed slot, with the SRIM boundary layer prediction in green. Red and blue lines are to aid in determining the bleed slot height

6.1.2. Second shock in double shock intake

Figure 6.1 also shows the second shock of the double shock intake. On the schlieren image, this shock is not very clearly defined, especially when compared to the first shock. This is explained by the fact that the deflection which is supposed to cause the second shock is not instantaneous due to limitations in the production process. Instead of an instantaneous deflection, a curve with a small radius of approximately $3mm$ is found on the double shock compression surface part, see Figure 6.3. The second deflection is weakened even further by the boundary layer that exists on the compression surface, in a fashion similar to described in Section 2.2.1. All in all the second shock is more similar to a compression fan that combines into a shock. The combined shock is not visible in the schlieren images, because the compression fan is interrupted by the shock that is formed off of the cowling. Having a compression fan instead of a shock may be beneficial to the intake performance, since less losses occur in a compression fan compared to a shock. However, it is a discrepancy between the SRIM and experimental values and therefore a possible source of inaccuracies. The SRIM should be adapted to compute the compression fan instead of a second shock on the double shock intake, or higher precision tooling should be used to produce a more accurate SSI wind tunnel model.

6.2. Angle of internal shock wave in supercritical condition

Figure 6.4 shows a detail of the averaged schlieren image of the intake in supercritical condition, over which the SRIM results of the reflecting shocks in the constant area duct are plotted. A clear difference exists between the Mach angle of the shock waves, which also exists in the corresponding Mach numbers, shown in Figure 6.5. Here, the Mach numbers for the double shock intake at free-stream Mach number of 2 in the supercritical condition are shown. The SRIM gives the Mach numbers at the upper and lower walls of the channel, which jump when they cross the reflecting shocks in the internal channel. The experimental results show steps because at each shock in the channel, the Mach number is computed using the Mach angle taken from the schlieren image. These Mach numbers vary somewhat because of the difficulty in determining the shock angle of the internal shock waves. The average measuring error in the internal shock angle was estimated to be $1°$, which, according to the

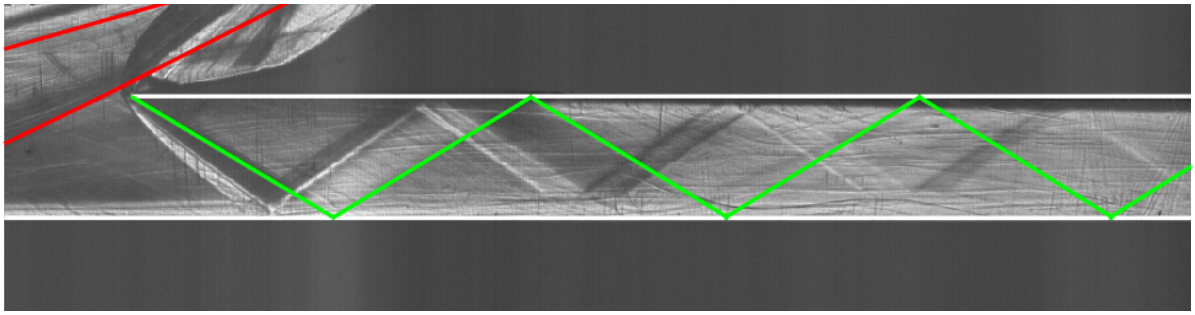

Figure 6.4: Detail of the averaged schlieren image of internal Mach waves in the double shock intake at Mach number 2 with SRIM results for internal shock waves

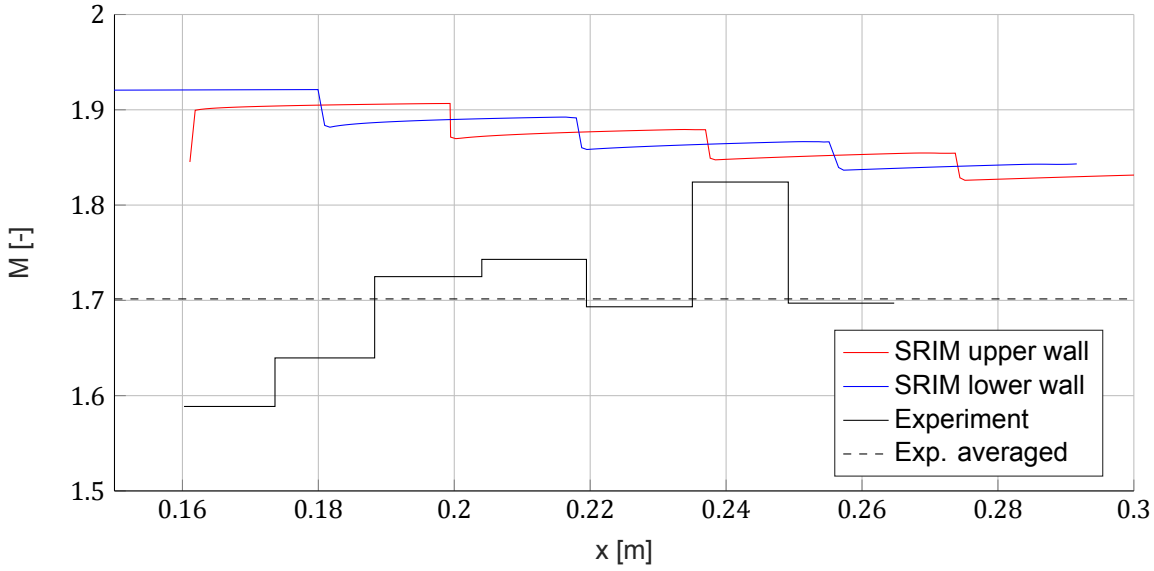

Figure 6.5: Internal Mach number results for the double shock intake at $M = 2$ at supercritical condition, taken from the SRIM and the experiments

error study in Section 5.5.3 results in an average Mach number error of 0.04.

The predicted error is too small to explain the Mach number discrepancy between the experimental and SRIM internal channel flow. An explanation may lie in the curved leading edge shock. Seeing as the curvature is an indication of lower Mach number, and the curve is located on the lower part of the leading edge shock, which is precisely in the streamtube that flows into the internal channel, it is possible that the phenomenon that causes the leading edge shock also causes the Mach number discrepancy. Another likely cause of difference in Mach number results lies in the SRIM computation of supercritical flow in the internal channel, which does little to include viscous effects. The absence of viscosity may lead to the overprediction of Mach number in the SRIM, see Section 6.4.

Figure 6.4 shows evidence of viscous effects being present in the internal channel. Around each internal shock wave a darker and lighter band develops in the schlieren image, which is due to sidewall interaction effects that make it difficult to indicate the actual shock wave. The sidewall shock wave-boundary layer interaction effects can be seen to increase when moving downstream in the internal channel, because the shock waves become increasingly less defined in the schlieren images. In an internal channel with growing boundary layer, this is to be expected. However, it can make accurately determining the Mach angle of the shock difficult. The inaccuracy resulting from the sidewall interaction effect is mitigated by averaging the Mach number over the entire internal channel for further computations.

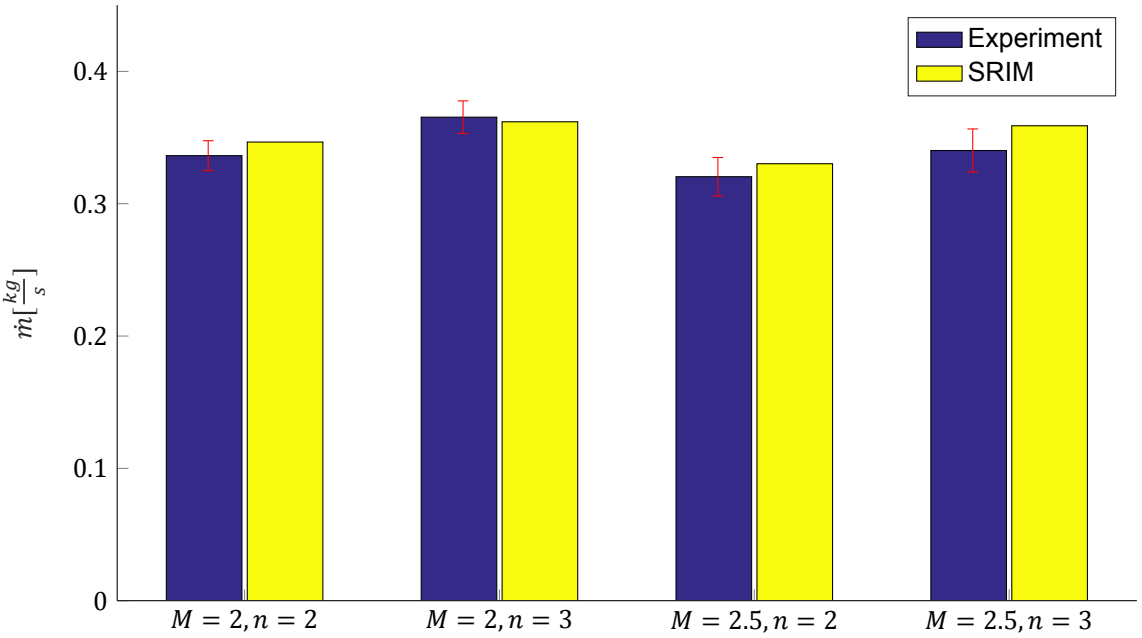

Figure 6.6: Experimental mass flow results taken from the total pressure correction procedure with their respective errors in red, plotted alongside the SRIM results for mass flow at the start of the internal channel

6.3. Mass flow

Since the experimental mass flow is derived from the supercritical condition, which shows discrepancies with the SRIM, it was decided to look further into the mass flow to shed light on the mismatch of results. Experimental and SRIM predicted mass flow for the four different flow cases are shown in Figure 6.6. The experimental mass flow as computed by the total pressure correction method described in Section 5.3 is shown, along with its error. Next to that the SRIM results for mass flow are shown. All flow cases show an agreement with the SRIM within their error bounds, save for the case of the double shock intake ($n = 3$) at Mach 2.5, which is very close to the upper error bound. The agreement exists despite the shortcomings of the SRIM treated earlier in this chapter, especially the discrepancy in Mach number.

The results for mass flow of the SRIM in Figure 6.6 are calculated at the start of the internal channel by integrating the mass flux over the intake height. The good agreement between experimental and SRIM results indicates that the mass flux (ρV) is predicted correctly by the SRIM, since the area of the intake is equal. Like the experimental case, the computation of the mass flow in the SRIM is done for flow in the supercritical condition. As explained in Section 5.3, the mass flow in the experimental case is computed using the local Mach number and pressure, as by equation 5.5.

To find out more about the Mach number overprediction in the SRIM supercritical condition, the mass flow in the internal channel was investigated. The SRIM can compute the mass flow in two ways. The first is a dedicated SRIM script computes mass flow solely based on inviscid output of the method of characteristics sub-model. The other mass flow computation is done in the Modified Diffusion Model, which includes the boundary layer. The results of both the inviscid and viscous SRIM predictions are shown in Figure 6.7. In both viscous and inviscid cases, the mass flow increases in the internal channel, although less so for the viscous computation. An increasing mass flow in an closed duct goes against the principle of conservation of mass and is an indication of an inaccuracy in the SRIM, which will be further investigated in the next section.

For further computations the mass flow can simply be computed at the start of the internal channel, where the inviscid calculations were shown to be relatively accurate. Meaning that for further computations in the SRIM, the consequences of the flawed mass flow are limited, as long as they are based on flow conditions close to the entrance of the internal channel. However, the SRIM usefulness would improve with an accurate prediction of supercritical flow in the intake.

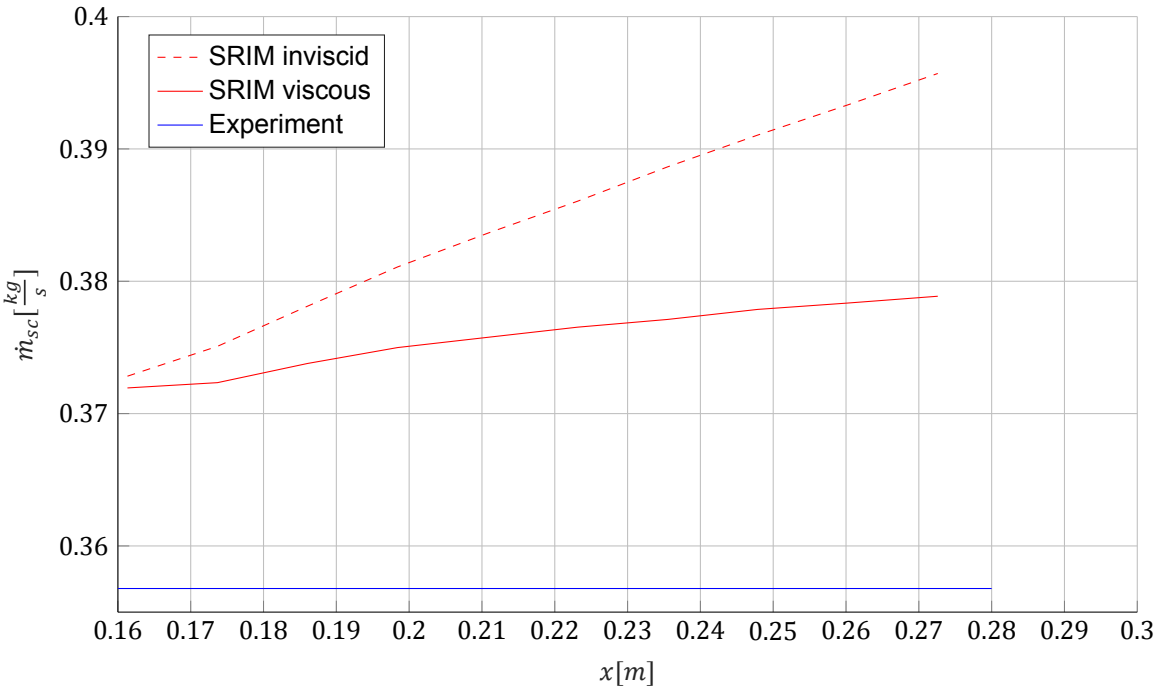

Figure 6.7: Mass flow in the internal channel computed by the SRIM and of the experimental model for the double shock SSI model at Mach 2.

6.4. Comparing SRIM supercritical flow to a Fanno prediction

Previous sections indicated that the SRIM prediction of the supercritical flow in the internal channel may not be very accurate, since the Mach number and mass flow of the SRIM prediction show discrepancies with the experimental values. The cause of this most likely lies in the way the internal supercritical flow is computed. As was mentioned in Section 2.5.2, the supercritical flow is computed with a combination of the method of characteristics, a shock wave angle determination and an integral boundary layer calculation. Outside the boundary layer, inviscid flow is assumed. Whilst this assumption may be valid for flow on the external compression surface of a supersonic intake, in an internal channel, friction effects are also present. A well-established analytical method that computes viscous adiabatic flow in a constant area duct is the Fanno flow method, see Section 2.2.3. Whilst Fanno flow does not account for shock waves in its flow field, the shock waves present are very weak and therefore of limited influence. It may be worthwhile to compare the SRIM supercritical internal channel prediction with a Fanno flow computation.

Using the differential equation given in 2.16, Fanno flow was computed with inputs from the SRIM, namely Mach number, hydraulic diameter, and friction coefficient, which the SRIM computes to be $f \approx 0.0025$ throughout the channel. A Mach number distribution was computed using the Fanno flow equation, from which the total and static pressure were obtained using isentropic relation. The results for the SRIM and Fanno flow computation are shown in Figure 6.8. Figures 6.8a and 6.8b show that the sole mode of compression in the SRIM supercritical condition is by the weak reflecting shocks, as the steps in the SRIM upper and lower wall values are caused by the reflecting shock waves and in between these steps Mach number seems to increase and pressure seems to decrease. Figure 6.8c shows that the reflecting shock waves are so weak that almost no total pressure is lost in the SRIM prediction (the total pressure jumps are approximately $0.01mbar$), which is impossible in viscous channel flow as shown by the Fanno flow prediction.

The Mach number rising outside of the jumps caused by the reflecting shocks is an indication that an error occurs in the inviscid computation by the Method of Characteristics. In between the shocks, the supersonic flow in the internal channel experiences contraction due to the growing boundary layers, which should reduce Mach number. As described in Section 2.5.2, the SRIM models the viscous element of the internal channel flow by adding the boundary layer displacement thickness to the wall in the internal channel. The displacement thicknesses for the upper and lower channel wall, as computed

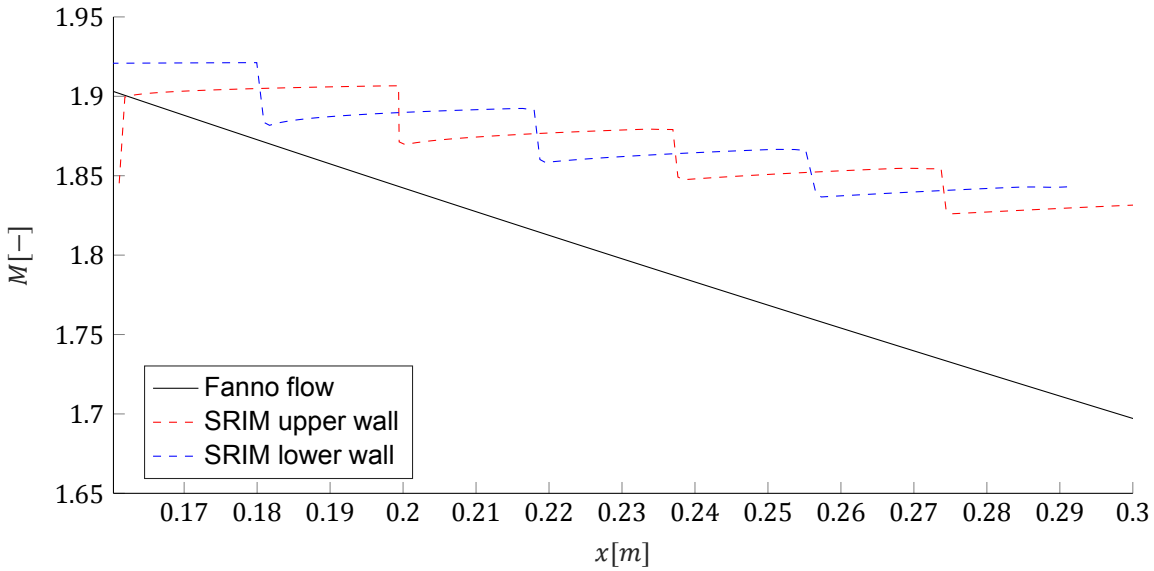

(a) Mach number

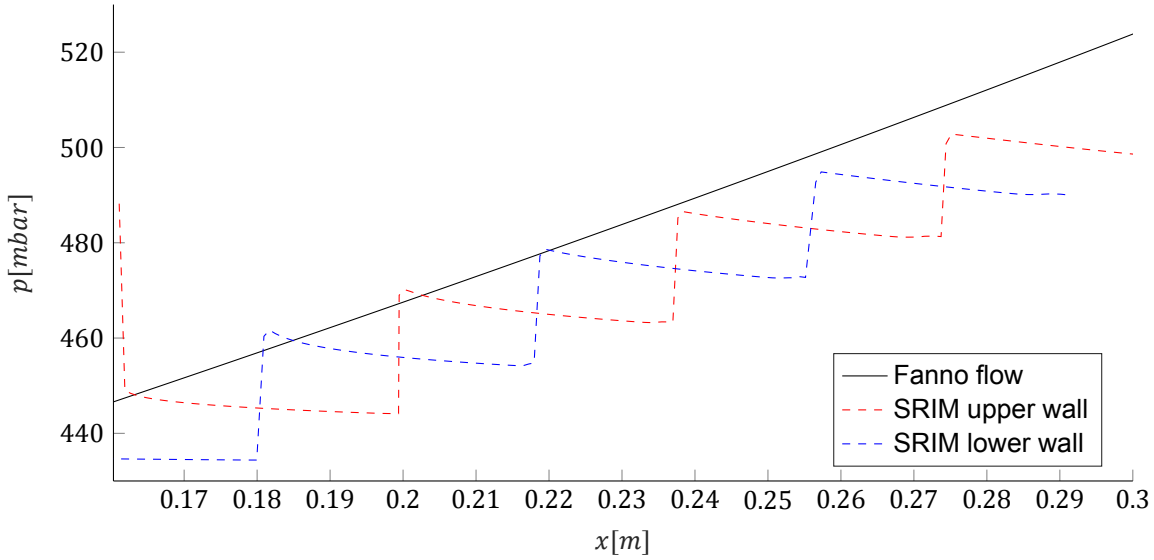

(b) Static pressure

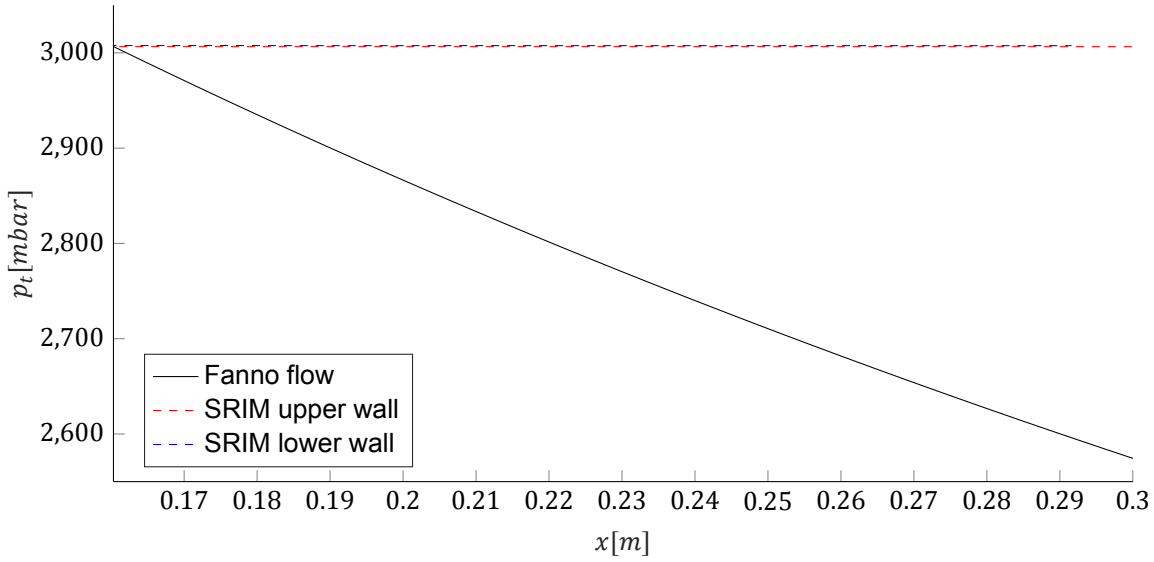

(c) Total pressure

Figure 6.8: Fanno flow and SRIM results for the double shock intake at $M = 2.5$ in supercritical condition

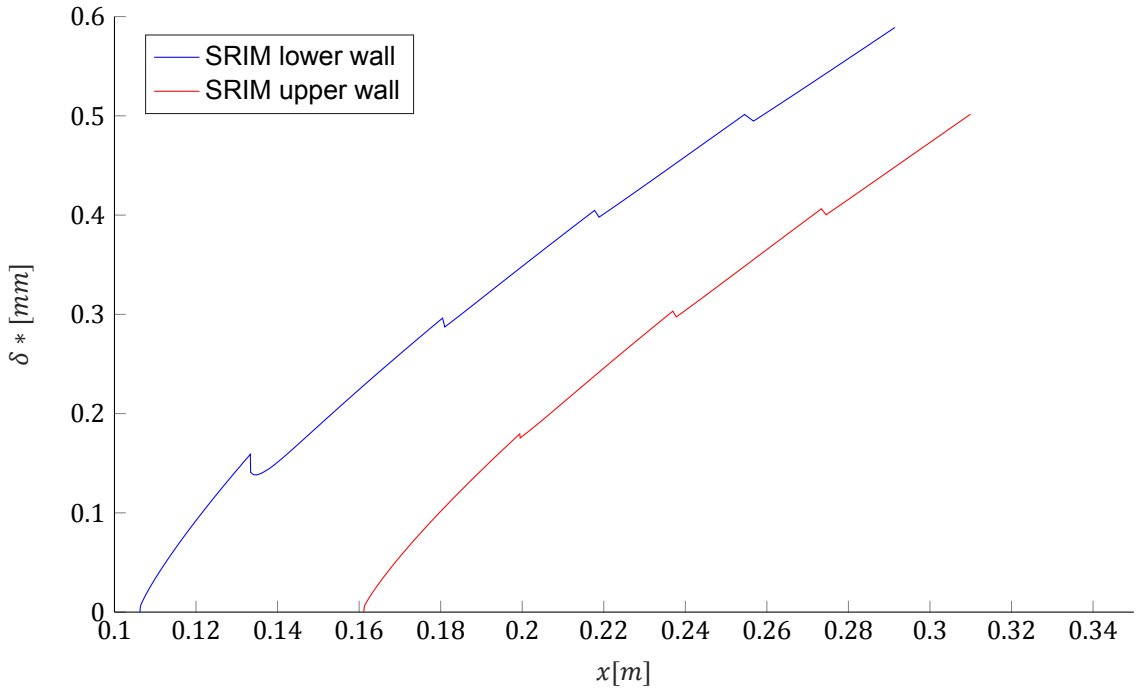

Figure 6.9: Displacement thickness on the upper and lower surface of the internal channel for the double shock SSI model at Mach 2.

by the SRIM, are shown in Figure 6.9. Amounting to a total of approximately $1.1mm$ of displacement in a channel with width of $12mm$ over a length of $200mm$ is a significant contraction, which should result in reducing Mach number.

A source of this error can be found in the manner in which the method of characteristics is applied. Figure 6.10 shows a detail of Figure 2.13, focusing on a flow block that is part of the supercritical internal channel computation. As explained earlier in Section 2.5.2, the method of characteristics is applied in the flow block, starting at the upstream reflecting shock at the left side, and moving downstream throughout the triangular flow block. The upper boundary layer displacement thickness is taken into account, as can be seen from the nodes impinging exactly on the red line of the displacement thickness in Figure 6.10. However, at the lower wall, a single node is seen between the geometric wall and the displacement thickness, indicating that at the lower wall, the displacement thickness is not applied for the second MoC computation. In addition, due to the triangular shape of the flow block, the method of characteristics takes little information about the lower wall into account. Considering the way information propagates in the method of characteristics, the lowermost node - which should contain flow information about the wall and boundary layer displacement - does not influence the MoC flow field except for the line of nodes most downstream in the flow block. Therefore, the computation within each flow block is virtually one of flow along a plate with a boundary layer, which explains why the Mach number and pressure do not change outside of the jumps across the weak shocks, as seen in Figures 6.8a and 6.8b. An explanation of the nearly unchanged total pressure lies in the fact that the reflected shocks are too weak to have any real influence. The error starts at the flow block entering the internal channel, A2 in Figure 2.13, since in the computation of the method of characteristics the presence of the cowl is neglected altogether. The error then propagates through all the internal flow blocks, indicated as 1, 2, 3, and so forth in Figure 2.13. Fixing the error so that the SRIM accounts for the viscous effects in internal channel flow will most likely reduce the Mach number and increase the shock angles in the SRIM prediction for supercritical flow.

The SRIM sub-models that predict the supercritical condition, erroneously neglect the viscous friction effects, which results in deteriorating accuracy as the solution moves downstream in the internal channel. Consequently, the SRIM is most accurate when computing the critical condition flow, where conditions of supercritical flow at the start of the internal channel are taken for further computation. In addition, the inaccuracy of the SRIM supercritical flow is the reason why the measurements of the

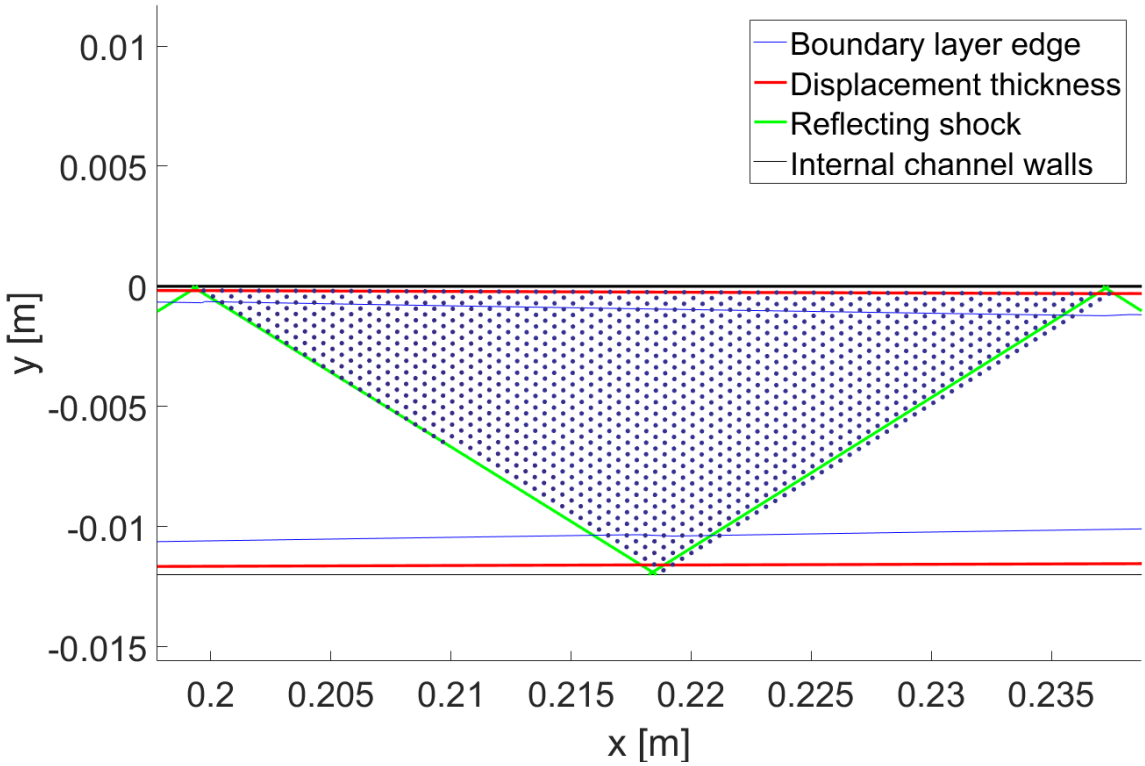

Figure 6.10: Detail of the SRIM output, showing the results of the computational elements in one internal flow block. The dots represent the nodes where the MoC solution is computed

slightly supercritical condition, as described in Chapter 4, are not useful for validation. No accurate corresponding SRIM solution was available, thus no validation could be done.

6.5. Pseudo-shock analysis

The pseudo-shock is an important aspect of the supersonic intake since it can incur heavy losses on the its performance. Moreover, a wrong prediction of the pseudo-shock length can have detrimental effects. When an intake is designed based on an inaccurately predicted pseudo-shock length, its constant area duct may be shorter or longer than the actual pseudo-shock. As was seen in Section 2.2.2, both scenarios incur total pressure losses, but the former is more severe. It will be seen that an asymmetry in the pseudo-shock exists in the submerged supersonic intake model, which will influence its length. Due to an underprediction of the pseudo-shock length during the design process, the pressure recovery in the pseudo-shock was suboptimal in the SSI models.

6.5.1. Asymmetric pseudo-shock

The asymmetry of the pseudo-shock was presented as a possible source of error in Section 2.5. Figure 6.11 shows the asymmetry of the pseudo-shock in the submerged supersonic intake in varying stages. First, let us focus on the most asymmetric pseudo-shock that occurs in the double shock SSI, shown in Figure 6.11a.

The thicker boundary layer on the compression surface can be seen to rapidly increase in thickness at the start of the internal channel at $x \approx 0.165m$ due to the adverse pressure gradient present. Further downstream, the upper boundary layer on the cowling also increases in thickness, which is visible from the shock it causes at $x \approx 0.175m$. Thus, the upper wall shock forms downstream of the lower wall shock due to the asymmetry in boundary layer thickness in the channel. The asymmetry in the boundary layers causes a different pseudo-shock than described by Matsuo et al. [27], one with a shock train region of interacting oblique shocks rather than bifurcated shock, as happens in a symmetric pseudo-shock, see Section 2.2.2. Further downstream, at $x > 0.2m$, weak normal shocks are visible,

indicating a low supersonic core. This supersonic core is located above the internal channel centerline as a consequence of the asymmetry in the boundary layers. At $x > 0.22m$ the flow dissipates into fully subsonic velocities, as indicated by the absence of shock waves.

The asymmetry of the pseudo-shock is more pronounced in the double shock intake, since it has a thicker lower boundary layer due to the longer compression surface, relative to to the single shock intake. Compare the double shock SSI in Figure 6.11a with the single shock SSI in Figure 6.11b. Both intakes experience boundary layer thickening and subsequent development of a shock wave at $x \approx 0.17$. For the double shock SSI, the stream-wise distance between the upper and lower wall oblique shocks at the start of the pseudo-shock is larger than for the single shock SSI in Figure 6.11a because the relative difference in boundary layer thickness between the upper and lower wall is smaller. Normal shocks are also visible from $x > 0.195$, again indicating a core region of supersonic flow, which is located more towards the centerline of the channel, relative to the double shock SSI case.

A factor contributing to the reduction of asymmetry in the pseudo-shock of Figure 6.11b is the fact that the pseudo-shock starts at a more downstream location in the channel. This gives the upper boundary layer more time to develop and reduces the relative difference in thickness between the upper and lower boundary layer, thus reducing the pseudo-shock asymmetry. This can be seen especially well when the pseudo-shock forms very far downstream in the channel. Figure 6.11c shows a pseudo-shock that is formed in the single shock intake operating at Mach 2 in slightly supercritical conditions. A rather symmetric pseudo-shock can be observed in the downstream part of the internal channel. The shocks caused by the thickening boundary layer start at approximately the same stream-wise x-coordinate of $x \approx 0.21$, because the difference between upper and lower boundary layer thickness is small, which causes a similar magnitude of boundary layer growth due to an adverse pressure gradient. In the pseudo-shock, normal shocks can be seen at decreasing lengthwise intervals, located in the centerline of the internal channel, which are typical of the shock train region of a symmetric pseudo-shock (see Section 2.2.2).

In the SRIM, the pseudo-shock is modeled by the Modified Diffusion Model (MDM), developed by Ikui et al. [21]. As described in Section 2.5, the MDM uses an empirical relation to compute the pseudo-shock characteristics based on upstream properties. Whilst the implementation of the MDM into the SRIM does account for two different boundary layer thicknesses, is does not compute their propagation throughout the pseudo-shock, since the two different boundary layer thicknesses at the start of the pseudo-shock are simply added together in the analysis. In addition, the empirical relation at the core to the MDM is based on symmetric pseudo-shocks. Since it computes the non-dimensional length of the pseudo-shock and bases the other pseudo-shock properties on this length, it is important to verify whether the computed pseudo-shock length is accurate, to determine the accuracy of the pseudo-shock subroutine of the SRIM.

6.5.2. Pseudo-shock length

The problem with determining the pseudo-shock length from the experimental data is the difficulty to pinpoint where exactly the pseudo-shock ends. The dissipation of the supersonic core into the subsonic outer region happens without any phenomena that are visible by schlieren photography. Alternatively, the static pressure rise in the constant area duct could give information about the pseudo-shock end, as shown in Figure 2.7, but the constant area duct is too short to show a definite peak in the static pressure within the constant area duct bounds, see Figure 6.13.

Whilst it is difficult to exactly determine the pseudo-shock end location from the schlieren images, in some cases it is easy to show that the predicted location where the pseudo-shock end is incorrect. Figure 6.12 shows a comparison between the schlieren results and the SRIM results for the double shock SSI model at a Mach number of 2. The pseudo-shock end location is plotted in red and it is surrounded by small normal shocks from the end of the experimental pseudo-shock. This is an indication that the SRIM prediction of the location where the pseudo-shock ends is not accurate. Given the inputs of the pseudo-shock subroutine, this can be caused by any of three properties at the start of the pseudo-shock: Mach number, static pressure and boundary layer thickness.

The Mach number in the internal duct is given in Figure 6.5. It can be seen that the predicted internal Mach number is higher than the experimental values, which follows from the fact that the Mach angles of the internal shocks are too high in the SRIM. Whilst a higher Mach number generally results in a longer pseudo-shock, in this particular case the pseudo-shock is shorter than predicted. Meaning that, next to the Mach number discrepancy, there is some other cause for the inaccuracy in the pseudo-shock

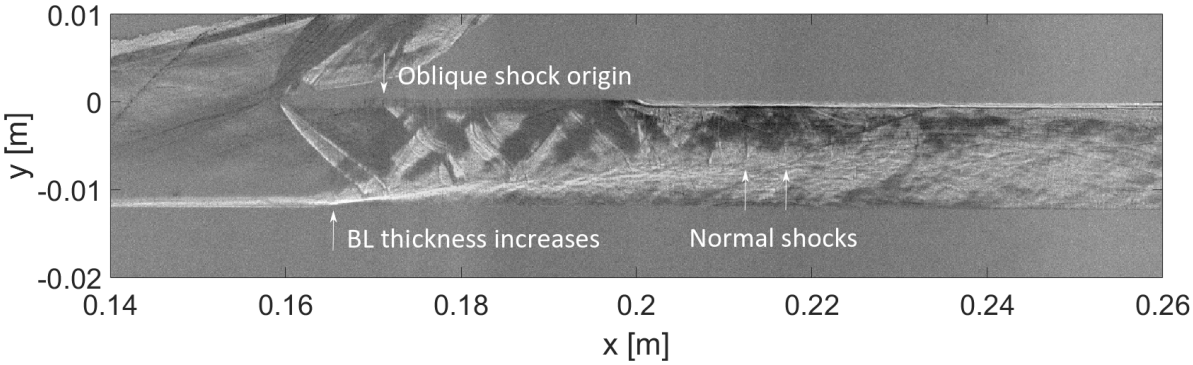

(a) Double shock SSI operating in critical condition and a Mach number of 2.

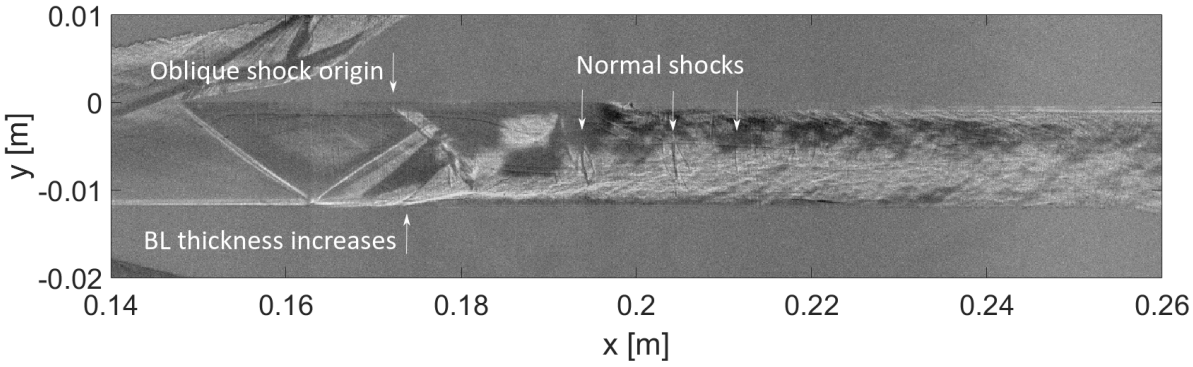

(b) Single shock SSI operating in critical condition and a Mach number of 2.

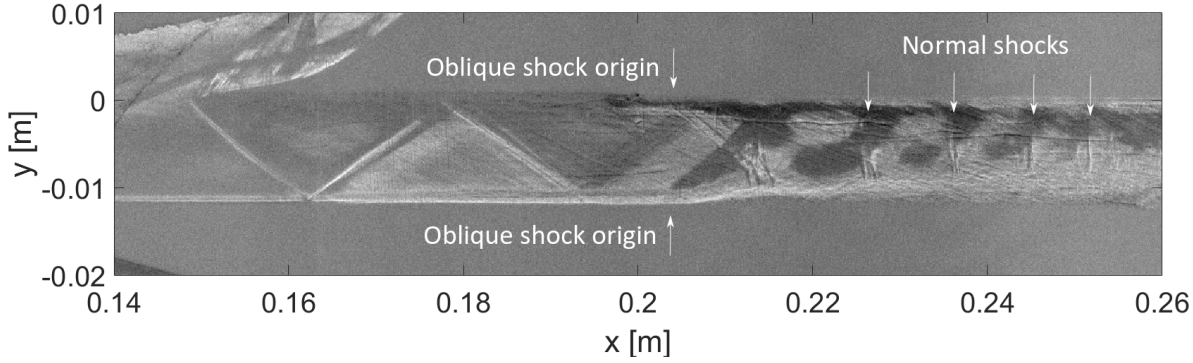

(c) Single shock SSI operating in slightly supercritical condition and a Mach number of 2.

Figure 6.11: Three details of single schlieren images that show the pseudo-shock in the intake, in varying stages of asymmetry.

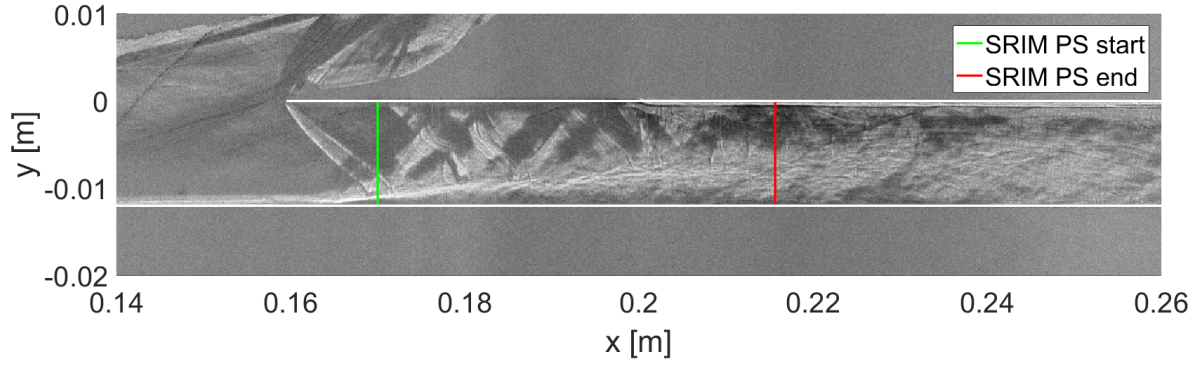

Figure 6.12: Detail of schlieren image showing the pseudo-shock in a double shock SSI in the critical condition at $M_\infty = 2$ with SRIM results for pseudo-shock

length prediction.

The static pressure at the start of the pseudo-shock for this particular case can be seen in Figure 6.13b. Prior to the pressure rise that starts at the beginning of the constant area duct, the static pressures predicted by the SRIM are quite similar to the experimental values. Section 6.6 also shows that in the supercritical condition, i.e. ahead of the pseudo-shock, the SRIM prediction and experimental values for static pressure are in relatively good agreement.

Figure 6.14 shows a detail of the boundary layer ahead of the start of the constant area duct of the double shock intake at $M = 2$ in the critical condition, along with the SRIM results for the same configuration and Mach number. It is visible that the predicted boundary layer thickness, shown in red, is exceeded by the boundary layer thickness as measured in the schlieren image. Since a thicker boundary layer at the pseudo-shock start generally results in a longer pseudo-shock, the underestimation of the boundary layer thickness by the SRIM may be the reason for the shorter predicted pseudo-shock.

Since the Mach number and boundary layer thickness seem to be the root causes of the discrepancy between the predicted and experimental pseudo-shock length, the influence of these two parameters on the pseudo-shock length is plotted in Figure 6.15. The pseudo-shock length is plotted for the SRIM-predicted Mach number of 1.92 and the experimental Mach number of 1.70 in the internal channel, with on the x-axis the boundary layer thicknesses (non-dimensionalized with the hydraulic diameter D of the internal channel) typically found at the start of the pseudo-shock. Note that the pseudo-shock sub-model, the Modified Diffusion Model, averages the boundary layer thicknesses before further computation. Thus, for comparison, the average of the non-dimensional boundary layer thicknesses for this SRIM and experimental case (double shock intake at $M = 2$) were indicated in Figure 6.15. The combinations of Mach number and boundary layer thickness for the SRIM and experimental cases give approximately equal pseudo-shock lengths in the results of the Modified Diffusion Model. So there must be another explanation for the fact that the pseudo-shock is much longer than predicted.

The explanation can be found in Wang et al. [43], who found that "the increase of the asymmetry degree of the flow at isolator entrance will lead to the increase of the shock train length for a given pressure ratio". Thus, the asymmetry due to the differing boundary layer thicknesses leads to longer pseudo-shock than predicted by the SRIM, whose pseudo-shock sub-model assumes a symmetric pseudo-shock. The validation of the MDM adaption in Figure 2.12 showed that the MDM is approximately 20% off when asymmetry occurs in the pseudo-shock, note that this is based on only one experimental campaign. Unfortunately, since no fully developed asymmetric pseudo-shock was measured, no definite claims can be made on the accuracy of the MDM.

6.6. Static pressure

The static pressure in the intake was measured by the scanivalve system. Whilst good data was collected, not all flow conditions gave a good agreement with the results of the SRIM. During supercritical intake flow, the scanivalve measurements are relateble to the SRIM data, see Section 6.6.2. However, for the critical conditions, scanivalve measurements are difficult to compare to the SRIM results, as will be seen in Section 6.6.1. The results of the static pressure measurements are shown in Figures 6.13 and 6.16. For a comparison between the visual flow phenomena and static pressure, the schlieren images and static pressure results are plotted in the same reference frame in Appendix C.

6.6.1. Static pressure measurements for the critical condition

As was seen in the pseudo-shock definition in Section 2.2.2, the pseudo-shock ends when a peak in static pressure is reached. Herein lies the difficulty of comparing the static pressure measurements to the SRIM results for the critical condition. For most critical flow cases, no peak in static pressure is reached before the constant area duct ends, which is shown in Figure 6.13. All flow cases have a steady pressure rise throughout the entire internal channel. One exception exists, namely the double shock SSI at Mach 2 in Figure 6.13b. In this intake the pressure starts to level off slightly, before the constant area duct ends, but it does not reach a maximum before the flow reaches the subsonic diffuser. Thus, by definition, no experimental data exists of a fully developed pseudo-shock.

The consequence of not having a fully developed pseudo-shock in the constant area duct of the SSI wind tunnel model is that the flow characteristics as predicted by the Modified Diffusion Model were not reached, and thus no data on post-pseudo-shock flow is available. Also, if the constant area duct would have been long enough to for the pseudo-shock to reach its peak values, the pressure ratios

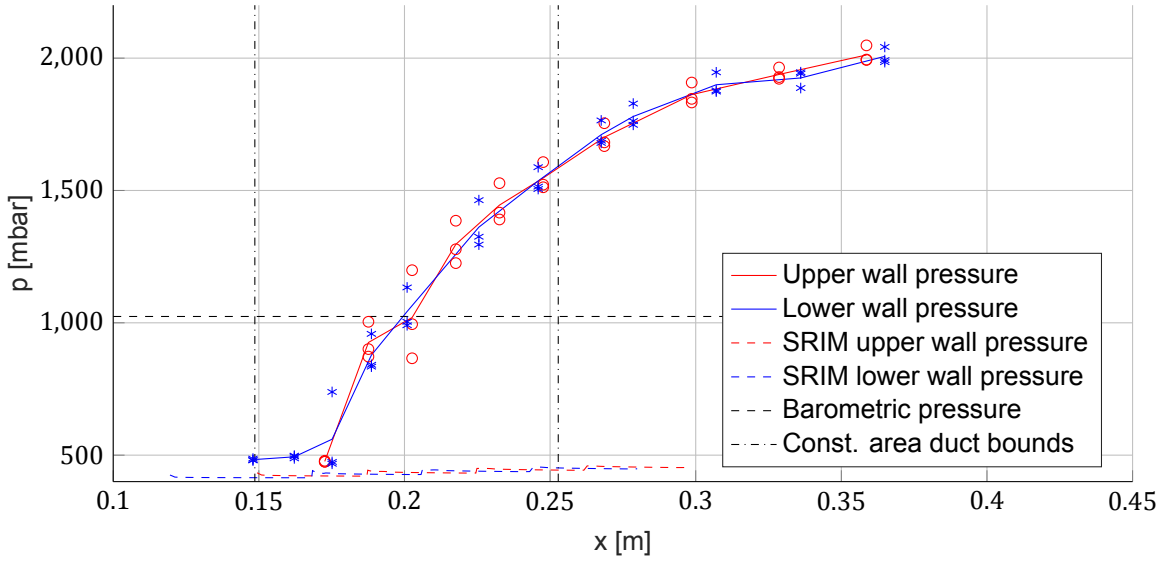

(a) Single shock SSI at $M = 2$

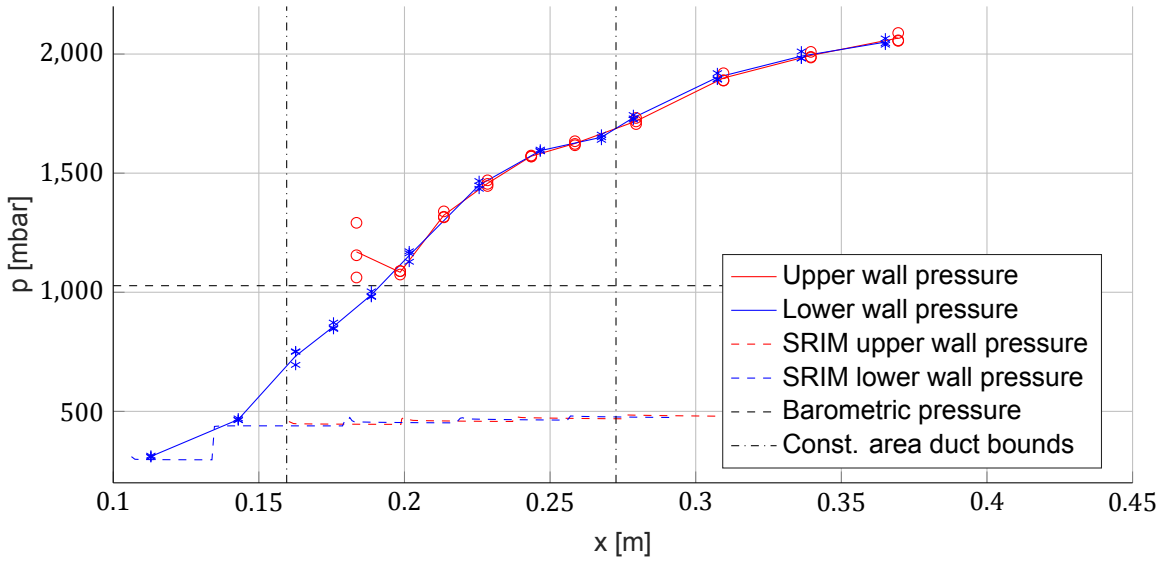

(b) Double shock SSI at $M = 2$

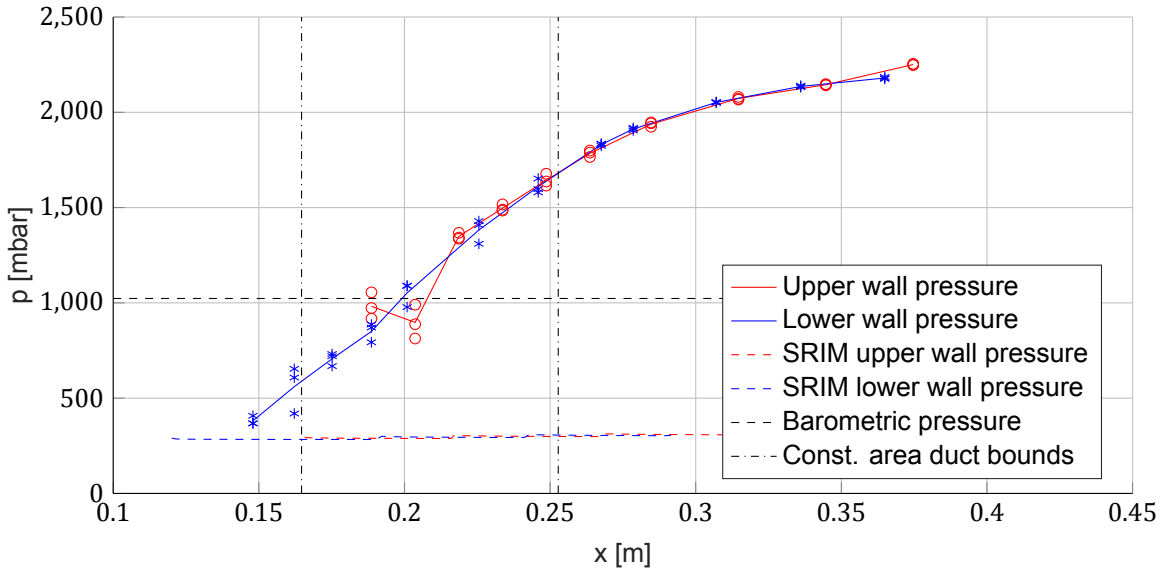

(c) Single shock SSI at $M = 2.5$

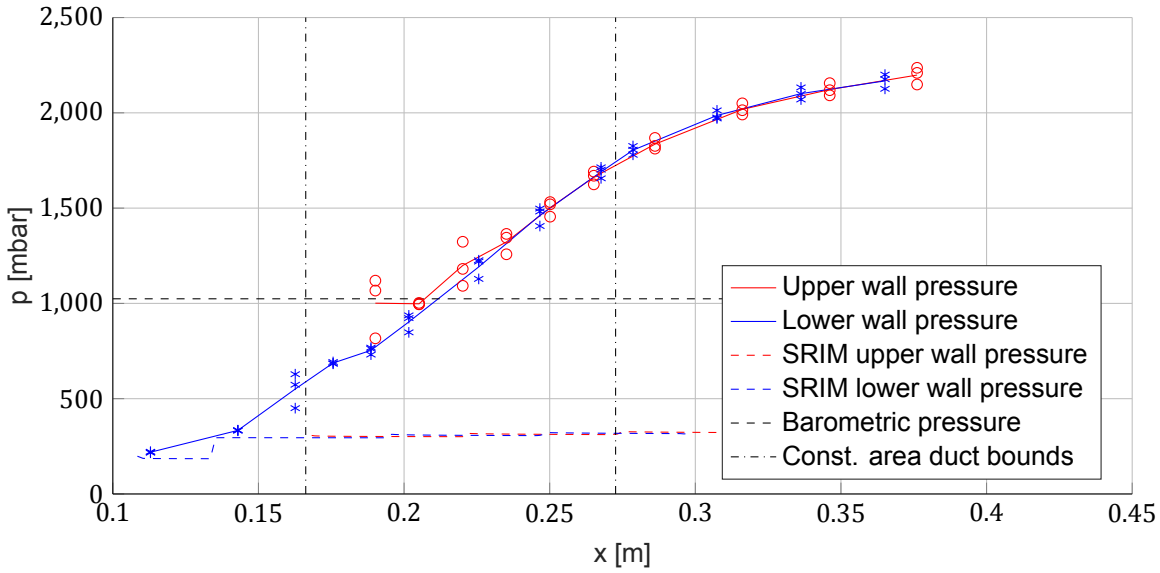

(d) Double shock SSI at $M = 2.5$

Figure 6.13: Static pressure result of the scanivalve measurements for submerged supersonic intakes in the critical condition. SRIM results of static pressure for the supercritical condition are also shown.

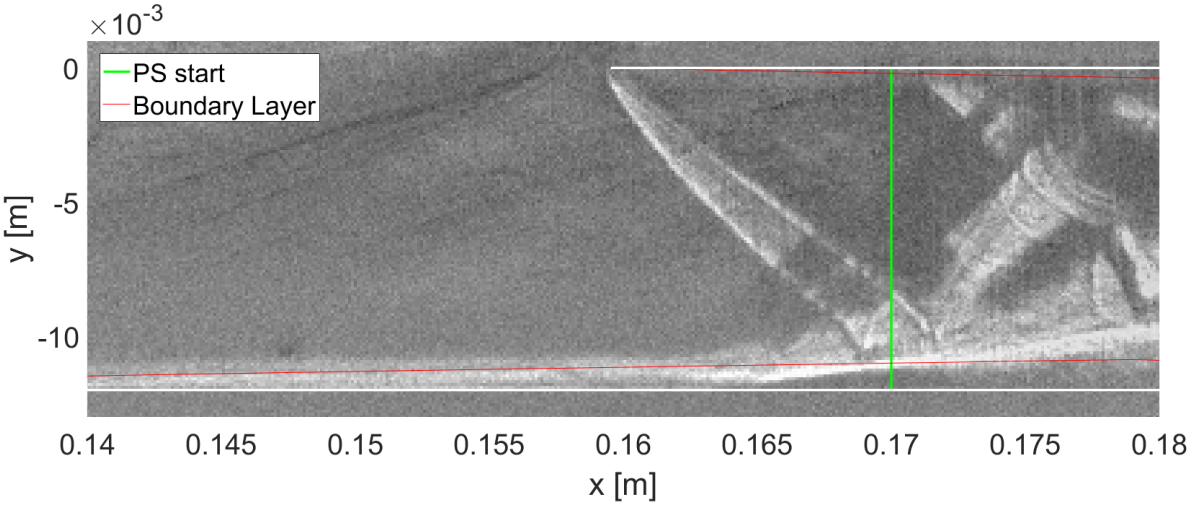

Figure 6.14: Detail of schlieren image showing the pseudo-shock in a double shock SSI for critical conditions at $M_\infty = 2$ with SRIM results for pseudo-shock start and boundary layer thickness

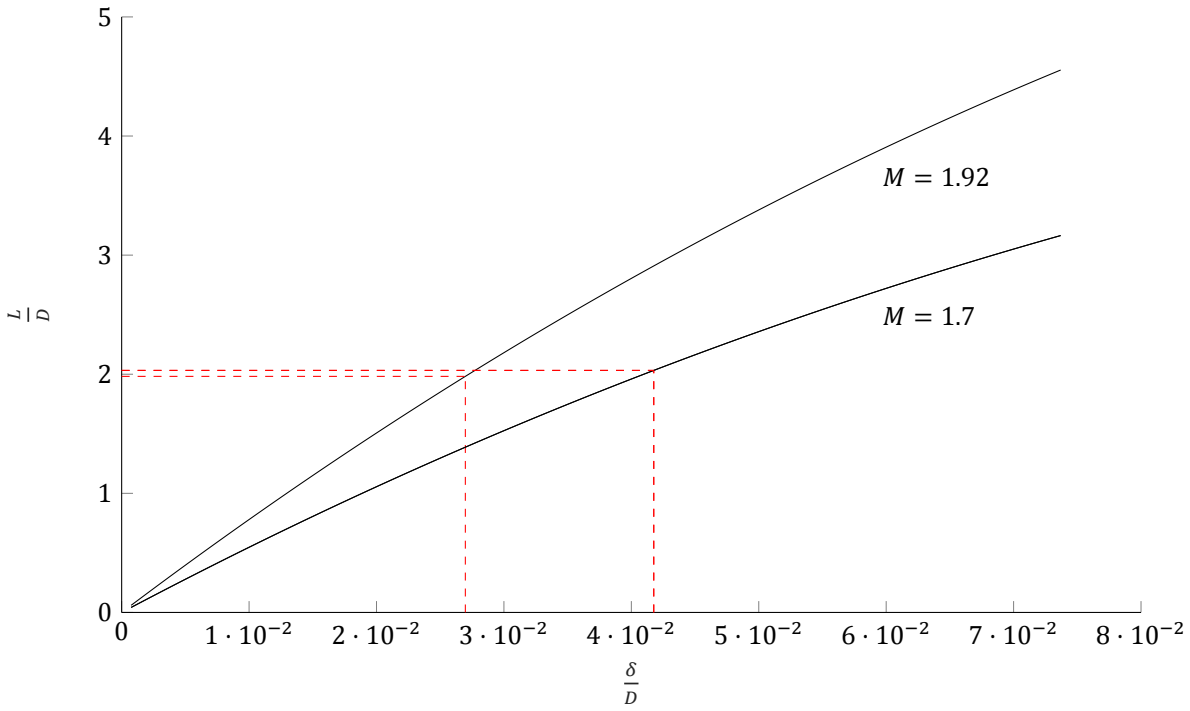

Figure 6.15: The two combinations of boundary layer thickness and Mach number of the SRIM and experimental results give similar pseudo-shock lengths when computed by the Modified Diffusion Model as given by Ikui et al. [21]

across the entire intake might have been higher.

Since the Modified Diffusion Model provides a prediction for static pressure distribution over the pseudo-shock, some valuable data might still be extracted for the static pressure measurements in the internal channel in critical condition. However, it was already shown in Section 6.5.2 that the pseudo-shock length prediction is inaccurate. Therefore, no fair comparison can be made between the SRIM and experimental results on pseudo-shock flow. In future work, it is important to modify the constant area duct length in the SSI wind tunnel models so that fully developed pseudo-shock can be measured.

6.6.2. Static pressure measurements for the supercritical condition

Contrary to the flow cases in critical condition, the supercritical condition data is readily comparable to the scanivalve data. The SRIM results and scanivalve data for all combinations of Mach number and intake configuration in supercritical condition are shown in Figure 6.16. The SRIM prediction for the static pressure is too low for most cases, which suits the picture of the Mach number overprediction, since the static pressure would be lower for higher Mach number and equal total pressure. The lack of viscous effects in the SRIM supercritical internal flow prediction is most likely the cause of the small discrepancy, since added viscosity will increase pressure, as was seen from the Fanno flow computation in Figure 6.8b.

Whilst the pressure in the internal channel should be relatively constant since the reflecting shock inside is very weak, for some measurements the pressure can be seen to have some spikes. For example, Figure 6.16b shows high variation in static pressure at the beginning of the constant area duct, whilst Figure 6.16a shows static pressure variations at the end of the internal channel duct. The data points in all three measurements have good agreement on the varying static pressures, therefore it must be a steady phenomenon. The cause may be the same reflecting shock wave interaction in the internal channel that caused the heavy outliers described in Section 5.5.2. Only, the shock impinged a little farther from the pressure holes, reducing the height of the spike. Therefore, the readings of these data points were not so far from the rest justify exclusion from further calculations.

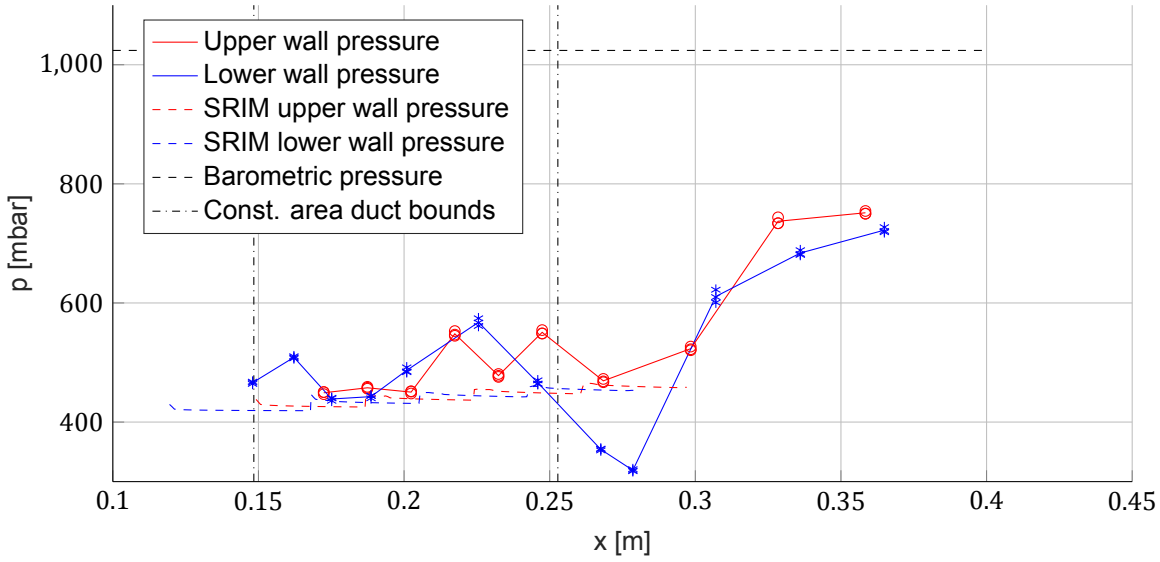

(a) Single shock SSI at $M = 2$

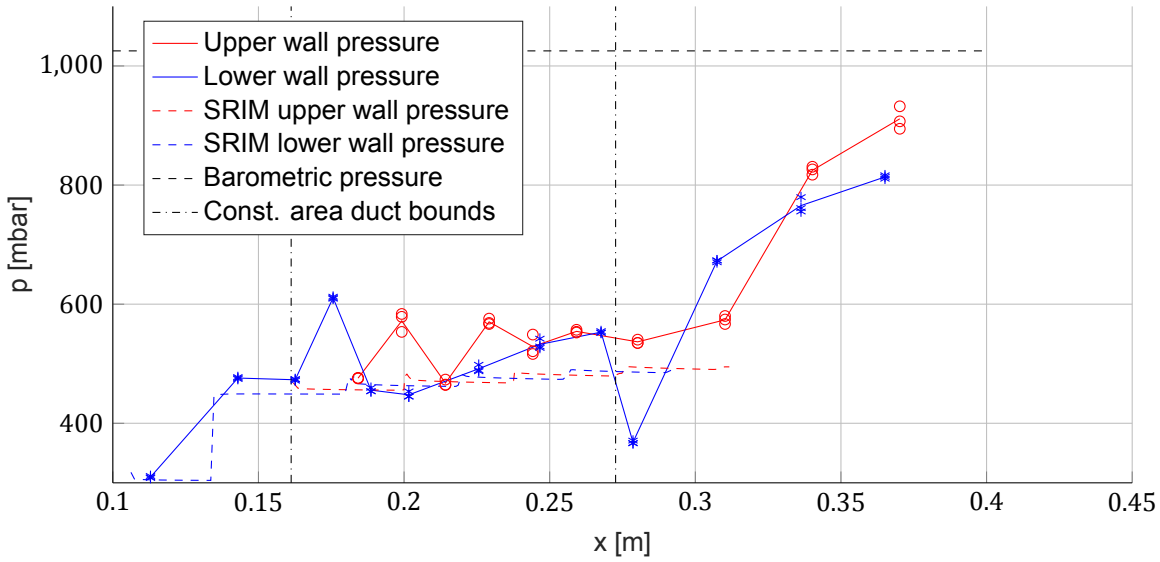

(b) Double shock SSI at $M = 2$

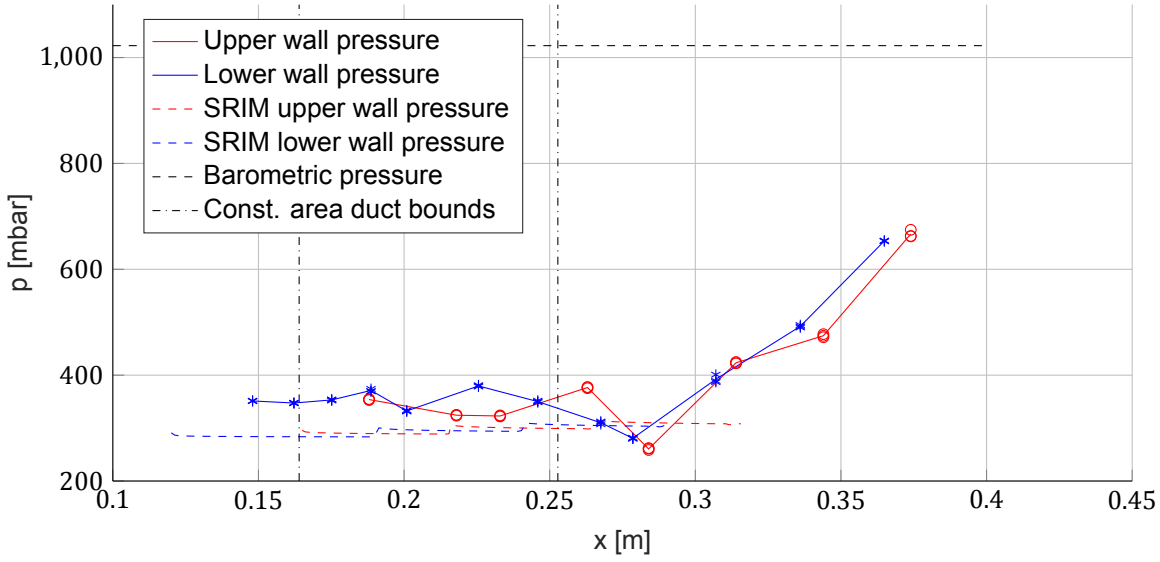

(c) Single shock SSI at $M = 2.5$

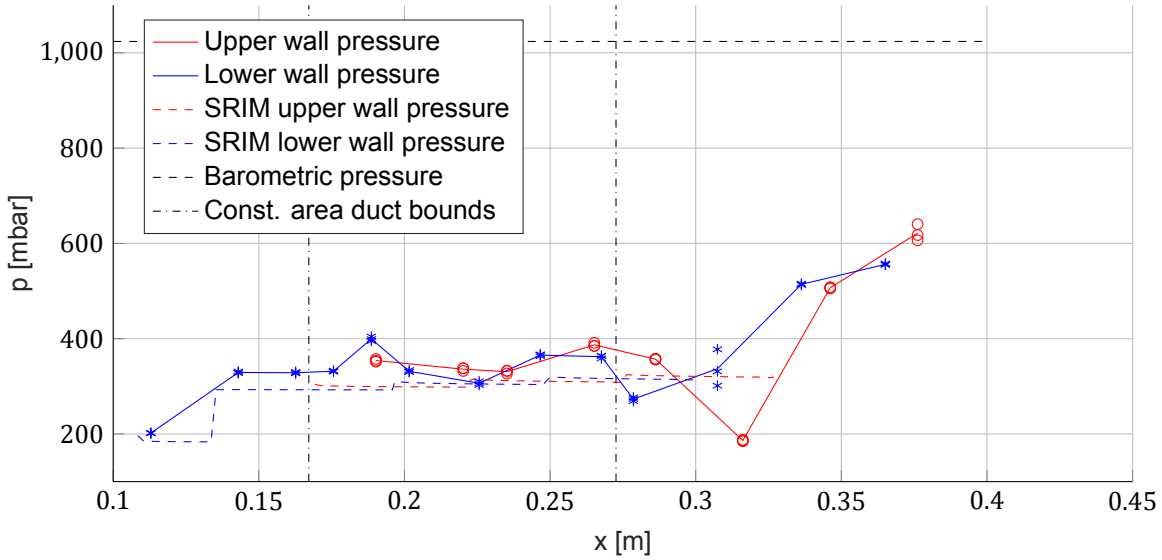

(d) Double shock SSI at $M = 2.5$

Figure 6.16: Static pressure result of the scanivalve measurements for submerged supersonic intakes in the supercritical condition. Data points of individual measurements are shown along with their averages.

6.6.3. Static pressure in the subsonic diffuser for the supercritical condition

Another noteworthy result in the static pressure data is the fact that in the supercritical condition, the static pressure for all flow cases increases in the subsonic diffuser. This goes against the inviscid expectation of supersonic flow entering a diverging channel, which is increasing Mach number and decreasing local static pressure of the flow. A slight drop in static pressure is visible at the start of the subsonic diffuser for all measurements in Figure 6.16. The beginning of the subsonic diffuser is marked by an outward deflection in the lower wall, which causes an expansion for supersonic flow, explaining the drop in static pressure directly aft of the subsonic differ start. However, after this drop, the static pressure immediately rises, indicating decelerating flow. The cause of this phenomenon is difficult to indicate, since only the static pressure data is available because the subsonic diffuser was outside the area of optical access.

A likely possibility for the pressure increase is boundary layer separation. At the start of the subsonic diffuser a sizable boundary layer will have been built up. Next to that, the supersonic flow from the constant area duct will have little tendency to change direction due to inertia. This results in flow separation an possibly a recirculation bubble in the lower part of the subsonic diffuser. As was mentioned, this is difficult to verify since no optical access was possible in subsonic diffuser.

However, in the scope of validating the SRIM, the subsonic diffuser flow is not very relevant, since the SRIM does not have a flow solution for the subsonic diffuser flow. As mentioned in Chapter 3, the only function of the subsonic diffuser was to stabilize the flow in the rest of the SSI wind tunnel model, so that experiment could be performed.

6.7. Total pressure

This section will focus on total pressure. Experimental results for static pressure were combined with data for mass flow in post-processing to arrive at total pressure. These results will be compared to the predictions of the SRIM. This will give a more holistic view of the intake performance, since the focus lies predominantly on the engine output, instead of individual flow phenomena.

The total pressure in the intake can only be derived from experimental data at locations where static pressure and Mach number are known. As the Mach number can only be derived from the total pressure correction method described in Section 5.3, which requires optical access to the wave angle measurement, the availability of information on total pressure is limited to the internal channel. However, this does allow for validation of the pseudo-shock sub-model, the Modified Diffusion Model, which will be done next. Table 6.2 shows the total pressures of all combinations of Mach number

Table 6.2: Pre- and post-pseudo-shock total pressures from experimental data and SRIM results and the ratios of experimental to SRIM values

			Pre-pseudo-shock			Post-pseudo-shock		
M	$p_0[bar]$	Configuration	SRIM $[bar]$	Exp. $[bar]$	**Ratio**	SRIM $[bar]$	Exp. $[bar]$	**Ratio**
2	3.17	Single shock	2.77	2.34	**0.84**	2.09	2.07	**0.99**
	3.12	Double shock	2.99	2.54	**0.85**	2.23	2.13	**0.96**
2.5	5.03	Single shock	4.50	2.86	**0.63**	2.17	2.19	**1.01**
	5.01	Double shock	4.80	3.21	**0.67**	2.39	2.22	**0.93**

and intake configuration upstream and downstream of the pseudo-shock. The pre-pseudo-shock total pressure was taken from the internal channel flow properties conditions in the supercritical condition, for several reasons:

- The total pressure ratio calculation method was unfit to accurately compute the total pressure in the constant area duct for the critical condition, as was seen in Section 5.4,
- the flow upstream of the internal channel is identical for the critical and supercritical condition and
- the SRIM also bases the pre-pseudo-shock inputs for the MDM on the supercritical SRIM predictions, as was explained in Section 2.5

Therefore, using the total pressure in the supercritical condition was deemed the most accurate method of determining the total pressure at the station between the oblique shock system and the pseudo-shock. The pressure behind the pseudo-shock is taken from the pressure measurements just upstream of the valve in the subsonic diffuser in the SSI wind tunnel model. Whilst the subsonic diffuser does not influence total pressure much, for completeness it is worth noting that the wind tunnel model did include a subsonic diffuser, but the SRIM does not. Also, no total pressure data is available of the flow after expansion, since no measurements were done there. It is assumed that the expansion section does not alter the total pressure in the flow, since it is isentropic. It is not likely that this assumption is invalid, but it might be worthwhile to install a pressure sensor behind the expansion section in future experiments.

From Table 6.2, it can be seen that for all intakes and free-stream Mach numbers the differences between the experimental and SRIM results are larger ahead of the pseudo-shock than after. This indicates that the efficiency of the oblique shock system of the intake is overpredicted and the efficiency of the pseudo-shock in the internal channel is underpredicted in the SRIM. Altogether it makes for a prediction of the total pressure with an error of approximately 5% by the SRIM. This seems to be a rather good result, but as was seen earlier some discrepancies still exist between the SRIM and experimental results. It may be worth asking if any of these discrepancies manifest themselves in these total pressure results.

Pre-pseudo-shock total pressure

The total pressure ahead of the pseudo-shock is lower in experiments because it is derived from the supercritical internal channel properties of static pressure and Mach number, which were shown to be higher and lower than the SRIM prediction, respectively. Therefore, the discrepancy in total pressure stems from the lower experimental Mach number in the internal channel and the higher static pressure. This may have a relation with the curved leading edge shock that has been found in the experimental results. Whatever its cause, the curvature in the shock implies that a velocity gradient is present in the streamtube ingested by the intake. Probable causes to the leading edge shock curvature were given in Section 6.1.1. The velocity gradient behind the leading edge shock causes the lower Mach number and higher static pressure, however, not in proportions such that the total pressure is equal to the SRIM prediction. Another likely cause is the error in the supercritical SRIM prediction, which leads to neglected viscosity in the internal channel. Higher viscosity should lead to a lower Mach number and higher pressure in the internal channel, which would reduce the difference with the experimental results. Since the viscous effects in the internal channel are still small at the entrance, where this data is taken, the consequences should be limited.

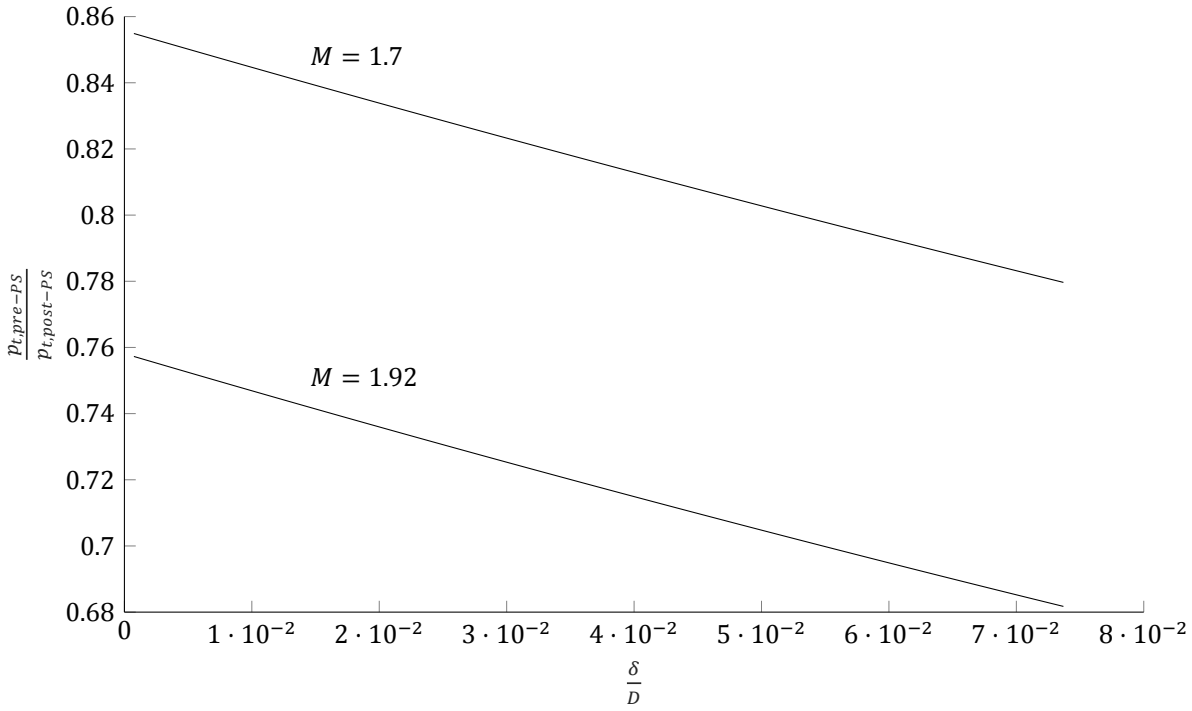

Figure 6.17: Total pressure ratio across the pseudo-shock vs. non-dimensional boundary layer thickness at varying Mach number, computed by the Modified Diffusion Model as given by Ikui et al. [21]

Another notable results in 6.2 is the lower pre-pseudo-shock SRIM accuracy for the double shock intake, compared to the single shock intake. It seems that the fact that the second shock of the double shock oblique system resembles a compression fan does influence the SRIM accuracy.

Post-pseudo-shock total pressure

During the pseudo-shock flow, the difference in total pressure between the SRIM and experimental results decreases. This indicates that the experimental pseudo-shock incurs less total pressure losses than the SRIM pseudo-shock. An explanation for this is the fact that for a higher inflow Mach number, the pseudo-shock total pressure ratio becomes lower. Therefore, the higher inflow Mach number for the SRIM caused a less efficient pseudo-shock than in the experimental case. The difference in pseudo-shock total pressure ratios between the SRIM and experimental flows canceled out the total pressure difference that existed ahead of pseudo-shock. Note, however, that the boundary layer in the experimental results was too low, which will slightly increase the total pressure ratio. Only, Figure 6.17 shows that this effect is smaller than the Mach number difference, since it shows that the adverse effect of higher Mach number on total pressure ratio is more pronounced than the increase in boundary layer thickness on the scale found in this case.

6.8. SRIM assumptions

As mentioned in Section 2.5.4, the SRIM makes some assumptions outside the sub-models that need to be validated by the experiments.

The first of them, the assumption that the boundary layer bleed is not choked can be easily verified by looking at Figure 6.3. From this schlieren image it immediately becomes clear that no choking occurs in the boundary layer. However, since the bleed slot does not run the entire test section span choking is easy alleviated. Also, it was shown in Section 6.1.1 that a curve exists, so it may be possible that not the entire boundary layer is bled off. Fortunately, this does not change the fact that the boundary layer bleed slot is shown to be free of choking.

The other two assumptions are both connected to transition of the boundary layer. The assumption that transition occurs instantly is of course easily verified to be false, since in reality a transition length is present. The consequences of this false assumption in SRIM accuracy is impossible to obtain form the

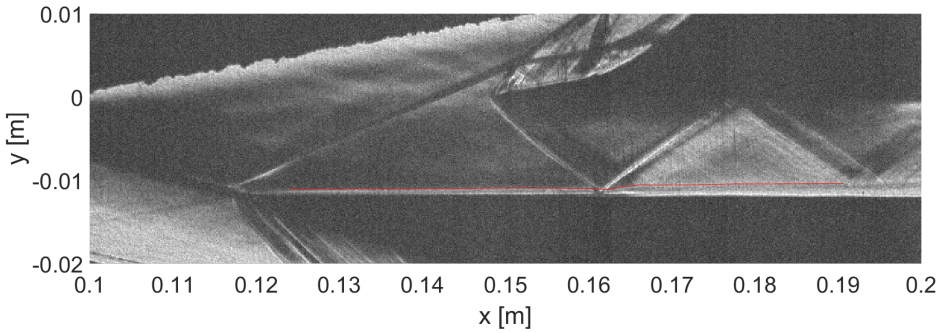

(a) Single shock

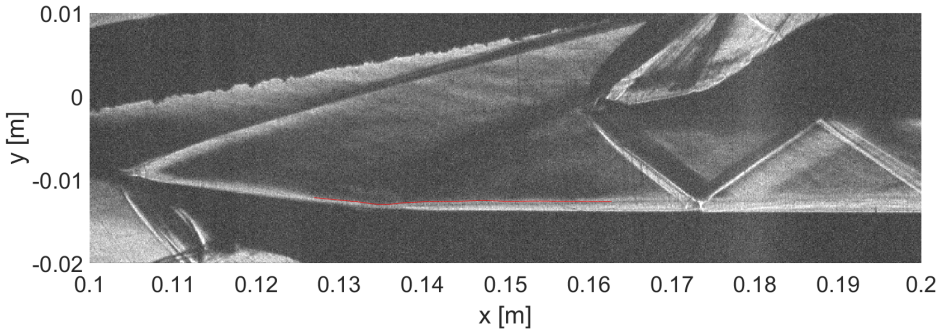

(b) Double shock

Figure 6.18: Details of the schlieren images of the boundary layer transitioning in the intake at Mach number 2

available data. The specified transition location gives opportunity to alter the SRIM conditions such that they agree with the experimental conditions. The other assumption that shock wave-boundary layer interaction triggers transition are difficult to verify using the available data. However, the schlieren images that feature the boundary layer in the SSI model may give an indication of the way transition occurs.

Figure 6.18 shows the boundary layer of a single shock intake. In this schlieren image, the edge of the boundary layer was indicated in red. It can be seen that the boundary layer of the single shock intake (Figure 6.18a) is relatively thin after the leading edge shock, and increases in thickness after interacting with the first reflecting shock in the internal channel. This may indicate that the interaction with the first reflecting shock transitioned the boundary layer to turbulent conditions. Whilst harder to make out, the double shock intake (Figure 6.18b) shows an increase in boundary layer thickness aft of the second oblique shock, indicating transition. This may verifies the assumption that boundary layer transition is triggered by shock wave-boundary layer interaction. For the SRIM an easy adaption is made to the boundary layer transition point. Note that whilst the transitioning is not instantaneous, the deficit in boundary layer thickness for the transitioning region is most likely insignificant. However, this cannot be determined with the available data. Also, the highly qualitative analysis provided above is unable to provide definite validation of the assumptions, but may grant insight on where to focus future research into transitioning boundary layers in submerged supersonic intakes.

6.9. Validation conclusions

Concluding, it has been seen that for the flow cases tested in this experimental campaign the SRIM has a good agreement with the experimental results for the key intake efficiency parameters: total pressure and mass flow. However, it should be noted that not all SRIM sub-models were accurate.

In the oblique shock system of the experimental SSI models, a curved shock wave is visible on the leading edge of all intakes. Looking at the schlieren images of the expansion section gave indication that this shock wave curvature may be caused by a velocity gradient that originates on the expansion section. Other explanations are three-dimensional effects or a slight bluntness on the leading edges

of the compression surface and cowling. Unfortunately, no definitive answer can be provided from the available data. Future work can verify or rule out the source of the leading edge shock curvature.

Mass flow is predicted very accurately at the start of the intake internal channel, but was found to increase when moving downstream in the constant area duct. Since the inputs for the mass flow routine are taken from the SRIM prediction of supercritical condition, it can be argued that when moving down the internal channel, the accuracy of the SRIM supercritical flow prediction deteriorates. This need not be a problem, since, when evaluating a SSI in the critical condition, the pseudo-shock sub-model bases its calculations on data close to the internal channel entrance, but for pseudo-shocks starting further downstream in the channel the solution becomes disputable. This should be taken into account when using the SRIM.

The SRIM prediction of the internal channel Mach number in the supercritical condition was found to be too high, as was seen from the Mach angles of the reflecting shock waves. In addition, the SRIM predicted physically impossible mass flow increase in the internal channel for the supercritical condition. Therefore, further investigation into the SRIM prediction was done, using a Fanno flow calculation with inputs from the SRIM as verification for the SRIM results. It was found that in the interaction between sub-models an error is present that prevents the computation of viscous effects in the internal channel. The consequences of the error were manageable for further computations of the SRIM, since the error only exists in the supercritical flow in the internal channel. However, the error should be fixed to ensure accurate SRIM results in the future.

The differences in flow properties between the SRIM and experiments are a lower experimental Mach number and higher static pressure, which result in a higher total pressure ratio across the pseudo-shock. This counteracts the difference in total pressure ratio contracted in the oblique shock system for the flow cases measured here. In the end, the SRIM prediction of total pressure is within 5% of the experimental values. However, it might be a false positive and it should be investigated whether changes can be made to improve the SRIM.

Another issue found in the SRIM is the prediction of the pseudo-shock length. Since the SRIM is unable to account for asymmetry, the pseudo-shock length was underpredicted. Whilst pseudo-shock asymmetry does not affect total pressure ratio potential, for the experiments the pseudo-shock length underprediction resulted in SSI models with constant area ducts of insufficient lengths, possibly compromising a fraction of pressure ratio across the pseudo-shock. Further experimental campaigns should redesign the SSI models to account for this.

To enable further use of the SRIM, a factor of 0.95 will be applied to its results. This factor is based on the outcomes of this study and is not necessarily applicable to other cases. Therefore, if the SRIM with this correction factor is used in the design of a submerged supersonic intake, the resulting intake should be tested with experimental or computational research.

7

Performance study

To study the consequences of submerging a supersonic intake, the submerged intake should be compared to its non-submerged counterpart. As was shown in Chapter 2, losses will occur. For designers, it is paramount to know the magnitude of these losses, since they need to make a trade-off between the aerodynamic losses and operational gains involved with submerging the intake. This chapter will show the performance of the submerged supersonic intakes that were tested in the wind tunnel by comparing it to the experimental data collected and shown in Chapter 2. Their performance will also be given in the terms of dynamic range, or the scope of total pressure ratios that can be achieved by the intakes. An inviscid SSI will be adapted to be suitable for SRIM analysis. Then, a preliminary investigation into the net thrust losses of a submerged supersonic intake with respect to a regular intake will be done.

7.1. Experimental intake performance

This section will provide a comparison between the intake performance data gained from the experiments and the data published in literature, see Chapter 2. This will give an indication on how the submerged supersonic intakes perform compared to their regular counterparts.

Figure 7.1 shows the same figures on total pressure recovery performance as found in Chapter 2, with the collected experimental data and corresponding theoretical maxima for similar intake configurations. Here, the experimental results for the SSI wind tunnel tests is added in red for comparison. Next to that, the inviscid analysis of an optimal intake with the same number of shocks is provided. This gives an idea on how the intake relates to its inviscid potential.

A large difference in total pressure ratios between submerged intakes and their regular counterparts can be seen in Figure 7.1. For a Mach number of 2 the loss in total pressure recovery is upwards of 25% for the single shock intake. For the case of the single shock intake at $M = 2.5$, the performance is approximately equal to a regular intake at $M = 3$, which is explicable by the fact that the expansion angle of $\theta = 14^\circ$ accelerates the flow to a similar Mach number of $M = 3.12$.

From the experimental results of the double shock intake (Figure 7.1b) it can be seen that in terms of absolute values, the total pressure ratio of the double shock intake only varies slightly from the single shock intake, which is also shown in Table 7.1. The optimal inviscid performance for intakes of multiple oblique shocks is higher than that of a single oblique shock, as was shown in Chapter 2. For the double shock intake ($n = 3$) however, the difference between its theoretical maximum and actual performance is larger than for the single shock intake ($n = 2$). This is explained by the fact that the double shock SSI model was not designed according to the Oswatitsch routine. For the double shock intake, the flow deflection by the expansion was simply countered in two steps of equal flow deflection, which resulted in two oblique shocks of unequal strength. Remembering the Oswatitsch design routine, which requires all oblique shocks to be of equal strength, two shock waves with equal flow deflection angle is not the most efficient way of compression by oblique shocks. In the case of the single shock intake, there is only one oblique shock that compresses the flow, no solution for multiple oblique shocks of equal strengths can be found. Therefore the Oswatitsch design routine cannot, by definition, improve the efficiency of a single oblique shock system. Thus, in the single shock case, the difference between the inviscid submerged performance and the actual performance is made up only of the viscous effects in

the intake. In the double shock intake, however, the difference between inviscid potential and actual performance consists of the viscous losses and the losses due to an inefficient oblique shock system.

This means that in terms of intake efficiency, the tested SSI models are far from optimal, and therefore only serve to validate the SRIM. The next step in determining the feasibility of a submerged supersonic intake is determining its optimal viscous performance. One can design an optimal submerged supersonic intake using the Oswatitsch routine, and then determine its viscous performance using the SRIM, albeit with a correction factor based on the experimental results described in Chapter 6.

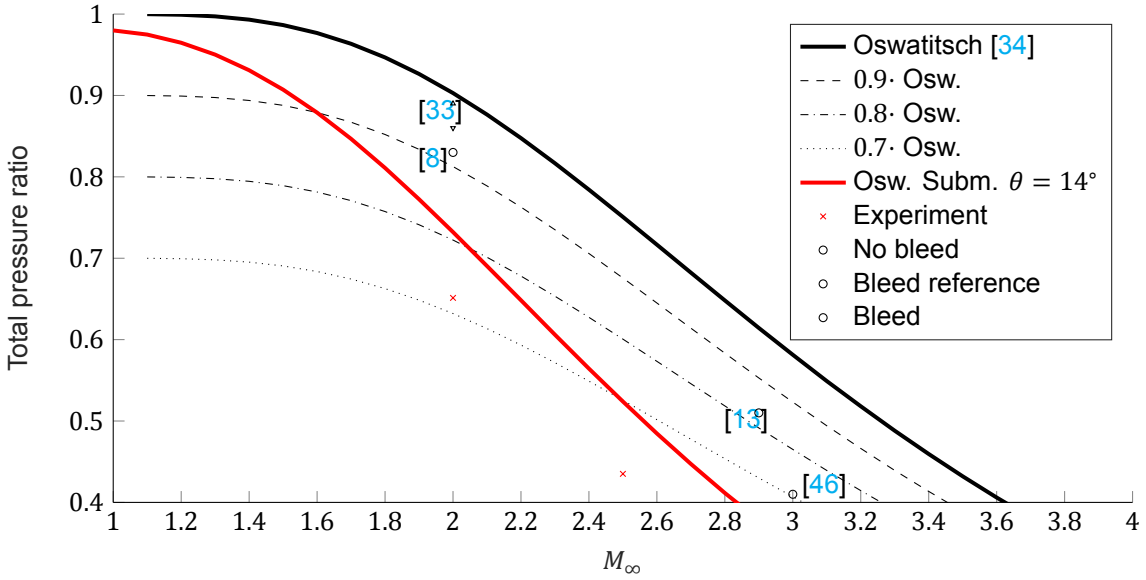

(a) $n = 2$

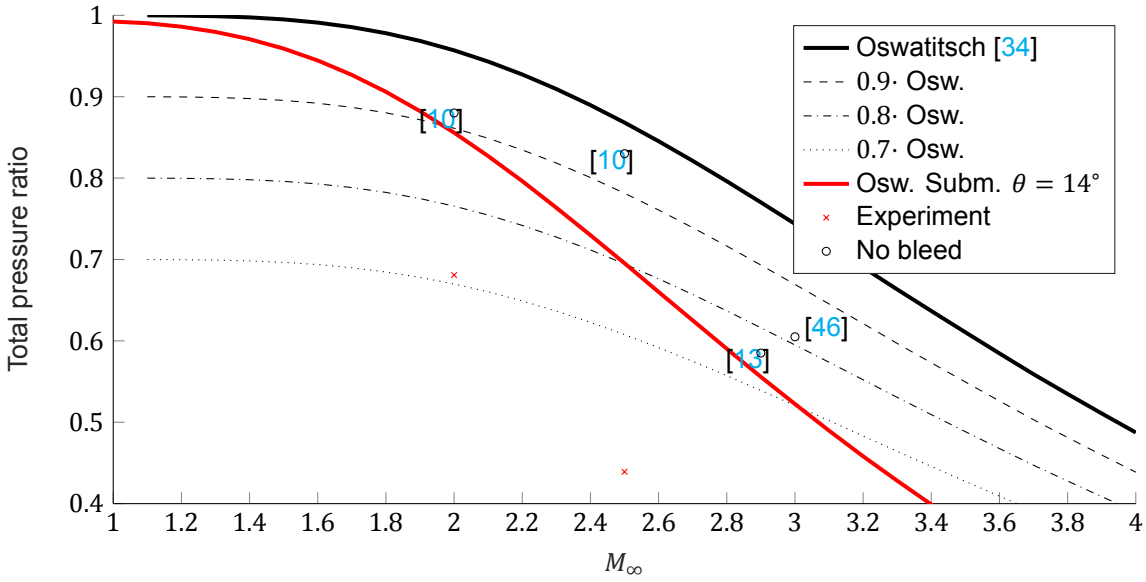

(b) $n = 3$

Figure 7.1: Total pressure ratios vs. Mach number of several experimental studies, an optimal inviscid submerged intake with a $14°$ expansion angle (red line), inviscid values for two-dimensional regualr intakes, and the submerged supersonic intake models tested in the ST-15 for two different numbers of shocks.

7.2. Dynamic Range

This section describes the dynamic range of the SSI models tested in the wind tunnel. The dynamic range was found by changing the valve position incrementally from the supercritical to critical condition,

Table 7.1: Total pressure ratios of all intake configurations

	$M = 2$	$M = 2.5$
Single shock ($n = 2$)	0.6513	0.4351
Double shock ($n = 3$)	0.6808	0.4391

and further until the intake is fully choked. Measuring the mass flow whilst doing this results in a graph similar to Figure 2.4. Since the valve in the SSI wind tunnel model represents the throttle in an actual ramjet engine, the dynamic range give insight in the upper and lower limits of the thrust a ramjet engine outfitted with a SSI will produce, in combination with combustion chamber performance. Note that this does not account for other phenomena, e.g. flame-out in the combustion chamber due to higher intake exit velocities in supercritical conditions.

Figure 7.2 shows the results for the dynamic range of the SSI models tested in the wind tunnel. The data was taken from the runs where the intake critical condition was found, and was unfortunately not available for the flow case of the single shock intake ($n = 2$) at $M = 2$, because the valve positions were not recorded. Note also, that no information is available for the subcritical region of the intake operating conditions. This is because the method of computing the mass flow in the intake depends on the assumption of supersonic flow at the entrance of the intake internal channel. For subcritical conditions, the terminal normal shock is expelled from the intake and turns the flow subsonic ahead of the internal channel. This means that no mass flow data is available for subcritical flow.

In Figure 7.2, the upper limits of the total pressure ratios are already known from earlier analysis, since in this figure it represents the critical condition. Therefore it might be of interest to look at the lower limits of the dynamic range. Comparing the double and single shock intake at Mach 2, thus a comparison based solely on geometric differences, it can be seen that the minimum total pressure ratio is lower for the case of the single shock intake ($n = 2$). This implies that from an intake perspective, the single shock intake can sustain lower thrusts outputs for the same ramjet engine. In terms of mass flow, it is seen that for intakes of the same geometry, in this case the double shock ($n = 3$), the higher Mach number intake has lower mass flow. This has to do with the leading edge shock angles being smaller, thus converting a smaller area into the oblique shock system and internal channel. The mass flow difference between the two flow cases with equal Mach number ($M = 2$) may be attributed to the fact that the extra shock in the double shock intake compresses the flow more than the single shock intake.

Unfortunately, it is impossible to acquire data on the dynamic range of submerged supersonic intakes from the SRIM, because of its shown inaccuracy in the supercritical condition. Therefore a comparison of this performance aspect has to be omitted from this report. Implementing the capability to study the dynamic range of an intake in the SRIM would definitely increase its usefulness.

7.3. Thrust losses due to submerging

In Section 2.3.1 the inviscid submergence losses in terms of intake total pressure ratio were shown for the Oswatitsch intakes. However, a more interesting comparison would be the losses of thrust coefficient in the entire ramjet engine due to submergence of the intake. This section will derive a method to adequately compare submerged and regular supersonic intakes in terms of their thrust coefficient.

To obtain a measure of the losses involved with submerging a supersonic air intake, the thrust coefficient will be computed for regular and submerged supersonic intakes. The losses in thrust coefficient as a consequence of submerging can be used to trade-off the aerodynamic losses with the operational gains. Intake data necessary for the comparison will be taken from the Oswatitsch design method, described in Section 2.3.1, for a submerged intake and a regular intake with the same free-stream conditions. This allows for a fair comparison, since both intakes are computed according to the same approach. The SRIM is not used in this comparison, since its accuracy is not undisputed, as was concluded in Chapter 6. Also, the SRIM has the potential for analysis of regular intakes, however, in its current state it would require significant adaptations to do so.

The equations of Wittenberg [45], as presented in Section 2.1.2, will be used to compute the thrust coefficients for both intakes. This procedure is rather trivial for a regular intake since Wittenberg's equations were derived for engines with such intakes. For a submerged intake, an additional step has to be made due to the influence of expansion on the intake, and thus on engine performance. In

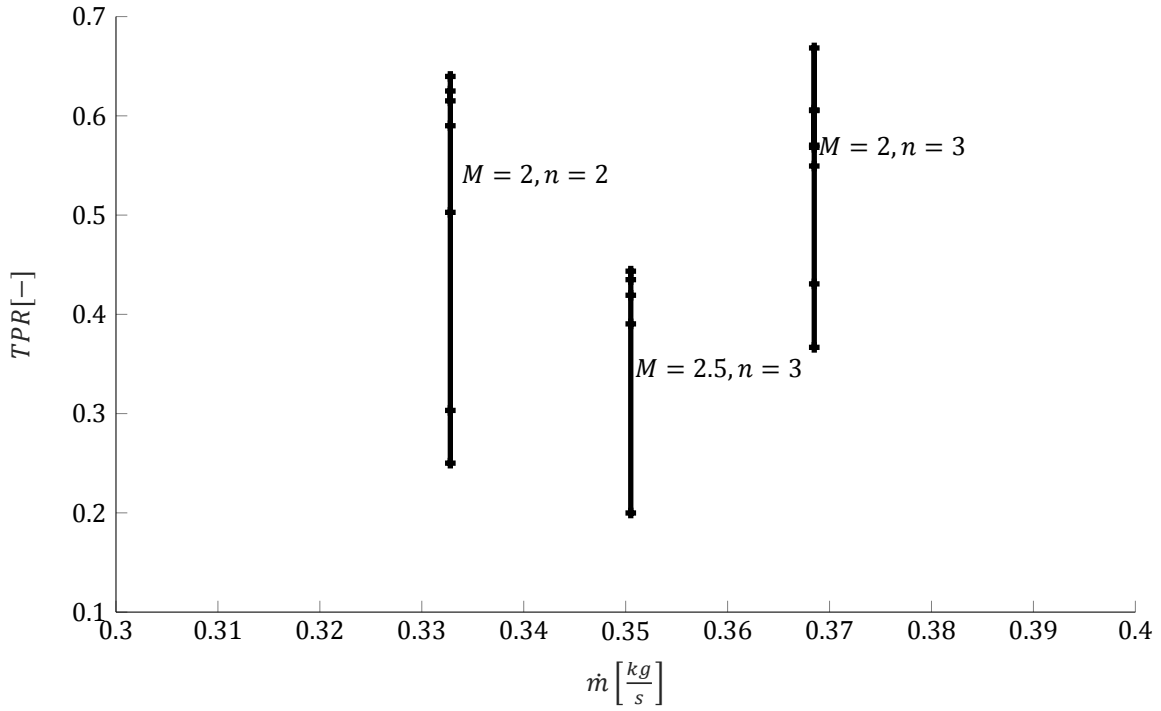

Figure 7.2: Dynamic range of experimentally tested SSI models from supercritical to the critical condition

addition to losses due to reduced efficiency of a submerged intake, the reduction of free-stream capture area due to expansion plays a role in the reduction of the thrust coefficient. A derivation to compute the capture area loss will be presented below. It will be seen that the reduction in capture area is directly dependent of free-stream Mach number and expansion angle.

Figure 7.3 shows definitions of stations and cross-sectional areas within the submerged intake which will be used in the coming derivations. Note that within the complete ramjet engine shown in the schematic in Figure 2.1, the intake is located between stations 1 and 2.

7.3.1. Streamtube area during expansion

When the streamtube that enters a submerged supersonic intake crosses the expansion its cross-sectional area increases. For a submerged intake, this results in a smaller free-stream capture area A_0 for an equal intake size compared to a regular intake. Since the smaller capture area results in a reduced mass flow into the engine, lower thrust is obtained, see equation 2.5.

The reduced capture area needs to be included in the thrust coefficient computations for submerged supersonic intakes. Noting the definitions given in figure 7.3, the derivation of the streamtube area ratio starts with the fact that the mass flow remains constant in the streamtube:

$$\dot{m}_0 = \dot{m}_{1a}$$
$$\rho_0 V_0 A_0 = \rho_{1a} V_{1a} A_{1a}$$

This equation can be rewritten to the ratio of streamtube areas before and after expansion. Note that the velocity can be expressed as the product of local Mach number and speed of sound.

$$\frac{A_0}{A_{1a}} = \frac{\rho_{1a} V 1a}{\rho_0 V_0} = \frac{M_{1a}\sqrt{\gamma R T_{1a}}}{M_0\sqrt{\gamma R T_0}}$$

The ratios of density and temperature across the expansion can be written as function of Mach number by isentropic flow relations

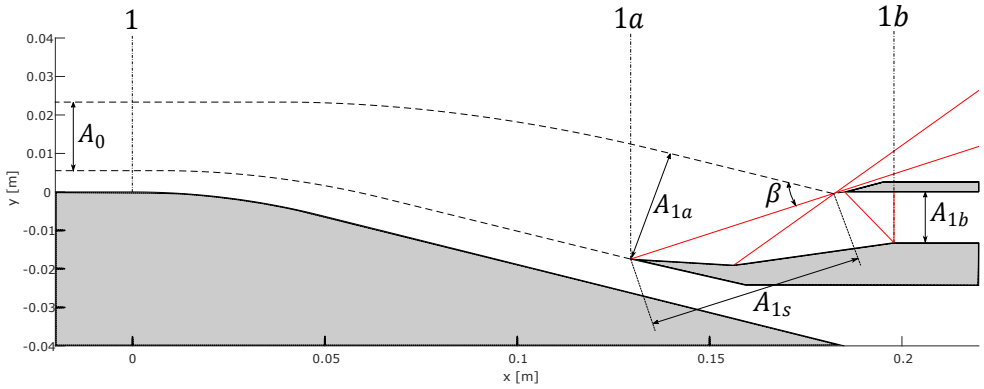

Figure 7.3: Schematic of a submerged supersonic intake with definitions of station numbers pre- and post-expansion and in the internal channel

$$\frac{A_0}{A_{1a}} = \left(\frac{1 + \frac{\gamma-1}{2} M_0^2}{1 + \frac{\gamma-1}{2} M_{1a}^2} \right)^{\frac{1}{\gamma-1}} \frac{M_{1a}}{M_0} \sqrt{\frac{1 + \frac{\gamma-1}{2} M_0^2}{1 + \frac{\gamma-1}{2} M_{1a}^2}}$$

Finally, combining yields

$$\frac{A_0}{A_{1a}} = \frac{M_{1a}}{M_0} \left(\frac{1 + \frac{\gamma-1}{2} M_0^2}{1 + \frac{\gamma-1}{2} M_{1a}^2} \right)^{\frac{\gamma+1}{2(\gamma-1)}} \tag{7.1}$$

It can be seen that the streamtube area ratio is only dependent of pre- and post-expansion Mach numbers and can therefore be easily derived from an inviscid Prandtl-Meyer expansion analysis (see Section 2.4). The results for the area ratio as a function of expansion angle are shown for multiple free-stream Mach numbers in Figure 7.4. It can be clearly seen that the expansion severely affects the free-stream capture area, which can result in thrust losses in the ramjet engine. This area ratio is obviously not applicable to regular intake since they lack an expansion section.

7.3.2. Thrust coefficient reference area adaptation

A well-designed supersonic intake changes the properties of a flow such that they are optimal for combustion at the end of the intake. This includes changing the area of the streamtube through the intake. The exact ratios of area at different stations throughout the intake depend on engine and design characteristics. In this study, submerging a supersonic intake affects area ratios across an intake in two ways. The first is the increase of streamtube area across expansion, as was explained in the previous section. The second is the fact that the Oswatitsch routine used to compute the intake characteristics designs a different intake geometries for submerged and regular intakes because of the higher Mach number behind expansion.

The Oswatitsch routine uses the area of the constant-area duct (A_{1b} in Figure 7.3) as a basis to derive the intake geometry. Because of the reasons stated above, this results in a completely different A_0 for submerged and regular supersonic intakes. To adequately compare the two and study the influence of submergence on the capture area, the thrust coefficients should be non-dimensionalized using the area of the constant-area duct, A_{1b}. This entails finding an area ratio between the free-stream and

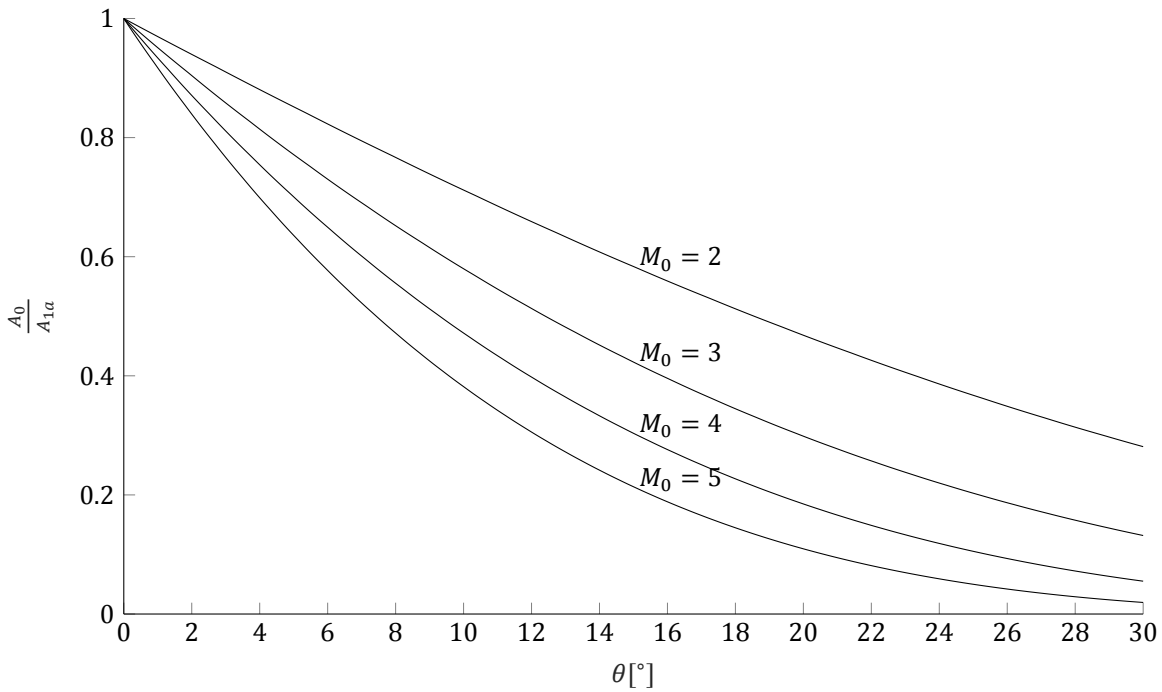

Figure 7.4: Ratio of pre- and post-expansion streamtube area as a function of expansion angle θ for varying free-stream Mach numbers

internal channel flow: $\frac{A_0}{A_{1b}}$, with which the thrust coefficients can be multiplied to change their reference areas, since

$$C_F = \frac{F_n}{q_0 A_0}\frac{A_0}{A_{1b}} = \frac{F_n}{q_0 A_{1b}} \tag{7.2}$$

Starting from the back of the intake and moving upstream, the first area ratio is inside the intake and is dependent on the intake geometry. In an inviscid case at design operating conditions, the length of the first shock will be the absolute distance between the leading edge of the cowling and compression surface. Multiplied by unit width this becomes the area of the first shock: A_{1s} (see also Figure 7.3). Since the cross-sectional area of the constant area duct (A_{1b}) is also known, the ratio of both terms will be $\frac{A_{1s}}{A_{1b}}$, which is easily obtained from intake geometry.

Then, the area ratio between the first shock area A_{1s} and the entering streamtube must be found. For a regular intake, these are already free-stream conditions, but in the submerged case, this is at station $1a$. Since the area of the streamtube is defined perpendicular to the flow, the ratio is obtained from the sine of the first shock angle, i.e. $\sin\beta$, which gives:

$$\begin{aligned}\left(\frac{A_0}{A_{1s}}\right)_r &= \sin\beta_r \\ \left(\frac{A_{1a}}{A_{1s}}\right)_s &= \sin\beta_s\end{aligned} \tag{7.3}$$

The area ratio through the entire intake is then easily obtained by multiplying all the ratios. For regular intakes:

$$\left(\frac{A_0}{A_{1b}}\right)_r = \frac{A_0}{A_{1s}}\frac{A_{1s}}{A_{1b}} = \frac{A_{1s}}{A_{1b}}\sin\beta \tag{7.4}$$

And for submerged intakes:

$$\left(\frac{A_0}{A_{1b}}\right)_s = \frac{A_0}{A_{1a}}\frac{A_{1a}}{A_{1s}}\frac{A_{1s}}{A_{1b}} = \frac{A_0}{A_{1a}}\frac{A_{1s}}{A_{1b}}\sin\beta \tag{7.5}$$

Where $\frac{A_0}{A_{1a}}$ as a function of Mach numbers pre- and post-expanions was already obtained in the previous section.

As shown in equation 7.2, the thrust coefficients as computed in Wittenbergs equations can be multiplied by these ratios to alter the reference area. This allows for better comparison between regular and submerged intakes.

7.3.3. Results of thrust coefficient comparison

Figure 7.5 shows the results of the investigation into the thrust losses in terms of the ratio of thrust coefficients of submerged and regular supersonic intakes. The dashed lines clearly imply that the losses due to submergence are rather limited. However, the dashed lines show the thrust coefficient non-dimensionalized with respect to the upstream capture area. Whilst it is a fair comparison, it fails to take into account the loss of capture area due to submergence. The solid line does account for the area correction by multiplying the thrust coefficients of both submerged and regular with the area ratio derived in the previous sections, to non-dimensionalize with the internal flow area of the constant-area duct. Applying this correction facilitates the comparison of submerged and regular intake performance based on similar volumetric flow into the engine, assuming the flow velocity in the constant-area duct is equal.

The data in Figure 7.5 shows that the inviscid thrust losses due to submergence predominantly lie with the reduced capture area, rather than losses in total pressure ratio. Some drawbacks come with this study, mainly the fact that it is based on inviscid theory. Any viscous losses in the intake are not taken into account, just like viscous losses and any other thermal effects in the engine. Also, for the efficiency of the combustion chamber and exhaust nozzle, two efficiencies were assumed, equal for both the submerged and regular case. Therefore, any effects emanating downstream from the intake into the engine are also not accounted for. Despite all this, the results of this study quantify the minimum losses involved with supersonic intake submergence and clearly indicate that they can be severe for high expansion angle at higher free-stream Mach numbers. The fact that the predominant part of the losses arises from the reduced capture area due to expansion suggest that if a submerged intake would be implemented, it would have to be relatively large compared to a regular counterpart. This means sufficient space should be allocated so that enough thrust can be produced by the engine.

This section has outlined a method to perform a simple inviscid study to compute the thrust coefficient losses and what the consequences of submergence are. It is up to the designers contemplating submerging a supersonic intake to decide whether operational gains of submergence outweigh the cost in vehicle space.

7.4. Design of a submerged intake following the Oswatitsch approach

One of the research questions asks if it is possible to design a submerged supersonic intake according to the theory developed by Oswatitsch. This section will explore those possibilities and implement them to a new SSI model that can be tested in the ST-15 with parts already available.

Section 2.3.1 describes the method by Oswatitsch [34] that determines the shock angles and Mach numbers in an oblique shock system that compresses inviscid flow optimally through $n-1$ shocks of equal strength. With known Mach numbers and shock angles per shock wave, the deflection angles can be determined. Then, assuming the external oblique shock waves impinge on the leading edge of the cowling, the length of each deflection surface can be determined with a simple geometric exercise. Naturally, this routine can be made submerged by taking the Mach number behind an expansion as the free-stream value.

A routine to compute such an inviscid Oswatitsch intake was developed and a resulting intake geometry can be found in Figure 7.6. Here the flow surfaces can be seen in black and the shocks are indicated in red. In this case, an intake with $n=4$ shocks, of which one internal and one terminal normal shock, was designed for a free-stream Mach number of 2.5. 4 shocks was determined to be a good compromise between intake efficiency and complexity. As a reference, in literature most ramjet intakes feature between two and four shocks.The internal shock reduces the total deflection angle of the intake, ensuring that it stays submerged. This inviscid intake has a total pressure ratio of approximately 0.8.

The intake designed using the Oswatitsch routine can be adapted for viscous analysis using the

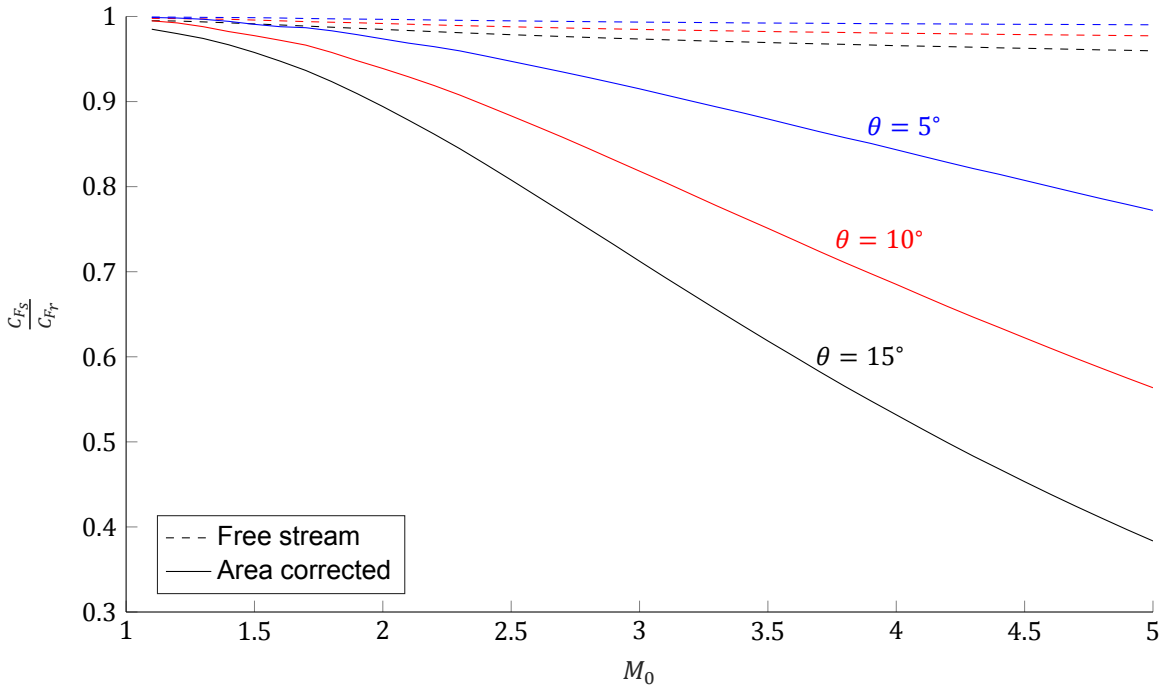

Figure 7.5: Results of the comparison between thrust coefficients submerged and regular supersonic intakes for various expansion angles and Mach numbers. The dashes line shows the ratio of thrust coefficients of submerged and regular supersonic intakes. The solid line shows those ratios including the capture area correction.

SRIM and made into an SSI wind tunnel model. Performing experiments with this wind tunnel model will result in more data to validate the SRIM with more complex intake geometries. However, the inviscid intake cannot be copied one to one into the SRIM and into a wind tunnel model, since some aerodynamic and operational limitations exist. These will be listed below.

- The inviscid intake features internal compression, and therefore the Kantrowitz limit (see Section 2.1.4) must be included in the design considerations. For this intake, the contraction ratio must be decreased in order for the intake to start without having to implement moving surfaces.
- The angle of the constant area duct is changed. This is necessary since the model must fit in the ST-15 test section whilst minimizing the blockage of flow above the intake.
- A constant area duct was added. In the current design it is based on the SRIM pseudo-shock length, which were shown to be too short in Section 6.5.2. Thus the constant area duct needs to be elongated in a next design iteration.
- A subsonic diffuser with the same half cone angle as the other SSI models was added aft of the constant area duct.

Figure 7.7 shows the geometry of the flow surfaces of the adapted intake. Preliminary CAD-drawings were also made by the author, these are shown in Appendix E. The pressure ratio of this intake is predicted by the SRIM to be 0.63, when accounted for the SRIM inaccuracy, this becomes 0.59. Compared to a regular supersonic intake with operating Mach number of 2.5 from experimental data, which has a total pressure ratio of approximately 0.85, this is significantly lower. However, it is an improvement over the single and double shock SSI tested in this experimental campaign, which came in at 0.43.

Next to designing a wind tunnel model that can be tested in future work, this section shows that an SSI geometry based on the Oswatitsch routine can be adapted to be analyzed by the SRIM. The intake in Figure 7.7 was adapted from an inviscid intake predominantly based on practical considerations, but it shows that an intake adapted based on viscous optimization can also be analyzed by the SRIM. This is useful for engineers looking to optimize submerged supersonic intake performance, since it provides

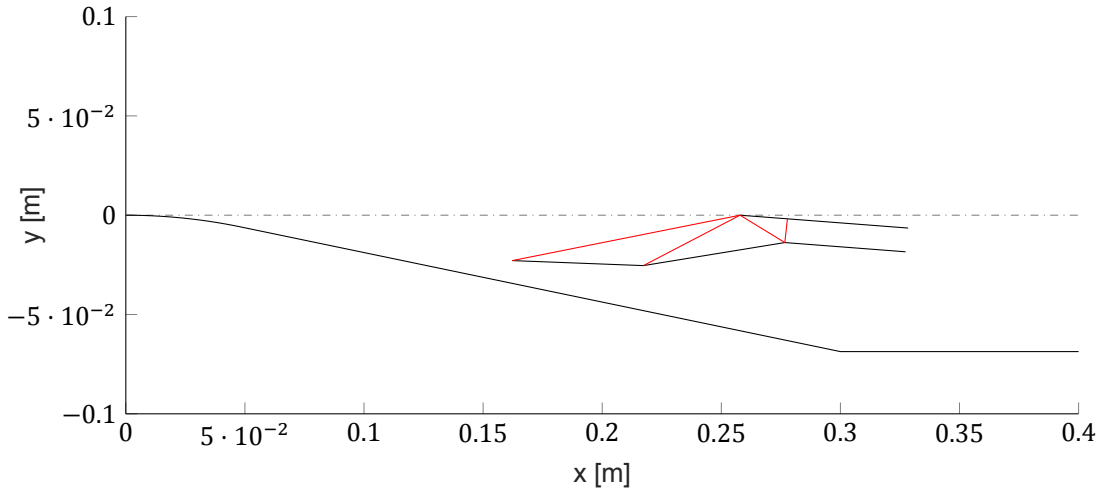

Figure 7.6: Submerged supersonic intake with 4 shocks, designed using the inviscid Oswatitsch routine. Its flow surfaces are shown in black and the shocks in red.

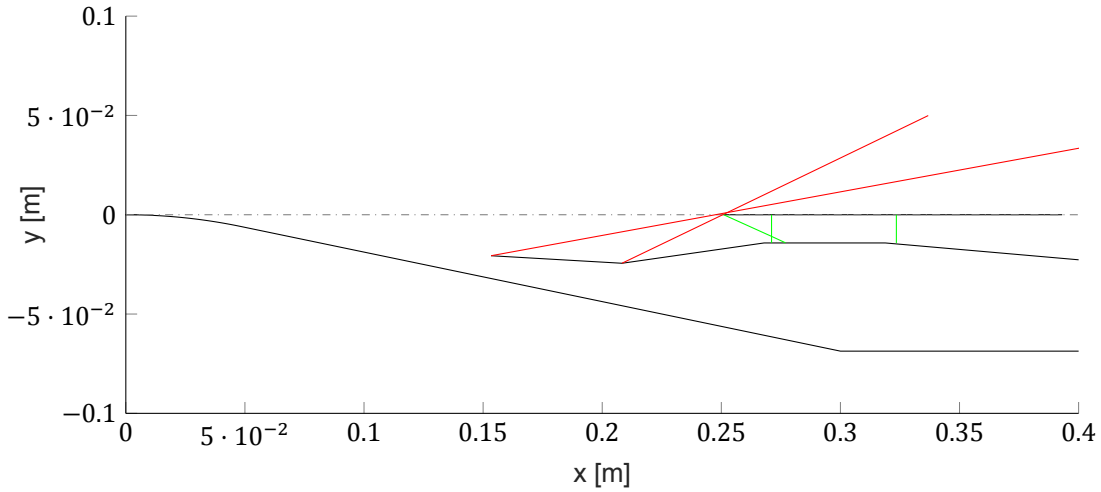

Figure 7.7: Viscous adaptation to the inviscid Oswatitsch intake with 4 shocks. Its flow surfaces are shown in black, shock waves as calculated by the SRIM in red (external shock) and green (internal shock).

them with an inviscid starting point, which can be adapted and optimized towards more complex viscous flows.

8

Conclusions

Looking back at the research objectives posed in Chapter 1, it can be said that all of these objectives were achieved. How successful the research objectives were reached can be determined by answering the research questions. This chapter will try to answer the research questions by relaying and combining the information given in earlier chapters. It will do so in three sections, one for each main research question. Then it will return to the design problem described in Chapter 1 to see whether these conclusions have brought any insight in the upper limits of submerged supersonic intake operational capabilities.

8.1. Flow behavior in a submerged supersonic intake

Starting with the experimental set-up, it was decided that a combination of static pressure measurements, Particle Image Velocimetry and schlieren photography would give sufficient information about the qualitative and quantitative aspects of the flow in a submerged supersonic intake. Using the static pressure measurements combined with the velocity from PIV, the total pressure, one of the most important intake performance aspects, could be determined throughout the intake. Another important supersonic intake aspect, mass flow, could also be derived from this measurement data. The experiments were to be performed at three available Mach numbers of 2, 2.5 and 3 at the ST-15 wind tunnel in the High Speed Laboratory at Delft University of Technology.

To spot any interference between the two distinct parts of the submerged supersonic intake, the expansion section and the intake itself, the experiments were divided into two slots. First, the expansion section alone was tested, which has a less complex flow structure around it.

During the expansion section experiments, it was learned that due to the extra expansion in the test section of the ST-15, no flow beyond the Mach number of 2.5 would be achievable. The extra expansion required higher settling chamber pressures than usual, and the settling chamber pressure required to achieve a Mach number flow of 3 was beyond the capabilities of the ST-15.

During the PIV measurements, it turned out that any flow beyond Mach 2 required settling chamber pressures outside the PIV-seeder limits, and therefore PIV was unavailable for flows of Mach numbers exceeding 2. Even with Mach numbers of only 2, seeding was an issue close to the expansion flow surface resulting in questionable PIV results. The decision was made to cancel the PIV measurements for the next experiments.

Due to the fact that no velocity data was obtained from PIV measurements, another method to acquire knowledge about the velocity in the submerged supersonic intake was required. The solution was found in the reflecting shock waves in the intake at supercritical condition. With the assumption that these shock waves are very weak, their Mach angle can be used to determine the local Mach number. With additional available data, i.e. static pressure, total temperature and local cross-sectional area, the mass flow in the internal channel in supercritical condition could be determined. Assuming that in the critical condition, the intake does not yet spill flow, the mass flow into the internal channel is equal for the critical and supercritical condition. Using this assumption the mass flow through the entire intake in critical condition is known, which enables computation of flow velocity and total pressure at locations where static pressure is known. Applying an error study of linearized error propagation on

the method described above resulted in errors smaller than 0.5% for total pressure. However, it is likely that additional errors exist in the total pressure correction method due to flow unsteadiness that are impossible to derive from the available data.

Returning to the research question and subquestions this section sought to answer, the relevant flow phenomena (i.e. the expansion section, oblique shock system and pseudo-shock) have been visualized successfully using schlieren photography. Despite the absence of flow velocity data due to the issues with PIV-measurements, the necessary quantitative flow data was nevertheless obtained. Using a method to compute the internal mass flow from available data the Mach number and total pressure at the intake exit could be obtained. Finally, by measuring only the expansion section separate from the rest of the intake, the flow field around the entrance of the submerged supersonic intake could be seen to retrace any anomalies that may occur, such as the curved leading edge shock. This will be discussed in the next section.

8.2. SRIM validation and improvements

Whilst the results of the experiments indicated that the SRIM is accurate within a 5% difference from the experimental results in terms of total pressure ratio, and accuracy within the experimental error of 3% for the mass flow, room for improvement always exists.

On of the discrepancies between the SRIM and the experiments was the slightly curved leading edge shock on the SSI model compression surface. The cause of this may be that the expansion surface imposes a slight velocity gradient that is not predicted by the SRIM. Else, a slight bluntness of $0.1mm$ is found on the leading edge of the compression surface, which might cause the shock to detach. Another possible source is three-dimensional effects around the SSI model. If this is the case, it is hard to prove since no three-dimensional measurements were made. It is also difficult to correct for three-dimensional effects, since the SRIM is based on two-dimensional flow. The question of whether the curved leading edge shock is caused by an expansion velocity gradient or three-dimensional effects should be answered in future experiments.

The SRIM mass flow predictions were seen to be very accurate, the differences with the experimental results being withing 3%, when calculated at the start of the internal channel. However, when the mass flow was computed using SRIM values from the supercritical condition further downstream in the channel, the accuracy quickly deteriorated because the mass flow seemed to increase, for both an inviscid and viscous SRIM prediction of mass flow.

Next to the mass flow, the experimental Mach number in the supercritical internal flow was seen to be significantly lower than the SRIM prediction. In addition, the only mode of compression in the SRIM flow was the weak reflecting shocks, whilst it could be expected that the Mach number would also continuously reduce due to viscous effects in the internal channel. The perceived negligence of viscosity and the inaccuracy in mass flow in the internal channel prompted an investigation into the viscous effects in the prediction of the SRIM supercritical condition. Using Fanno flow as a reference it was found that due to an error in the method of interaction between the sub-models the SRIM erroneously neglects viscous effects in the internal channel.

Fortunately, the SRIM error only extends to the flow in the internal channel in supercritical condition. Since at the start of the internal channel inviscid terms dominate the flow field, the error remains of limited influence. E.g., the mass flow at the beginning of the internal channel is accurate and suffices for further computations. Especially since the critical condition calculation, which is of interest, uses the mass flow prediction at the start of the internal channel. Therefore, the SRIM predictions for critical flow still remain accurate, however, their performance should be thoroughly checked.

The several inconsistencies in flow patterns between the SRIM and experimental results in the oblique shock system cause the total pressure at the start of the internal channel, as computed using experimental data from supercritical condition, to be lower than predicted in the SRIM. However, after the pseudo-shock for the critical condition, the total pressure ratio deviates only 5% from the SRIM prediction. It was shown that this is most likely caused by the fact that the predicted pseudo-shock is less efficient for the higher Mach number, and therefore corrects most of the difference that existed at the start of the internal channel.

Whilst the accuracy of the two most important intake characteristics, total pressure ratio and mass flow, is good in the tested cases, this may be a false positive. Two things can be done to verify the validity of the results. The first is to improve the SRIM to take into account the flow phenomena that

were measured, and to correct the erroneous supercritical flow computation. The second is to repeat and extend the experiments with other intake configurations to gain a bigger dataset to base the SRIM validity on.

Returning to the second research question: the differences in qualitative and quantitative aspects of the flow have been discussed, as well as the origins of the discrepancies. This led to some suggested improvements, both for future experiments and in the Submerged Ramjet Intake Model. These recommendations are listed in the next chapter. Whilst room for improvement always exists, a judgment call must be made based on the current work. It was found that for the flow cases tested in this experimental campaign, the accuracy lies at 95%. Therefore, it is advised that in using the SRIM for analysis or optimization, a factor of 0.95 is implemented to its total pressure ratio outputs. The mass flow outputs seemed to be accurate, so correction factor is needed.

8.3. Submerged supersonic intake performance

This section will treat the research question and subquestions involved with submerged supersonic intake performance. As an alternative to regular supersonic intakes, submerged supersonic intakes lose some efficiency due to the supersonic expansion the flow into the intake must cross.

The inviscid approach of Oswatitsch to compute the shock angles of an optimal oblique shock system for a given number of shocks and upstream and downstream Mach number was used in studies to compute intake losses due to submergence. Using a reverse computational method and simple geometric study it was adapted to a method to design an optimal inviscid intake geometry. These optimal intake geometries were also used in the SRIM and gave relatively good results, with total pressure ratio losses of approximately 30% compared to a regular supersonic intake.

As was seen in Chapter 2, an inviscid study into the optimal Oswatitsch intake showed that the losses involved in the maximum attainable total pressure ratios depend on expansion angle and free-stream Mach number. For higher Mach numbers and expansion angles, the total pressure losses compared to regular supersonic intakes can be quite severe.

Submerging of a supersonic intake can invoke large losses on the performance of the intake itself. However, the intake is only a single part of a complete ramjet engine. Therefore, a more interesting comparison in terms of performance lies in the thrust coefficient of the entire ramjet engine. An inviscid study was done to compute the thrust coefficients of both a regular and submerged supersonic intake, with intake performance based on the Oswatitsch approach. For the combustion chamber and exhaust nozzle efficiencies the same values were assumed for both types of intake. The difference in thrust coefficients non-dimensionalized on free-stream properties turned out to be quite limited. However, due to the expansion section, the capture area for submerged intakes reduces significantly with increasing expansion angle and Mach number. What follows is that for the same free-stream capture area, a submerged intake must be much larger. To correct for this, the thrust coefficient was non-dimensionalized with respect to a quantity more representative of intake size: the internal duct area. The result of the capture area correction was significant, reducing the thrust coefficient for submerged supersonic intake significantly with increasing expansion angle and Mach number.

8.4. Finding the upper operational limits of submerged supersonic intakes

Looking back at the two methods to find the operational limits of submerged supersonic intakes, both have been treated by this report. The first way, an inviscid study into the maximum attainable efficiencies and engine performance, is suitable for early design stages. For this method, two different inviscid studies have been done, both based on the Oswatitsch [34] optimization routine. The results are:

- a method to determine the inviscid losses and geometry of an optimal submerged supersonic intake
- a method to determine the thrust coefficient of a submerged supersonic intake and compare it with a regular supersonic intake optimized for equal free-stream conditions.

These two methods provide designers with the ability to easily assess the feasibility of a submerged intake compared to a regular intake for the early stages of projectile design.

The second method proposed to find the upper limits to submerged supersonic intake performance involves current day optimization techniques. Now that it is validated, albeit with a correction factor, the Submerged Ramjet Intake Model, which is computationally inexpensive due to its analytical nature, can be used in optimization schemes to provide optimized intake geometries based on specific design requirements. This enables engineers to investigate the feasibility of integrating submerged supersonic intakes in their ramjet engine designs in later stages of the design process.

9 Recommendations

Based on lessons learned during experiments, data processing and writing of this report, several recommendations can be made to improve the Submerged Ramjet Intake Model and perfect future experiments to be conducted with the submerged supersonic intake wind tunnel model. These improvements could serve to further validate the SRIM and verify some uncertainties left by this report. This chapter will be separated into a section on recommendations regarding future experiments and a section on improvements to the SRIM that have been revealed by this work.

9.1. Recommendations for future experiments

Since some uncertainties about the SRIM accuracy still remain it is advisable to perform more experiments in the future. A more complicated submerged intake, based on the Oswatitsch design routine was already designed, see Section 7.4. This should be tested to verify the SRIM accuracy for more complicated intake geometries. Some other recommendations can be made for the original single- and double shock intake, these are listed in the following sections.

9.1.1. Increase bleed slot width to investigate the curved leading edge shock

As was seen in Section 6.1.1 the leading edge in the SSI model shows a slight curve close to the surface for all experimental cases. Several causes have been suggested, namely a velocity gradient existing perpendicular to the expansion surface or three-dimensional effects in the intake. Unfortunately, the available data could not give a decisive judgment on the underlying phenomenon. Since a velocity gradient would most likely only exist close to the expansion surface, its existence can be verified by increasing the bleed slot width in the SSI model. If the curved leading edge shock subsequently disappears, it was caused by a velocity gradient on the expansion section. If the curvature in the leading edge shock remains, the leading edge bluntness may be a cause, which can be verified by using SSI model parts with a sharper leading edge. Otherwise, most likely three-dimensional effects play a role around the SSI model. These effects would be hard to compute, since the SRIM is based on two-dimensional methods. However, with sufficient experimental data, an empirical correction may be applied.

In the SSI wind tunnel model the ability to increase the bleed slot width already exists. In the submerged intake support slots are present to which the pylon and compression surface parts are attached. The slot extend downstream thus the entire intake can easily be moved to increase bleed slot width. The maximum downstream displacement allowed by the slots in the SSI support is $2cm$, using the maximum should eliminate all boundary layer interference.

9.1.2. Increase constant area duct length

Several aspects of SRIM validation fell short because the pseudo-shock was not able to fully develop within the bounds of the constant area duct, which was seen from the absence of peak pressures in the static pressure data in Section 6.6.1. Because the pseudo-shock was cut off short, its final static and total pressure recoveries could not be determined as well as its total length, despite the obvious fact that it was longer than predicted. The underestimation of the pseudo-shock length was caused

by the pseudo-shock asymmetry, which was not predicted by the SRIM due to limitations in one of its sub-models.

In future experiments, it is advised to increase the length of the constant area duct of the SSI model, so that the actual length of the pseudo-shock can be found, along with the flow properties there. Alternatively to increasing the constant area duct length, a bleed slot can be implemented in the internal channel to reduce the pseudo-shock asymmetry and therefore its length. Implementing the latter solution also has the added benefit of the ability to investigate the effects of boundary layer bleed in submerged supersonic intakes.

9.1.3. PIV-measurements

The decision to omit PIV-measurements for this experimental campaign had extensive consequences in the further work. An elaborate method based on far-reaching assumptions had to be devised to obtain information about flow velocity in the intake, instead of using PIV-velocity fields. Whilst acceptable results came out in the end, assumptions and additional computations give rise to error and uncertainties. PIV results are not without uncertainty themselves, but they would have given greater insight in the flow in and around the SSI model.

However, PIV-measurements are in no way trivial, especially for the SSI wind tunnel model. As was seen in Section 6.1, seeding is an issue with the expansion surface ahead of the SSI model. This gives rise to the need for high density seeding, to counteract the seeding lost during expansion. For the high settling chamber pressures seen in these experiments, a high performance seeder is required.

Next to seeding issues, the SSI model also needs laser sheet access in the internal channel. During the wind tunnel model design, this was taken into account by implementing an asymmetric choke valve with a slit where the laser sheet would enter the intake, see Section 3.3.2. However, during testing it was found that the valve control servo was of insufficient strength to counter the forces involved with the asymmetric loading on the asymmetric valve. Therefore the original valve was replaced with a butterfly valve requiring less servo strength due to its more symmetric loading. To enable PIV-measurements, the original asymmetric valve needs to be used, which requires a stronger servo than the one used in these experiments.

9.1.4. Wind tunnel model limitations

As was mentioned in Section 6.1, the second shock in the oblique shock system of the double shock intakes was not very well defined, being closer to a compression fan than an actual shock wave. Next to that, a bluntness on the leading edge of the compression surface and cowling parts existed, which may have resulted in detached leading edge shock waves. The origin of these discrepancies lies in the fact that in the double shock compression surface part, the deflection that causes the second shock is not instantaneous. Naturally, this will never be the case in practice due to limitations in manufacturing, however, higher precision tooling might improve the accuracy of the double shock SSI model. Alternatively, the SRIM can be adapted to be able to compute curved compression surface with very high radii of curvature.

9.2. Improvements to the Submerged Ramjet Intake Model

It was seen that an error exists in the interaction of the SRIM sub-models in the supercritical internal channel flow. Removing that error is essential to improving the SRIM predictions. Going back to the description of the error in the SRIM, in Section 6.4, a quick improvement is ensuring that the boundary layer displacement thickness in each flow block is added on both sides of the MoC computation. However, this fix will most likely not improve the SRIM much, since it will not change the fact that due to the triangular shape of each flow computation block information of only one channel wall is taken into account. The nature of the flow in the internal channel in supercritical condition is such that it is very hard to compute analytically, due to the presence of shock waves. Available methods, e.g. the MoC or steady one-dimensional viscous flow, break down when crossing a shock wave or simply assume that none are present. No recommendation of a computational method to combine the steady internal channel flow and the reflecting shock waves can be made at this point. However, the reflecting shocks are very weak and are of negligible influence on the total pressure. Therefore, an integral internal channel method based on Fanno flow may at least provide information about the total pressure aft of the internal channel in supercritical condition.

The length of the pseudo-shock was predicted incorrectly in the SRIM. The origin of this SRIM inaccuracy lies with the fact that the pseudo-shock subroutine, the Modified Diffusion Model, was derived based on symmetrical pseudo-shocks. As was seen, asymmetry in a pseudo-shock influences its length, but not its pressure ratio. Therefore it is advised to extend the SRIM by adding an asymmetry correction for the pseudo-shock sub-model, that adjusts the length according to a measure of asymmetry. Another solution, as was stated in the previous section also, is implementing a boundary layer bleed in the internal channel. This can be done in the SRIM just as in the SSI wind tunnel model to enhance the SRIM with the capability to investigate the effects of boundary layer bleeds.

Bibliography

[1] https://www.mbda-systems.com/product/meteor/, Accessed on 28-05-2019.

[2] https://defpost.com/nammo-introduces-new-ramjet-powered-155-mm-artillery-ammunition-concept/, Accessed on 28-05-2019.

[3] . https://en.wikipedia.org/wiki/Sabot, Accessed on 28-05-2019.

[4] . http://vatsrohit.blogspot.com/2013/11/indian-tank-ammunition-scenario-ke.html, Accessed on 28-05-2019.

[5] John D. Anderson. *Fundamentals of Aerodynamics*. McGraw-Hill, fifth edition, 2011.

[6] P. Bakker and B. van Leer. Lecture notes on gasdynamics. Delft University of Technology, feb 2005.

[7] Sally Bane. Lecture on shadowgraph and schlieren techniques, feb 2010. URL https://www.slideserve.com/calvin/shadowgraph-and-schlieren-techniques.

[8] Robert C. Campbell. Performance of a supersonic ramp inlet with internal boundary-layer scoop. Research memorandum RM E54I01, NACA, nov 1954.

[9] C.B. Cohen and E. Reshotko. The compressible laminar boundary layer with heat transfer and arbitrary pressure gradient. Technical report 1294, NACA, 1956.

[10] Raymond J. Comenzo. Preliminary investigation of the pressure recovery of several two-dimensional supersonic inlets at a mach number of 2.01. Research Memorandum RM L54D14, NACA, jun 1954.

[11] James F. Connors and Rudolf C. Meyer. Design criteria for axisymmetric and two-dimensional supersonic inlets and exits. Technical report, NACA, 1956.

[12] R.J. Cresci and P.K. Sasman. Compressible turbulent boundary layer with pressure gradient and heat transfer. *AIAA Journal*, 4(1):19–25, 1966.

[13] R.A. Dutton and E.L. Goldsmith. Some characteristics of rectangular multi-shock and isentropic external compression intakes at a mach number of 2.9. Current Paper 630, Aeronautical Research Council, sep 1961.

[14] Antonio Ferri and Louis M. Nucci. The origin of aerodynamic instability of supersonic inlets at subcritical conditions. Research Memorandum RM L50K30, NACA, jan 1951.

[15] R.H.M. Giepman, F.F.J. Schrijer, and B.W. van Oudheusden. High□resolution PIV measurements of a transitional shock wave–boundary layer interaction. *Experiments in Fluids*, 56(113), 2015.

[16] H. Fred Goelzer and Jr. Edgar M. Cortright. Investigation at mach number of 1.88 of half of a conical spike diffuser mounted as a side inlet with boundary layer control. Research memorandum RM E51G06, NACA, sep 1951.

[17] I. Greber, R.J. Hakkinen, and L. Trilling. Laminar boundary layer oblique shock wave interaction on flat and curved plates. *Zeitschrift für Angewandte Mathematik und Physik*, 9b:312–331, 1958.

[18] J.E. Green. Interactions between shock waves and turbulent boundary layers. *Progress in Aerospace Sciences*, 11:235–260, 1970.

[19] I.M. Hall. Inversion of the prandtl-meyer relation. *The Aeronautical Journal*, 79(777):417–418, 1975.

[20] T.T. Hartley, R. Brandis, and F. Mossayvbi. Exact and approximate solutions to the oblique shock equations for real-time applications. Contractor Report 187173, NASA, 1991.

[21] T. Ikui, K. Matsuo, and K. Sasaguchi. Modified diffusion model of pseudo-shock waves considering upstream boundary layers. *Bulletin of the JSME*, 24(197):1920 – 1927, 1981.

[22] Arthur Kantrowitz and Coleman duP. Donaldson. Preliminary investigation of supersonic diffusers. Advance Confidential Report L5D20, NACA, may 1945. Wartime report.

[23] E. Katzer. On the lengthscales of laminar shock/boundary-layer interaction. *Journal of Fluid Mechanics*, 206:477–496, 1989.

[24] N.F. Krasnov. *Aerodynamics of Bodies of Revolution*. American Elsevier Publishing Company, 1970.

[25] H.W. Liepmann, A. Roshko, and S. Dwahan. On reflection of shock waves from boundary layer. Technical Note 2334, NACA, apr 1951.

[26] John J. Mahoney. *Inlets for Supersonic Missiles*. AIAA, 1991.

[27] K. Matsuo, Y. Miyazato, and H-D. Kim. Shock train and pseudo-shock phenomena in internal gas flow. *Progress in Aerospace Sciences*, 35(1):33–100, 1999.

[28] MBDA. Meteor BVRAAM Data Sheet, 2017.

[29] G. H. McLafferty, E.L. Krasnoff, E.D. Ranard, W.G. Rose, and R.D. Vergara. Investigation of turbojet inlet design parameters. Report R-0790-13, United Aircraft Corporation, dec 1955.

[30] W.D. McNally. Fortran program for calculating compressible laminar and turbulent boundary layers in arbitrary pressure gradients. Technical note D-5681, NASA, 1970.

[31] M.C. Neale and P.S. Lamb. Tests with a variable ramp intake having combined external/internal compression and a design mach number of 2.2. Current Papers 805, Aeronautical Research Council, 1965.

[32] C. Nebbeling and W.J. Bannink. Enige visuele waarnemingen van de stroming in een twee-dimensionale inlaat met uitwendige compressie, ontworpen voor een getal van mach van 2,94. Memorandum M151, TH Delft, aug 1969.

[33] Leonard J. Obery and Robert W. Cubbison. Effectiveness of boundary-layer removal near throat of ramp-type side inlet at free-stream mach number of 2.0. Research Memorandum RM E54I14, NACA, nov 1954.

[34] Kl. Oswatitsch. Pressure recovery for missiles with reaction propulsion at high supersonic speeds (the efficiency of shock diffusers). Technical Memorandum 1140, NACA, 1947.

[35] B.U. Reinhartz, C.D. Hermann, J. Ballmann, and W.W. Koschel. Aerodynamic performance analysis of a hypersonic inlet isolator using computation and experiment. *Journal of Propulsion and Power*, 19(5):868–875, 2003.

[36] E. Reshotko and M. Tucker. Approximate calculation of the compressible turbulent boundary layer with heat transfer and arbitrary pressure gradient. Technical Note 4154, NACA, 1957.

[37] D. P. Rizzetta, O. R. Burggraf, and R. Jenson. Triple-deck solutions for viscous supersonic and hypersonic flow past corners. *Journal of Fluid Mechanics*, 89(3):535–552, 1978.

[38] J. Seddon and E.L. Goldsmith. *Intake Aerodynamics*. AIAA, 1985.

[39] John W. Slater. Design and analysis tool for external-compression supersonic inlets. Technical Memorandum NASA/TM-2012-217660, NASA, 2012.

[40] L.J. Souverein, P.G. Bakker, and P. Dupont. A scaling analysis for turbulent shock-wave/boundary-layer interactions. *Journal of Fluid Mechanics*, 714:505–535, 2013.

[41] E. van Wijk. Submerged Ramjet Intake Modelling. Master's thesis, Delft University of Technology, dec 2017.

[42] R.G. Veraar. A calculation method for off-design performance prediction of a supersonic axi-symmetric two-shock inlet. TNO-report PML-1994-A85, apr 1995.

[43] Cheng-Peng Wang, Kun-Yuan Zhang, and Ke-Ming Cheng. Pressure distribution measurements in scramjet isolators under asymmetric supersonic flow. In *44th AIAA Aerospace Sciences Meeting and Exhibit*, jan 2006.

[44] M.E.N. Wisse. *An Asymptotic Analysis of Compressible Base Flow and the Implementation into Linear Plug Nozzles*. PhD thesis, Delft University of Technology, jun 2005.

[45] H. Wittenberg. *Some Fundamentals on the Performance of Ramjets with Subsonic and Supersonic Combustion*. TNO Prins Maurits Laboratory, 2000.

[46] Richard R. Woollett and James F. Connors. Zero angle-of-attack performance of two-dimensional inlets near mach number 3. Research Memorandum E555K01, NACA, feb 1956.

A

Error propagation study

This appendix will show the steps taken in the study of error propagation through the total pressure computation method. As derived in Section 5.3, the method uses the following equations to obtain the total pressure in the submerged supersonic intake. First, the mass flow in the supercritical condition is obtained through

$$\dot{m}_{sc} = p_{sc} A_{cad} M_{sc} \sqrt{\gamma \left(\frac{1 + \frac{\gamma-1}{2} M_{sc}^2}{RT_t} \right)}. \tag{A.1}$$

Here, the Mach number in the supercritical condition is deduced from the shock angles obtained from schlieren images using the well-known equation

$$M_{sc} = \frac{1}{sin(\mu)}. \tag{A.2}$$

Then, since it was assumed that the supercritical condition mass flow equals the critical condition mass flow, all information is known to obtain the Mach number at any point in the critical internal channel where the static pressure is known, by

$$M_v = \sqrt{\frac{-p_v^2 A_v^2 \gamma \pm \sqrt{\left(p_v^2 A_v^2 \gamma\right)^2 - 4\left(p_v^2 A_v^2 \frac{\gamma(\gamma-1)}{2}\right)\left(-\dot{m}_{sc}^2 R T_t\right)}}{2\left(p_v^2 A_v^2 \frac{\gamma(\gamma-1)}{2}\right)}}. \tag{A.3}$$

With the Mach number and the static pressure known, computing the total pressure is trivial through the isentropic flow relation of

$$\frac{p_t}{p_v} = \left(1 + \frac{\gamma - 1}{2} M^2\right)^{\frac{\gamma}{\gamma-1}}. \tag{A.4}$$

To compute the error in the total pressure due to the error in measurements, and specifically the error in the shock angles (μ), which were proven to be the largest source of error, relatively, the derivatives of these equations w.r.t. all their variables must be taken. WolframAlpha was used to obtain these derivatives. To illustrate the error propagating through the equations, values of the same example case as in Section 5.4 are added to the equations. As mentioned in Section 5.5.3, the error in shock angle $\varepsilon_\mu = 1° = 1.75\text{e}{-2} rad$, the error in all pressure measurements is $\varepsilon_p = 0.02 mbar$ and the error in total temperature measurement is $\varepsilon_{T_t} = 0.1K$. The dependencies are obtained by evaluating them at the relevant values for their parameters. Then, assuming the error is small and each dependency behaves linearly on the small domain, the propagation of the error is obtained.

Starting with equation A.2, which has only one variable:

$$\frac{\partial M_{sc}}{\partial \mu} = \frac{\partial}{\partial \mu}\left(\frac{1}{\sin(\mu)}\right) = \frac{-\cos\mu}{\sin^2\mu} = -2.43 rad^{-1} \tag{A.5}$$

Equation A.1 has variables M_{sc}, T_t and p_{sc}. The derivatives are

$$\frac{\partial \dot{m}_{sc}}{\partial M_{sc}} = \frac{\partial}{\partial M_{sc}}\left(p_{sc} A M_{sc}\sqrt{\gamma\left(\frac{1+\frac{\gamma-1}{2}M_{sc}^2}{RT_t}\right)}\right) = p_{sc} A\gamma \frac{1+2\frac{\gamma-1}{2}M_{sc}^2}{\sqrt{\gamma R T_t\left(1+\frac{\gamma-1}{2}M_{sc}^2\right)}} = 0.29 kg s^{-1}, \tag{A.6}$$

$$\frac{\partial \dot{m}_{sc}}{\partial T_t} = \frac{\partial}{\partial T_t}\left(p_{sc} A M_{sc}\sqrt{\gamma\left(\frac{1+\frac{\gamma-1}{2}M_{sc}^2}{RT_t}\right)}\right) = -\frac{A\gamma M_{sc} p_{sc}\left(1+\frac{\gamma-1}{2}M_{sc}^2\right)}{2RT_t^2\sqrt{\gamma\left(\frac{1+\frac{\gamma-1}{2}M_{sc}^2}{RT_t}\right)}} = -6.59\text{e}{-4} K^{-1} \tag{A.7}$$

and

$$\frac{\partial \dot{m}_{sc}}{\partial p_{sc}} = \frac{\partial}{\partial p_{sc}}\left(p_{sc} A M_{sc}\sqrt{\gamma\left(\frac{1+\frac{\gamma-1}{2}M_{sc}^2}{RT_t}\right)}\right) = A M_{sc}\sqrt{\gamma\left(\frac{1+\frac{\gamma-1}{2}M_{sc}^2}{RT_t}\right)} = 7.34\text{e}{-6} ms. \tag{A.8}$$

Equation A.3 has dependencies on p, $\dot{m}_{sc}$ and T_t. These are

$$\frac{\partial M_v}{\partial p_v} = \frac{\partial}{\partial p_v}\left(\sqrt{\frac{-p_v^2 A_v^2\gamma \pm \sqrt{\left(p_v^2 A_v^2\gamma\right)^2 - 4\left(p_v^2 A_v^2\frac{\gamma(\gamma-1)}{2}\right)\left(-\dot{m}_{sc}^2 RT_t\right)}}{2\left(p_v^2 A_v^2\frac{\gamma(\gamma-1)}{2}\right)}}\right) \tag{A.9}$$

$$= -\frac{\sqrt{2}\dot{m}_{sc}^2 RT_t}{p_v\sqrt{p_v^2\left(A_v^4\gamma^2 p_v^2 + 4A_v^2\gamma\frac{\gamma-1}{2}\dot{m}_{sc}^2 RT_t\right)}\sqrt{\frac{\sqrt{p_v^2\left(A_v^4\gamma^2 p_v^2+4A_v^2\gamma\frac{\gamma-1}{2}\dot{m}_{sc}^2 RT_t\right)}-A_v^2\gamma p_v^2}{A_v^2\gamma\frac{\gamma-1}{2}p_v^2}}} = -1.44\text{e}{-6} ms^2 kg^{-1}, \tag{A.10}$$

$$\frac{\partial M_v}{\partial T_t} = \frac{\partial}{\partial T_t}\left(\sqrt{\frac{-p_v^2 A_v^2\gamma \pm \sqrt{\left(p_v^2 A_v^2\gamma\right)^2 - 4\left(p_v^2 A_v^2\frac{\gamma(\gamma-1)}{2}\right)\left(-\dot{m}_{sc}^2 RT_t\right)}}{2\left(p_v^2 A_v^2\frac{\gamma(\gamma-1)}{2}\right)}}\right) \tag{A.11}$$

$$= \frac{\dot{m}_{sc}^2 R}{\sqrt{2}\sqrt{p_v^2\left(A_v^4\gamma^2 p_v^2 + 4A_v^2\gamma\frac{\gamma-1}{2}\dot{m}_{sc}^2 RT_t\right)}\sqrt{\frac{\sqrt{p_v^2\left(A_v^4\gamma^2 p_v^2+4A_v^2\gamma\frac{\gamma-1}{2}\dot{m}_{sc}^2 RT_t\right)}-A_v^2\gamma p_v^2}{A_v^2\gamma\frac{\gamma-1}{2}p_v^2}}} = 5.13\text{e}{-4} K^{-1}. \tag{A.12}$$

and

$$\frac{\partial M_v}{\partial \dot{m}_{sc}} = \frac{\partial}{\partial \dot{m}_{sc}}\left(\sqrt{\frac{-p_v^2 A_v^2\gamma \pm \sqrt{\left(p_v^2 A_v^2\gamma\right)^2 - 4\left(p_v^2 A_v^2\frac{\gamma(\gamma-1)}{2}\right)\left(-\dot{m}_{sc}^2 RT_t\right)}}{2\left(p_v^2 A_v^2\frac{\gamma(\gamma-1)}{2}\right)}}\right) \tag{A.13}$$

$$= \frac{\sqrt{2}\dot{m}_{sc} RT_t}{\sqrt{A_v^4\gamma^2 p_v^4 + 4A_v^2\gamma\frac{\gamma-1}{2}\dot{m}_{sc}^2 RT_t}\sqrt{\frac{\sqrt{A_v^4\gamma^2 p_v^4+4A_v^2\gamma\frac{\gamma-1}{2}\dot{m}_{sc}^2 RT_t}-A_v^4\gamma p_v^2}{A_v^2\gamma\frac{\gamma-1}{2}p_v^2}}} = 0.78 kg^{-1} s \tag{A.14}$$

At last, equation A.4 depends on M_v and p_v. The dependencies are

$$\frac{\partial p_t}{\partial M_v} = \frac{\partial}{\partial M_v}\left(p_v\left(1+\frac{\gamma-1}{2}M_v^2\right)^{\frac{\gamma}{\gamma-1}}\right) = \gamma M_v p_v\left(1+\frac{\gamma-1}{2}M_v^2\right)^{\frac{1}{\gamma-1}} = 8.74\text{e}4 ms^2 kg^{-1} \tag{A.15}$$

and

$$\frac{\partial p_t}{\partial p_v} = \frac{\partial}{\partial p_v}\left(p_v\left(1+\frac{\gamma-1}{2}M_v^2\right)^{\frac{\gamma}{\gamma-1}}\right) = \left(1+\frac{\gamma-1}{2}M_v^2\right)^{\frac{\gamma}{\gamma-1}} = 1.06[-] \tag{A.16}$$

To find the propagation of error in equations A.1 through A.4 the dependencies derived above were evaluated for the measured and calculated values. The error in each equation can then be computed by taking the norm of the product of each dependency and error, as by equation 5.15. Considering the parameters and dependencies per equation, the propagation of error is computed through these equations. Starting with the error in the shock angle, which directly results in an error in Mach number for internal channel flow in supercritical condition,

$$\varepsilon_{M_{sc}} = \sqrt{\left(\frac{\partial M_{sc}}{\partial \mu}\varepsilon_\mu\right)^2} = \sqrt{(-2.43\cdot 1.75\text{e}{-2})^2} = 4.25\text{e}{-2}. \tag{A.17}$$

This error, combined with the error in temperature and pressure measurements provide the error in mass flow into the intake,

$$\varepsilon_{\dot{m}_{sc}} = \sqrt{\left(\frac{\partial \dot{m}_{sc}}{\partial M_{sc}}\varepsilon_{M_{sc}}\right)^2 + \left(\frac{\partial \dot{m}_{sc}}{\partial T_t}\varepsilon_{T_t}\right)^2 + \left(\frac{\partial \dot{m}_{sc}}{\partial p_{sc}}\varepsilon_{p_{sc}}\right)^2} \tag{A.18}$$

$$= \sqrt{(0.29\cdot 4.25\text{e}{-2})^2 + (-6.59\text{e}{-4}\cdot 0.1)^2 + (7.34\text{e}{-6}\cdot 3)^2} = 1.26\text{e}{-2} kgs^{-1}. \tag{A.19}$$

With error in mass flow known, the error in temperature and pressure are used again to compute the error in Mach number at the valve

$$\varepsilon_{M_v} = \sqrt{\left(\frac{\partial M_v}{\partial \dot{m}_{sc}}\varepsilon_{\dot{m}_{sc}}\right)^2 + \left(\frac{\partial M_v}{\partial p_v}\varepsilon_{p_v}\right)^2 + \left(\frac{\partial M_v}{\partial T_t}\varepsilon_{T_t}\right)^2} \tag{A.20}$$

$$= \sqrt{(0.78\cdot 1.26\text{e}{-2})^2 + (-1.44\text{e}{-6}\cdot 3)^2 + (5.13\text{e}{-4}\cdot 0.1)^2} = 0.99\text{e}{-2}. \tag{A.21}$$

And finally for the error in total pressure, the Mach number error and error in valve pressure are needed.

$$\varepsilon_{p_t} = \sqrt{\left(\frac{\partial p_t}{\partial M_v}\varepsilon_{M_v}\right)^2 + \left(\frac{\partial p_t}{\partial p_v}\varepsilon_{p_v}\right)^2} \tag{A.22}$$

$$= \sqrt{(8.743\text{e}4\cdot 0.99\text{e}{-2})^2 + (1.06\cdot 3)^2} = 9.18 mbar \tag{A.23}$$

Note that, as mentioned in Section 5.5.3, the error for pressure and temperature measurements are relatively small compared to error in the shock angle. It can be seen to propagate through equations A.17 through A.22 in the first terms in the square root. Its contribution to all errors is large relative to the other terms.

B

PIV measurements

It was found that due to hardware limitations PIV was impossible at Mach numbers higher than 2. In addition, the results from the successful measurements of the expansion section were not useful due to a lack of seeding close to the flow surface after the expansion. It was therefore decided to cancel the PIV measurements in the second test slot, where the full SSI model would be tested. However, the lessons learned from setting up the PIV measurements are still worth noting, thus the experimental setup and the few successful results will be discussed briefly.

B.1. PIV setup

The seeder installed in the settling chamber of the ST-15 used Di-Ethyl-Hexyl-Sebacat, or DEHS. Its operating range was limited to $5bar$ of pressure in the settling chamber. When the settling chamber pressure exceeded that, no particles are seeded into the flow.

The PIV laser was a Quantel Evergreen 200. The laser sheet is formed in a probe located downstream of the test section. Using a set of mirrors the probe converts the laser beam from the Evergreen laser to a sheet that is directed into the test section from the downstream direction.

The cameras used are SCMOS cameras with a pixel size of $6.5\mu m$ and a resolution of 2160 by 2560 pixels. Two cameras were used in a stereo PIV setup, with one camera on either side of the wind tunnel. The angles between the cameras and the laser sheet plane normal being approximately $32°$ and $151°$. The lens attached to the camera had a focal length of $35mm$ and an f_{stop} of 11 was used. Taking into account the pixel size and flow velocity, the time between PIV images was decided to be $\Delta t = 2\mu s$. The frame rate was decided based on the need for sufficient images, namely 300, and the fact that the measurement should not be longer than about 20 seconds, because the PIV particles will cloud the wind tunnel windows and the PIV laser probe which would reduce the accuracy of the results. The 300 required images and the maximum measurement time determined the frame rate at $15Hz$.

B.2. Experiments

The stereo PIV system was set up as described in Section B.1. This allowed for the opening of the wind tunnel side doors without having to remove the cameras and recalibrate the PIV-system. The set-up with cameras attached to the side doors does however get in the way of schlieren measurements, which means that this set-up did not enable performing schlieren and PIV measurements simultaneously.

Test measurements were done at Mach 2. In the PIV images from the first test runs, the laser reflections caused a lot of noise in the images. Therefore, part of the expansion section was covered with low-reflection tape, just like some edges on the windows where reflections were an issue. Figure B.2 shows such reflections in a raw PIV image. The edge of the ST-15 window in the background is clearly visible. The area of light background would impede the PIV post-processing and was therefore taped off with a matte black cover. Also, the area where the laser sheet hits the expansion surface was covered with matte black tape, also visible in Figure B.2.

No PIV measurements could be done for Mach numbers higher than 2, since the required total pressure of $7.0bar$ for Mach 2.5 free stream flow exceeded the maximum allowable pressure of the seeder of $5.0bar$.

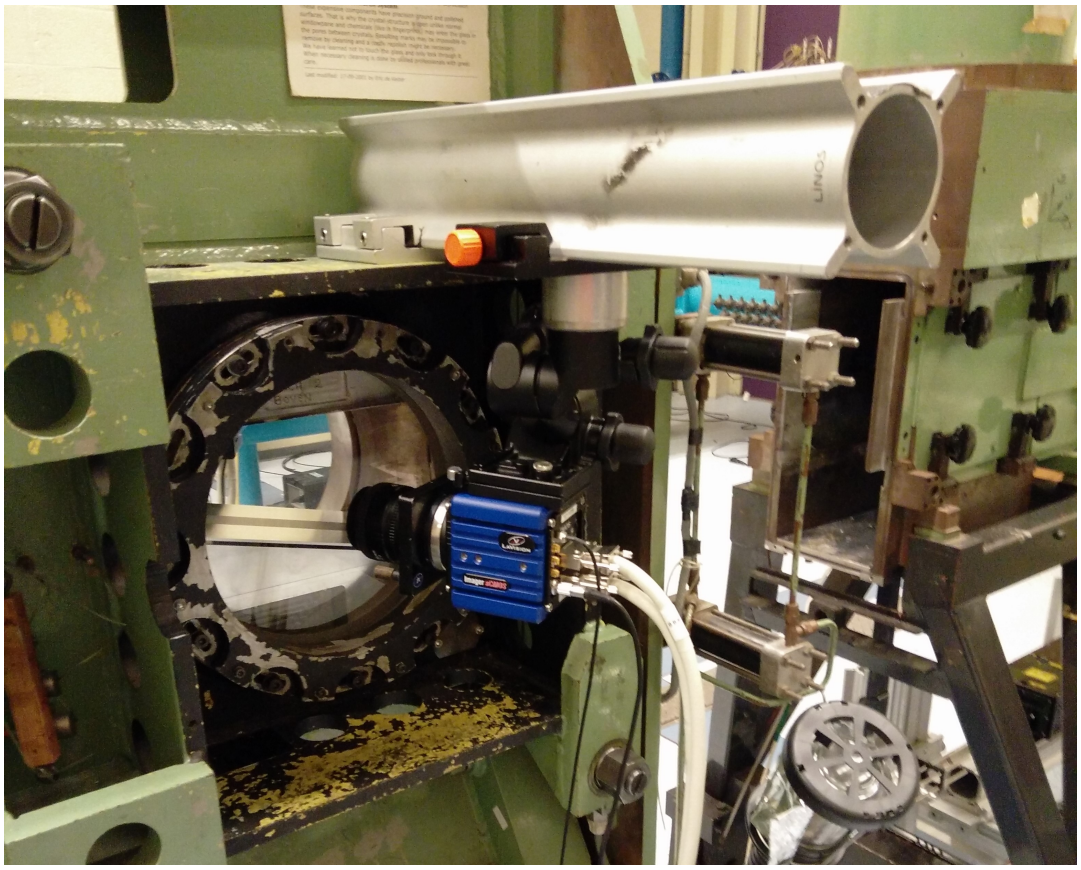

Figure B.1: Picture of the PIV-camera setup, suspended from an x-beam clamped to the ST-15 side door

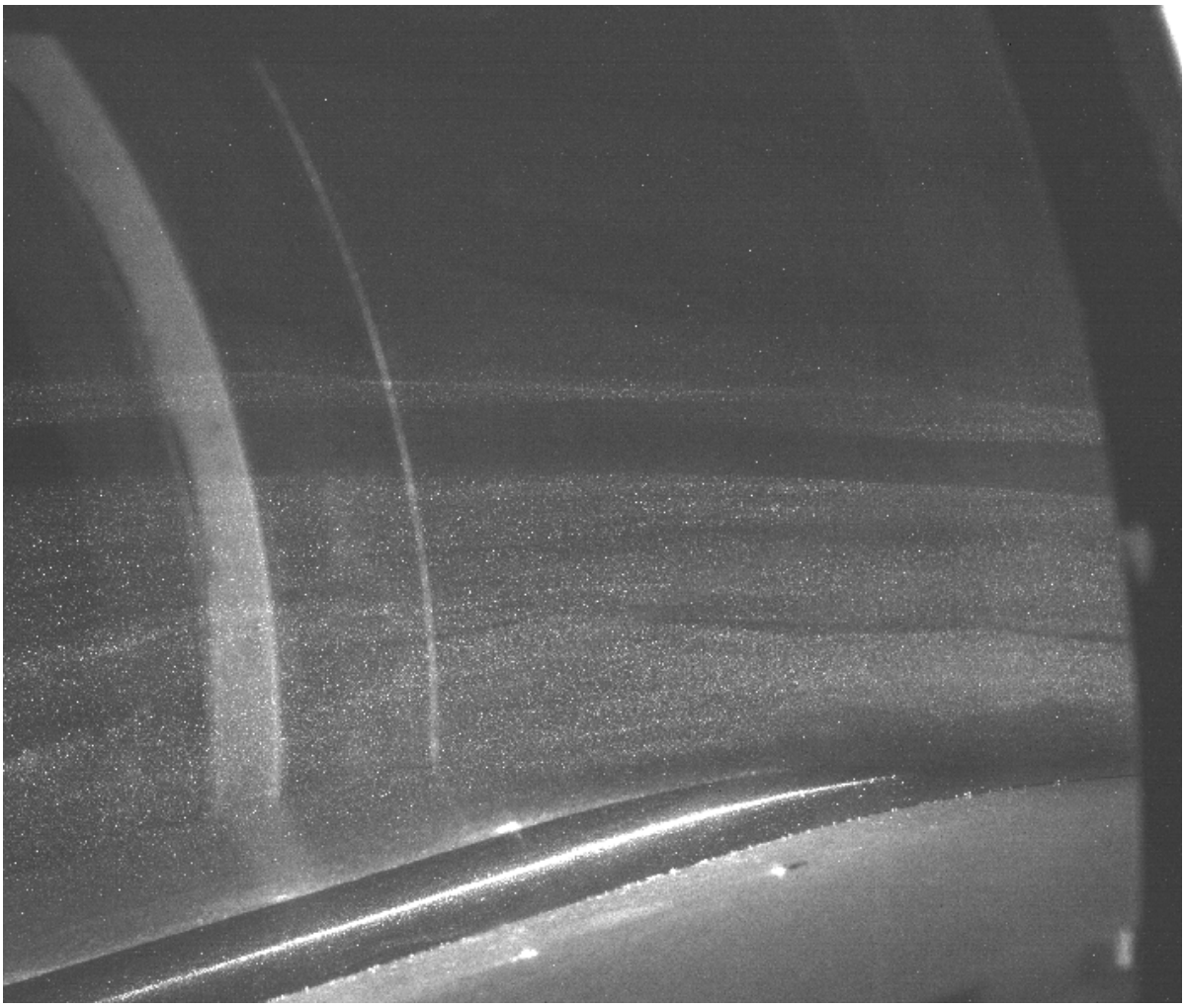

Figure B.2: Example of unwanted laser light reflections in the test section of the ST-15

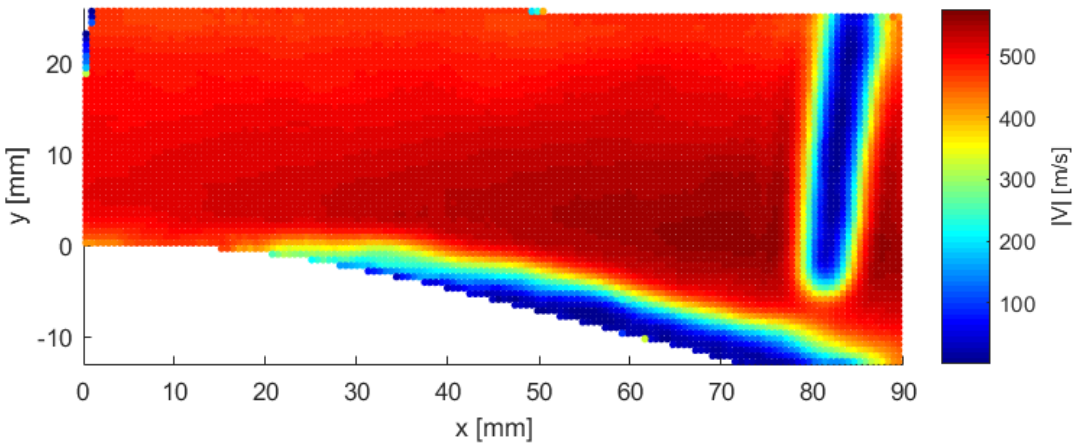

Figure B.3: Absolute velocity of the PIV flowfield around the expansion section at Mach number 2

B.3. Results

PIV processing was done in DaVis 8. The processing used window sizes of 64 pixels, with an overlap of 75% and two passes through each image. The result for these processing settings is seen in Figure B.3. It is clear that close to the flow surface, the velocity seems to drop significantly, which most likely was caused by a lack of seeding. If the velocity drop was due to a thick boundary layer, it would have been visible on the flow surface ahead of the expansion, at $x < 10mm$.

An effort was made to use the little seeding available close to the flow surface by masking any flow but the boundary layer. The result of this can be seen in Figure B.4. The same processing settings were used, but also some vector post-processing was used that removed all vectors outside a certain range, which provided a filter for noise. Then using interpolation a flowfield may still be formed. However, the focus on the boundary layer also gave in disappointing results.

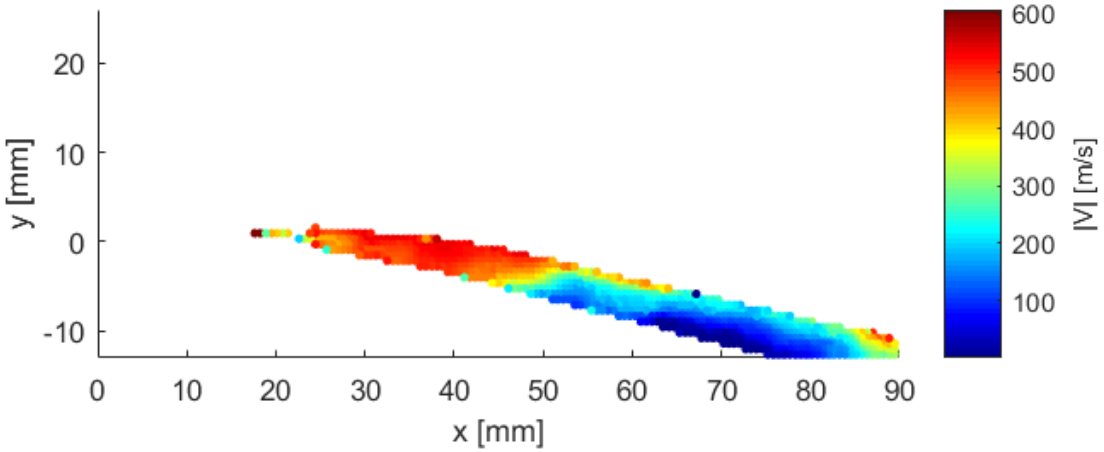

Figure B.4: Absolute velocity of the PIV flowfield around the expansion section at Mach number 2, focused on the boundary layer

C

Comparison of static pressure and schlieren images

To obtain a good view of the relation between the static pressure and visible flow phenomena, this appendix shows the results of the static pressure measurements with corresponding schlieren visualizations in the same reference frame. Critical and supercritical flow are shown in this appendix. Note that the raw static pressure measurements are shown in the figures below. Any outliers, as described in Section 5.5.2, have not been removed from the shown data.

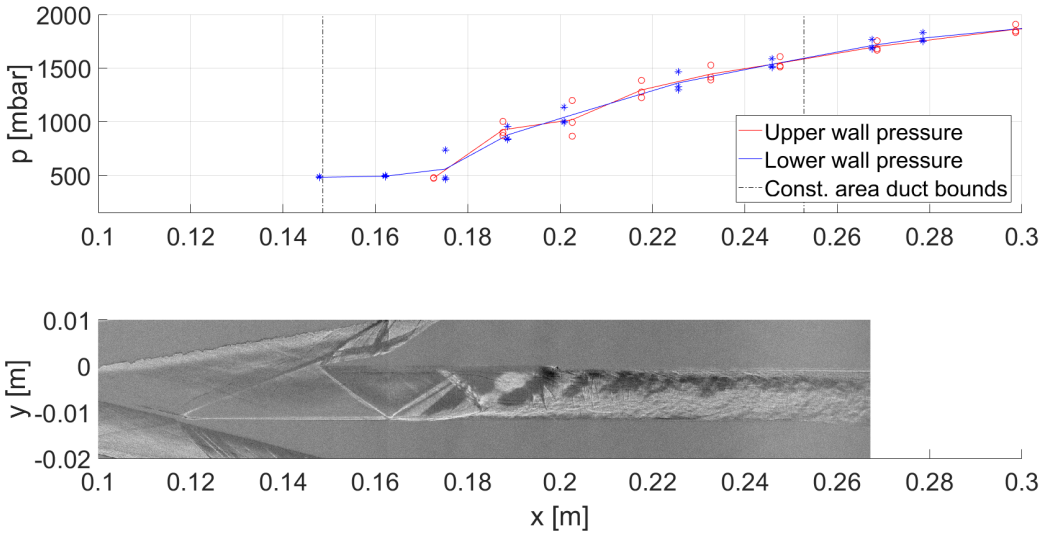

Figure C.1: Critical condition of single shock intake at $M = 2$

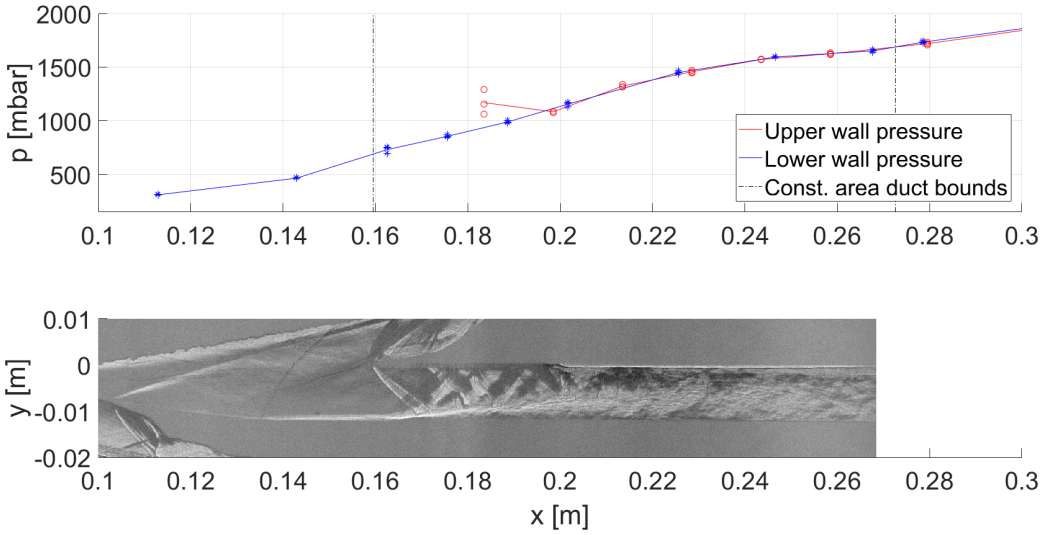

Figure C.2: Critical condition of double shock intake at $M = 2$

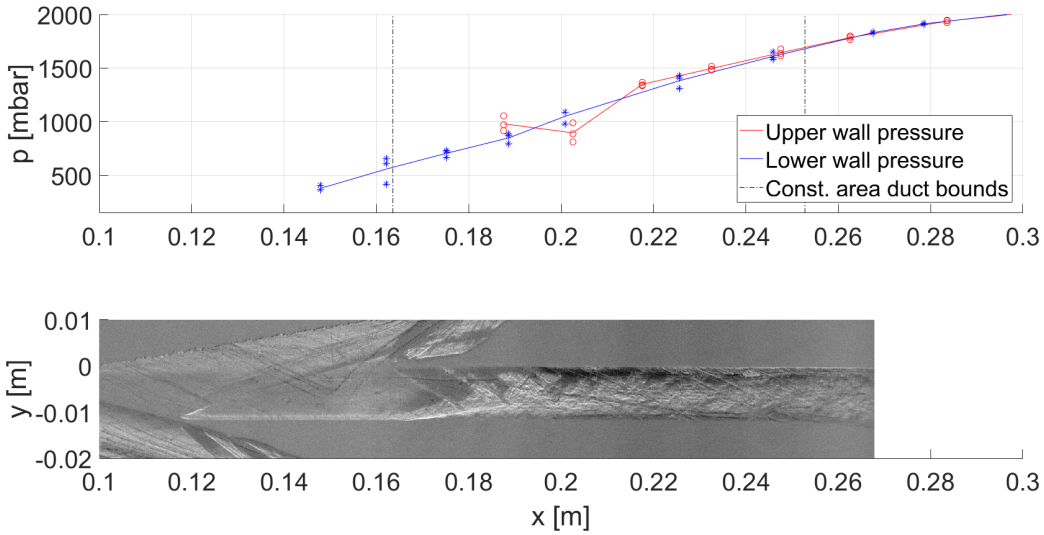

Figure C.3: Critical condition of single shock intake at $M = 2.5$

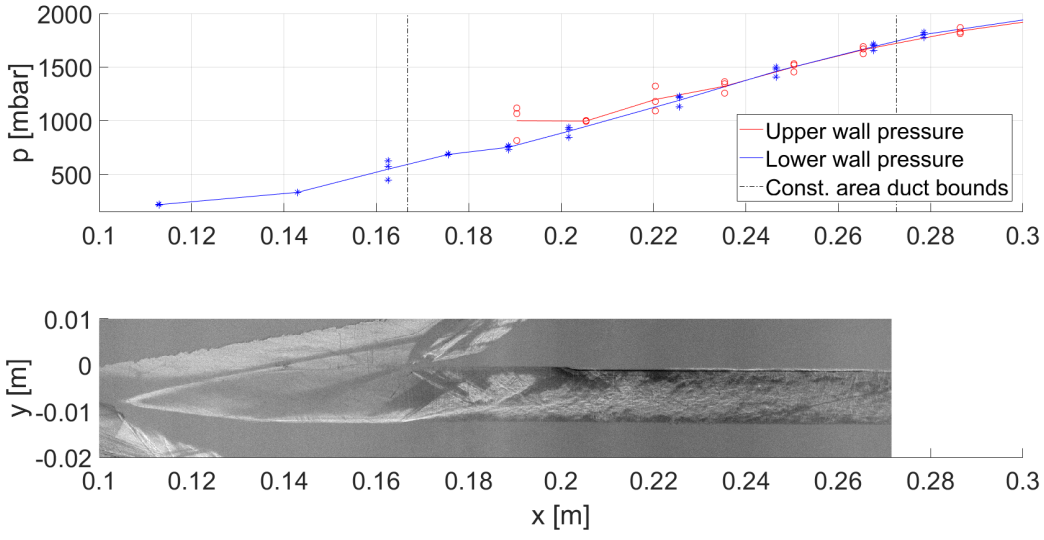

Figure C.4: Critical condition of double shock intake at $M = 2.5$

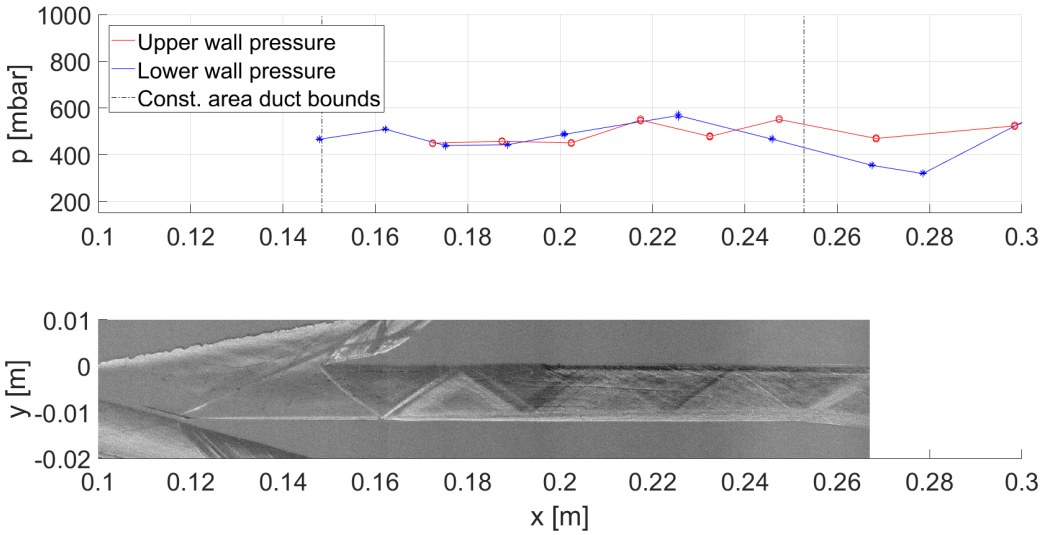

Figure C.5: Supercritical condition of single shock intake at $M = 2$

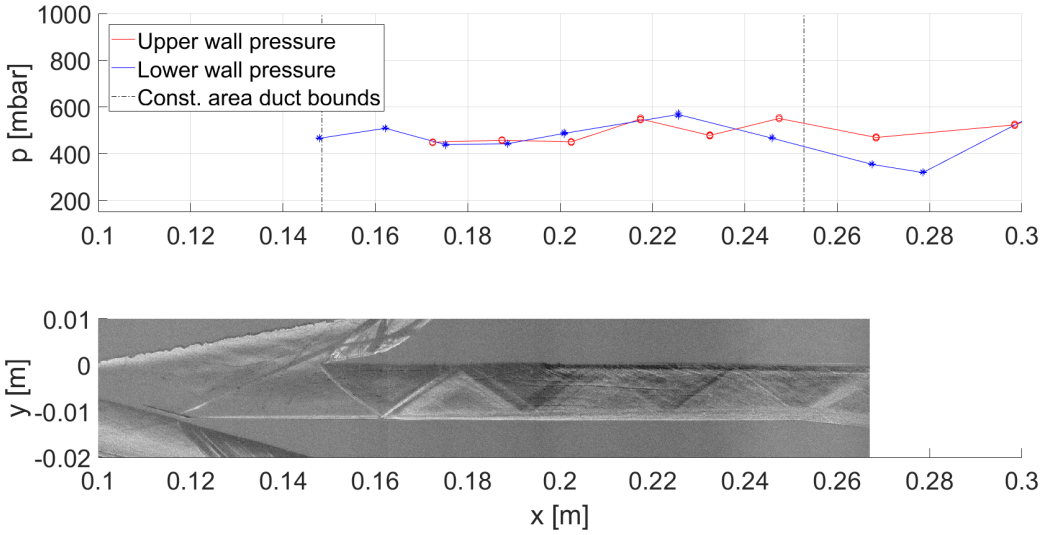

Figure C.6: Supercritical condition of double shock intake at $M = 2$

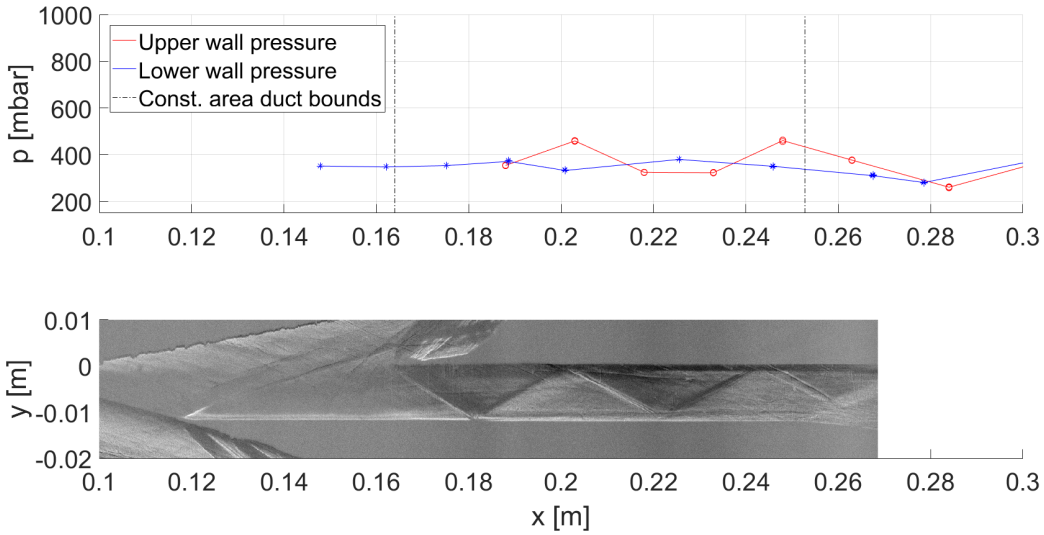

Figure C.7: Supercritical condition of single shock intake at $M = 2.5$

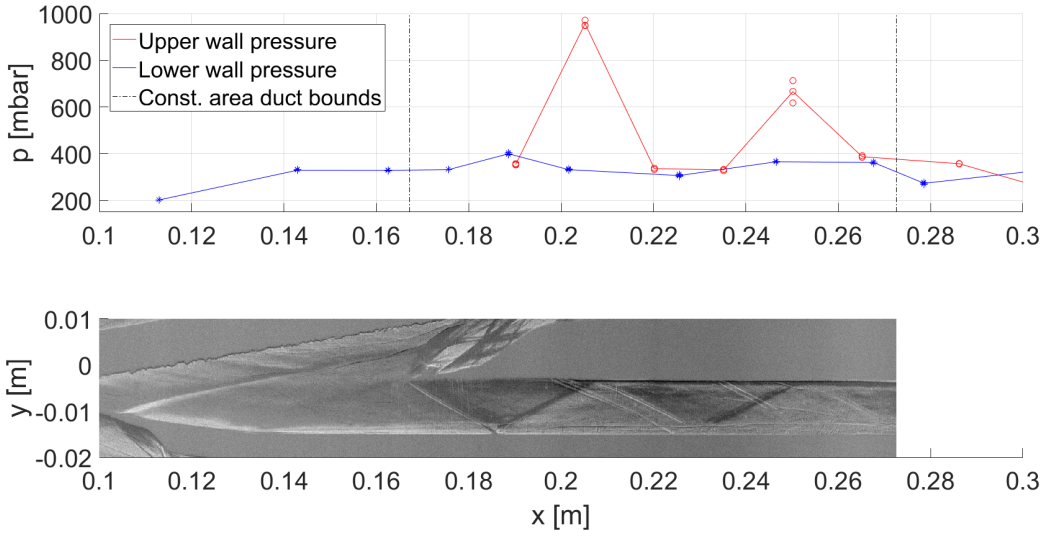

Figure C.8: Supercritical condition of double shock intake at $M = 2.5$

D

Technical drawings of submerged supersonic intake wind tunnel model

This appendix contains the technical drawings of the different parts of the submerged supersonic intake wind tunnel model.

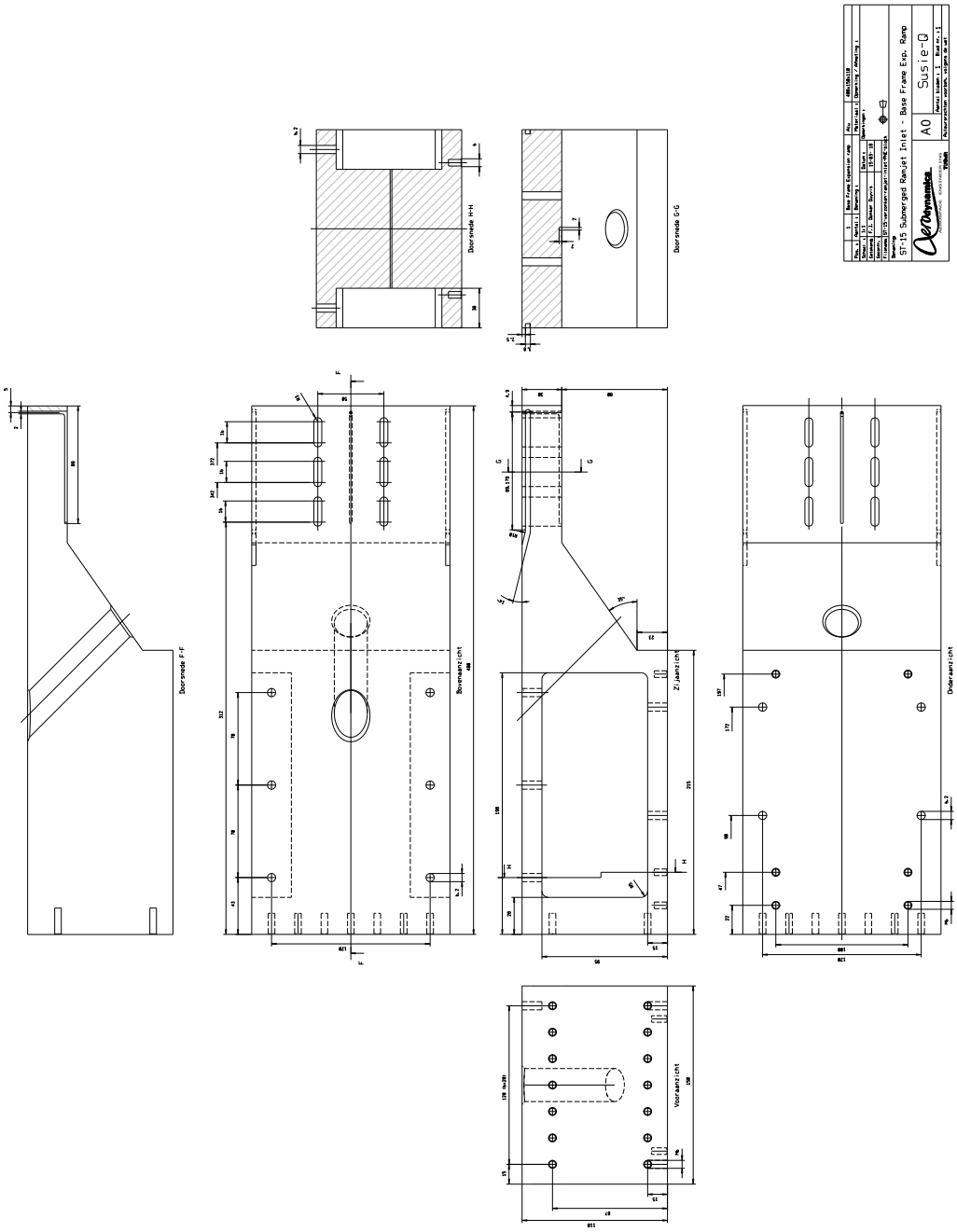

Figure D.1: Submerged supersonic intake support block

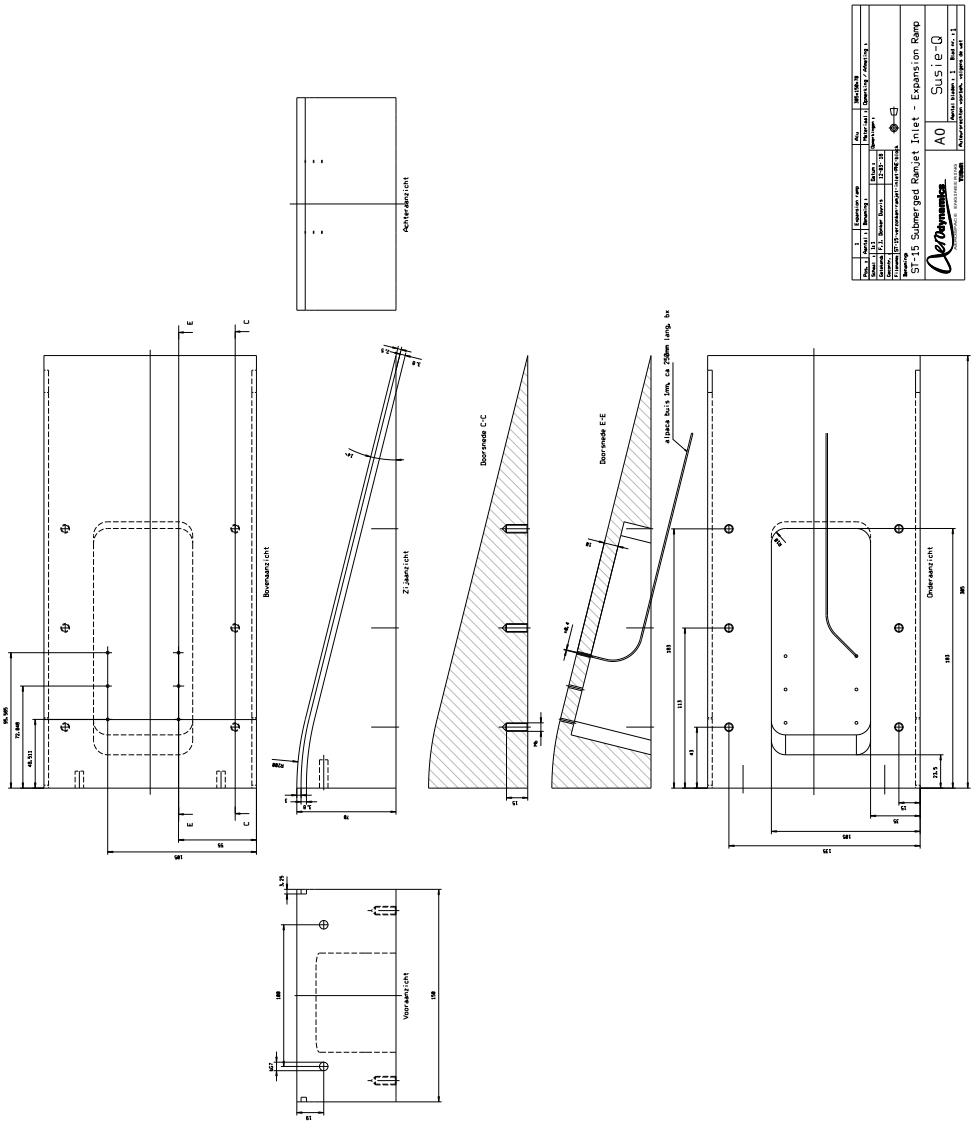

Figure D.2: Expansion section

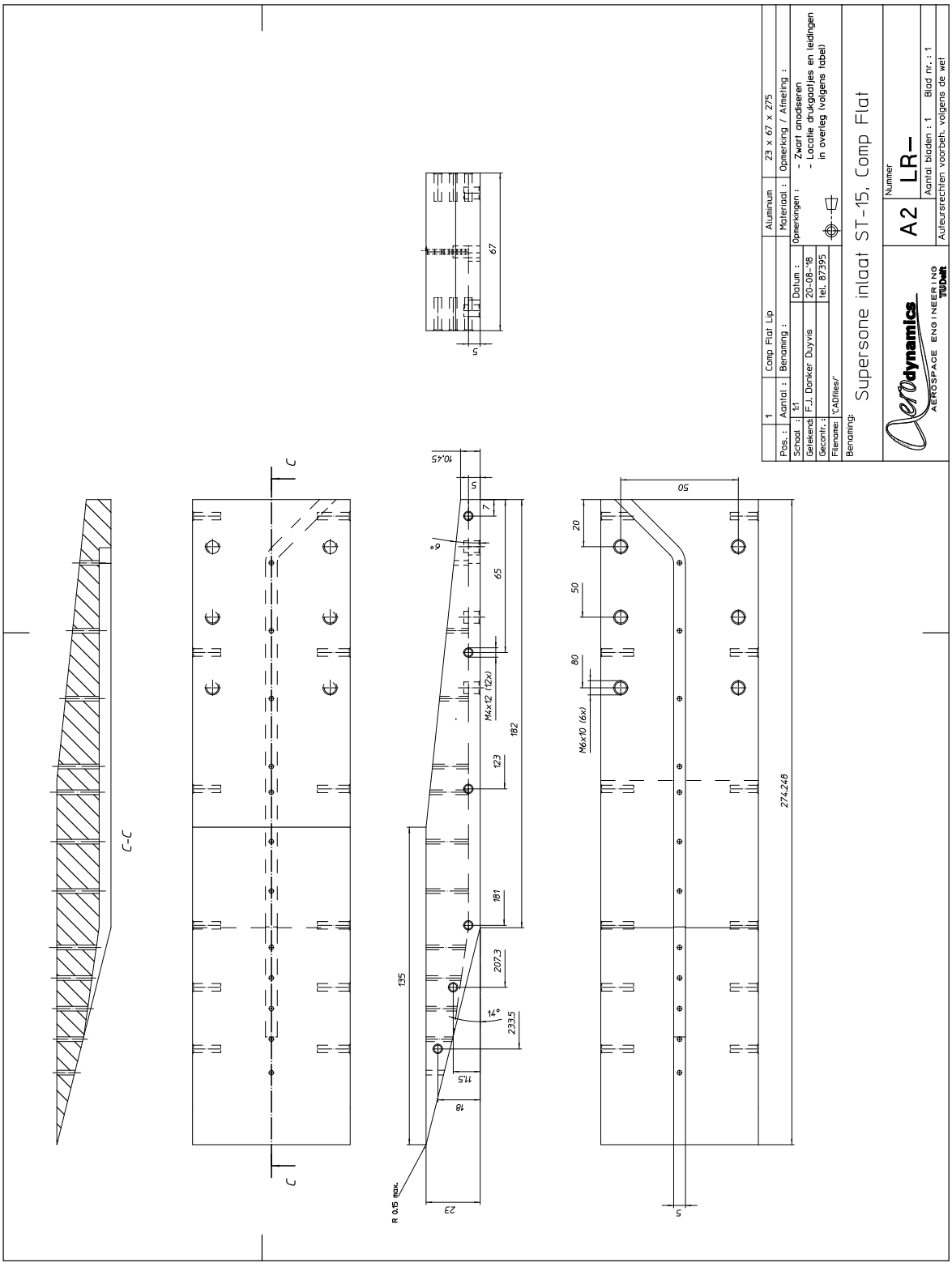

Figure D.3: Single shock compression surface

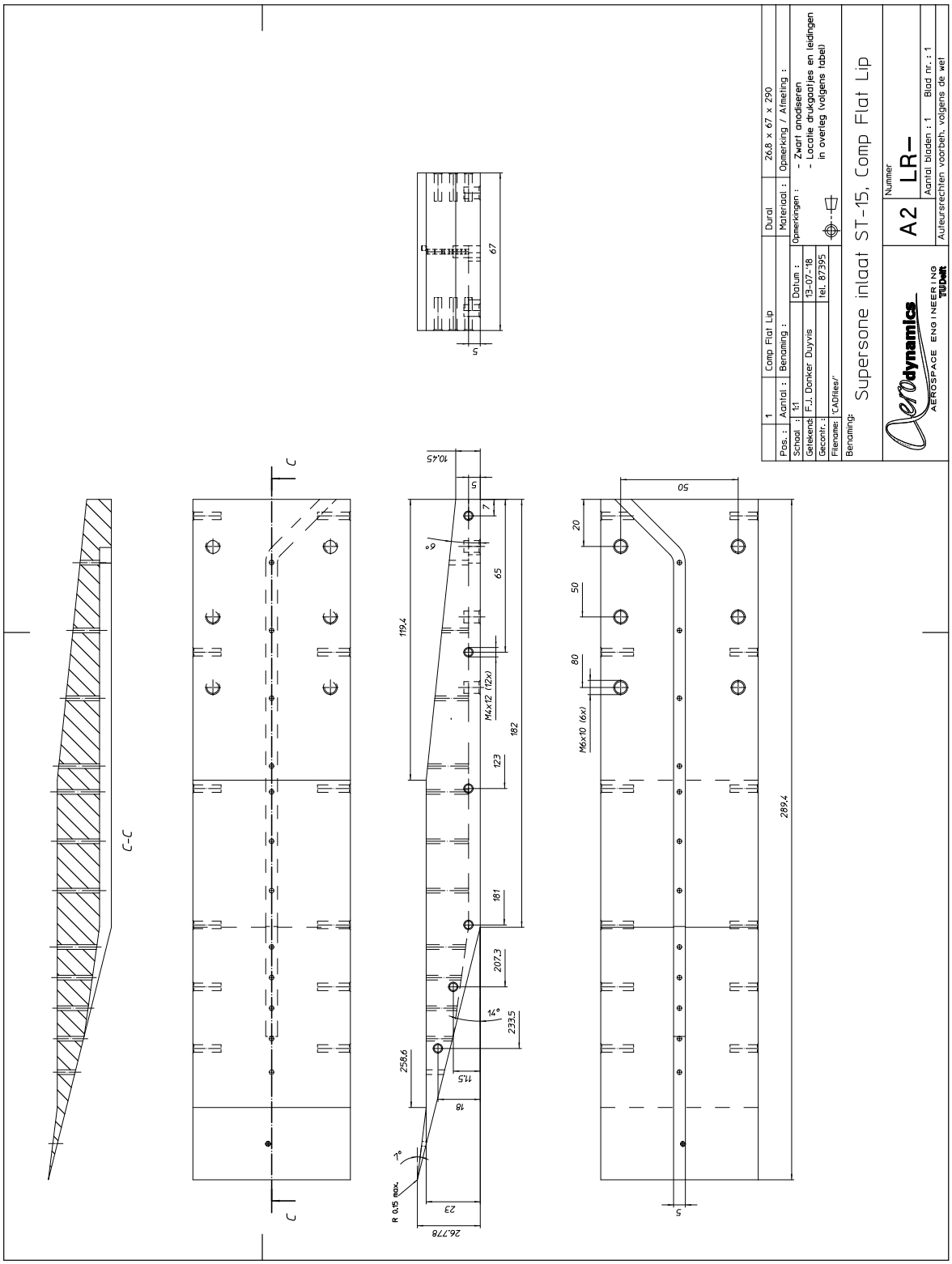

Figure D.4: Double shock compression surface

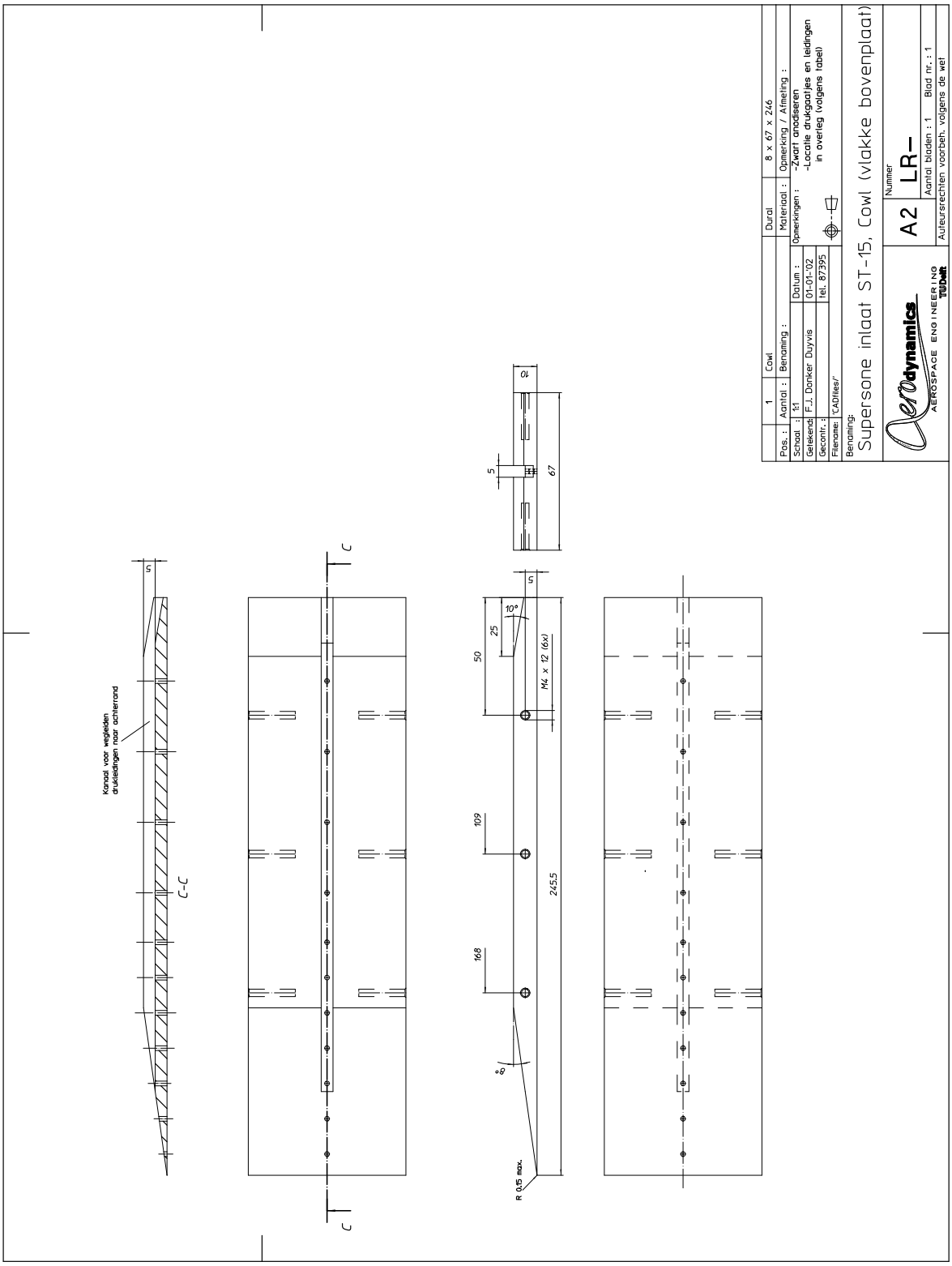

Figure D.5: Cowling

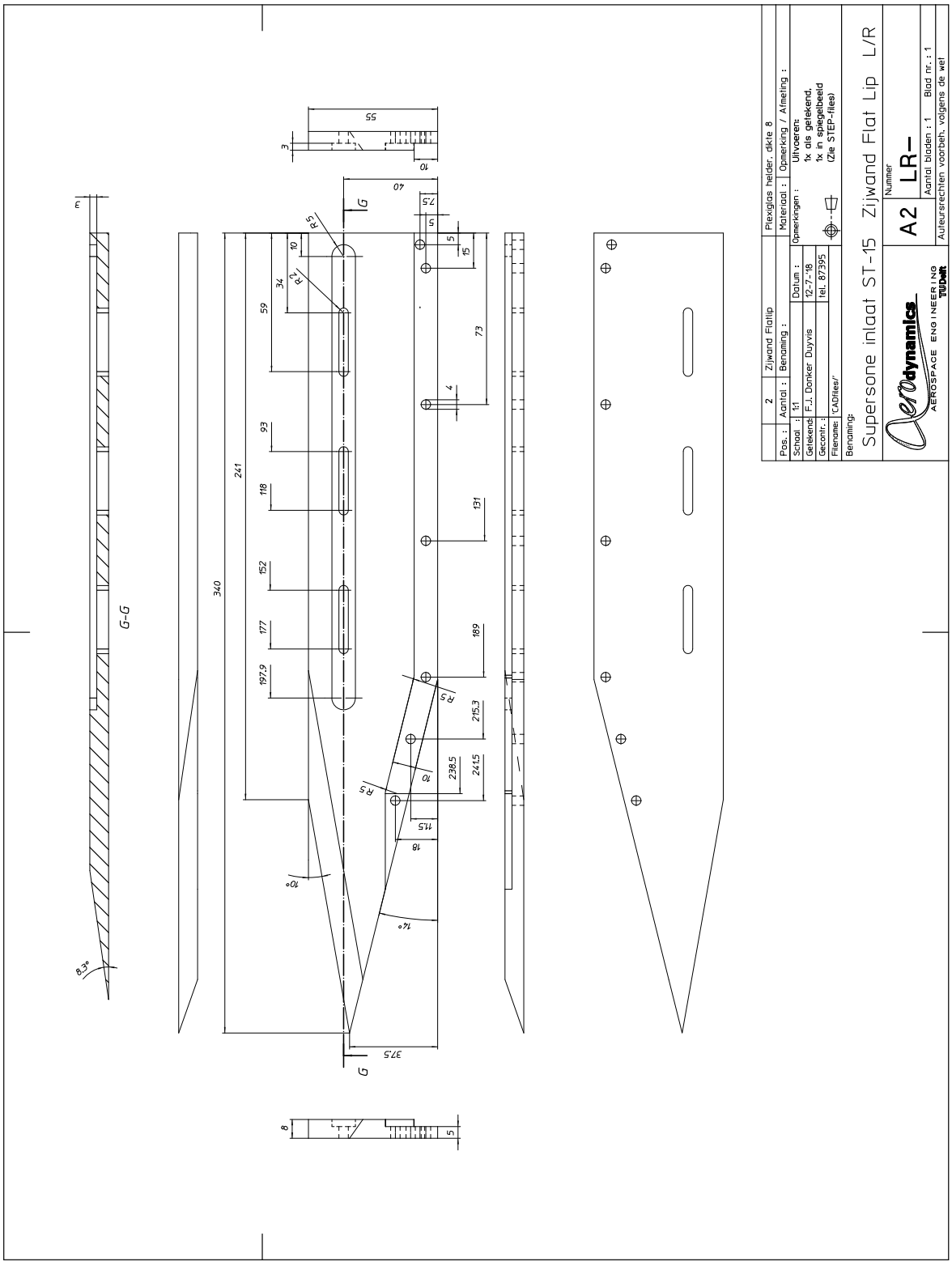

Figure D.6: Sidewalls

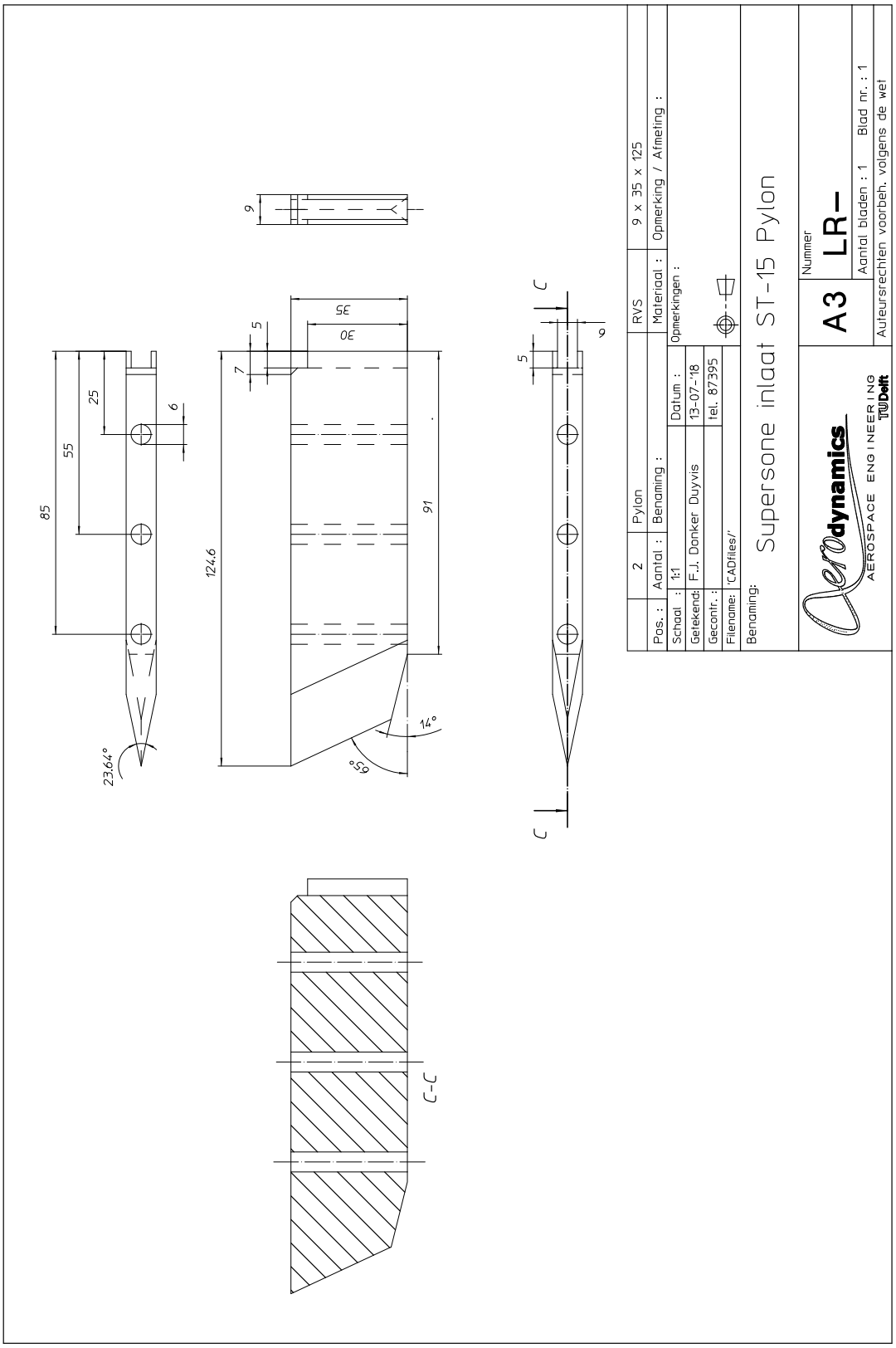

Figure D.7: Support pylon

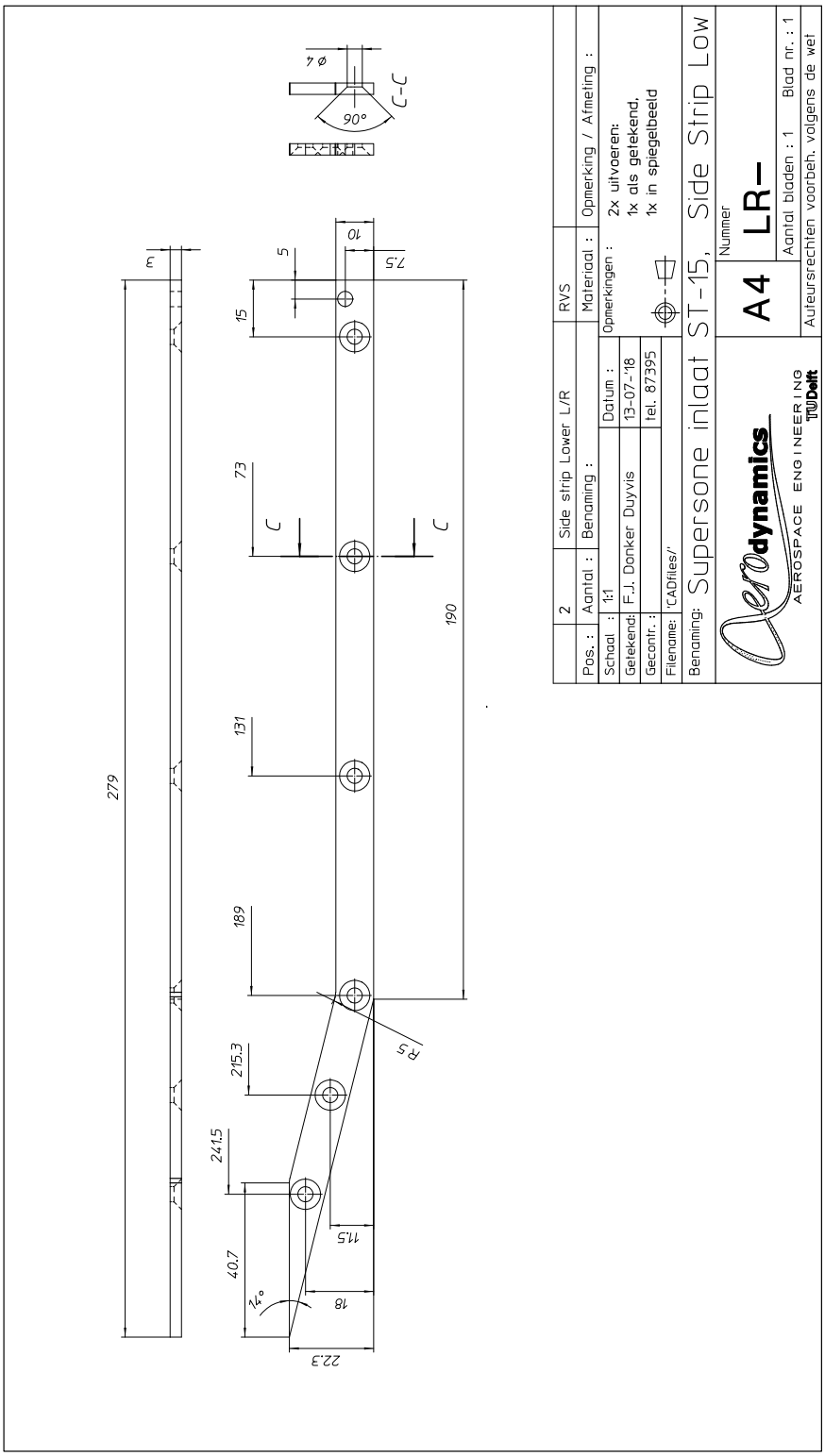

Figure D.8: Lower sidewall strip

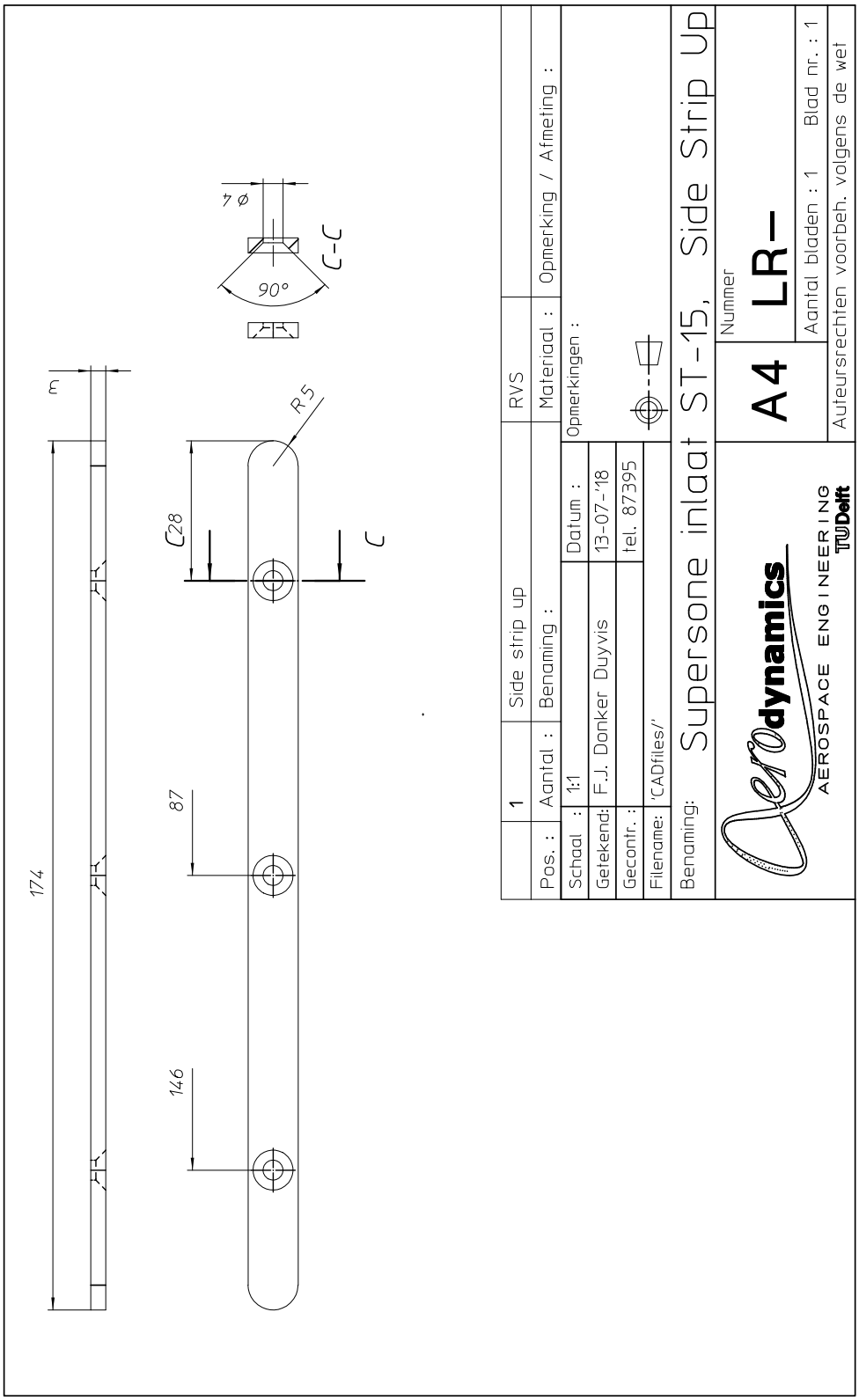

Figure D.9: Upper sidewall strip

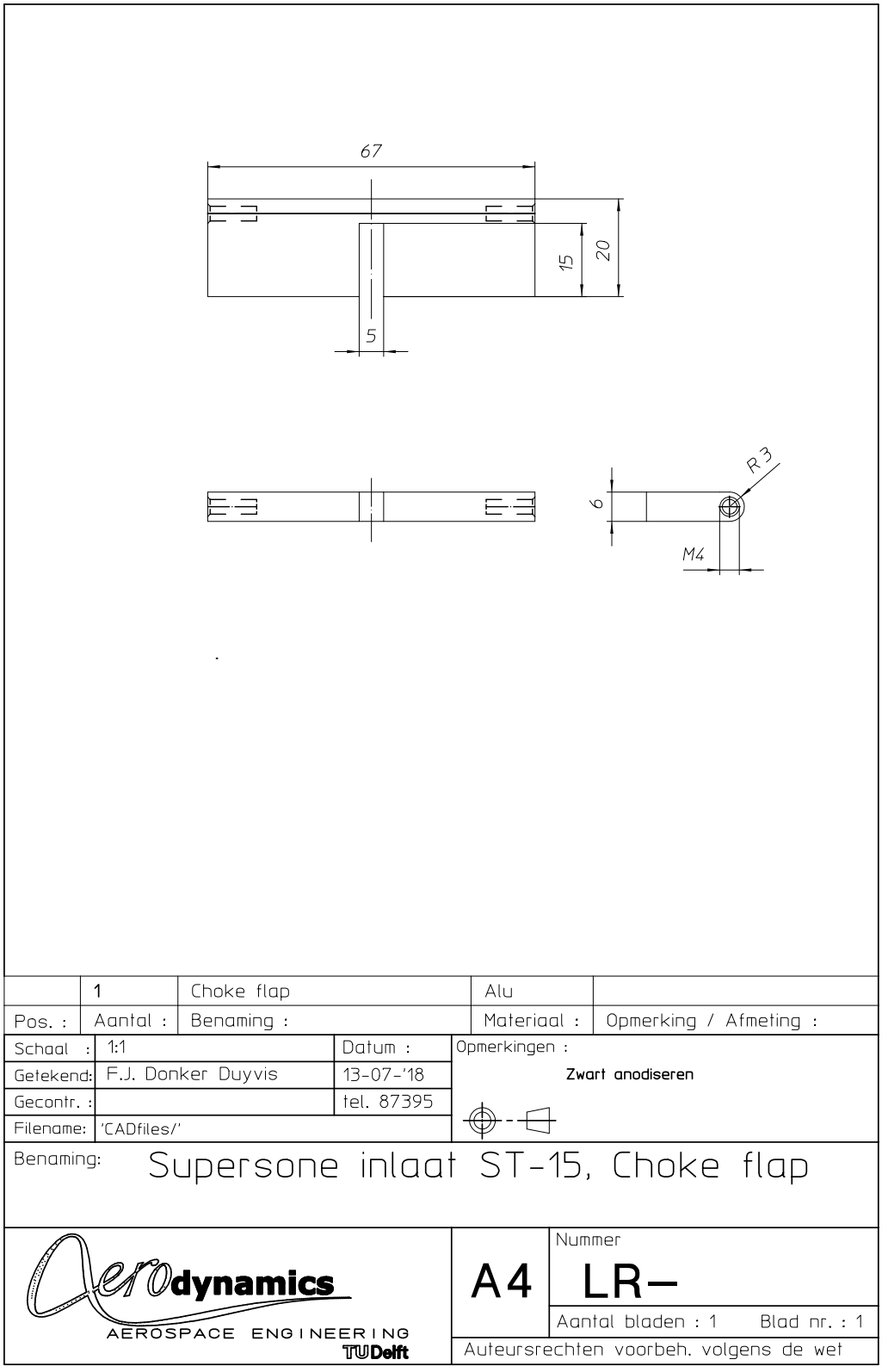

Figure D.10: Mass flow choke valve

E

Technical drawings of Oswatitsch intake windtunnel model

This appendix contains some preliminary drawings of parts of an SSI wind tunnel model of an intake based on the Oswatitsch design routine, introduced in Chapter 7. Note that for the total intake model, many parts of the existing SSI model can be reused, namely the expansion section, SSI support block, support pylons, cowling and mass flow valve system. The parts that have to be newly made are the compression surface and the sidewall, the drawings for these are shown below.

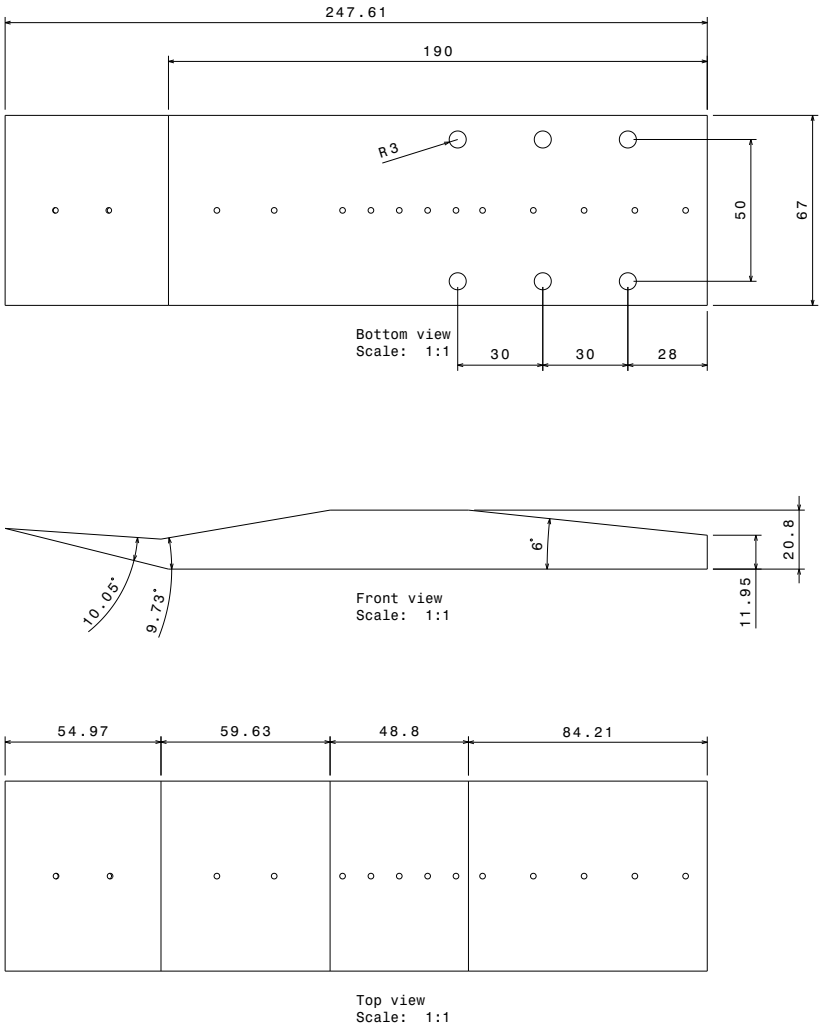

Figure E.1: Compression surface of Oswatitsch intake wind tunnel model compression surface

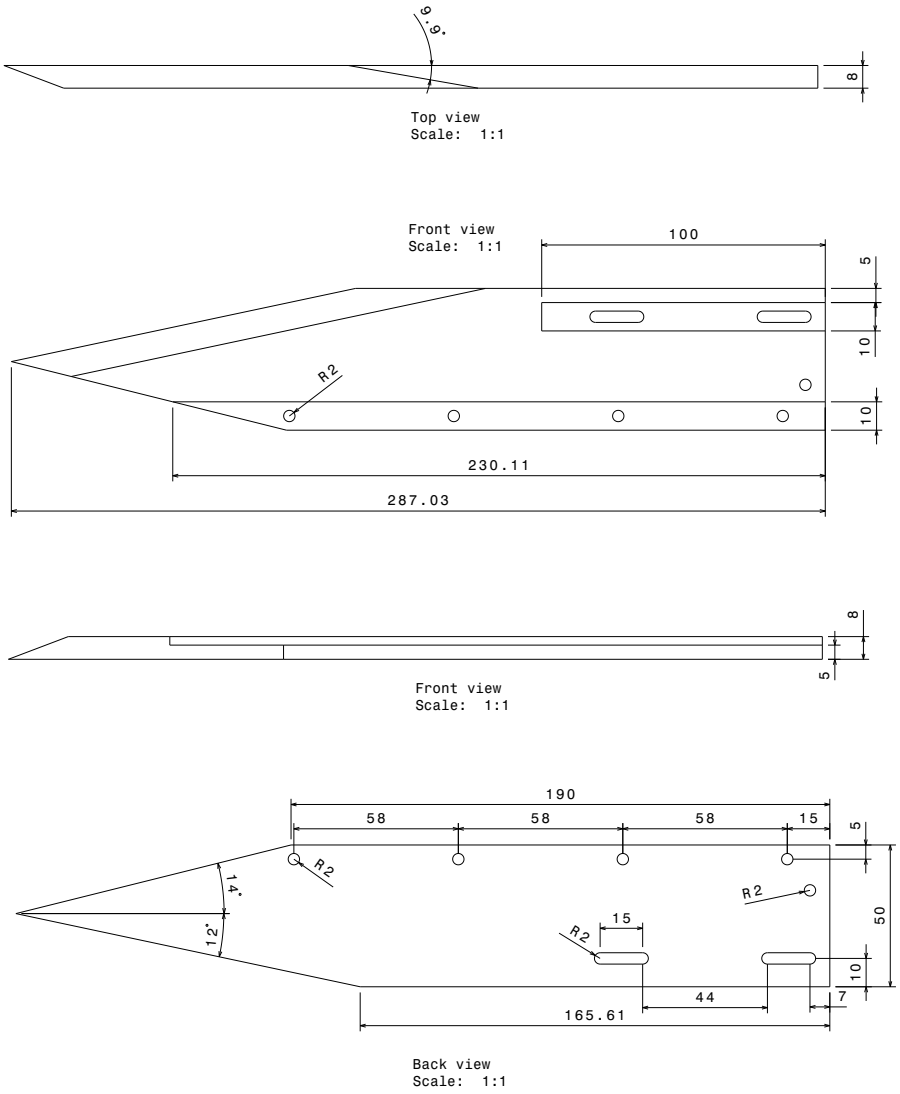

Figure E.2: Compression surface of Oswatitsch intake wind tunnel model sidewall